

©Copyright 2018
Nasser Abdulazim Marafi

Impacts of an M9 Cascadia Subduction Zone Earthquake on Structures Located in Deep Sedimentary Basins

Nasser Abdulazim Marafi

A dissertation
submitted in partial fulfillment of the
requirements for the degree of

Doctor of Philosophy

University of Washington

2018

Reading Committee:

Jeffrey W. Berman, Chair

Marc O. Eberhard, Chair

Arthur D. Frankel

Dawn E. Lehman

Steve L. Kramer

Program Authorized to Offer Degree:
Civil and Environmental Engineering

University of Washington

Abstract

Impacts of an M9 Cascadia Subduction Zone Earthquake on Structures Located in Deep Sedimentary Basins

Nasser Abdulazim Marafi

Co-Chairs of the Supervisory Committee:

Associate Professor Jeffrey W. Berman
Civil and Environmental Engineering

Professor Marc O. Eberhard
Civil and Environmental Engineering

Thirty scenarios of magnitude-9 Cascadia subduction interface earthquakes were simulated by a research team from the United States Geological Survey and the University of Washington. These motions were strongly modified by the deep sedimentary basins that underlie much of the Puget Sound region. The simulated motions within the basin had high spectral accelerations at moderate-to-long periods, damaging spectral shapes, long durations, and varied greatly among the scenarios. The simulated effects of the Seattle basin were consistent with those observed for Japanese basins during subduction earthquakes.

The response of deteriorating single-degree-of-freedom oscillators suggests that an M9 event could inflict widespread damage across much of the Puget Sound region. Using an improved modeling methodology, the seismic response was estimated for 32 reinforced concrete wall archetypes designed for Seattle. The collapse risk for these structures exceeded values targeted by current codes, particularly when the archetypes were designed to barely meet the code requirements. The damage estimates correlated well with a new measure of ground-motion intensity that reflects the contributions from spectral acceleration, spectral shape, and duration.

TABLE OF CONTENTS

| | Page |
|---|------|
| List of Figures | v |
| List of Tables | xvi |
| Chapter 1: Introduction | 1 |
| 1.1 Problem Statement | 1 |
| 1.2 M9 Project | 2 |
| 1.3 Key Research Objectives | 4 |
| 1.4 Dissertation Organization | 5 |
| Chapter 2: Background and Research Needs | 9 |
| 2.1 Chapter Overview | 9 |
| 2.2 Overview of the Seismic Hazard in the Pacific Northwest | 9 |
| 2.3 Geologic Evidence of Interface Earthquakes in the Cascadia Subduction Zone | 9 |
| 2.4 Effects of Large Magnitude Earthquakes | 11 |
| 2.5 Evidence of Damage in Large Magnitude Earthquakes | 12 |
| 2.6 Effects of Sedimentary Basins | 19 |
| 2.7 Research Needs | 25 |
| Chapter 3: Ductility-dependent intensity measure that accounts for ground-motion spectral shape and duration | 31 |
| 3.1 Chapter Overview | 31 |
| 3.2 Introduction | 32 |
| 3.3 Desirable Features of an Intensity Measure | 33 |
| 3.4 Existing IMs for Duration and Spectral Shape | 35 |
| 3.5 A New Intensity Measure | 37 |

| | | |
|--|---|-----|
| 3.6 | Evaluating the Intensity Measure using SDOF Elastic-perfectly Plastic Systems | 41 |
| 3.7 | Evaluating the Intensity Measure using Deteriorating SDOF Systems | 48 |
| 3.8 | Evaluating IM_{comb} Using Analyses of Building Collapse | 53 |
| 3.9 | Comparing Efficiency of IM_{comb} to Efficiencies of Other Shape Intensity Measures | 57 |
| 3.10 | Influence of Ductility Demand on Optimal SS_a | 58 |
| 3.11 | Chapter Conclusions | 58 |
| Chapter 4: Effects of Deep Basins on Structural Collapse during Large Subduction Earthquakes | | |
| 4.1 | Chapter Overview | 62 |
| 4.2 | Introduction | 63 |
| 4.3 | Current Treatment of Basin Effects | 65 |
| 4.4 | Seismic Stations in or Near Basins | 67 |
| 4.5 | Effects of Basin on Spectral Acceleration | 71 |
| 4.6 | Relating GMM Residuals to $Z_{2.5}$ | 74 |
| 4.7 | Effect of Earthquake Magnitude | 79 |
| 4.8 | Comparison with the Puget Lowland Basin | 80 |
| 4.9 | Evaluation of Existing Basin Terms | 82 |
| 4.10 | Effects of Basin on Significant Duration | 84 |
| 4.11 | Effects of Basin on Spectral Shape | 90 |
| 4.12 | Effects on Structural Collapse | 95 |
| 4.13 | Relative Collapse Capacity | 95 |
| 4.14 | Combined Intensity Measure | 98 |
| 4.15 | Design Factors | 102 |
| 4.16 | Compariosn with CB14 | 105 |
| 4.17 | Chapter Conclusions | 106 |
| Chapter 5: Ground Motions Simulations for an M9 Cascadia Subduction Zone Earthquake | | |
| 5.1 | Chapter Overview | 108 |
| 5.2 | Ground-Motion Generation | 108 |
| 5.3 | Spectral Acceleration | 113 |

| | | |
|---|---|-----|
| 5.4 | Summary | 127 |
| Chapter 6: Impacts of Simulated M9 Cascadia Subduction Zone Motions on Idealized Systems 128 | | |
| 6.1 | Chapter Overview | 128 |
| 6.2 | Introduction | 129 |
| 6.3 | Simulations of M9 Cascadia Subduction Zone Earthquake | 130 |
| 6.4 | Spectral Accelerations | 131 |
| 6.5 | Spectral Shape | 138 |
| 6.6 | Duration | 141 |
| 6.7 | Representative SDOF Systems | 142 |
| 6.8 | Drift Demands | 145 |
| 6.9 | Collapse Potential of Ground Motions | 147 |
| 6.10 | Accounting for Effects of Spectral Acceleration, Duration and Shape | 147 |
| 6.11 | Ductility Demands | 150 |
| 6.12 | Regional Variation of Ductility Demands | 157 |
| 6.13 | Chapter Conclusions | 158 |
| Chapter 7: Variability in Seismic Collapse Probabilities of Solid and Coupled-Wall Buildings 160 | | |
| 7.1 | Chapter Overview | 160 |
| 7.2 | Introduction | 161 |
| 7.3 | Archetype Models | 165 |
| 7.4 | Nonlinear Modelling Methodology | 170 |
| 7.5 | Collapse Probability at MCE for Archetypes: Base Model and Parametric Study | 184 |
| 7.6 | Shear Amplification | 203 |
| 7.7 | Building Performance: Probability of Exceeding res (Concrete Crushing) | 205 |
| 7.8 | Chapter Conclusions | 207 |
| Chapter 8: Performance of RC Core-Walls during Simulated M9 Cascadia Subduction Zone Earthquake Scenarios 210 | | |
| 8.1 | Chapter Overview | 210 |
| 8.2 | Introduction | 210 |

| | | |
|---|--|-----|
| 8.3 | Spectral Acceleration | 213 |
| 8.4 | Spectral Shape | 215 |
| 8.5 | Ground-Motion Duration | 218 |
| 8.6 | Archetype Development | 218 |
| 8.7 | Archetype Nonlinear Modelling | 224 |
| 8.8 | Maximum Interstory Drift | 226 |
| 8.9 | Probability of Collapse | 232 |
| 8.10 | Relating Collapse Probabilities to Ground-Motion Characteristics | 237 |
| 8.11 | Implementation Considerations | 240 |
| 8.12 | Chapter Conclusions | 242 |
| Chapter 9: Conclusions | | 244 |
| 9.1 | A New Ground-Motion Intensity Measure | 244 |
| 9.2 | Basin Effects in Japan | 244 |
| 9.3 | Evaluation of Simulated Ground Motions | 245 |
| 9.4 | Regional Impacts on Idealized Systems | 245 |
| 9.5 | Modeling of RC Core Wall Buildings | 246 |
| 9.6 | Suite of RC Core Wall Archetypes and Models | 247 |
| 9.7 | Impact of M9 Motions on RC Core Wall Buildings | 247 |
| 9.8 | Broader Impacts | 248 |
| Appendix A: Conditional Mean Spectrum Summary | | 249 |
| Appendix B: Archetype Characteristics | | 252 |
| Appendix C: Conditional Mean and Variance Spectra Summary | | 260 |
| Appendix D: Archetype Modelling | | 264 |
| Appendix E: Tall Building Initiative Checks | | 269 |
| Appendix F: RC Wall Archetype Response Sensitivity | | 278 |
| Bibliography | | 281 |

LIST OF FIGURES

| Figure Number | Page |
|---|------|
| 1.1 M9 Project Overview. | 3 |
| 1.2 Dissertation Organization. | 6 |
| 2.1 Sources of earthquakes in the Pacific Northwest Region. (Figure from USGS). | 10 |
| 2.2 Evidence of "Ghost" forests (Photo credit: Brian Atwater, USGS) | 12 |
| 2.3 Collapse of the Alto Rio building after the 2010 Maule Earthquake (Photo Credit: USGS Open-File Report 2011-1053 v1.1) (2011). | 13 |
| 2.4 BC-Hydro (2016) GMM prediction of spectral acceleration with respect to period for a (1) large-magnitude distant earthquake and (2) a lower-magnitude close earthquake for sites with V_{S30} equal to 760 m/s. | 15 |
| 2.5 Histogram of significant duration observed in crustal ground-motions part of the far-field FEMA P695 set and series of subduction zone motions compiled by Raghunandan and Liel (2013). | 16 |
| 2.6 Graphical depiction of how basin amplify ground motions due to (a) impedance contrasts between sedimentary layers, (b) focusing of shear-wave due to the basin's lens-like shape and (c) conversion of the shear-waves to surface waves | 19 |
| 2.7 Localized chimney damage (in West Seattle) after 2001 Nisqually (Photo Credit: Booth (2004)) | 21 |
| 2.8 Oil storage tank damage due to long-period shaking after 2003 Tokachi-Oki (Photo Credit: http://mycommittees.api.org/standards/cre/scast/) | 22 |
| 2.9 Mapping of Seattle basin from Blakely et al. (2000). | 25 |
| 2.10 3D view of the Tualatin basin from McPhee et al. (2014) | 26 |
| 2.11 Contour map of $Z_{2.5}$ for the Pacific Northwest computed using the Stephenson et al. (2017) seismic velocity model. The contour map shows the basins underlying the Puget Lowland region (underneath Seattle) and the Tualatin Basin (underneath Portland). | 27 |
| 2.12 North-South cross section of velocity profile in the Puget Sound region. | 28 |
| 2.13 East-West cross section of velocity profile in the Puget Sound region. | 28 |

| | | |
|------|---|----|
| 2.14 | Contour map of $Z_{2.5}$ for the (a) Puget Sound region and for the (b) Seattle region showing the locations of all buildings in King County that are 10 stories or taller. Building locations were retrieved from the King County tax assessor database, (2016). | 30 |
| 3.1 | Graphical depiction of (a) SS_a less than 1 and (b) SS_a greater than 1. | 38 |
| 3.2 | Comparison of two ground motions in terms of (a) response spectrum, and (b) spectral shape intensity measure, SS_a | 39 |
| 3.3 | Intensity measure SS_a calculated for (a) $\mu=4$ and (b) $\mu=8$ with respect to significant duration for the expanded FEMA P695 ground motion set. | 40 |
| 3.4 | Ductility-dependent force-reduction factors with respect to SS_a for the expanded FEMA P695 ground motion set for (a) $\mu=4$ and (b) $\mu=8$ | 42 |
| 3.5 | Ductility-dependent force-reduction factors with respect to SS_a (log-scale) for the expanded FEMA P695 ground motion set for (a) $\mu=4$ and (b) $\mu=8$ | 43 |
| 3.6 | Statistics of R_μ versus SS_a linear regression models for various μ factors: (a) R^2 and (b) RSE_{ln} | 44 |
| 3.7 | Residual versus magnitude and site-to-source distance for $T_n=1s$ and $\mu=4$ | 45 |
| 3.8 | P-values for the β coefficients of magnitude, site-to-source distance and V_{S30} to predict the residual of the estimate for (A) $\mu=4$ and (B) $\mu=8$ | 46 |
| 3.9 | Measured R_μ versus estimated R_μ using Eq. 3.8 | 48 |
| 3.10 | Incremental dynamic analysis using the expanded FEMA P695 set for a ductile, slowly deteriorating system with $T_n = 1.0$ | 50 |
| 3.11 | R_c with respect to $\frac{IM_{comb}}{S_a(T_n)}$ for (a) brittle, quickly deteriorating system and (b) ductile, slowly deteriorating system for the FEMA ground motion set. | 52 |
| 3.12 | (a) Collapse fragility functions of an reinforced concrete (RC) special moment frame buildings (SMF) structural archetype (b) Fitted collapse fragility functions of all Haselton RC SMF archetypes using IM_{comb} and $S_a(T_n)$ | 56 |
| 3.13 | Variation of R^2 statistic for estimating R_μ with respect to α values for the (a) expanded FEMA set and (b) the crustal/subduction set. | 59 |
| 3.14 | Variation of R^2 statistic for estimating R_c with respect to α values for the (a) expanded FEMA set and (b) the crustal/subduction set. | 60 |
| 4.1 | Basin amplification factors from the Campbell and Bozorgnia (2014) GMM with respect to (a) structural period and (b) $Z_{2.5}$ | 66 |
| 4.2 | $Z_{2.5}$ contour map of the Puget Sound region. | 68 |

| | | |
|------|--|----|
| 4.3 | $Z_{2.5}$ contour map of Japan showing epicenters of two large magnitude earthquakes. | 69 |
| 4.4 | $Z_{2.5}$ contour maps of the (a) Yufutsu basin, (b) Kosen basin, (c) Kanto basin, and (d) Niigata basin. | 70 |
| 4.5 | Geometric mean of response spectrum of recordings binned in terms of $Z_{2.5}$ for the (a) Yufutsu basin, (b) Kosen basin, (c) Kanto basin, and (d) Niigata basin. | 73 |
| 4.6 | The selected station's V_{S30} parameter with respect to $Z_{2.5}$ for the (a) Yufutsu basin, (b) Kosen basin, (c) Kanto basin, and (d) Niigata basin. | 75 |
| 4.7 | Basin amplification factors with respect to period for the (a) Yufutsu basin, (b) Kosen basin, (c) Kanto basin, and (d) Niigata basin. | 78 |
| 4.8 | (a) Standard deviation of the GMM residual of S_a with respect to period and (b) R^2 statistic with respect to period for the GMM residual of S_a vs. $Z_{2.5}$ | 79 |
| 4.9 | Basin amplification factors for earthquakes of varying magnitudes for the (a) Yufutsu basin, (b) Kosen basin, (c) Kanto basin, and (d) Niigata basin. BAF_{S_a} for the basin within the Puget Lowland region during the 2001 Nisqually earthquake is shown for comparison. | 81 |
| 4.10 | Basin amplification factors for spectral acceleration normalized with the amplification predicted using the CB14 basin terms. | 83 |
| 4.11 | Basin amplification factors for spectral acceleration normalized with the amplification predicted using the CB14 basin terms for the (a) Yufutsu basin, (b) Kosen basin, (c) Kanto basin, and (d) Niigata basin. | 85 |
| 4.12 | Basin amplification factors for spectral acceleration (computed using MK13 residuals without the optional basin term) for the (a) Yufutsu basin, (b) Kosen basin, (c) Kanto basin, and (d) Niigata basin. BAF_{S_a} for the basins within the Puget Lowland region during the 2001 Nisqually earthquake is shown for comparison. | 86 |
| 4.13 | Basin amplification factors for spectral acceleration (computed using MK13 residuals with the optional basin term) for the (a) Yufutsu basin, (b) Kosen basin, (c) Kanto basin, and (d) Niigata basin. BAF_{S_a} for the basins within the Puget Lowland region during the 2001 Nisqually earthquake is shown for comparison. | 87 |
| 4.14 | Significant Duration with respect to $Z_{2.5}$ for the (a) Yufutsu basin, (b) Kosen basin, (c) Kanto basin, and (d) Niigata basin. | 89 |

| | | |
|------|--|-----|
| 4.15 | Geometric mean of SS_a for various $Z_{2.5}$ bins with respect to period for the (a) Yufutsu basin, (b) Konsen basin, (c) Kanto basin, and (d) Niigata basin. The geometric mean of SS_a for the FEMA motions are also shown for comparison. | 92 |
| 4.16 | R^2 statistic for SS_a with respect to period for the (a) Yufutsu basin, (b) Konsen basin, (c) Kanto basin, and (d) Niigata basin. | 94 |
| 4.17 | Collapse fragility functions for three ground-motion sets computed using spectral acceleration. | 96 |
| 4.18 | Ratio of geometric mean of spectral accelerations at collapse for the (a) outside-basin to inside-basin set (b) FEMA to inside-basin set for all archetypes. | 97 |
| 4.19 | Collapse fragility function for three ground-motion sets computed using IMcomb. | 100 |
| 4.20 | Ratio of $\tilde{S}_{a,c}$ of a ground-motion set to the $\tilde{S}_{a,c}$ for the inside-basin set with respect to the ratio of $D_s^{C_{dur}}SS_a^{C_{shape}}$ geometric mean of $D_s^{C_{dur}}SS_a^{C_{shape}}$ for a ground-motion set to the geometric mean of for the inside-basin set computed for the 30 archetypes using both the outside-basin set and the FEMA set. | 101 |
| 4.21 | Basin design factor with respect to period for the (a) Yufutsu basin, (b) Konsen basin, and (c) Kanto basin. | 104 |
| 5.1 | M9 CSZ ground-motion generation research plan. | 110 |
| 5.2 | Illustration of M9 CSZ rupture variables. | 111 |
| 5.3 | Procedure for generating broadband ground motions from the simulated deterministic time series. | 112 |
| 5.4 | Spectral acceleration for both horizontal components for all thirty M9 simulations for (a) Seattle and (b) La Grande. Response spectra corresponding to the risk-targeted maximum considered earthquake for Seattle and La Grande (using the 2014 USGS NSHM) are shown in red. . . . | 114 |
| 5.5 | Spectral acceleration with respect to distance for non-basin (designated with a grey dot) and basin (designated with a plus symbol) sit for (a) 1.0-second, (b) 3.0-second, and (c) 5-second oscillator periods for a particular realization (<i>csz006</i>). | 115 |
| 5.6 | Contour map of the geometric mean of the spectral acceleration for all thirty realizations at (a) 0.5-second and (b) 2.0-second period. | 116 |
| 5.7 | Contour map of average GMM residual for S_a at 0.5-second and 2-seconds for all thirty M9 CSZ realizations. | 118 |

| | | |
|------|--|-----|
| 5.8 | Mean GMM (BC-Hydro 2016) residual for all thirty realizations at (a) 0.5-second and (b) 2.0-second period. | 119 |
| 5.9 | Bias (mean residual in natural-log) with respect to period for multiple realizations computed using (a) Abrahamson et al. (2016) and (b) Morikawa and Fujiwara (2013) GMM. | 120 |
| 5.10 | Standard deviation of GMM residual for sites that are outside the basin ($Z_{2.5} < 1.5$ km). Total, within, and between event standard deviation as predicted by the Abrahamson et al., 2016 (BC-Hydro 2016) GMM is shown in red. | 121 |
| 5.11 | Contour map of $Z_{2.5}$, $Z_{1.5}$, and $Z_{1.0}$ for the Puget Sound Region. | 123 |
| 5.12 | Residual with respect to $Z_{2.5}$ for (a) 1.0-second, (b) 3-second, and (c) 5-second periods | 124 |
| 5.13 | Residual with respect to $Z_{1.5}$ for (a) 1.0-second, (b) 3-second, and (c) 5-second periods | 124 |
| 5.14 | Residual with respect to $Z_{1.0}$ for (a) 1.0-second, (b) 3-second, and (c) 5-second periods | 124 |
| 5.15 | The regression coefficients of β_0 and β_1 with respect to period for $Z_{2.5}$, $Z_{1.5}$, and $Z_{1.0}$ | 125 |
| 5.16 | The coefficient of determination, R^2 , for the simple linear regression analyses conducted for $Z_{2.5}$, $Z_{1.5}$, and $Z_{1.0}$ | 125 |
| 6.1 | Geometric mean of the spectral acceleration for both horizontal components for all thirty M9 simulations for (a) Seattle and (b) La Grande. Response spectra corresponding to the risk-targeted maximum considered earthquake for Seattle and La Grande (using the 2014 USGS NSHM) are shown in red. | 132 |
| 6.2 | Map of $Z_{2.5}$ for the Puget Lowland Region | 133 |
| 6.3 | Regional variation of geometric mean of S_a for all M9 realizations of the spectral accelerations at periods of (a) 0.5 seconds and (b) 2.0 seconds. | 134 |
| 6.4 | Regional variation residual of spectral accelerations (BC-Hydro) at periods of (a) 0.5 seconds and (b) 2.0s seconds for all M9 realizations. | 136 |
| 6.5 | BAF_{S_a} for Seattle basin locations within 2 km of the $Z_{2.5,i} = 7$ km contour computed using different reference $Z_{2.5,o}$: (a) locations on the $Z_{2.5}$ contour line equal to 1 km and (b) locations on the $Z_{2.5}$ contour line equal to 3.0 km | 137 |
| 6.6 | Basin Amplification Factors with $Z_o = 2$ km (a) with respect to period for various $Z_{2.5}$ and (b) with respect to $Z_{2.5}$ for various periods for the Puget Sound region computed using the thirty M9 CSZ simulations. | 138 |

| | | |
|------|--|-----|
| 6.7 | Regional Variation of SS_α for a period of (a) 0.5s and (b) 2.0s where α is taken as $\sqrt{13.4}$ and is representative of a ductile system. | 140 |
| 6.8 | The geometric mean of SS_α for various $Z_{2.5}$ bins with respect with period. . | 142 |
| 6.9 | Regional variation of the geometric mean of the $D_{s,5-95\%}$ for all thirty M9 CSZ realizations. | 143 |
| 6.10 | Deteriorating SDOF system backbone and cyclic force-displacement response for (a) brittle and (b) ductile system. | 144 |
| 6.11 | Drift demands for SDOF systems with response to period subjected to M9 Motions at Seattle and La Grande and motions selected to match the CMS for (a) low-strength-brittle, (b) high-strength-brittle, (c) low-strength-ductile, and (d) high-strength-ductile deteriorating SDOF systems. | 146 |
| 6.12 | Fragility function prediction probability of collapse for (a) brittle and (b) ductile systems using S_α | 148 |
| 6.13 | Mean and standard deviation of the γ_{shape} and γ_{dur} parameters for ductile (a) 0.5-second, (b) 1.0-second, and (c) 2-second systems for μ equal to 8. One standard deviation above and below the mean is indicated using the arrows. | 149 |
| 6.14 | Fragility function prediction probability of collapse for (a) brittle and (b) ductile systems using $S_{\alpha,eff}/\eta$ | 150 |
| 6.15 | Fragility function predicting probability of ductility demand exceeding half the ductility capacity for (a) brittle and (b) ductile systems using S_α/η | 152 |
| 6.16 | Fragility function predicting probability of ductility demand exceeding half the ductility capacity for (a) brittle and (b) ductile systems using $S_{\alpha,eff}/\eta$. Regional Variation of Collapse Probability | 152 |
| 6.17 | Regional variation of geometric mean of $S_{\alpha,eff}$ for (a) 0.5-second and (b) 2.0-second for the suite of M9 earthquakes for a low-strength-ductile structure. | 154 |
| 6.18 | Regional variation of the collapse probability for a high-strength-brittle system at (a) 0.5 s, (b) 1 s, and (c) 2.0 s period. | 156 |
| 6.19 | Regional variation of the collapse probability in a M9 CSZ earthquake for a low-strength-ductile system at (a) 0.5 s, (b) 1 s, and (c) 2.0 s period. | 156 |
| 6.20 | Regional variation of the probability of exceeding $\mu_{cap.}/2$ for a high-strength-brittle system at (a) 0.5 s, (b) 1 s, and (c) 2.0 s period. | 157 |
| 6.21 | Regional variation of the probability of exceeding $\mu_{cap.}/2$ for a low-strength-ductile system at (a) 0.5 s, (b) 1 s, and (c) 2.0 s period. | 158 |

| | | |
|------|--|-----|
| 7.1 | Typical floor plan for the (a) 4- and 8-story archetypes and (b) 12-story archetype. | 170 |
| 7.2 | Moment strength and demand (per ELF) along the height of the (a) 4-, (b) 8-, and (c) 12-story solid wall archetype | 173 |
| 7.3 | Moment strength and demand (per ELF) along the height of the (a) 4-, (b) 8-, and (c) 12-story coupled wall archetype | 174 |
| 7.4 | Typical detail of (a) solid wall (including boundary element region) and (b) coupled wall (including coupling beam) | 175 |
| 7.5 | Roof-drift time history for the 8-story archetype subjected to ground-motion NGA RSN 953 at Sa(1s) equal to 2g. | 175 |
| 7.6 | Roof-drift time history for the 8-story archetype subjected to ground-motion NGA RSN 953 at Sa(1s) equal to 4g. | 176 |
| 7.7 | Diagram of the <i>OpenSees</i> analytical model illustrating the (a) solid wall archetypes (b) displacement-based elements (c) coupled wall archetypes (d) planar wall fiber | 178 |
| 7.8 | Stress-strain relationship for the fiber-section (a) reinforcing steel and (b) concrete. Confined concrete properties are shown in parenthesis. | 179 |
| 7.9 | Median of the prediction to experimental for various values of G_{fcc}/G_{fc} and G_{fc}/f'_c values for 15 RC wall specimens with a compression-controlled failure mechanism. | 182 |
| 7.10 | Optimal confined to unconfined crushing energy with respect to the ratio of confined to unconfined concrete peak compressive stress as predicted using Saatcioglu and Razvi (1992) for the following wall specimens: S5 from Vallenias et al. (1979), WR20 from Oh et al. (2002), W1 from Liu (2004), RW1 and RW2 from Thomsen and Wallace (2004), WSH6 from Dazio et al. (2009), S38, S51, S63, and S78 from Tran and Wallace (2015), and C10, A10, A14, and A20 from Shegay et al. (2017). | 183 |
| 7.11 | Experiment and <i>OpenSees</i> prediction (using $G_{fc}/f'_c = 2.$ and $G_{fcc}/G_{fc} = 1.75$ for wall specimen S38 from Tran and Wallace (2015) (solid circles indicate the drift at significant strength loss) | 184 |
| 7.12 | Partial building collapse due to failure slab-column connections after the 1994 Northridge Earthquake (photo by NOAA/NGDC, J. Dewey, U.S. Geological Survey). | 185 |
| 7.13 | Drift capacity of slab-column connections with and without shear reinforcement with respect to gravity shear ratio (data from Matzke et al. 2015). | 186 |

| | | |
|------|---|-----|
| 7.14 | Incremental dynamic analysis results for the (a) 8SW and (b) 8CW archetype using the reference modeling approach. The black line indicates the median S_a at a given max. inter-story drift. | 189 |
| 7.15 | Collapse Fragilities for the (a) solid and (b) coupled wall archetypes. using base model. | 189 |
| 7.16 | The average change in the probability of collapse at MCE for (a) solid wall archetypes and (b) coupled wall archetypes (percentages near the bars indicate the percentage change from the base model). Note that the top bar (solid black) corresponds to the base model and the length of each of the bars corresponds to the probability of collapse. | 190 |
| 7.17 | Incremental dynamic analysis results for a 4-story coupled core wall (4CW) modelled using (a) displacement-based elements and (b) force-based elements in <i>OpenSees</i> | 191 |
| 7.18 | Stress-strain relationship of confined concrete using the Saatcioglu and Razvi (1992) model, Mander et al. (1988), and Richart et al. (1928) model to predict the confined concrete stress and strain. | 192 |
| 7.19 | Pushover of 8SW using the (a) Saatcioglu and Razvi model and the (b) Mander et al. model to predict the confined concrete stress and strain (red lines show base model). | 193 |
| 7.20 | Strain field of the coupled wall piers (Archetype: 8CW) at multiple drift states under monotonic loading (boundary element is abbreviated as BE). | 194 |
| 7.21 | Pushover response for the 8-story (a) solid and (b) coupled wall archetype with varying concrete residual strengths. | 194 |
| 7.22 | Pushover response for the 8-story (a) solid and (b) coupled wall archetype with varying concrete residual strengths in the boundary element and web region (red line shows base model). | 196 |
| 7.23 | Normalized base shear with respect to roof drift for an 8-story (a) continuous wall archetype and (b) coupled wall archetype with varying values of G_{fc}/f'_{ce} (red line shows base model). | 197 |
| 7.24 | Normalized base shear with respect to rood drift for the 8-story (a) continuous and (b) coupled wall archetype assuming various values of G_{fcc}/G_{fc} (red line shows base model). | 197 |
| 7.25 | Pushover of archetype (a) 8SW and (b) 8CW with varying the ultimate strain of the reinforcing bars (red line shows base model). | 198 |
| 7.26 | Pushover varying axial load ratio due to gravity forces (red line shows base model). | 199 |

| | | |
|------|---|-----|
| 7.27 | Box-and-whisker diagram showing axial ratio in (a) solid walls and (b) coupled walls at the MCE ground-motion spectral acceleration. | 201 |
| 7.28 | Pushover varying wall thickness for archetypes (a) 8PW and (b) 8CW (red line shows base model). | 202 |
| 7.29 | Box-and-whisker diagram showing the normalized minimum strain (compression) in any wall pier at MCE for the 8-story coupled wall archetype. | 202 |
| 7.30 | Box-and-whisker diagram showing the max. shear (due to dynamic amplification) at MCE normalized by the expected shear strength of the (a) solid wall archetypes and (b) coupled wall archetypes. | 204 |
| 7.31 | Box-and-whisker diagram showing the max. shear (due to dynamic amplification) at MCE normalized by SEAOC (2009) (shown here in Eq. 7.3) for the (a) solid wall archetypes and (b) coupled wall archetypes. | 205 |
| 7.32 | The average change in the probability of exceeding ϵ_{res} at MCE for (a) solid wall archetypes and (b) coupled wall archetypes. Note that the top bar (solid black) corresponds to the base model and the length of each of the bars corresponds to the probability of exceeding ϵ_{res} | 206 |
| 8.1 | Map of $Z_{2.5}$ for the Puget Lowland Region. | 212 |
| 8.2 | Realization of an M9 CSZ earthquake showing velocity time history for Seattle and La Grande, Washington. | 213 |
| 8.3 | Maximum direction spectral acceleration for all 30 M9 simulations for (a) Seattle and (b) La Grande. Response spectra corresponding to the risk-targeted maximum considered earthquake for Seattle and La Grande (using the 2014 USGS NSHM) are shown in red. | 214 |
| 8.4 | Ground motions selected and scaled to the target 2475-year return conditional mean spectrum at 2.0 s for crustal, intraslab, and interface earthquakes. | 217 |
| 8.5 | SS_{α} with respect to period for M9 Seattle and motions selected to match the MCE_R CMS considering basins. SS_{α} computed for α equal to 8 which is typical for ductile systems. | 217 |
| 8.6 | Empirical probability density function of $D_{s,5-95\%}$ for FEMA P695 motions, M9 Tohoku motions recorded at stations with a source-to-site distance between 100 and 200 km, and M9 CSZ Simulated motions in Seattle. | 219 |
| 8.7 | Archetype typical floor plans for the (a) typical floors and (b) basements. | 220 |
| 8.8 | Archetype design flow chart. | 222 |

| | | |
|------|---|-----|
| 8.9 | Distribution of inter-story drift with height for (a) 8-story and (b) 32-story ASCE 7-10 code enhanced archetypes, subjected to Simulated M9 Motions in Seattle. | 227 |
| 8.10 | Median of the maximum inter-story drift with respect to archetype story for (a) code-minimum ASCE 7-10 archetypes, (b) code-minimum ASCE 7-16 archetypes, (c) code-enhanced ASCE 7-10 archetypes, and (d) code-enhanced ASCE 7-16 archetypes | 228 |
| 8.11 | Ground motion targeting mean and variation of the conditional spectrum at 2.0s (corresponding to the period of archetype S12-16-E) for crustal, intraslab, and interface earthquakes. | 231 |
| 8.12 | Probability of exceedance with respect to maximum inter-story drift for ASCE 7-10 code-minimum (a) 8-Story and (b) 32-Story archetypes. | 231 |
| 8.13 | Probability of collapse due to slab-column connection failure with respect to the max. inter-story drift (filtered for experiments with shear-reinforcements and a gravity shear ratio between 0.4 to 0.6). | 233 |
| 8.14 | Probability of Collapse with respect to archetype story for (a) code-minimum ASCE 7-10 (10-E) archetypes, (b) code-minimum ASCE 7-16 (16-M) archetypes, (c) code-enhanced ASCE 7-10 (10-E) archetypes, and (d) code-enhanced ASCE 7-16 (16-E) archetypes. | 235 |
| 8.15 | Collapse fragility for all code minimum archetypes subjected to M9 Seattle motions and MCE_R (with and without basins) with respect to (a) normalized spectral acceleration and (b) normalized effective spectral acceleration. | 239 |
| D.2 | Stress-strain response of a modified <i>OpenSees</i> (a) Concrete02 model with revised pre-peak properties and (b) Steel02 model that accounts for cyclic strength degradation based on Kunnath et al. (2009). | 266 |
| E.1 | Peak interstory drifts with respect to story for all ASCE 7-10 Code Enhanced Designs 24-stories and taller. | 270 |
| E.2 | Peak interstory drifts with respect to story for all ASCE 7-16 Code Enhanced Designs 24-stories and taller. | 271 |
| E.3 | Residual interstory drifts with respect to story for all ASCE 7-10 Code Enhanced Designs 24-stories and taller. | 272 |
| E.4 | Residual interstory drifts with respect to story for all ASCE 7-16 Code Enhanced Designs 24-stories and taller. | 273 |
| E.5 | Min. and Max. Strains with respect to story for all ASCE 7-10 Code Enhanced Designs 24-stories and taller. | 274 |

| | | |
|-----|--|-----|
| E.6 | Min. and Max. Strains with respect to story for all ASCE 7-16 Code Enhanced Designs 24-stories and taller. | 275 |
| E.7 | Story Shear with respect to story for all ASCE 7-10 Code Enhanced Designs 24-stories and taller. | 276 |
| E.8 | Story Shear with respect to story for all ASCE 7-16 Code Enhanced Designs 24-stories and taller. | 277 |
| F.1 | (a) Probability of Exceedance with respect to maximum inter-story drift during the M9 CSZ motions in Seattle with varying material modelling assumptions for a 24-story ASCE 7-10 Code-Minimum archetypes (b) Probability of collapse with respect to story for ASCE 7-10 Code-Minimum Archetypes during the M9 CSZ with varying material modelling assumptions. | 280 |

LIST OF TABLES

| Table Number | Page |
|--|------|
| 3.1 Results of regression analysis for R_{μ} ($\mu=8$). | 47 |
| 3.2 Model parameters used for the Ibarra et al. (2005) peak-oriented deterioration model. | 49 |
| 3.3 Results of regression analysis for IM_{comb} for brittle' and ductile' systems. | 51 |
| 3.4 R^2 statistic for using IM_{somb} or $IM_{comb,exp}$ to predict R_c for brittle' and ductile' systems. | 53 |
| 3.5 Intensity measure statistics for the expanded FEMA ground motion set. | 54 |
| 4.1 Statistics on station recordings for each $Z_{2.5}$ bin | 72 |
| 4.2 Statistics on significant duration GMM residual. | 90 |
| 4.3 Geometric mean of various measures | 99 |
| 5.1 Results of Simple Linear Regression Analysis. | 126 |
| 6.1 Location and scale parameters for fragility curves conditioned on $\ln S_a$ and $\ln S_{a,eff}$ | 151 |
| 7.1 Properties of the solid and coupled wall archetypes. | 166 |
| 7.2 Coupling beam dimensions and reinforcement layout. | 169 |
| 7.3 Solid Wall Archetype dimensions and reinforcement layout. | 171 |
| 7.4 Coupled Wall Archetype dimensions and reinforcement layout. | 172 |
| 7.5 Results comparing predicted to experimental results for various wall specimens. | 181 |
| 7.6 Percentage change in collapse probability for studied values of modelling and design parameters. | 188 |
| 8.1 Key archetype properties. | 225 |
| 8.2 Summary of Mean Collapse Probabilities for simulated M9 motions in Seattle. | 237 |
| B.1 Archetype dimensions and reinforcement layout for ASCE 7-10 code minimum archetypes. | 253 |

| | | |
|-----|---|-----|
| B.2 | Archetype dimensions and reinforcement layout for ASCE 7-16 code minimum archetypes. | 254 |
| B.3 | Archetype dimensions and reinforcement layout for ASCE 7-10 code enhanced archetypes. | 255 |
| B.4 | Archetype dimensions and reinforcement layout for ASCE 7-10 code enhanced archetypes (continued). | 256 |
| B.5 | Archetype dimensions and reinforcement layout for ASCE 7-16 code enhanced archetypes. | 257 |
| B.6 | Archetype dimensions and reinforcement layout for ASCE 7-16 code enhanced archetypes (continued). | 258 |
| B.7 | Boundary element information for the 4-story archetypes. | 259 |

ACKNOWLEDGMENTS

Jeff and Marc, you have guided me throughout my PhD, treated me as a colleague, often entertained (patiently) my stubborn opinions, and above all mentored me along the way. Your mentorship has allowed me to evolve from an ordinary engineer to a capable scholar.

My research would not have been possible without Art Frankel and Erin Wirth, who introduced me to the world of seismology and ground-motion simulation, answered my naive questions, and considered my suggestions. For all that and more, I am very grateful. I would like to thank Dawn Lehman and Laura Lowes for their contribution in the research related to reinforced concrete walls. I would also like thank Daniel Kirschen for being my graduate student representative.

This work was also made possible with researchers and collaborators outside of the University of Washington. I would like to thank Meera Raghunandan and Abbie Liel for sharing their subduction ground-motion sets, and Curt Haselton for sharing his RC SMF archetype models. I would like to thank Josh Pugh for sharing his RC wall specimen database and wall modelling scripts. Special thanks to Silvia Mazzoni for sending a large subset of intraslab motions from the PEER NGA-Subduction project, Andrew Makdisi for reviewing various chapters in this dissertation and assisting with the CMS calculations, and to Doug Lindquist from Hart Crowser for providing access to the EZ-Frisk software. The numerous analyses in this dissertation would not have been possible without the "endless" computational hours provided by Tim Cockerill and Ellen Rathje.

The quality of the research was improved through the feedback I received from other researchers. I appreciate the comments and suggestions from Mehmet Celebi and

Nicolas Luco on two papers that are featured in this dissertation as chapters. The feedback received from Steve Kramer was unique and from a geotechnical engineers perspective. I would also like to mention others that have inspired my work along the way: John Vidale, Joe Wartman, Mike Motley, and Carlos Molina-Hutt.

I must acknowledge all the practicing engineers who assisted in the development of the reinforced concrete core wall archetypes through the Earthquake Engineering Committee at the Structural Engineers Association of Washington. In particular, I am grateful for the feedback received from David Fields and John Hooper from MKA, Andrew Taylor, Brian Pavlovec, and Scott Neuman from KPFF, and Terry Lundeen, Bryan Zagers, and Zach Whitman from CPL, Tom Xia from DCI-Engineers, Clayton Binkley from ARUP, Bill Perkins from Shannon & Wilson, Doug Lindquist from Hart Crowser, C.B. Crouse from AECOM, Kai Ki Mow from City of Bellevue, and Cheryl Burwell and Susan Chang from City of Seattle.

This research was primarily funded by the National Science Foundation under Grant No. EAR-1331412 and partly funded by the Applied Technology Council 123 Project. The computations were facilitated through the use of advanced computational, storage, and networking infrastructure provided by the University of Washington through the Hyak advanced computing system and through DesignSafe-CI (NSF Grant No. 152081, NHERI Cyberinfrastructure) which provides computational resources from the Texas Advanced Computing Center. I am also appreciative for the recognition and funding that I have received from the Earthquake Engineering Research Institute through the Graduate Fellowship program and through the Graduate Student Paper Award.

Finally, I must acknowledge the vital role that my friends have had throughout my PhD program. Of the many, I will call out my PhD colleagues (Andy Sen, Max Stephens, Travis Thonstad, Ramona Barber, Alex Grant, Andrew Makdisi, Mike Greenfield, Kamal

Ahmed, and Alex Shegay) and my confidants (Yousef Abdulsalam, Landon Roberts, Abdullah Alaryan, Ahmed Hashem, and Yasser Marafi).

DEDICATION

To my wife, *Noura*,
who has provided immense love, support, and patience.

To my children, *Zaina* and *Bader*,
who give me purpose outside of engineering.

To my parents,
who have given me a lifetime worth of inspiration.

Chapter 1

INTRODUCTION

1.1 Problem Statement

In the past, large-magnitude subduction earthquakes have caused numerous casualties and severe damage to buildings and infrastructure (e.g., Sumatra 2004, Maule 2010, and Tohoku 2011). Similarly, megathrust earthquakes along the Cascadia subduction zone pose a great threat to the Pacific Northwest. Geologic and historic evidence indicates that this region has a history of megathrust earthquakes (Goldfinger et al., 2012), including one that occurred in the 1700s (Atwater et al., 1995). According to Petersen et al. (2002), a large-magnitude earthquake along the Cascadia Subduction zone (CSZ) has a 10-14% chance of occurring within the next 50 years.

Engineers' understanding of the effects of large earthquakes is based primarily on the observed response of structures and ground-motion recordings. Such observations and recordings are largely unavailable for the Pacific Northwest (PNW), so engineers often resort to using lessons from other tectonic environments to develop general codes and to design structures. The ground motions in other environments will likely differ from those expected in the PNW, because each tectonic environment is unique, and many cities in the region are located on deep sedimentary basins that will modify the ground motions. These basins are known to increase the damage caused by earthquakes.

Research is needed to estimate the range of ground motions that would result from a magnitude-9 (M9) earthquake, and to evaluate the impacts of these motions on structures. Current codes do not consider the frequency-dependent amplification of motions by basins, which results in high spectral accelerations and damaging spectral

shapes in some critical frequency ranges. In addition, building codes do not consider the effects of long-duration shaking expected during large-magnitude earthquakes.

To address the paucity of recorded ground motions, a research team from the United States Geological Survey and the University of Washington numerically simulated ground motions that would result from an M9 interface event. This dissertation evaluates the effects of a large-magnitude earthquake on structures in deep sedimentary basins by: (1) characterizing the simulated M9 ground motions and those measured in other sedimentary basins during interface events, (2) developing a new intensity measure that can account for these characteristics, and (3) evaluating the impacts of these motions on idealized and detailed structural models.

1.2 M9 Project

The work documented in this dissertation is part of a large research collaboration between the United States Geological Survey and the University of Washington, with funding from the National Science Foundation. For convenience, this collaboration will be referred here as the "M9 Project". Figure 1.1 shows an overview of the M9 project. This project aimed to reduce the catastrophic consequences of a large-magnitude Cascadia Subduction earthquake on the social, built, and natural environments through research advances in: (1) physics-based ground-motion simulations, (2) earthquake early warning systems, (3) engineering design, and (4) community planning.

A key feature of the collaboration is the generation of a suite of thirty simulated ground motions for various rupture scenarios of a magnitude-9 earthquake, which makes it possible to evaluate the consequences of an M9 event probabilistically. The M9 project included teams that studied the effects of tsunamis, liquefaction, and landslides, as well as the impact of deploying earthquake early warning systems. The project also developed new strategies for community planning, including the use of integrated risk maps. This dissertation addresses key issues on the impacts of an M9 earthquake on building structures.

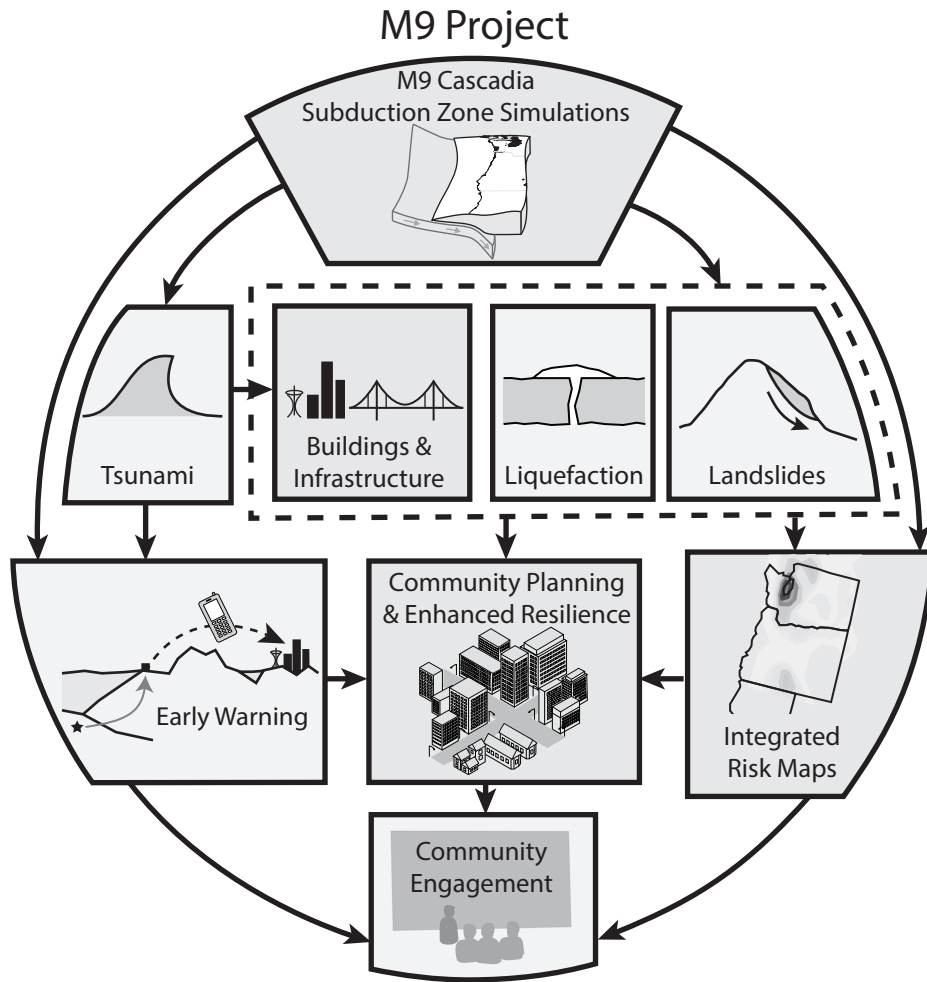


Figure 1.1: M9 Project Overview.

1.3 Key Research Objectives

This dissertation contributed to the field of earthquake engineering by achieving the following research objectives:

- Formulated a robust ground-motion intensity measure (IM) that captures three key ground-motion characteristics that correlate with structural performance (Marafi et al., 2016): spectral acceleration, spectral shape, and ground-motion duration. The combined intensity measure includes a new measure of spectral shape that accounts for effects of structural yielding on period elongation. The intensity measure was also normalized ($S_{a,eff}$) to make it easier to compare it with motions typically used in structural evaluations (Marafi et al., 2018a)
- Quantified the effects of basins and large subduction earthquakes on key ground-motion characteristics and on structural performance, using motions recorded inside and outside basins in Japan (Marafi et al., 2017).
- Evaluated the ground-motion characteristics of the simulated motions by comparing them with those predicted by subduction earthquake ground-motion models (GMM) (Frankel et al., 2018b; Wirth et al., 2018). A large portion of the discrepancies between the simulated motions and GMMs are explained in terms of basin proxies (e.g., depth to sediments with shear-wave velocity equal to 2,500 m/s, $Z_{2.5}$).
- Quantified the variation in collapse risk throughout the Puget Sound region for an M9 event for idealized yielding systems that are representative of a wide range of structural systems (Marafi et al., 2018a).
- Evaluated the deformation demands and collapse risk for a series of developed archetypes subjected to ground motions from the M9 scenarios and to motions that are consistent with existing design practice. This was achieved by:

- Building on previous work by Pugh et al. (2015), developed a robust and calibrated modelling methodology to predict multiple damage states (up to collapse) for reinforced concrete walls (Marafi et al., 2018c). The sensitivity of collapse predictions to key model parameters was also established.
- Developed suites of models of modern reinforced concrete core wall archetypes located in Seattle that are representative of minimum and current design practice (Marafi et al., 2018b).

1.4 Dissertation Organization

The dissertation organization is illustrated in Figure 1.2 and described below:

- Chapter 2 provides background on the seismic hazard of the Cascadia Subduction zone. The chapter also includes a brief literature review on the effects of long-duration shaking and on the effects of basins. Additional background information is provided at the beginning of each chapter.
- Chapter 3 identifies three ground-motion characteristics that strongly affect structural response, using ground motions from crustal and subduction earthquakes. A new ground-motion intensity measure (IM_{comb}) is proposed that combines spectral acceleration, significant duration, and a newly developed intensity measure for spectral shape. The new measure for spectral shape depends on the system's ductility and accounts for the period range the structure is expected to undergo during the ground motion. The new intensity measure is normalized in Chapter 6 to make it easier to compare with typical design motions (and called effective spectral acceleration, $S_{a,eff}$).
- Chapter 4 uses ground-motion data from past earthquakes (e.g., 2003 Tokachi-Oki, 2010 Tohoku) to study the effects of basins during large magnitude subduction zone

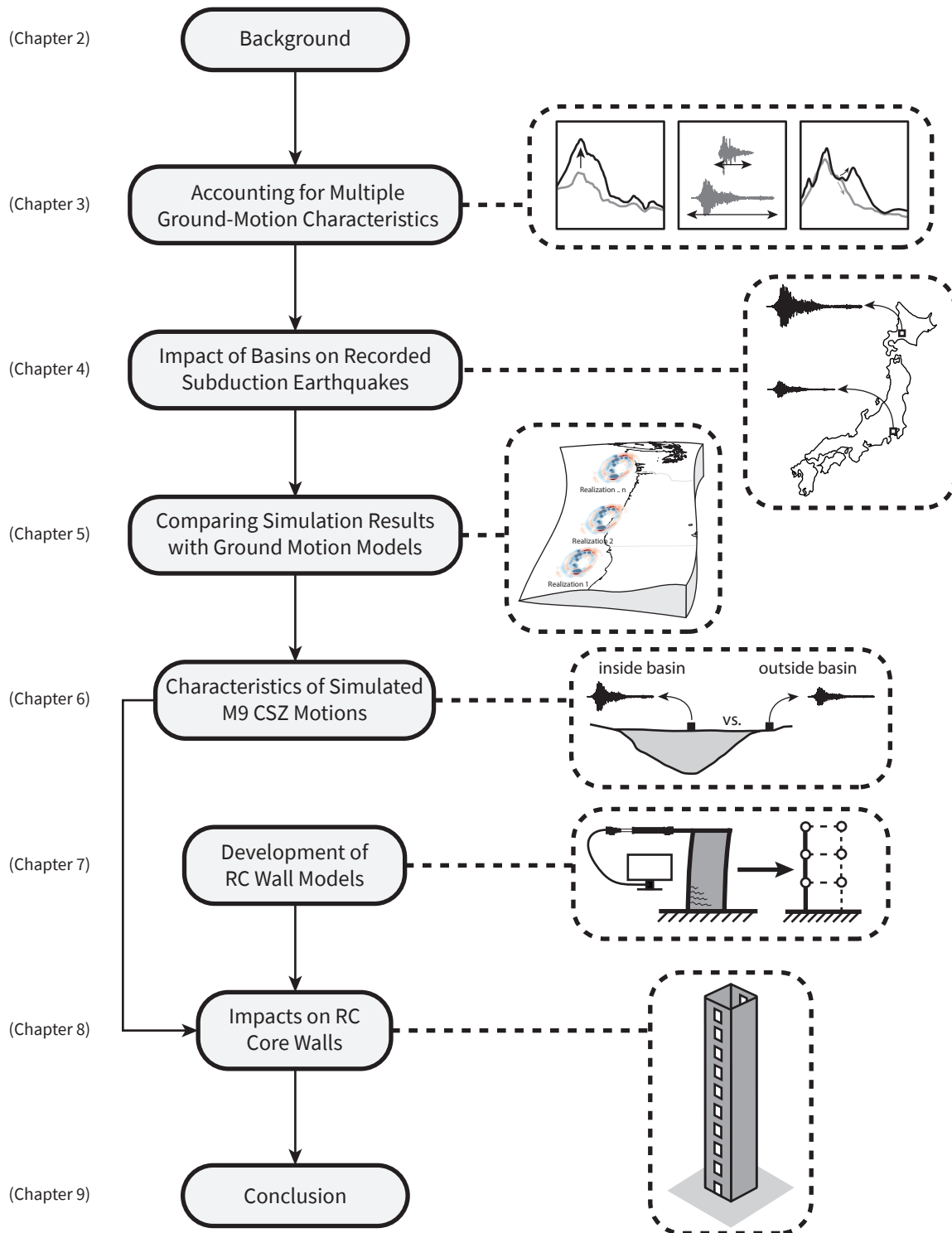


Figure 1.2: Dissertation Organization.

earthquakes, using measured data from four basins in Japan. The characteristics of the motions were compared for motions recorded inside and outside basins. Finally, the effects of the basin motions were quantified in terms of structural collapse for thirty well-studied (by others) building archetypes of reinforced concrete moment frame buildings (Haselton et al., 2011b). Factors were developed to account for basin amplification on spectral acceleration, and design factors that account for the combined effects of basins on spectral acceleration, shape, and duration were also computed.

- Frankel et al. (2018b) and Wirth et al. (2018) generated a wide range (around 50) of magnitude-9 CSZ scenarios using physics-based, finite-difference simulations for long periods (above 1s), combined with a stochastic approach for shorter periods (below 1s). Chapter 5 compares the simulated ground motions with subduction ground-motion models (GMM) for spectral acceleration. For sites in basins, a large portion of the variation between spectral accelerations for the simulations and GMM predictions were explained using various basin proxies.
- Chapter 6 extends the evaluation of the M9 simulations (Chapter 5) using ground-motion intensity measures that quantify spectral acceleration, spectral shape, and duration. The combined intensity measure from Chapter 3 is normalized to make it more convenient to use. The impacts of the motions on structures were evaluated across the Puget Sound region using deteriorating, single-degree-of-freedom oscillators with properties that were representative of idealized structures in the Pacific Northwest. The properties of these idealized systems were varied to simulate the response of old and modern structures, and of brittle and ductile structures. Finally, the variation in response between structures and between ground-motions were explained using an enhanced version of the IM formulated in Chapter 3.

- Chapter 7 extends a modelling methodology developed by Pugh et al. (2015) to predict nonlinear response of reinforced concrete shear walls using OpenSees displacement-based elements. The chapter also discusses the robustness of the collapse predictions by varying OpenSees element and constitutive modelling parameters. The effects of these parameters on damage states prior to collapse is also discussed.
- Chapter 8 studies the impacts of the M9 simulations on 32 modern, mid- and high-rise reinforced concrete core-wall archetypal structures, ranging from 4 to 40 stories. The archetypes were designed to ASCE 7-10 (2013) and ASCE 7-16 (2017). For each code provision, two performance groups were considered: "code-minimum," corresponding to archetypes designed to the minimum allowable by code; and "code-enhanced," corresponding to archetypes designed with lower drifts and higher strengths targets, which were typical practice for tall-building design in Seattle. The effects of the M9 motions on these archetypes were evaluated in terms of drift demands and structural collapse risk. Finally, the collapse risks expected from the simulations were compared to those of the maximum considered earthquake currently assumed in design.
- Chapter 9 summarizes overarching conclusions and identifies areas for further research.

Chapter 2

BACKGROUND AND RESEARCH NEEDS

2.1 Chapter Overview

This chapter reviews the seismic hazard in the Pacific Northwest and summarizes the current state of research in large magnitude earthquakes and their effects on structures in deep sedimentary basins. The chapter first reviews current evidence that suggests the Pacific Northwest is prone to interface earthquakes. Then summarizes recent research on (i) the effects of large magnitude interface earthquakes, and (ii) the effects of deep sedimentary basins during these earthquakes. The final section in the chapter identifies current needs of research in this area.

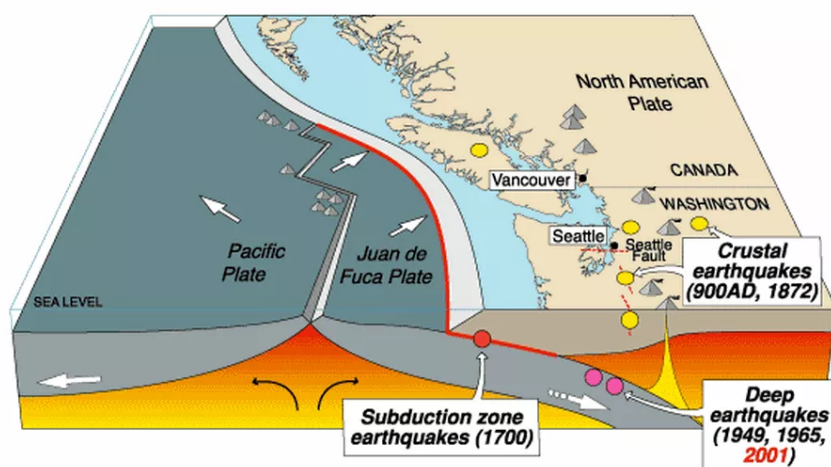
2.2 Overview of the Seismic Hazard in the Pacific Northwest

The seismic hazard in the Pacific Northwest is controlled by several sources; earthquakes can occur from (1) shallow crustal faults (e.g., Seattle Fault), or from (2) the subduction of the Juan de Fuca plate beneath the North American Plate, commonly known as the Cascadia Subduction Zone (CSZ). The CSZ can produce two types of earthquakes, known as deep intraslab earthquakes and shallower interface earthquakes (illustrated in Figure 2.1). Additionally, the strong shaking from these earthquakes is expected to be amplified by the deep sedimentary basins underlying most of populated areas in the Pacific Northwest.

2.3 Geologic Evidence of Interface Earthquakes in the Cascadia Subduction Zone

Heaton and Hartzell (1987) recognized that large subduction earthquakes are possible along the Cascadia Subduction Zone. Atwater et al. (1995) later found coastal geologic

Cascadia earthquake sources



| Source | Affected area | Max. Size | Recurrence |
|---------------------------|---------------|-----------|-----------------|
| ● Subduction Zone | W.WA, OR, CA | M 9 | 500-600 yr |
| ● Deep Juan de Fuca plate | W.WA, OR, | M 7+ | 30-50 yr |
| ● Crustal faults | WA, OR, CA | M 7+ | Hundreds of yr? |

Figure 2.1: Sources of earthquakes in the Pacific Northwest Region. (Figure from USGS).

evidence along the Washington-Oregon border that confirmed that the CSZ could produce up to a magnitude-9 interface earthquake. Atwater et al. found evidence of: (1) subsiding forest soils due to tidal water pressure, (2) sand layer deposits due to tsunamis, and (3) buried sand boils caused by liquefaction due to seismic shaking. Figure 2.2 shows a photograph of a subsided forest with dead trees taken by Atwater near the Washington coast and estimate the last event occurred as recently as the year 1700.

In addition, Goldfinger et al. (2012) found off-shore earthquake evidence by sampling deep-sea cores along submarine channels and canyons located off the coast of Northern California to Washington State. These deep-sea cores were used to date large-magnitude earthquakes within the past 10,000 years where the average recurrence period is 500 years. Using this data, time-dependent statistical analyses estimated a M9 had a 17% chance of occurring during the next 50 years and a 25% chance of occurring within the next 100 years (Kulkarni et al., 2013). These estimates are similar to those by other researchers (e.g., Petersen et al., 2002) indicating that a large-magnitude CSZ event has a high probability of occurrence relative to the seismic hazard considered for building and bridge design. Research is needed to study impact on the PNW region.

2.4 Effects of Large Magnitude Earthquakes

Megathrust earthquakes (e.g., Sumatra 2004, Maule 2010, and Tohoku 2011) have caused tremendous damage over wide regions. Coastal communities have experienced strong ground shaking, and they have been devastated by tsunamis triggered by the movement of the ocean floor. Communities further away from the earthquake source have experienced long-duration shaking that has large low-frequency components that tend to affect long-period structures. The following sections show (a) evidence of damage due to these earthquakes, (b) the effect of ground-motion attenuation of short- and long-period waves, and (c) effects of long-duration shaking.



Figure 2.2: Evidence of "Ghost" forests (Photo credit: Brian Atwater, USGS)

2.5 Evidence of Damage in Large Magnitude Earthquakes

After the 2010 Maule earthquake in Chile, Wallace et al. (2012) observed that only 2% (40/1,939) of 9-stories or more buildings constructed between 1985 and 2009 were severely damaged. Out of the 40 damaged buildings, only one collapsed, a 15-story, residential building, Torre Alto Rio Building (shown in Figure 2.3) in Concepcin (Deger and Wallace, 2015). The Torre Alto Rio Building was the only modern concrete wall building that collapsed during the 2010 Maule earthquake (Song et al., 2012) due to a number of number of issues (a) flexural-compression failure, (b) vertical irregularities, (c) shear damage, and (d) tensile fracture and splice failure. The combination of these issues caused failure in the first story that led the building to overturn (shown in Figure 2.3).

The remaining buildings that were severely damaged buildings sustained concrete crushing at the end or throughout the wall. This was mainly due to high axial load and



Figure 2.3: Collapse of the Alto Rio building after the 2010 Maule Earthquake (Photo Credit: USGS Open-File Report 2011-1053 v1.1) (2011).

lack of well-detailed boundary elements (Wallace et al., 2012). The evidence of damage due to ground-motion duration resulted in abrupt bar buckling (towards the end of the earthquake) and eventual fracture under large cyclic strain demands.

In Japan, most of the building damage after the 2011 Tohoku earthquake was a result of the large tsunami that followed the earthquake. Okazaki et al. (2013) examined damage after the 2011 Tohoku earthquake in Japan. Okazaki et al. concluded that the majority of steel buildings performed well. However, even if the lateral force resisting system performed well, buildings that used older cladding systems still observed damage in facade.

2.5.1 *Ground Motion Attenuation in Large Magnitude Earthquakes*

At large distances from the earthquake source, the relative proportion of low-frequency to high-frequency contributions increases, due to differences in the attenuation of low

and high frequencies. For example, Figure 2.4 shows the BC-Hydro (Abrahamson et al., 2016) ground-motion model (GMM) prediction of spectral acceleration with respect to period for a distant (closest distance to rupture, R_{CD} , equal to 120 km) large-magnitude (M_w 9) earthquake versus a closer (R_{CD} equal to 20km) moderate-magnitude (M_w 7) earthquake. Both predicted spectra have similar spectral accelerations, S_a , at a period of about 1s. At short periods, the S_a values are larger for the M_w 7 event than for the M_w 9 event. In contrast, at longer periods, the S_a values are much larger for the M_w 9 event. Thus low-frequency motions are expected to attenuate with distance less than high-frequency motion. These differences in attenuation between moderate- and large-magnitude earthquakes would result in varying response of tall structures with the same source-to-distance to the earthquake. Moreover, the current BC-Hydro GMM model used does not include basin effects, therefore, the spectral accelerations shown in Figure 2.4 would further increase if basins were considered.

2.5.2 *Effects of Long-Duration Shaking on Structural Response*

The long durations of motions from large-magnitude earthquakes can cause structures susceptible to strength and stiffness degradation to collapse at lower spectral accelerations (e.g., Bommer et al., 2004) than lower magnitude events. Raghunandan and Liel (2013) compiled a set of ground motions from various subduction zone earthquakes around the world and compared them to crustal ground-motions (far-field set) compiled in the FEMA P695 (2009) document. Figure 2.5 shows a histogram of significant durations ($D_{s,5-95\%}$), a measure of ground-motion duration (Trifunac and Brady, 1975), computed for crustal and subduction earthquakes. The median duration for crustal earthquakes is around 12s, whereas the duration is 42s for subduction earthquakes (compiled by Raghunandan and Liel, 2013). Similar long-duration motions would be expected in a magnitude-9 CSZ earthquake. The effects of long duration motions from large-magnitude earthquakes have been investigated by many researchers. Bommer

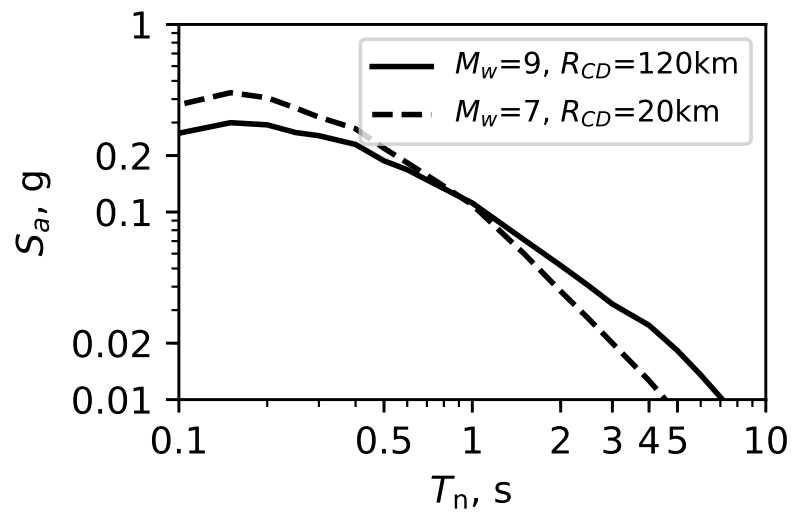


Figure 2.4: BC-Hydro (2016) GMM prediction of spectral acceleration with respect to period for a (1) large-magnitude distant earthquake and (2) a lower-magnitude close earthquake for sites with V_{S30} equal to 760 m/s.

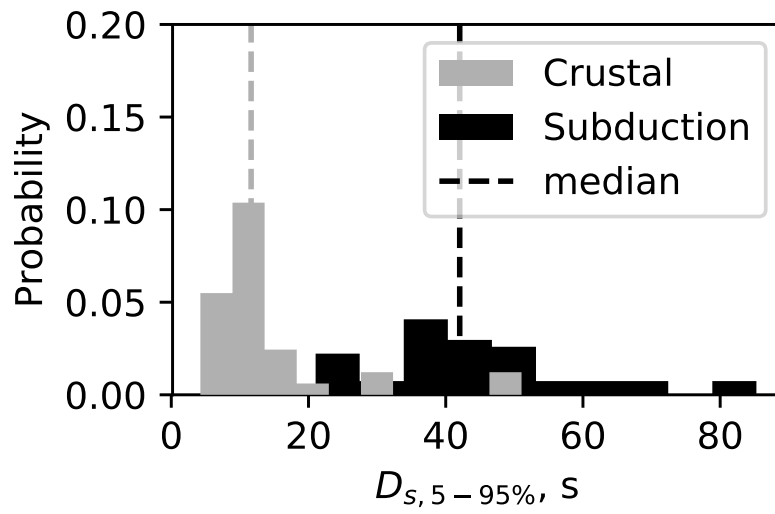


Figure 2.5: Histogram of significant duration observed in crustal ground-motions part of the far-field FEMA P695 set and series of subduction zone motions compiled by Raghunandan and Liel (2013).

et al. (2004) have found that the effects of durations are more pronounced in structures that are susceptible to low-cycle fatigue and who also undergo strength and stiffness degradation with dynamic loading. They also decoupled the effects of duration and spectral shape on structural response by using intensity measures that accounted for duration and spectral shape, separately. Hancock and Bommer (2007) later took an alternative approach by comparing the effects of duration on an 8-story RC wall-frame building using spectrally matched records. They found that the effects of duration correlated to cumulative damage measures, such as hysteretic energy and fatigue damage.

More recently, Raghunandan and Liel (2013), Raghunandan et al. (2015), and Chandramohan et al. (2016b) found that ground-motion duration can affect the minimum design strength needed to achieve an acceptable probability of collapse. Raghunandan and Liel (2013) studied the effects of duration on 17 reinforced concrete moment frames archetypes designed for California. These archetypes were classified into two categories, archetypes with modern ductile frames ranging from 1 to 20 stories, and archetypes with older non-ductile frames ranging from 2 to 12 stories. This study concluded that the collapse capacity of all the archetypes reduced as the duration of the motion increased. However, the collapse capacity was observed to be larger in the modern ductile archetypes and varied highly with duration relative to older non-ductile archetypes which collapsed sooner and were less sensitive to duration. The authors attributed these long duration effects to an increase in the imposed energy demands on the structure rather than peak drifts which were found to be weakly correlated to ground-motion duration.

Raghunandan et al. (2015) later studied the collapse risk due to long-duration subduction earthquakes motions of similar reinforced concrete archetypes (both modern and old) but designed for Seattle, Portland, and Los Angeles. This study concluded the probability of collapse in 50 years would be slightly higher in Seattle than Los Angeles

and that the collapse risk could be up to 7.6 times larger in older frames than modern reinforced concrete moment frames in both Portland and Seattle.

Chandramohan et al. (2016b) later studied the effects of long-duration motions using recordings with similar spectral shapes. This study specifically looked at a 5-story special steel moment frames and showed a 29% decrease in median collapse capacity when subjected to long-duration (geometric mean of 42 s) versus short-duration (geometric mean of 6 s) ground-motions. The authors also concluded similar observations in a ductile concrete bridge pier model which showed a 17% reduction in median collapse capacity between the two ground-motion sets. This study also showed that the collapse capacity is highly dependent on the structure's ductility and cyclic deterioration; structures that were ductile and deteriorate rapidly were found to be most sensitive to duration.

Chandramohan (2016, see Chapter 6) developed a framework that incorporates the effect of duration into the equivalent linear seismic design procedure in ASCE 7. The framework uses either an incremental dynamic analysis (Vamvatsikos and Cornell, 2002) or a multiple stripe analysis (Jalayer and Cornell, 2009) to determine a hazard-consistent collapse fragility using the generalized conditional intensity measure (GCIM) framework (Bradley, 2010). The proposed method considers changes in collapse risk due to the expected duration and spectral shape from all the earthquake sources that control the seismic hazard. Finally, duration and shape adjustment factors to the equivalent linear design base shears in ASCE 7 were proposed that target a uniform collapse risk over a geographical region and over various structural systems. As an example, this methodology found that 1-second special reinforcement concrete moment frame in Seattle required a 29% increase in base shear strength to achieve a similar collapse risk of its counterpart on site in Los Angeles. While this methodology accounts for the effects of spectral shape and duration on building response in Seattle, it does not take into account the effect of basins on spectral acceleration and duration.

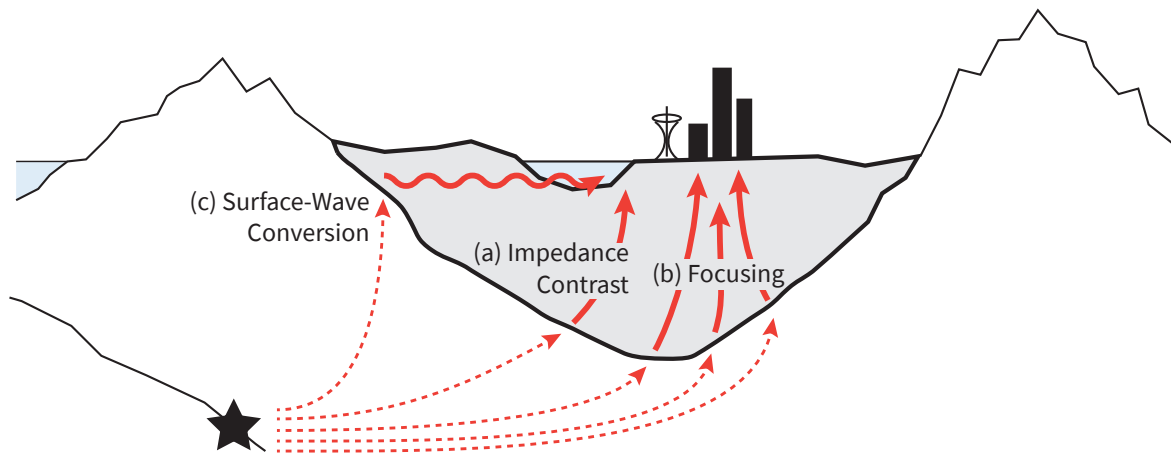


Figure 2.6: Graphical depiction of how basin amplify ground motions due to (a) impedance contrasts between sedimentary layers, (b) focusing of shear-wave due to the basin's lens-like shape and (c) conversion of the shear-waves to surface waves

2.6 Effects of Sedimentary Basins

Cities around the Pacific Northwest (Seattle, Tacoma, and Portland) overlie deep sedimentary basins which are known to amplify seismic waves at long periods. The sources of basin amplification are depicted in Figure 2.6 and include: (a) impedance contrasts between basin layers, (b) focusing of shear-waves at the surface, and (c) conversion of both P- and S-waves into surface waves at the basin edges (Choi et al., 2005). The combination of these effects would amplify low-frequency waves (Choi et al., 2005), hence increasing spectral accelerations at a period range that corresponds to the elastic period of tall structures and expected inelastic periods of mid-rise structures, resulting in more damage relative to structures located outside basins. These effects are corroborated with evidence of building damage in basins after major earthquakes. A number of examples are discussed in the following section.

2.6.1 Evidence of Basin Damage

Several researchers have shown earthquake damage in areas overlying basins. One of the early examples of basin damage was observed after the 1985 Michoacan earthquake. Hall and Beck (1986) found evidence of severely damaged 6- to 15-story buildings founded on ancient lake bed deposits overlying hard rock in Mexico city. These buildings were damaged due to the lake bed deposit amplifying ground-motion frequency content that resonated with mid-rise buildings. While these lake bed deposits surround a large region of Mexico City their amplification on spectral acceleration were explained using 1-dimensional wave propagation (Dobry and Iai, 2000).

Similar to the damage observed in Mexico City, Kawase (1996) identified a damage belt in Kobe, Japan comprising from both reinforced concrete and steel buildings. The buildings were damaged due to ground-motion amplification at the basin-edge after the 1994 Kobe earthquake. In California, Graves et al. (1998) found similar evidence of damage due to basin-edge effects in the Santa Monica area after the 1994 Northridge earthquake.

Basin damage was also observed with deep intraslab earthquakes in Seattle. For example, Booth (2004) identified an area in West Seattle that repeatedly observed unreinforced brick chimney damaged after the 1949 Olympia, 1965 Puget Sound, and 2001 Nisqually earthquake. The concentrated damage in this area was attributed to focusing of S-waves at the southern edge of the Seattle basin. As an example, Figure 2.7 shows evidence of chimney damage after the 2001 Nisqually earthquake. For structures located in basins and subjected to subduction interface earthquakes, the damage could be more severe because of the addition of long-duration shaking with basin amplification. This was observed in Japan by Hatayama et al. (2007). They attributed oil tank damage (shown in Figure 2.8) in the Yufutsu basin to the combination of long-period shaking (low frequency content) and long-duration shaking (large amount of cycles). More recently, Goda et al. (2015) also found long-period amplification in



Figure 2.7: Localized chimney damage (in West Seattle) after 2001 Nisqually (Photo Credit: Booth (2004))



Figure 2.8: Oil storage tank damage due to long-period shaking after 2003 Tokachi-Oki (Photo Credit: <http://mycommittees.api.org/standards/cre/scast/>)

shaking was due to the Kathmandu basin after the 2015 Gorkha Nepal subduction earthquake. However, many of the buildings constructed in Nepal are non-engineered (Goda et al., 2015) and are therefore expected to have poor seismic performance. For the buildings that collapsed in Nepal, it was difficult to isolate the effects of basins during subduction earthquakes and poor performance due to the structural system that would have likely resulted from any strong earthquake.

2.6.2 *Effects of Basins on Ground Motion Intensity and Structural Response*

Structures located in the Seattle metropolitan area will experience both long-duration motions during an M9 CSZ earthquake and basin amplifications due to the Seattle basin. The seismic performance of modern buildings in deep basins during subduction earthquakes has been investigated by some researchers. Heaton et al. (2006) investigated the effects of basins during the Tokachi-Oki earthquake motions by studying the response of 6- and 20-story steel moment-resisting frame buildings. Heaton et al. found that the long-period energy in the basin motions would have caused irreparable damage to steel moment-resisting frame buildings, and some of these buildings were close to

collapse. This research also studied moments frames with pre- and post-Northridge welds and concluded that the post-Northridge frames would have performed significantly better inside basins.

Yang (2009) expanded the work described above to consider the effects of basins in Seattle using simulated M_w 9.2 Cascadia subduction earthquakes that was based on the source model for the 2004 Sumatra earthquake. The study considered basin amplification using a transfer function that was derived by deconvolving rock site teleseismic recordings from basin site recordings. The rock site (PNSN station SEA) and basin site (PNSN station SHIPS02) were both located in Seattle. This study concluded that the basin site motions would have caused collapse in structures with brittle welds, whereas, structures with "perfect" welds would have avoided collapse. Yang (2009) also noted that the effects of duration may not have been fully captured because the model used did not completely consider the effects of cyclic degradation.

Recognizing the effects of basins on the built environment in Seattle, Frankel et al. (2007) developed a series of urban seismic hazard maps for Seattle that accounted for (a) 3D basin effects, (b) rupture directivity, and (c) nonlinear local-site amplification. The maps were derived using seismic hazard curves generated from 500 3D simulations for the Seattle fault, South Whidbey Island fault, and other gridded sources. However, due to the computational limitations at the time, basin amplifications from a Cascadia subduction zone earthquake were only determined using point-source runs along a portion of 1,000 km length subduction zone. While this was determined to be computationally efficient, it did not include the effect of rupture directivity that might be evident in large-scale 3D simulations. The results from the suite of simulations identified variations in basin amplification with earthquakes at different azimuths from the center of the Seattle basin.

Olsen et al. (2008) later conducted a simulation of an M_w 9 CSZ earthquake scenario which showed similar larger peak velocities (i.e., long-period accelerations) in the Seattle

area than in other metropolitan areas (Vancouver, Portland, Tacoma, and Olympia). This was attributed to amplifications caused by the underlying deep sedimentary basins.

The use of physics-based ground-motions to understand basin effects on building performance is used in other seismic prone regions as well. For example, Bijelić et al. (2018) performed collapse risk assessments for tall reinforced-concrete frame and reinforced-concrete core wall buildings in California using simulated motions from the Southern California Earthquake Center (SCEC) Broadband platform simulations (Maechling et al., 2015).

2.6.3 Mapping of Basins in the Pacific Northwest

Three-dimensional P- and S-wave velocity models of the Cascadia subduction zone have been assembled by Stephenson et al. (2017). The model includes several basins in the Pacific Northwest that were retrieved from several seismic wave mapping projects in the region. For example, the model includes the basins that surround the Puget Lowlands region that have been mapped up to 11 km depth through the Seismic Hazards Investigations in the Puget Sounds (SHIPS) project (Brocher et al., 2001). Figure 2.9 shows a 3D contour map of the Seattle basin which reaches depths up to 8 km in terms of depth to sediment layer with a 2,500 m/s shear-wave velocity (denoted $Z_{2.5}$) and is the largest in terms of depth compared to the other basins in the Puget Sound region (e.g., Tacoma basin, Everett basin). The velocity model also includes the Tualatin and Willamette basin underlying Portland and the surrounding metropolitan areas (e.g., Beaverton). The Tualatin and Willamette basin reaches depths of 3 km (in terms of $Z_{2.5}$). Figure 2.10 shows a 3D view of the basin surrounded Portland that is mapped by McPhee et al. (2014).

The full extent of the model can be visualized in Figure 2.11 which shows a $Z_{2.5}$ contour map outlining the extent of basins that surround the several metropolitan regions in the Pacific Northwest. To visualize the basins surrounding Seattle, Figures

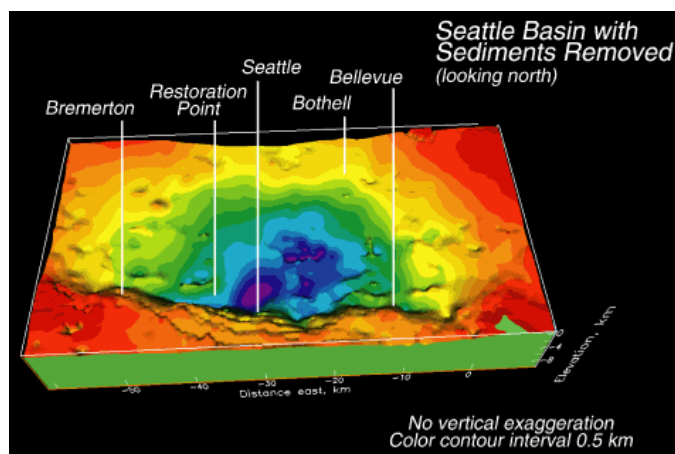


Figure 2.9: Mapping of Seattle basin from Blakely et al. (2000).

2.12 and 2.13 show a North-South (at -122.35 degrees longitude) and East-West (at 47.6 degrees longitude) cross-section of the shear-wave velocity profile of the Puget Sound region.

2.7 Research Needs

Many tall buildings in Seattle are expected to undergo long-duration shaking and resonate with motions that are amplified by the basin. Figure 2.14a shows the locations of tall buildings (≤ 10 -stories) in King County and Figure 2.14b shows the locations within the city of Seattle. Most of the tall buildings are located in the deepest part of the basin where amplifications are expected to be largest according to current GMM predictions (e.g., Campbell and Bozorgnia, 2014). To assess the seismic vulnerability of these structures, more research that builds off of the previously discussed research is needed. The key research needs in this area are listed below:

- (a) The paucity of strong-motion recordings in the Seattle basin is motivating the use of simulated ground-motions from physics-based approaches. Prior to the M9 project, the suite of 3D ground motion simulations for possible earthquakes in the

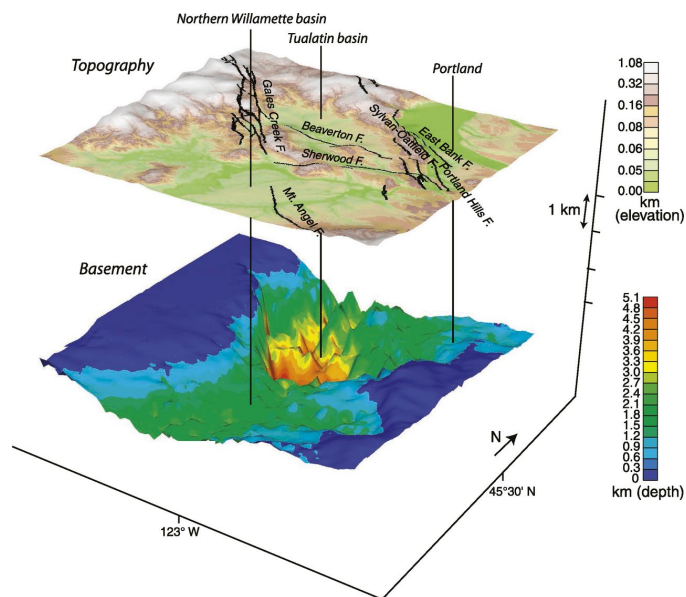


Figure 2.10: 3D view of the Tualatin basin from McPhee et al. (2014)

Seattle basin were limited to (i) crustal faults (Frankel et al., 2007), or (ii) simulations that did not explicitly model 3D basin effects (Yang, 2009), or (iii) included basin effects but only modelled a single scenario that is difficult to use for probabilistic evaluations (Olsen et al., 2008). Capturing the range of expected ground motion in Seattle would be difficult with a single scenario because basin amplifications are sensitive to the source's azimuthal angle (Frankel et al., 2007). To probabilistically evaluate the effects of basins on structures during large earthquakes, 3D physics-based simulations for multiple M9 CSZ scenarios are needed and is the focus here.

- (b) Many researchers have quantified the effects of duration on structural response (e.g., Raghunandan et al., 2015; Chandramohan et al., 2016b), however, few considered the effects of basin amplification in conjunction with long-duration shaking. The combined effects of long-duration motions from an M9 CSZ

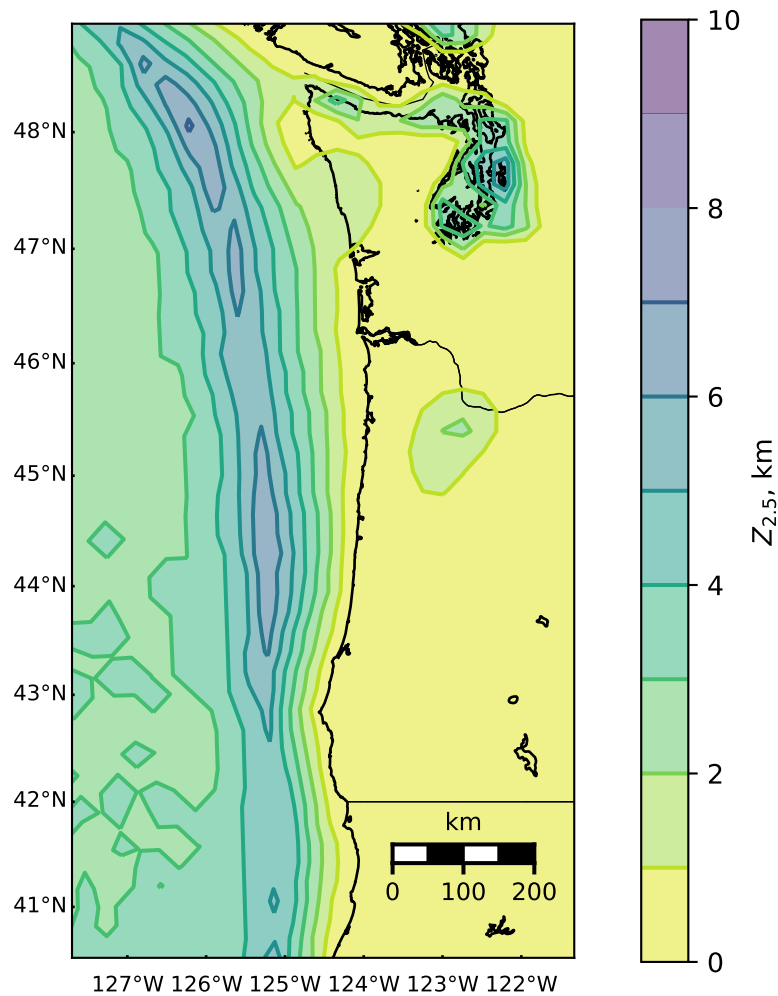


Figure 2.11: Contour map of $Z_{2.5}$ for the Pacific Northwest computed using the Stephenson et al. (2017) seismic velocity model. The contour map shows the basins underlying the Puget Lowland region (underneath Seattle) and the Tualatin Basin (underneath Portland).

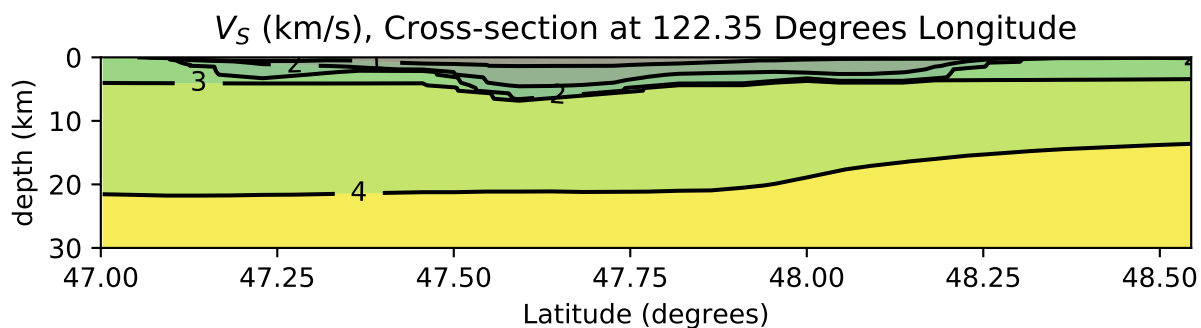


Figure 2.12: North-South cross section of velocity profile in the Puget Sound region.

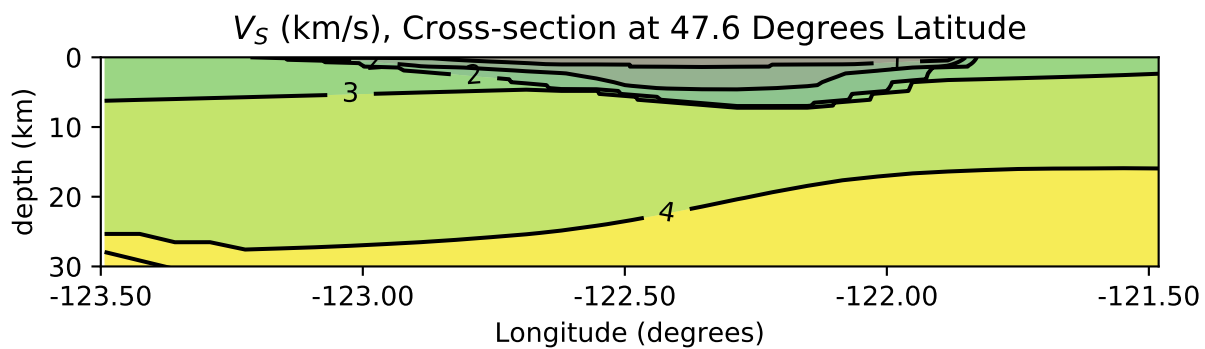


Figure 2.13: East-West cross section of velocity profile in the Puget Sound region.

earthquake and amplifications due to the basins in the Pacific Northwest has yet to be studied by others and is a research area of focus here.

- (c) The effects of basins on spectral acceleration have been accounted for and implemented in several NGA-West-2 GMMs for crustal earthquakes (Gregor et al., 2014). However, the current national seismic hazard maps (2014) do not account for the effects of basins because fine-scale seismic-wave velocities are unavailable for much of the US. Research is needed to study the effects of this omission in current building provisions (ASCE 7-16).
- (d) Previous work has focused on the effects of duration on the performance of reinforced concrete moment frame structures (e.g., Raghunandan et al., 2015; Chandramohan et al., 2016a) and steel moment frames (e.g., Heaton et al., 2006; Yang, 2009; Chandramohan et al., 2016a). However, the majority of new mid-rise and tall buildings in the Seattle area use reinforced concrete shear wall cores as the main lateral force resisting system. The effects of duration (and basin effects) on other systems, such as concrete wall buildings should also be studied.

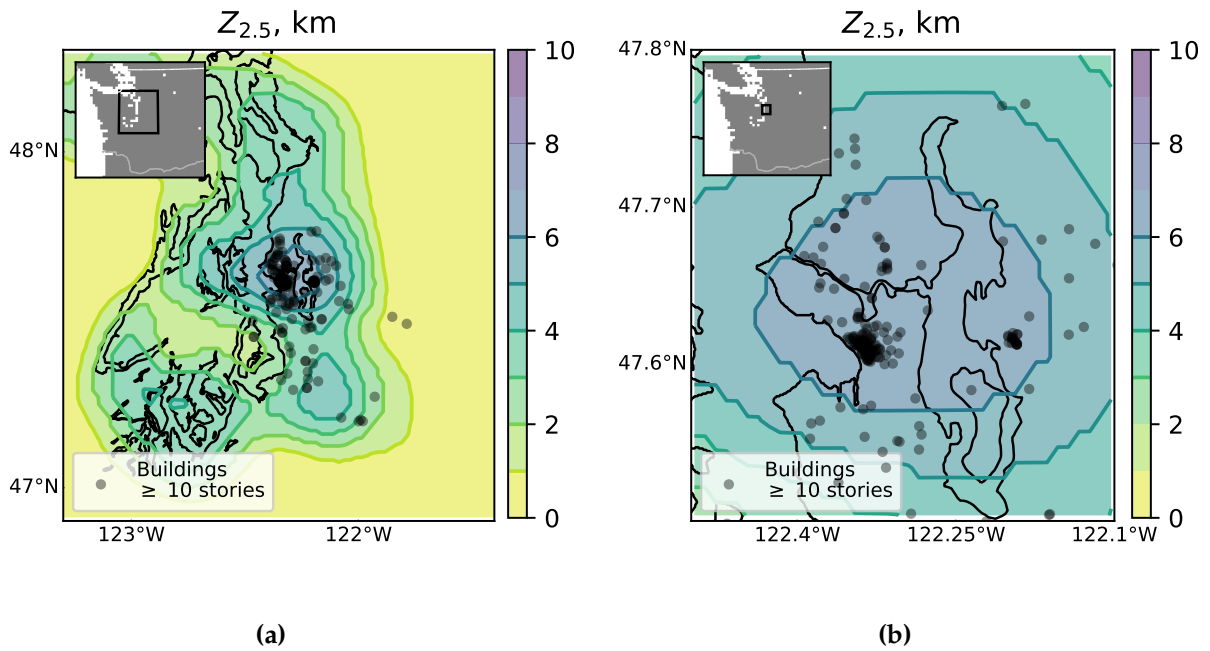


Figure 2.14: Contour map of $Z_{2.5}$ for the (a) Puget Sound region and for the (b) Seattle region showing the locations of all buildings in King County that are 10 stories or taller. Building locations were retrieved from the King County tax assessor database, (2016).

Chapter 3

DUCTILITY-DEPENDENT INTENSITY MEASURE THAT ACCOUNTS FOR GROUND-MOTION SPECTRAL SHAPE AND DURATION

This chapter is based on the following reference:

Marafi, Nasser A., Jeffrey W. Berman, and Marc O. Eberhard (2016). “Ductility-dependent intensity measure that accounts for ground-motion spectral shape and duration”. en. In: *Earthquake Engineering & Structural Dynamics* 45.4, pp. 653–672. ISSN: 00988847. DOI: [10.1002/eqe.2678](https://doi.org/10.1002/eqe.2678)

3.1 Chapter Overview

Large subduction earthquakes are expected to produce long-duration shaking which have been shown by other researchers to increase damage (Chapter 2). In addition, basins are expected to alter the ground-motion characteristics that affect the spectral accelerations and spectral shape. Therefore, the calculated nonlinear structural responses of a building can vary greatly, even if ground motions have similar spectral acceleration at a building’s fundamental period. To reduce the variation in structural response at a particular ground-motion intensity, this chapter proposes an intensity measure (IM_{comb}) that accounts for the combined effects of spectral acceleration, ground-motion duration, and response spectrum shape. The intensity measure includes a new measure of spectral shape that integrates the spectrum over a period range that depends on the structure’s ductility. The new IM is efficient, sufficient, scalable, transparent, and versatile. These features make it suitable for evaluating the intensities of measured (Chapter 4) and simulated ground motions (Chapter 6). The IM formulated in this chapter was then normalized in Chapter

6 to make it easier to compare it with motions used in structural evaluation. The normalized combined IM is called effective spectral acceleration, and denoted as $S_{a,eff}$.

The efficiency and sufficiency of the new IM is demonstrated for the following: (i) elastic-perfectly plastic single-degree-of-freedom (SDOF) oscillators with a variety of ductility demands and periods; (ii) ductile and brittle deteriorating SDOF systems with a variety of periods; and (iii) collapse analysis for 30 previously designed frames (by others). The efficiency is attributable to the inclusion of duration and to the ductility dependence of the spectral shape measure. For each of these systems, the transparency of the intensity measure made it possible to identify the sensitivity of structural response to the various characteristics of the ground motion. Spectral shape affected all structures, but in particular, ductile structures. Duration only affected structures with cyclic deterioration.

3.2 Introduction

In the design of new structures and the evaluation of existing ones, it is important to understand how key characteristics of both earthquake ground motions and structures are likely to affect structural demands. The effects of spectral acceleration and of structural force-deformation characteristics are already considered in current building codes through the design response spectrum and the response modification factor (ASCE, 2017). Bommer et al. (2004) and Hancock and Bommer (2007) investigated the influence of duration on structural damage measures (e.g., inter-story drift and absorbed hysteretic energy). Chandramohan et al. (2016b) and Raghunandan et al. (2015) showed that the ground-motion's duration can affect the minimum design strength needed to avoid collapse. Haselton et al. (2011a) and Eads et al. (2015), among others, have shown the influence of spectral shape on the collapse probabilities of structures. Recognizing these dependencies, recent guidelines (ASCE, 2013; PEER, 2010) have recommended that code-alternative or existing structures be evaluated with ground motions that have similar characteristics to the seismic events that control the hazard at the structure's site. Bradley et al. (2015) and Kwong et al. (2015) recently proposed ground motion selection procedures that depend on a vector of intensity measures.

To help select ground motions for structural analysis, a new scalar intensity measure (IM) is proposed that accounts for the effects of the following: (i) the elastic spectral acceleration at the structure's fundamental period; (ii) the duration of the motion; (iii) the shape of the response spectrum; and (iv) the structure's cyclic force-deformation properties. The new IM is evaluated in terms of key features that make an IM desirable. In particular, the chapter evaluates its efficiency and sufficiency in predicting force-reduction factors that lead to a target ductility demand in elastic-perfectly plastic SDOF systems, as well as collapse in brittle and ductile deteriorating SDOF systems. This chapter also investigates the dispersion of the IM at collapse for 30 archetypical building models subjected to 78 ground motions (Haselton et al., 2011b).

3.3 Desirable Features of an Intensity Measure

The goal of developing a new intensity measure is to help engineers design or evaluate structures. Tothong and Luco (2007) proposed that an IM be evaluated in terms of its *efficiency*, *sufficiency*, and *scalability*. Kramer (2014) suggested that the IM also needs to be *predictable*. Here, it is proposed that an IM should also be *transparent*, structurally *independent*, and *versatile*.

Ideally, an *efficient* IM would correlate perfectly with various measures of structural response. In such a scenario, the structure would reach a particular value of an engineering demand parameter at the same intensity of the IM, for any particular ground-motion record. In this case, only a single analysis would be required to characterize the response of the structure at that level of IM. In practice, an *efficient* measure will correlate strongly with structural response (i.e., low $\sigma_{\text{EDP}|\text{IM}}$), so that only a manageable number of computationally demanding, nonlinear dynamic analyses would be necessary to characterize the structure's response.

The seismic hazard at a site often includes contributions from a range of earthquake sources, with a variety of site-to-source distances, R , magnitudes, M , and rupture characteristics. The motions also depend on the local site characteristics, such as the average shear-wave velocity over the upper 30 m, V_{S30} . If the response of structures can be characterized by a scalar IM alone, independently of M , R , and V_{S30} , then the IM is deemed to be *sufficient*. A *sufficient* IM decouples the seismic hazard analysis from the probabilistic structural response analysis (Eads et al., 2015).

In this case, the engineer can select motions based on the IM, without considering earthquake hazard parameters.

To incorporate nonlinear, dynamic analyses into structural design or evaluation, ground motions are scaled either to a target spectral intensity, such as the design, or uniform hazard spectrum (ASCE, 2013; ASCE, 2014), or alternatively, they are scaled incrementally until collapse (Vamvatsikos and Cornell, 2002). To be compatible with these procedures, a new intensity measure needs to be *scalable*, in that its value is proportional to the ground-motion scaling factor. To achieve this goal, the contributions of duration and spectral shape to the new IM should be unaffected by scaling.

The IM's *predictability* is characterized by the variability in the intensity measure for a given earthquake scenario (Kramer, 2014), that is, the dispersion in the estimated IM calculated with a ground-motion model (GMM). Carrying this variability through a performance-based earthquake engineering analysis (FEMA (Federal Emergency Management Agency), 2009) can result in higher engineering demand parameters, damage measures, and decision variables than for a less *efficient* but more *predictable* IM.

To help an engineer compare and select ground motions, the intensity measure should clearly quantify the individual contributions of spectral acceleration, shape, and ground-motion duration, making the IM *transparent*. If the intensity measure does not explicitly identify these contributions, it would be difficult to evaluate why the effects of two motions differ. For example, the inelastic displacement of a bilinear oscillator, S_{di} (Tothong and Luco, 2007), depends on a variety of ground motion characteristics (and the oscillator strength). However, S_{di} does not indicate which particular ground-motion characteristic makes the intensity particularly large or small, or why the inelastic displacements differ for two ground motions.

Ideally, an IM would be *independent* of structural properties. Such measures are convenient, because they need to be computed (and tabulated) once for each motion, and used in the evaluation of a wide variety of structures. For example, the peak ground acceleration is *independent* of the structural properties. In practice, total independence often leads to poor efficiencies, so the IM should be evaluated by its degree of structural independence. For example,

S_a , which depends on the structure's period, is more independent than S_{di} , which depends both on the structure's period and its yield strength.

Finally, an IM should also be *versatile*, meaning that it can be used in a variety of situations. For a conventional probabilistic seismic hazard analysis (PSHA), the statistics of a *versatile* IM could be predicted using GMMs (preferably already available) (Kramer, 1996). For example, epsilon (Baker and Cornell, 2006), an indirect measure of spectral shape depends explicitly on the statistics of the GMM for S_a . A *versatile* IM could also be used in other situations where the PSHA is performed without GMMs. For example, Graves et al. (2011) proposed generating numerous ground motions for a PSHA with physics-based 3D models by varying earthquake rupture parameters. Such modeling may be necessary for situations not modeled adequately with existing GMMs. For example, the effects of basins can depend greatly on the particular properties of each basin and its tectonic environment (Graves et al., 1998; Hatayama et al., 2007; Frankel et al., 2009), which can only be approximated with existing GMMs (Choi et al., 2005; Abrahamson and Silva, 1996). In addition, a *versatile* IM could be used (independently of GMMs) to compare sets of ground motions that have differences resulting from a number of factors (source and site conditions) and which cause different structural responses.

The IM should also correlate well with a variety of engineering demand parameters. For this reason, the proposed intensity measure will be evaluated with a wide range of ground motions and systems, including the following: (i) a large number of elastic-perfectly plastic SDOF systems with a wide range of oscillator frequencies and ductility demands; (ii) brittle, quickly deteriorating' and ductile, slowly deteriorating' SDOF systems; and (iii) a set of archetypical buildings models.

3.4 Existing IMs for Duration and Spectral Shape

Other researchers have investigated the effects of ground-motion duration and spectral shape. Bommer et al. (2004) found that the effects of duration are more pronounced in structures that are susceptible to low-cycle fatigue and that also undergo strength and stiffness degradation under dynamic loading. They also showed that using IMs that account for spectral shape with duration intensity measures decouple the two effects on structural response. Hancock and Bommer (2007)

later took an alternative approach by comparing the effects of duration using spectrally matched records.

Chandramohan et al. (2016b) found that, compared with other measures, significant duration (D_s) was the most suitable IM for ground-motion duration. Significant duration is defined as the time between two target values of the integral, $\frac{\int_0^t a_g(t)^2 dt}{\int_0^{t_{\max}} a_g(t)^2 dt}$, where a_g is the ground acceleration, and t_{\max} is the total duration of the record. Chandramohan et al. (2016b) found that D_s correlates well with structural collapse capacity (as computed with nonlinear dynamic analysis); it is unaffected by ground-motion scaling; and it is not correlated to other common IMs. Bommer et al. (2004) and Chandramohan et al. (2016b) both evaluated other IMs for duration (e.g., bracketed duration) that are not considered in this chapter because of their lack of scalability.

De Biasio et al. (2014) evaluated several intensity measures that account for the effects of spectral shape. Those summarized here have many of the identified desirable features. Cordova et al. (2000) developed an IM based on spectral acceleration, $S^*(T_n)$, where T_n is the fundamental period of the structure. S^* accounts for spectral shape by multiplying the spectral acceleration by the square root of the ratio of spectral accelerations at two periods:

$$S^* = S_a(T_n) \left[\frac{S_a(2T_n)}{S_a(T_n)} \right]^{0.5} \quad (3.1)$$

De Biasio et al. (2014) showed that the intensity measure S^* correlated with building response. However, the spectral shapes for ground motions and the effective period of nonlinear structures can vary greatly, and this measure does not include the effects of peaks occurring at periods other than the two considered.

Baker and Allin Cornell (2006) introduced an IM that quantifies the spectral shape by computing the geometric mean of a series of spectral accelerations, $S_{a,geo}$. This IM is computed as,

$$S_{a,geo} = \left[\prod_{i=a}^N S_a(c_i T_n) \right]^{1/N} \quad (3.2)$$

where $c_i T_n$ corresponds to several periods of interest. Bojórquez and Iervolino (2011) found that, if $c_i T_n$ were taken at consistent intervals between T_n to $2T_n$, the resulting intensity measure better correlated with structural collapse. Eads et al. (2015) found that $c_i T_n$ computed between $0.2T_n$ to

$3T_n$ resulted in an intensity measure that accounted for higher mode effects and nonlinearity. This approach resulted in lower dispersions in the prediction of the IM to cause collapse of numerous building models with various ground motions sets. De Biasio et al. (2014) showed similar trends through another intensity measure, ASAR, which also quantifies the spectral shape in terms of values at several period ranges.

3.5 A New Intensity Measure

The proposed ground-motion intensity measure combines the spectral acceleration at the first natural period of a structure, a measure of the ground-motion duration, and a measure of the shape of the ground-motion elastic response spectrum:

$$IM_{\text{comb}} = S_a(T_n)IM_{\text{dur}}^{C_{\text{dur}}}IM_{\text{shape}}^{C_{\text{shape}}} \quad (3.3)$$

where $S_a(T_n)$ is the spectral acceleration at the fundamental period of interest (T_n), IM_{dur} is the IM for duration, and IM_{shape} is the IM for spectral shape. The empirical exponent C_{dur} accounts for the structure's sensitivity to IM_{dur} , and the C_{shape} exponent accounts for its sensitivity to IM_{shape} . Once the IMs have been selected, the exponents are found by regression analyses. In this chapter, $S_a(T_n)$ was computed for a damping ratio of 5%. IM_{dur} was taken as the significant duration, computed as the time interval between 5% and 95% of the maximum value of the integral. For the ground-motion sets considered, this time interval resulted in a marginal benefit to the IM's efficiency compared with other intervals (e.g., 5-75%).

A new measure of spectral shape (IM_{shape}) is developed here that accounts for the differences in period elongation between brittle and ductile structures. Haselton et al. (2011a) showed that ductile structures are more susceptible to spectral shape effects. To account for this dependence, IM_{shape} is calculated over a period range that depends on its ductility demand, if that is known, or alternatively, on the structure's ductility capacity. A new IM_{shape} , denoted SS_a , is defined using the integral of the ground-motion response spectrum (damping ratio of 5%) between the fundamental period of the building (T_n) and the nominal elongated period (αT_n), as shown in Figure 3.1. To make IM_{shape} independent of scale, the integral is then normalized by the area of a rectangle with height of $S_a(T_n)$ and width of $(\alpha - 1)T_n$.

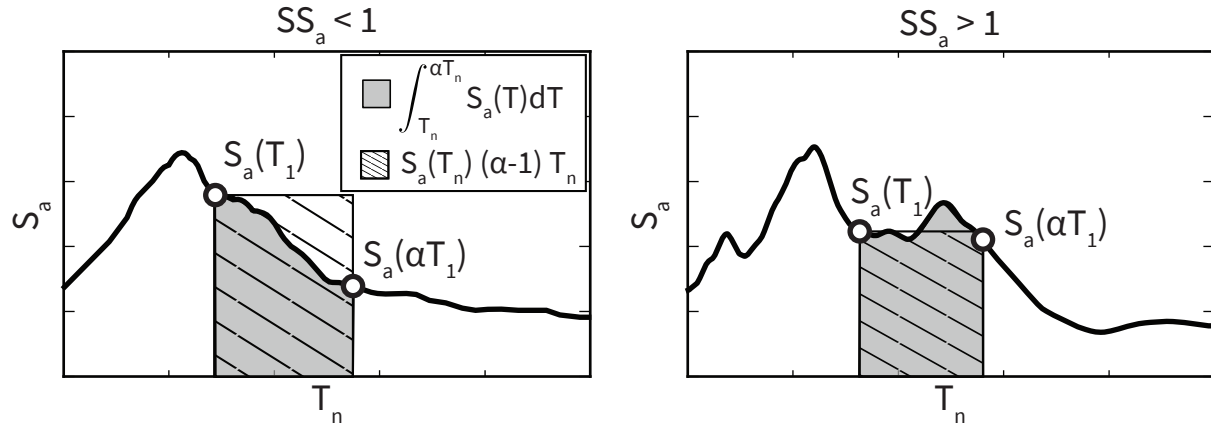


Figure 3.1: Graphical depiction of (a) SS_a less than 1 and (b) SS_a greater than 1.

$$IM_{\text{shape}} = SS_a(T_n, \alpha) = \frac{\int_{T_n}^{\alpha T_n} S_a(T) dT}{S_a(T_n)(\alpha - 1)T_n} \quad (3.4)$$

where αT_n is computed as a multiple of the secant stiffness of the structure at maximum displacement resulting in Equation 3.4 where C_α is set to 1.3 (its variations are shown later), and μ is the system's displacement ductility factor.

SS_a can also be interpreted as the arithmetic mean of the response spectrum over the period range, T_n to αT_n , normalized by $S_a(T_n)$. A similar IM_{shape} , SS_d , can be computed using the displacement response spectrum.

To illustrate its variation, SS_a is plotted in Figure 3.2a versus period for two records selected from the Next Generation Attenuation database (PEER, 2014). The two records have nearly identical values of S_a at a period of 1s, but their spectral shapes differ. The SS_a for each ground-motion was calculated using Eq. 3.4 for a range of periods (0.1-3s), in which μ was assumed equal to 4 for this example. Figure 3.2b shows that SS_a is larger than 1.0 if the average spectral ordinate increases with increasing period, and it is smaller than 1.0 if the average spectral ordinate decreases with increasing period. For the set of ground motions considered here, the variation of SS_a is better represented by a log-normal distribution than a normal distribution (Kolmogorov-Smirnov test).

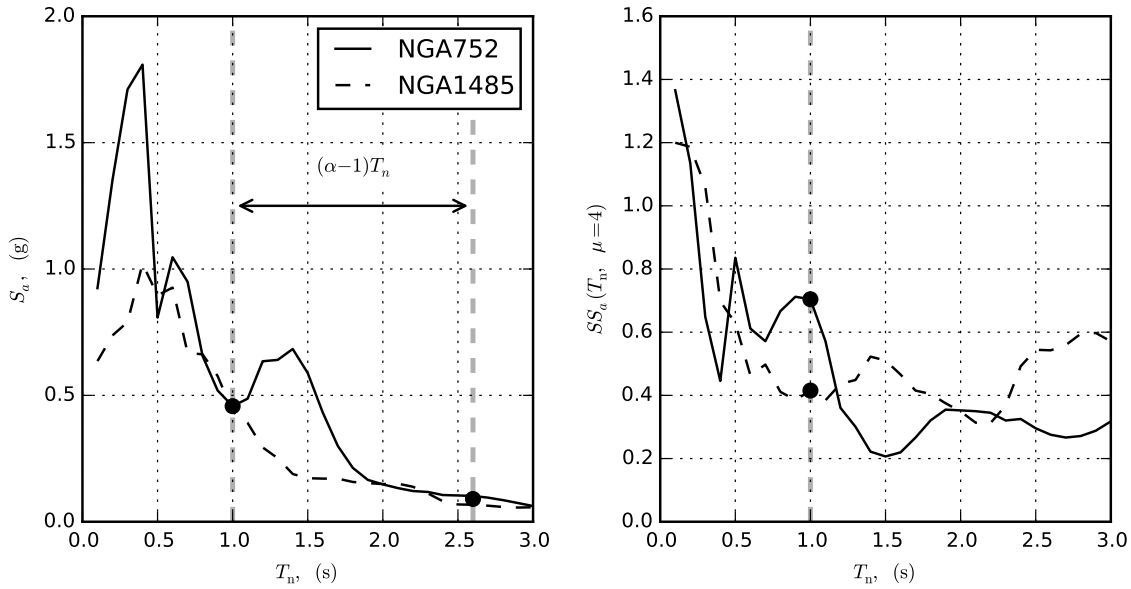


Figure 3.2: Comparison of two ground motions in terms of (a) response spectrum, and (b) spectral shape intensity measure, SS_a .

Two previously assembled ground-motion sets, with a variety of source mechanisms, source-to-site distances and magnitudes, were used to evaluate IM_{comb} , as computed with $IM_{dur} = D_{s,5-95}$ and $IM_{shape} = SS_a$. The first set, compiled by Haselton et al. (2011b), consists of 39 record pairs, mainly of large-magnitude ($M_w 6.5 - 7.6$) earthquakes, recorded at moderate site-to-source distances (10-45km). This set is an expanded version of the far-field ground motion set used in Federal Emergency Management Agency (FEMA) P695 (2009) and in this chapter is referred to as the FEMA ground motion set. The second set, compiled by Raghunandan et al. (2015), consists of 77 earthquake records, 42 of which are long-duration recordings from large-magnitude ($6.8 - 9.0 M_w$) subduction interface events, and the remaining 35 are short-duration recordings selected from the expanded FEMA set. For this chapter, this ground motion set is referred to as the crustal/subduction set. The ground motions from both sets were recorded at stiff soil or rock sites.

The proposed intensity measure has many desirable features. The effects of S_a , D_s , and SS_a are transparent and uncorrelated. Figure 3.3 evaluates the collinearity of $\ln SS_a$ and $\ln D_{s,5-95}$ (in

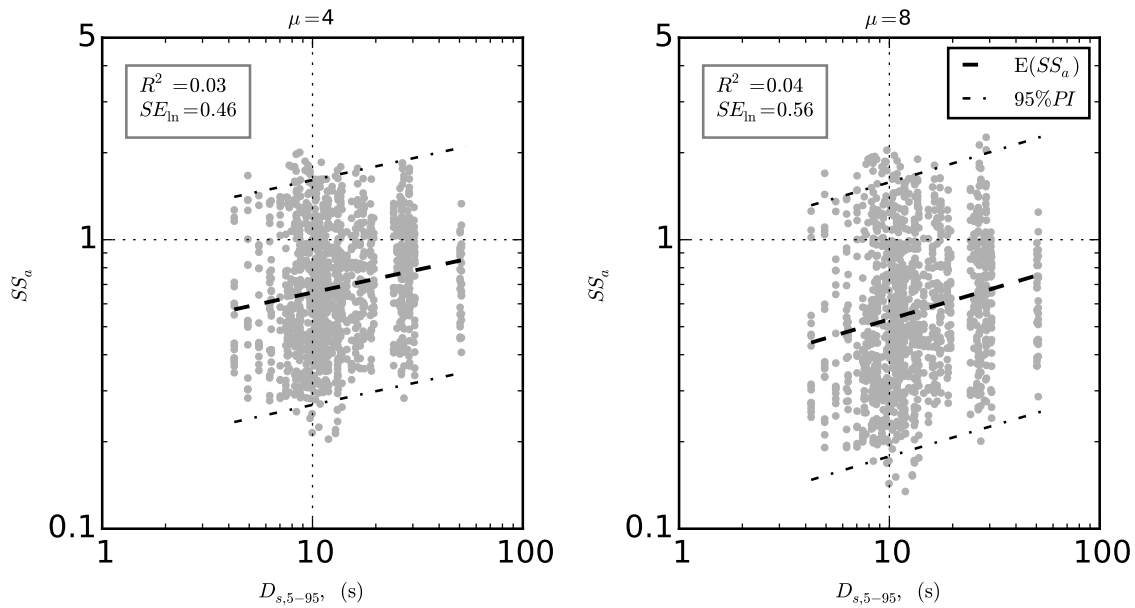


Figure 3.3: Intensity measure SS_α calculated for (a) $\mu=4$ and (b) $\mu=8$ with respect to significant duration for the expanded FEMA P695 ground motion set.

terms of the coefficient of determination, R^2 in log-space) using the expanded FEMA ground-motion set, in which SS_α is shown for a range of periods (0.1-3s) for values of $\mu = 4$ and $\mu = 8$. The value of R^2 , indicates the goodness of fit and also corresponds to the square of the sample correlation coefficient (r^2) in a simple linear regression model. The expected value of the response variable, $E(SS_\alpha)$, from the linear regression model is plotted along with the 95% prediction intervals (95% confidence that SS_α lies within this interval). The dispersion can be quantified by the prediction intervals, or alternatively, by the standard error of the estimate (in log-space) from the regression model (SE_{ln}). The values of $R^2 = 0.03$ and 0.04 , respectively, for $\mu = 4$ and $\mu = 8$, indicate that the two variables (SS_α and $D_{s,5-95}$) are independent of each other for the FEMA ground motions (Figure 3.3). The results are similar for other ductility demands and for the crustal/subduction ground-motion set.

The normalized intensity measures for IM_{shape} and IM_{dur} are independent of scaling, so IM_{comb} increases linearly with the ground-motion scaling factor. The mean and standard

deviation of S_a and $D_{s,5-95}$ used in IM_{comb} can be predicted with commonly available GMMs 25, so the predictability of these components have been established. However, to incorporate the proposed IM into the existing framework for PSHA, it would be necessary to characterize the variability of SS_a with respect to M , R , and the structure's site characteristics. In the case where the site hazard is estimated using numerous physic-based 3D ground motion simulations of various rupture scenarios 20, IM_{comb} is versatile enough to quantify the effects of these synthetic motions without referring to GMMs. One of the drawbacks of IM_{comb} is its dependence on structural properties other than the structure's period, making it less independent of structural properties than some existing IMs. Using the structure's ductility in SS_a results in a more efficient IM at the expense of less independence from structural properties. The following sections discuss the efficiency and sufficiency of IM_{comb} .

3.6 Evaluating the Intensity Measure using SDOF Elastic-perfectly Plastic Systems

In the past, the shape of the spectrum has often been accounted for indirectly through ductility-dependent force-reduction factors and period, $R_\mu - \mu - T_n$ relationships (e.g., 32). Miranda and Bertero 33 compared numerous $R_\mu - \mu - T_n$ relationships, some of which depended on site soil properties and peak spectral velocity (e.g., 34), or only on the period of the structure (e.g., 35). Such relationships are unlikely to be efficient and sufficient for a wide range of ground motions, particularly if these relationships refer explicitly to fixed period ranges, because different site conditions will lead to different spectral shapes. In this chapter, the influence of period is accounted for explicitly as part of the calculation of IM_{shape} .

In this section, the efficiency and sufficiency of IM_{comb} in predicting R_μ is evaluated for elastic-perfectly plastic SDOF systems. R_μ factors are computed as the strength required for an SDOF oscillator to remain elastic, divided by the minimum yield strength (F_y) required to achieve the target ductility demand, μ , (i.e., $R_\mu = S_a(T_n)m/F_y$), where m is the mass of oscillator. The effect of $S_a(T_n)$ is already reflected in the equation for F_y , so R_μ should capture the effects of other key features, such as ductility demand, spectral shape, and duration.

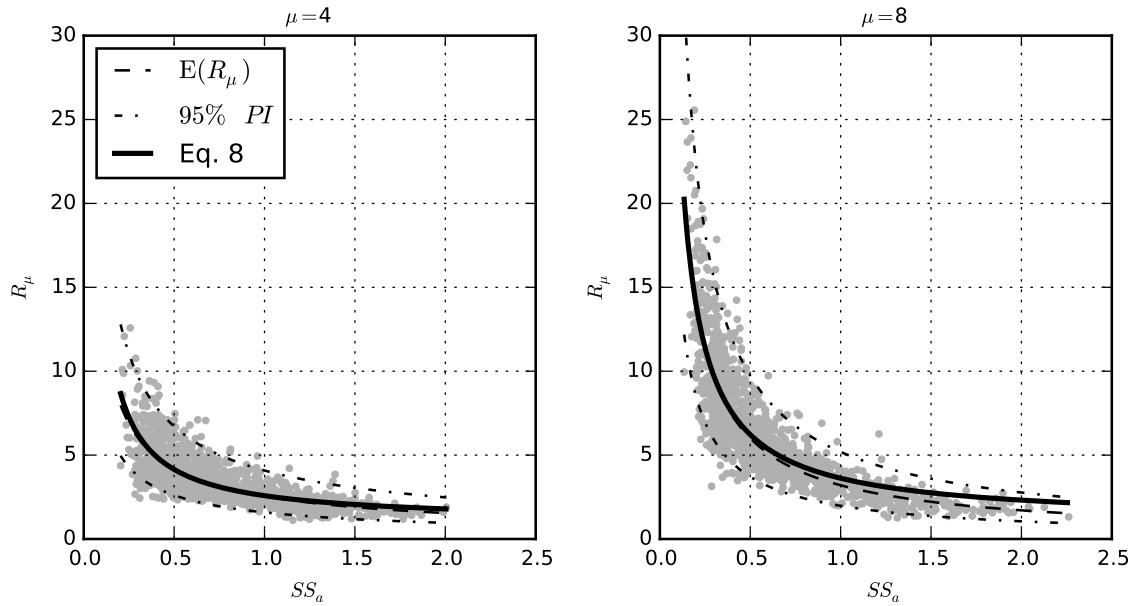


Figure 3.4: Ductility-dependent force-reduction factors with respect to SS_a for the expanded FEMA P695 ground motion set for (a) $\mu=4$ and (b) $\mu=8$.

3.6.1 Efficiency of estimates of R_μ

Figure 3.4 plots the computed R_μ factors with respect to the SS_a for systems with $\mu=4$ and 8 using the expanded FEMA set for a range of 17 periods, ranging from 0.1 to 3s, spaced equally in log scale. The correlations are computed with respect to SS_a , rather than IM_{comb} , because the maximum displacement of elastic-perfectly plastic systems are known to be unaffected by ground-motion duration (Hancock and Bommer, 2007). This independence is re-confirmed later. For $\mu=8$, the calculated values of SS_a range from 0.13 to 2.26, and the calculated values of R_μ range from 1.26 to 25.6. As expected, R_μ increases with increasing μ , and decreases consistently with increasing SS_a .

In Figure 3.5, R_μ and SS_a have been transformed using the natural-log function to make it possible to perform a simple linear regression analysis with an ordinary least squares (OLS) optimization. In Figure 3.4, the reported values of RSE_{ln} are the standard error of the estimate normalized by the sample mean, enabling the comparison of regression models with different

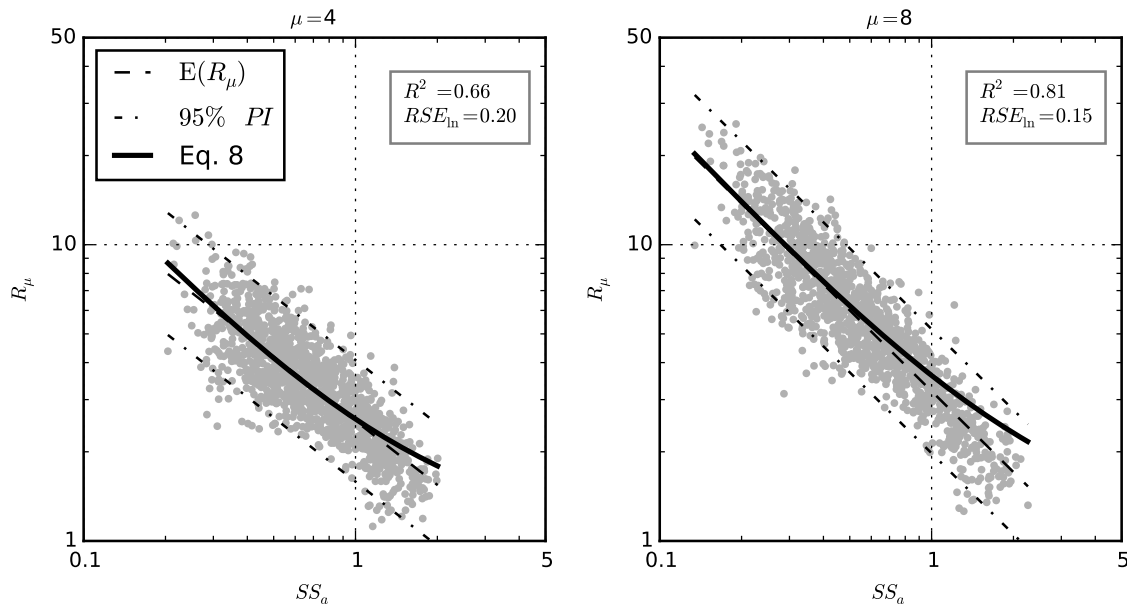


Figure 3.5: Ductility-dependent force-reduction factors with respect to SS_a (log-scale) for the expanded FEMA P695 ground motion set for (a) $\mu=4$ and (b) $\mu=8$.

mean response variable distributions. The R^2 statistic shows that the correlation between $\ln R_\mu$ and $\ln SS_a$ is high (0.66 and 0.81 for $\mu=4$ and 8, respectively).

Figure 3.6 shows the results of linear regression for a wide range of values of μ and for both sets of ground motions. The figure shows that the correlation between $\ln R_\mu$ and $\ln SS_a$ increases (i.e., higher R^2 , lower RSE_{\ln}) consistently with increasing values of μ and that the statistics are similar for both ground-motion sets. Based on these results, it appears that SS_a is an efficient IM for predicting the force-reduction factor for elastic-perfectly plastic SDOF systems.

3.6.2 Sufficiency of estimates of R_μ

The sufficiency of the new IM can be evaluated in terms of the significance of the relationship between the residual of the estimate to the ground motion's magnitude, M , the site-to-source distance, R , and the average shear-wave velocity, V_{S30} . The residual of the estimate (using IM_{comb}/S_a) was computed as the natural-log of the ratio between R_{measured} to $R_{\text{estimated}}$

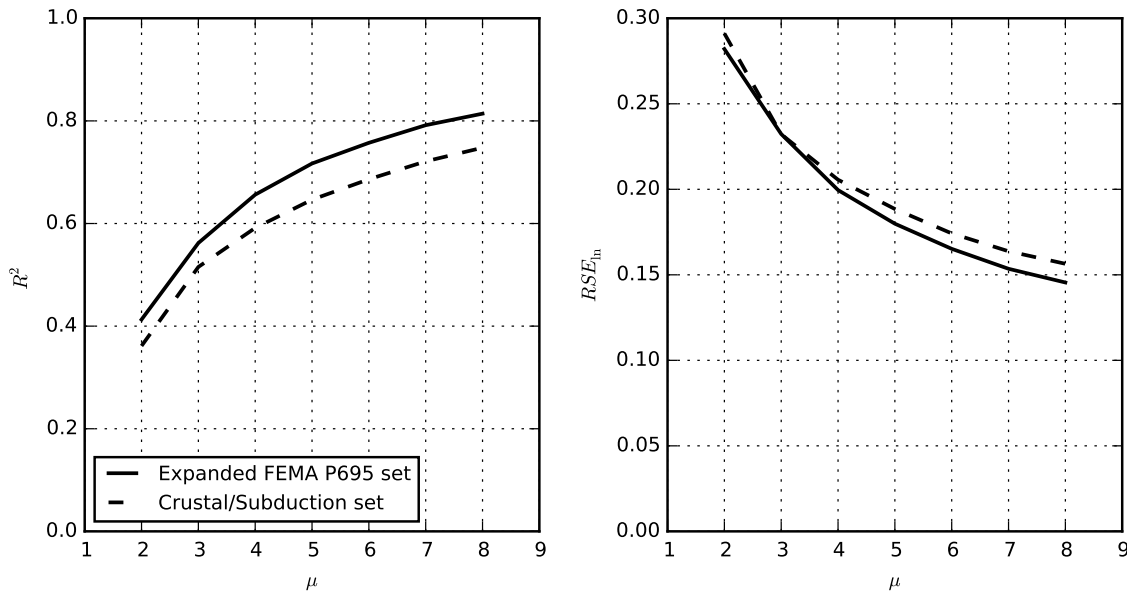


Figure 3.6: Statistics of R_μ versus SS_α linear regression models for various μ factors: (a) R^2 and (b) RSE_{In} .

(Figure 3.4). Figure 3.7 shows 78 residuals with respect to M and R for an oscillator with $T_n = 1$ s and $\mu=4$ for the expanded FEMA set. The figure also shows the approximated slope ($\tilde{\beta}$) from a simple linear regression model, along with the corresponding p-value.

The p-value is the probability of obtaining the observed results (or more extreme results), if the null hypothesis holds true. In this context, the null hypothesis states that the true β coefficient is zero. Figure 3.8 shows the p-values for the 17 periods for $\mu=4$ and 8. This chapter uses a 0.05 level of significance to determine whether the null hypothesis can be rejected, that is, IM_{comb} is sufficient. For example, for $\mu=8$, Figure 3.8b shows that the IM is sufficient with respect to M for 76% (13/17) of the oscillator periods, and it is sufficient with respect to R for 71% (12/17) of the periods. The IM is also sufficient with respect to V_{S30} for all (17/17) oscillator periods for both $\mu=4$ and $\mu=8$.

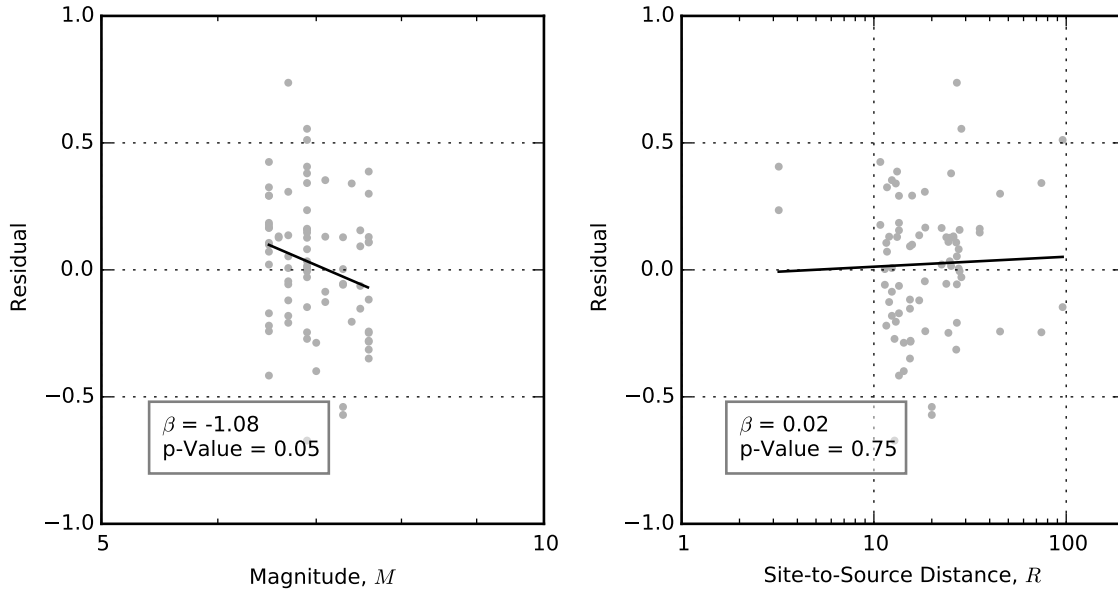


Figure 3.7: Residual versus magnitude and site-to-source distance for $T_n=1s$ and $\mu=4$.

Another perspective on sufficiency can be gained by expanding Eq. 3.3 to include the record's magnitude and distance, as well as the oscillator period. The expanded IM is defined as,

$$IM_{\text{comb,exp}} = S_a(T_n) D_s^{C_{\text{dur}}} SS_a^{C_{\text{shape}}} M^{C_M} R^{C_R} T^{C_{T_n}} \quad (3.5)$$

Both IM_{comb} (with SS_a and D_s) and $IM_{\text{comb,exp}}$ (including the additional parameters) can be used to predict R_μ using multiple linear regression. Because R_μ is normalized, both IMs need to be normalized by spectral acceleration as well. This is done by defining the regression model as,

$$R_\mu = C_0 \frac{S_a}{IM} \quad (3.6)$$

where C_0 and the IM's exponents are determined by an OLS optimization.

Table 3.1 reports the approximated standardized coefficients, $\hat{\beta}_i^s$, determined from multiple linear regression analysis on each of the predictor variables in log-space. The $\hat{\beta}_i^s$ quantify the change (in terms of standard deviations) in the response variable resulting from a change of one standard deviation in the predictor variable. For both ground motions sets, the low standardized coefficients for $\ln D_s$ confirm that ground-motion duration does not significantly influence the

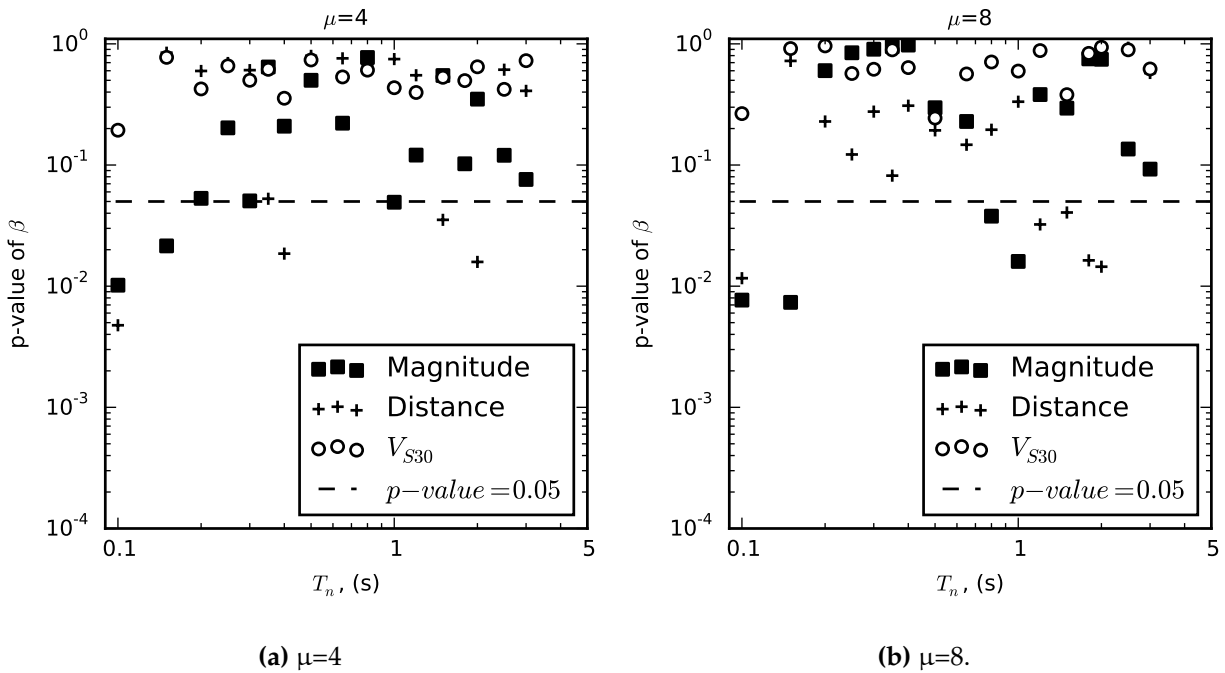


Figure 3.8: P-values for the β coefficients of magnitude, site-to-source distance and V_{S30} to predict the residual of the estimate for (A) $\mu=4$ and (B) $\mu=8$.

Table 3.1: Results of regression analysis for R_μ ($\mu=8$).

| Variable | Expanded FEMA Set | | Custal/Subduction Set | |
|------------------------------|---------------------|-----------------|-----------------------|-----------------|
| | $S_a/IM_{comb,exp}$ | S_a/IM_{comb} | $S_a/IM_{comb,exp}$ | S_a/IM_{comb} |
| $\hat{\beta}_{Magnitude}^s$ | -0.02 | — | 0.04 | — |
| $\hat{\beta}_{Distance}^s$ | -0.04 | — | -0.07 | — |
| $\hat{\beta}_{T_n}^s$ | 0.07 | — | 0.08 | — |
| $\hat{\beta}_{D_{s,5-95}}^s$ | -0.01 | 0.00 | -0.07 | -0.09 |
| $\hat{\beta}_{SS_a}^s$ | 0.85 | -0.9 | -0.82 | -0.87 |
| R^2 | -0.82 | 0.81 | 0.76 | 0.76 |
| SE_{ln} | 0.24 | 0.25 | 0.26 | 0.26 |
| RSE_{ln} | 0.14 | 0.15 | 0.15 | 0.15 |

response of elastic-perfectly plastic systems. The low values of standardized coefficients for $\ln M$, $\ln R$, and $\ln T_n$ (Table 3.1) for $IM_{comb,exp}$ show that, by this measure, IM_{comb} is sufficient with respect to these variables. This sufficiency is also shown by the fact that R^2 and the standard errors are nearly identical for $IM_{comb,exp}$ and IM_{comb} .

3.6.3 Explicit prediction of R_μ based on SS_a and μ

Because ground-motion duration has a negligible effect on the force-reduction factor for an elastic-perfectly plastic system, R_μ can be estimated explicitly in terms of SS_a and μ . The prediction equation using the two predictor variables were linearized and constrained so that R_μ would be equal to 1.0 when μ is equal to 1.0. The prediction equation is defined as

$$\ln R_\mu = \hat{\beta}_0 + \hat{\beta}_1 \ln(\mu - 1) + \hat{\beta}_2 \ln SS_a + \text{error} \quad (3.7)$$

where $\hat{\beta}$ is the approximated beta coefficient. The transformed variable $\ln(R_y - 1)$ was predicted from the multiple linear regression model with an OLS optimization. The mathematical expression for R_μ transformed back to normal space is

$$R_\mu(\mu, SS_a) = 1 + C_0(\mu + 1)^{C_1} SS_a^{C_2} + \text{error} \quad (3.8)$$

where $C_0 = e^{\hat{\beta}_0} = 2.31$, $C_1 = \hat{\beta}_1 = 0.57$, and $C_2 = \hat{\beta}_2 = -1.02$.

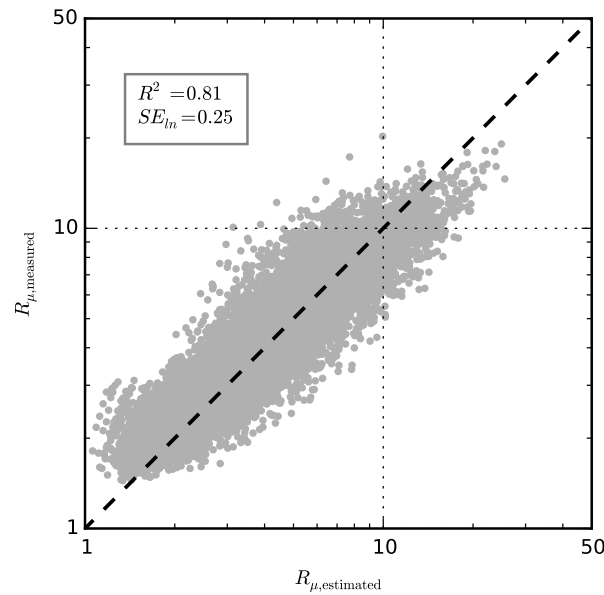


Figure 3.9: Measured R_{μ} versus estimated R_{μ} using Eq. 3.8

The estimated and measured R_{μ} factors are plotted in Figure 3.9 for μ factors ranging from 2 to 8 and for periods ranging from 0.1 to 3.0s. The model's R^2 statistic indicates that Eq. 3.8 can explain 81% of the total variation of R_{μ} for an elastic-perfectly plastic oscillator for a given μ and subjected to a record with a given SS_{α} . The standard error of the estimate in log-space (SE_{ln}) is equal to 0.25. The generalized prediction curves calculated with Eq. 3.8 are shown in Figures 3.4 and 3.5. These curves are shown in relation to the expected values, $E(R_{\mu})$ from the individual regression analysis for each μ factor.

3.7 Evaluating the Intensity Measure using Deteriorating SDOF Systems

To ensure that IM_{comb} is versatile and efficient, it should also correlate with the results of nonlinear dynamic collapse analyses of deteriorating systems. The force-deformation behaviors of the deteriorating SDOF systems were modeled using the peak-oriented deteriorating model (Ibarra et al., 2005) as implemented in *OpenSees* (McKenna, 2016). Two sets of SDOF models were developed to represent *brittle, quickly deteriorating* and *ductile, slowly deteriorating* systems. The

Table 3.2: Model parameters used for the Ibarra et al. (2005) peak-oriented deterioration model.

| Ibarra model parameter | Brittle, quickly deteriorating ^a | Ductile, slowly deteriorating ^a |
|--------------------------|---|--|
| Post-yield stiffness | $0.03K_e^b$ | $0.03K_e^b$ |
| Post-capping stiffness | $-0.1K_e^b$ | $-0.1K_e^b$ |
| $\delta_{cap.}/\delta_y$ | 4 | 8 |
| $\gamma_{s,c,a}$ | 25 | 100 |
| γ_k | 50 | 200 |
| Residual strength | ≈ 0 | ≈ 0 |

K_e is the elastic stiffness of the oscillator; $\delta_{cap.}/\delta_y$ is the ratio of the capping displacement to the yielding displacement; $\gamma_{s,c,a}$ is the cyclic deteriorating parameter for yield strength, post-capping strength, and acceleration reloading stiffness; γ_k is the cyclic deterioration parameter for the unloading stiffness. ^a η is equal to 5% of critical damping, ^b Rate of deterioration (c) is equal to 1.0.

values of the model parameters (shown in Table 3.2) were similar to those proposed by Haselton et al. (2008) and Ibarra and Krawinkler (2011), based on their calibration of the model with experimental results. To capture the effects of spectral shape at various periods (0.1-3s), the SDOF oscillators had varying initial elastic stiffnesses and were subjected to both ground motions sets. Previous studies have incorporated p-delta effects by rotating the backbone curve of the nonlinear spring. In this study, p-delta effects have not been explicitly incorporated in the analysis, but rather, are incorporated into the assumed elastic, post-yield and post-capping stiffness values.

Using an incremental dynamic analysis (Vamvatsikos and Cornell, 2002), the spectral acceleration at collapse ($S_{a,c}$) was computed as the point where the system reached its residual strength and had negligible stiffness. Figure 3.10 shows incremental dynamic analysis curves for a ductile oscillator subjected to the 78 ground motion records in the expanded FEMA set, scaled incrementally until collapse. To normalize the building response parameter, $S_{a,c}$, so that the oscillators at various periods could be compared, the results are summarized in terms of the relative intensity, R_c (Ibarra and Krawinkler, 2011). R_c was computed as the ratio of $S_{a,c}$ for a given ground motion to the yield strength of the system normalized by the weight of the

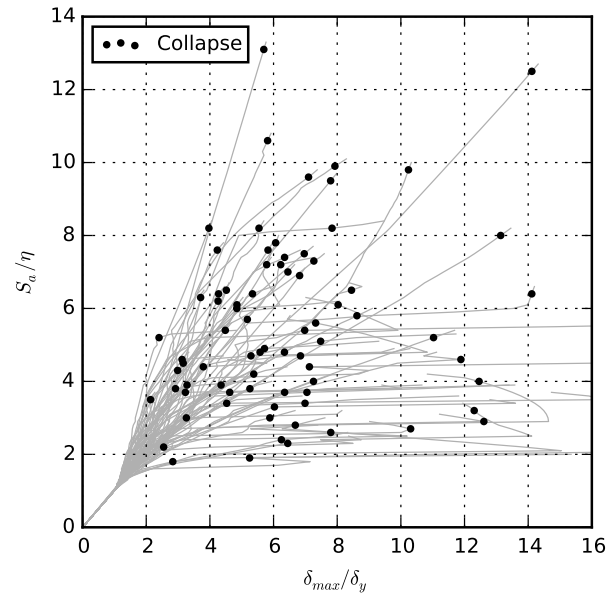


Figure 3.10: Incremental dynamic analysis using the expanded FEMA P695 set for a *ductile, slowly deteriorating* system with $T_n = 1.0$.

structure, shown as,

$$R_c = \frac{S_{a,c}}{\eta g} \quad (3.9)$$

where $\eta = \frac{F_y}{mg}$, F_y is the system strength, m is the mass of the structure, and g is the gravitational acceleration. R_c quantifies the ground-motion's intensity on a particular system, and it can be viewed as the equivalent of R_μ (Ibarra and Krawinkler, 2011).

3.7.1 Efficiency of estimates of R_c

Efficiency can be quantified through the dispersion of the IM's intensity that causes collapse for a particular system using a set of ground motions. A similar relationship to Eq. 3.7 can be established using R_c , where SS_a in IM_{comb} can be computed using values of α that depend on the structure's properties:

$$\alpha = C_\alpha \sqrt{\delta_c/\delta_y}, \quad (3.10)$$

Table 3.3: Results of regression analysis for IM_{comb} for brittle' and ductile' systems.

| Variable | Brittle, quickly deteriorating | | Ductile, slowly deteriorating | |
|-------------------------|--------------------------------|--------------|-------------------------------|--------------|
| | FEMA | Crustal/Sub. | FEMA | Crustal/Sub. |
| C_{dur} | | 0.07 | | 0.11 |
| C_{shape} | | 0.49 | | 0.72 |
| $\hat{\beta}_{dur}^s$ | | -0.14 | | -0.17 |
| $\hat{\beta}_{shape}^s$ | | -0.51 | | -0.79 |
| R^2 | 0.26 | 0.27 | 0.65 | 0.60 |
| SE_{In} | 0.30 | 0.36 | 0.27 | 0.31 |
| RSE_{In} | 0.31 | 0.33 | 0.18 | 0.19 |

where C_α is set to 1.3 (variations are discussed later), and δ_c/δ_y is determined from the system's backbone curve, defined in Table 3.3 lists the values of the C_{dur} and C_{shape} exponents for both representative systems, optimized for the combined ground-motion sets. The fit using these exponents are then shown for the two individual ground-motion sets in terms of the values of R^2 , SE_{In} and RSE_{In} . The standardized beta coefficients for the *ductile* systems, $\hat{\beta}_i^s$, are 21% larger for D_s and 54% in SS_α relative to the *brittle* system, suggesting that the collapse of ductile structures is more sensitive to the shape of the spectrum and duration. The period of ductile systems elongates more than those of brittle systems before they collapse, making them more sensitive to the shape of the spectrum. This observation is consistent with those of Haselton et al. (2011a).

Figure 3.11 plots the predictor variable R_c with respect to IM_{comb} (computed using the optimized C_{dur} and C_{shape} exponents in Table 3.3), normalized by S_a . As expected, the R^2 statistics are larger for *ductile* systems (0.65 and 0.60) than for *brittle* systems (0.26 and 0.27) for both ground-motions sets. In addition, R_c decreases with increasing IM_{comb}/S_a .

3.7.2 Sufficiency of estimates of R_c

As before, trends in the residuals of the estimate (using IM_{comb}/S_a) for both the *brittle* and *ductile* systems were evaluated with a simple linear regression model. For the *brittle* systems, the results showed that the intensity measure was sufficient (p-values more than 0.05) with respect to M for

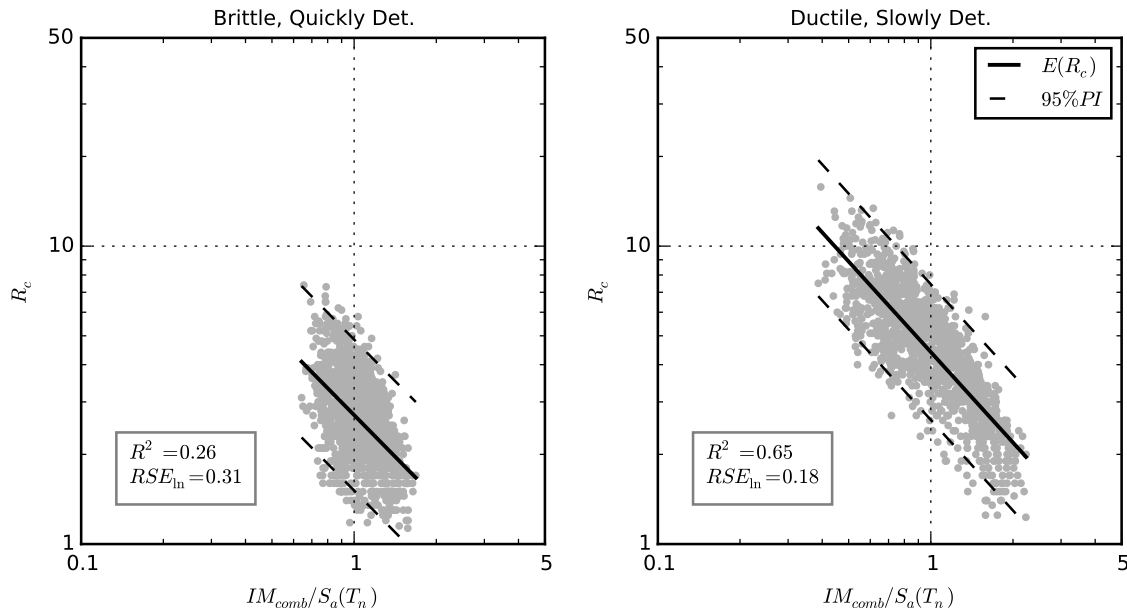


Figure 3.11: R_c with respect to $\frac{IM_{comb}}{S_a(T_n)}$ for (a) *brittle, quickly deteriorating* system and (b) *ductile, slowly deteriorating* system for the FEMA ground motion set.

65% (11/17) of the oscillator periods and sufficient with respect to R for 53% (9/17) of the periods. In comparison, for the *ductile* system, 59% (10/17) were sufficient with respect to M and 29% (5/17) for R. The oscillators with periods smaller than 1s were all sufficient with respect to M. The oscillators with periods larger than 1s were all sufficient with respect to R. For both systems, IM_{comb} was sufficient with respect to V_{S30} for 94% (16/17) of the oscillator periods.

Sufficiency can also be quantified by noting the change in the R^2 between $IM_{comb,exp}$ and IM_{comb} . Table 3.4 reports R^2 statistics for predicting R_c with IM_{comb} or $IM_{comb,exp}$, in which their exponents are optimized individually to achieve the largest possible R^2 for each dataset. For the *ductile* system, the values of R^2 for $IM_{comb,exp}$ were larger than those for IM_{comb} by 8% and 15% for the FEMA and crustal/subduction sets, respectively. The small change in R^2 for the *ductile* system suggests that IM_{comb} is sufficient for such systems.

On the other hand, for the brittle systems, the corresponding increases in R^2 are 41% and 80% when M, R, and T_n are explicitly taken into account. The larger change in R^2 for the brittle system

Table 3.4: R^2 statistic for using IM_{somb} or $IM_{comb,exp}$ to predict R_c for brittle' and ductile' systems.

| Ground motion set | Brittle, quickly deteriorating | | Ductile, slowly deteriorating | |
|--------------------|--------------------------------|-----------------|-------------------------------|-----------------|
| | IM_{comb} | $IM_{comb,exp}$ | IM_{comb} | $IM_{comb,exp}$ |
| FEMA | 0.35 | 0.48 | 0.68 | 0.73 |
| Crustal/subduction | 0.27 | 0.47 | 0.60 | 0.68 |

indicates that there are other ground motion properties, such as cyclic pulses, that correlate with M , R , or T_n but are not accounted for by IM_{comb} .

3.8 Evaluating IM_{comb} Using Analyses of Building Collapse

The new IM was evaluated further using the results reported by Haselton et al. (2011b). They report the results of the dynamic collapse analysis for 30 MDOF archetypical reinforced concrete (RC) special moment frame buildings (SMF), subjected to the expanded FEMA ground motion set. The IMs at collapse were computed for each of the building models and for a variety of IMs. To compute IM_{comb} , the μ in SS_a , was extracted from the results of nonlinear, push-over analyses (Haselton et al., 2011b). Instead of the ductility demand, the system ductility, μ_T , was used instead. It was calculated as the ratio of the ultimate roof displacement (80% of the structure's yield base shear) to the effective roof yield displacement.

3.8.1 Efficiency of IM_{comb} at collapse

Efficiency was assessed based on the dispersion of the IM at collapse using mean of the natural-log standard deviation (σ_{ln}) of the IM computed at collapse for the 30 archetypes. When SS_a was computed using $\mu = \mu_T$ for each archetype, the mean σ_{ln} of IM_{comb} at collapse was equal to 0.271 (Table 3.5). The exponents (C_{dur} and C_{shape}) used to compute IM_{comb} were optimized for the collapse results of the combined 30 archetypes.

Table 3.5: Intensity measure statistics for the expanded FEMA ground motion set.

| IM | Comment | Equation | Period range | R ² for SDOF systems | | | Mean σ_{in} of IM at collapse for 30 RC moments frames | | |
|------------------------|--|-----------------------|--|---|---|------------------------|---|---------------|-----------|
| | | | | R _{μ} $\mu = 4$ | R _{μ} $\mu = 8$ | R _c Brittle | R _c Ductile | $\mu = \mu_T$ | $\mu = 8$ |
| S _a | Elastic spectral acceleration using 5% damping | - | T _n | - | - | - | - | 0.40 | 0.40 |
| IM _{comb} | Includes, S _a , D _s , and SS _a | Eq. 3.3 | 2T _n | - | - | - | - | 0.40 | 0.40 |
| IM _{comb,exp} | Adds M, R, and T _n to IM _{comb} | Eq. 3.3 | T _n - α T _n | 0.66 | 0.81 | 0.35 | 0.68 | 0.27 | 0.27 |
| SS _a | Arithmetic mean using μ dependent period range | Eq. 3.5 | T _n - α T _n | 0.66 | 0.82 | 0.48 | 0.73 | 0.27 | 0.27 |
| SS _d | Arithmetic mean of displacement response spectrum using μ dependent period range | Eq. 3.2 | T _n - α T _n | 0.66 | 0.81 | 0.21 | 0.60 | 0.27 | 0.28 |
| S* | Accounts for S _a at two periods Cordova et al. (2000) | Eq. 3.11 | T _n - α T _n | 0.65 | 0.81 | 0.20 | 0.61 | 0.27 | 0.28 |
| S _{a,geo} | Geometric mean using period range as recommended by Bojórquez and Iervolino (2011) | Eq. 3.1 | T _n , 2T _n | 0.60 | 0.71 | 0.18 | 0.55 | 0.31 | 0.31 |
| S _{a,geo} | Geometric mean using period range as recommended by Eads et al. (2015) | Eq. 3.11 ^a | T _n - 2T _n | 0.60 | 0.69 | 0.20 | 0.52 | 0.34 | 0.34 |
| S _{a,geo} | Geometric mean using μ dependent period range | Eq. 2 | 0.2T _n -3T _n | 0.64 | 0.71 | 0.23 | 0.58 | 0.30 | 0.30 |
| S _{a,geo} | Geometric mean using μ dependent period range | Eq. 3.2 | T _n - α T _n | 0.65 | 0.80 | 0.14 | 0.57 | 0.27 | 0.28 |

Note: $\alpha = 1.3\sqrt{\mu}$ ^aThe IM was computed using SS_d instead of SS_a.

The average value of μ_T for the 30 archetypes was 9.2. To simplify the computation of SS_a , a value of $\mu=8$, was used for all of the frames, which is the seismic response modification factor given in ASCE/SEI 7-10 (2013) for RC SMF systems. With this assumption, the mean σ_{ln} of IM_{comb} at collapse increased to 0.275, which was only slightly larger than the value computed using $\mu = \mu_T$. These results suggest that the mean value of σ_{ln} is insensitive to small changes of μ , so only an approximate estimate of μ is necessary.

To illustrate the impact of the smaller dispersion of the IM at collapse, Figure 3.12a shows the empirical cumulative distribution of the IM for a particular building archetype along with its fitted collapse fragility function. Both IM_{comb} and the commonly used $S_a(T_n)$ are shown in Figure 3.12. To allow direct comparison of the results, the IMs have been normalized by the median value of the IM at collapse, $IM_{col,50}$, so that a value of one corresponds to collapse of half of the structures. Figure 3.12b shows the dispersion in the fitted collapse fragility functions of all 30 archetypes was smaller for IM_{comb} than for $S_a(T_n)$. As shown in Table 3.5, the mean σ_{ln} for IM_{comb} was 0.275, whereas it was 0.404 for $S_a(T_n)$ and 0.401 for S_a computed at twice the initial period to account for structural softening. These results show that the mean σ_{ln} was around 31% lower for IM_{comb} than for $S_a(T_n)$ or $S_a(2T_n)$.

3.8.2 Sufficiency of IM_{comb} at collapse

To evaluate sufficiency of IM_{comb} , its value at collapse (computed with the recommended IM's exponents in Table 3.3) for the 30 archetypes were evaluated with a simple linear regression model. The model's p-values of the approximated slopes ($\hat{\beta}$) show the IM was sufficient (p-value more than 0.05) for 93% (28/30) of the archetypes for M, 100% (30/30) for R and 90% (27/30) for V_{S30} .

Sufficiency was also evaluated by the mean σ_{ln} of IM_{comb} and $IM_{comb,exp}$ at collapse and are reported as 0.27 (for SS_a computed using either $\mu=\mu_T$ or $\mu=8$) in Table 3.5. This insensitivity indicates that there would be no significant benefit to including M, R, and T_n in the intensity measure. By both measures, IM_{comb} was sufficient with respect to these ground-motion characteristics in predicting the collapse of the Haselton et al. (2011b) frames.

The values reported in Table 3.5 were optimized for the particular set of ground motions and building inventory. A mean σ_{ln} of IM_{comb} equal to 0.275 could be obtained by using the more

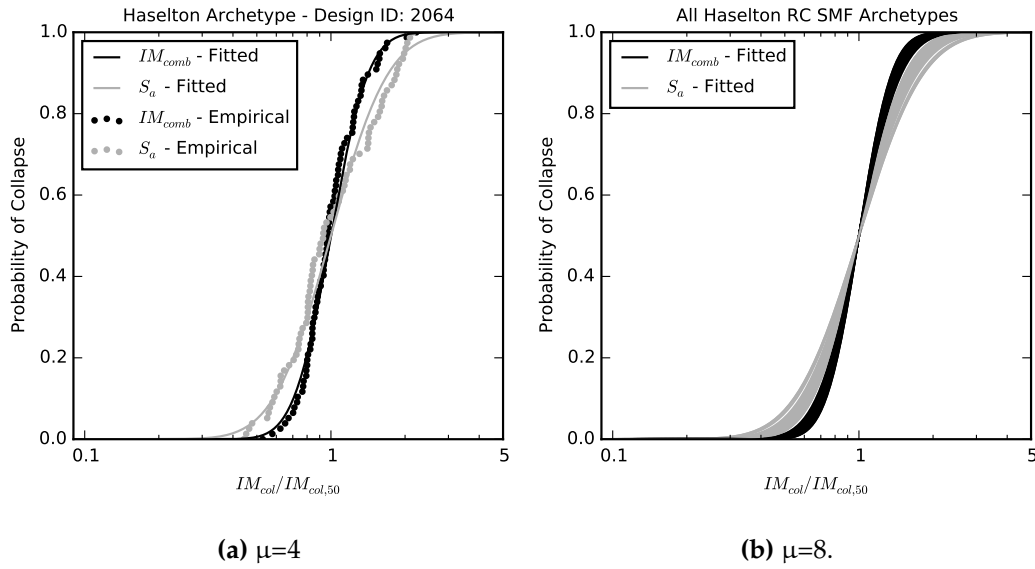


Figure 3.12: (a) Collapse fragility functions of an reinforced concrete (RC) special moment frame buildings (SMF) structural archetype (b) Fitted collapse fragility functions of all Haselton RC SMF archetypes using IM_{comb} and $S_a(T_n)$.

general exponents (C_{dur} and C_{shape}) reported in Table 3.3, which were optimized for SDOF deteriorating systems.

3.9 Comparing Efficiency of IM_{comb} to Efficiencies of Other Shape Intensity Measures

Table 3.5 compares the efficiency of the proposed IM_{comb} with existing shape IMs and with variations of the new IM for the expanded FEMA set. Table 3.5 describes each of the IMs, the equation that defines it, and the period range over which the spectral shape intensity measure was evaluated. The comparisons are made in terms of R^2 for R_{μ} in elastic-perfectly plastic systems and R_c in deteriorating systems. For the collapse results for 30 frames, the results are compared in terms of the mean dispersion of the intensity measure at collapse.

To evaluate the efficiency of the new spectral shape intensity measure, SS_a must be isolated from duration (and to remove the added benefit for including duration). For predicting force-reduction factors, the correlation is made directly with SS_a and other normalized (dividing by S_a) measures of shape. For the collapse results of 30 frames, the efficiency of SS_a is evaluated for a variation of the IM that includes the effects of spectral acceleration and shape (but not duration).

$$IM_{SS_a} = S_a SS_a^{C_{shape}}, \quad (3.11)$$

where C_{shape} is optimized using the dataset.

The effects of including duration can be evaluated by comparing the IM_{comb} and SS_a rows in Table 3.5. Ground-motion duration had no significant effect on the response of elastic-perfectly plastic SDOF systems and the ductile MDOF frames. The deteriorating SDOF systems (in particular, the brittle one) were more sensitive to duration. The results are similar using the acceleration response spectrum (SS_a) or the displacement spectrum (SS_d).

In Table 3.5, the normalized measures of SS_a , S^* , and $S_{a,geo}$ have been transformed into log-scale, and their exponents have been optimized to achieve the largest possible R^2 statistic (or minimum mean σ_{ln} of IM at collapse). $S_{a,geo}$ were computed using period ranges that were recommended by Bojórquez and Iervolino (2011) and Eads et al. (2015). SS_a had a higher R^2 (or lower σ_{ln} of IM at collapse) than the existing IMs for all of the analyses but one. For brittle, deteriorating systems, the R^2 was 0.23 for $S_{a,geo}$, whereas it was slightly lower (0.21) for SS_a .

The benefits of using the arithmetic versus the geometric mean of S_a values can be evaluated by comparing SS_a to $S_{a,geo}$ for the same period range. For all analyses, the statistics were preferable for the arithmetic mean (SS_a) than the geometric mean ($S_{a,geo}$). In particular, Table 3.5 shows that R^2 increased up to 50% for the *brittle* system (0.14 to 0.21).

3.10 Influence of Ductility Demand on Optimal SS_a

An important difference among the existing and proposed IMs is the period range over which the shape intensity measure is calculated. The proposed IM uses period ranges that depend on the displacement ductility ($\alpha = C_\alpha \sqrt{\mu}$). The shape intensity measure was computed over numerous period ranges for both elastic-perfectly plastic and deteriorating systems and for both ground-motions sets. Figure 3.13 shows the variation in the R^2 statistic for predicting the variation of R_μ with α . According to this figure, R^2 consistently increases with increasing μ . This trend is attributable to the fact that the coefficient of variation of SS_a for a record set increases with increasing μ . The optimal value of α (maximum R^2) is lower for lower ductility demands (e.g., $\mu = 2$) than for larger ductility demands (e.g., $\mu = 8$). The assumption of $C_\alpha = 1.3$ results in period ranges that are slightly smaller than those that result in the optimal predictions.

Figure 3.14 shows similar results for *brittle* and *ductile* deteriorating systems. In this case, the optimal period range corresponds to lower values of C_α for the *brittle* system but relatively close to the optimal C_α for the *ductile* system. A value of $C_\alpha = 1.3$ is slightly larger than the optimal range, but it represents a good compromise between the optimal ranges for the elastic-perfectly plastic and deteriorating systems. In practice, the assumed value of μ used in SS_a 's computation would only need to be approximate, because the results are not sensitive to this assumption. For example, this value could also be taken as the ductility capacity of the system determined from the seismic response modification factor from ASCE/SEI 7-16 (2017).

3.11 Chapter Conclusions

A new ground-motion intensity measure, IM_{comb} , is proposed that accounts for the effects of spectral acceleration, duration, and spectral shape. IM_{comb} characterizes ground-motion duration in terms of significant duration, D_s . IM_{comb} also incorporates a new measure of

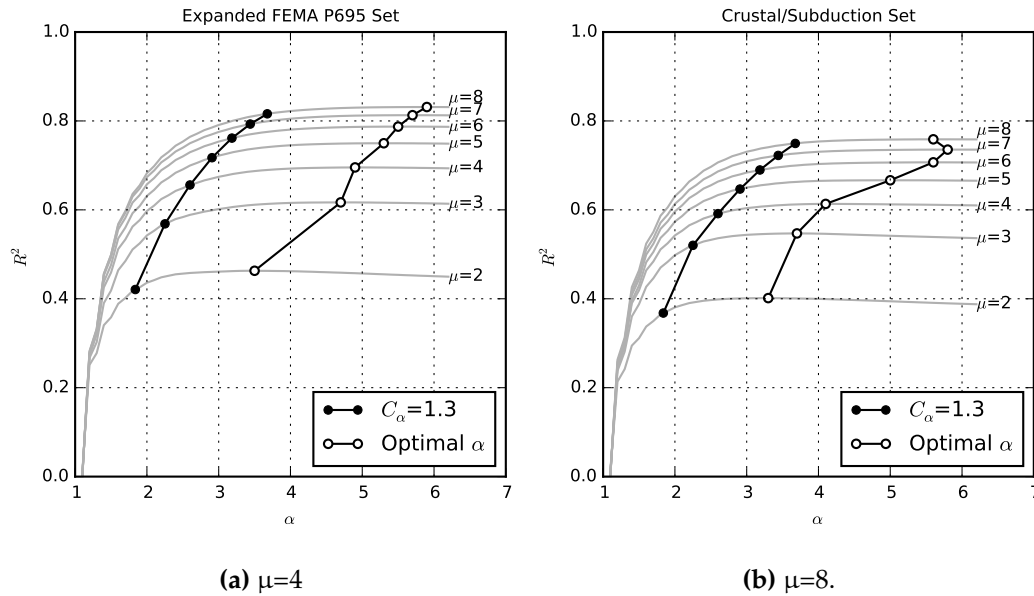


Figure 3.13: Variation of R^2 statistic for estimating R_μ with respect to α values for the (a) expanded FEMA set and (b) the crustal/subduction set.

spectral shape, SS_α , which corresponds to the normalized integral of the response spectrum over a ductility-dependent period range. The form of IM_{comb} (Eq. 3.3) makes it scalable and transparent.

The transparency of the IM made it possible to identify the effects of duration and spectral shape on the response of various systems. For example, the spectral shape affected all structures, but in particular, ductile structures. Duration only affected structures with cyclic deterioration.

An efficient IM enables engineers to either evaluate structures with fewer ground motions or to predict structural performance with higher degrees of certainty. Compared with existing IMs, IM_{comb} is more efficient in predicting force-reduction factors to achieve targeted ductility demands in elastic-perfectly plastic SDOF systems (R_μ) for a wide range of system properties. Similarly, IM_{comb} is efficient in predicting force-reduction factors for collapse in brittle and ductile deteriorating SDOF systems (R_c). The new IM also results in lower dispersions of the IM at collapse for 30 RC SMF archetypes (Haselton et al., 2011b).

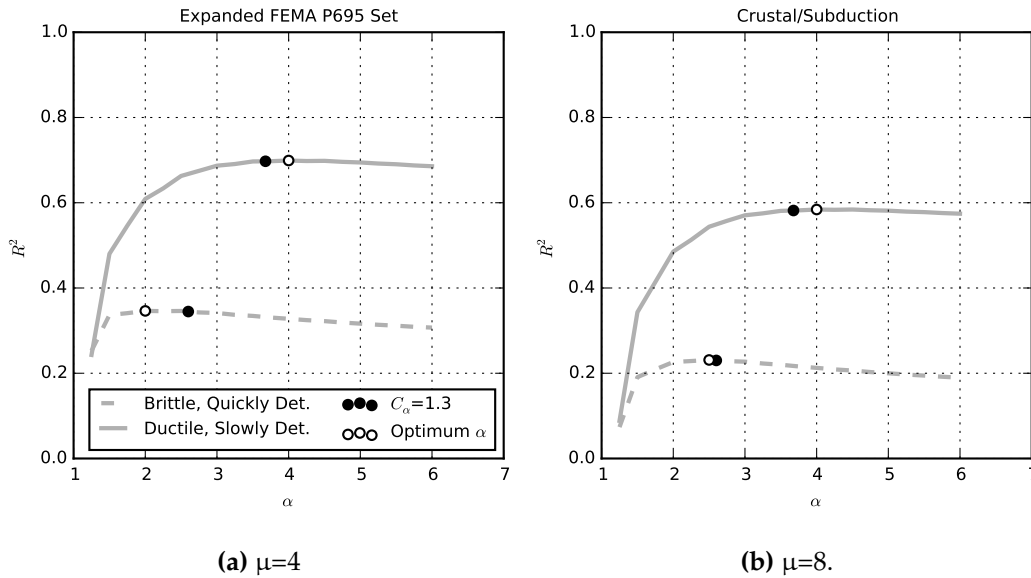


Figure 3.14: Variation of R^2 statistic for estimating R_c with respect to α values for the (a) expanded FEMA set and (b) the crustal/subduction set.

The improved efficiency is attributable to the inclusion of duration and a ductility-dependent measure of spectral shape. This ductility dependence makes the IM structure specific (i.e., less structure independent). However, the results (e.g., Figure 3.14) show that nearly all of the added efficiency can be gained from using an approximate estimate of the ductility capacity.

The new IM is versatile enough to evaluate the intensity of recorded and simulated ground motions, even in the absence of GMMs. To incorporate the IM into traditional PSHA, it would be necessary to develop GMMs for spectral shape, at which time the predictability of the IM could be evaluated.

A sufficient IM enables engineers to select ground motions for nonlinear dynamic analyses of structures without considering source and site parameters. The sufficiency of IM_{comb} depended on the criteria for measuring sufficiency. Based on a p-value criteria of 0.05, IM_{comb} was sufficient with respect to ground-motion magnitude, M , site-to-source distance, R , or average shear-wave velocity of the upper 30 m, V_{S30} , (or combinations thereof) for all oscillator periods of the elastic-perfectly plastic and deteriorating SDOF systems. Similarly, IM_{comb} was sufficient with respect

to M , R , and V_{S30} for nearly all of the 30 building archetypes. Another criteria for sufficiency is the improvements in efficiency that resulted from adding M , R , and T_n ($IM_{comb,exp}$) to the IM. By this criteria, the sufficiency was high for all of the considered SDOF ductile systems. For brittle deteriorating systems, the IM's sufficiency was improved by including additional parameters (M , R , and T_n).

The recommended values of the exponents, C_{dur} and C_{shape} used in IM_{comb} are listed in Table 3.3. These values have been optimized using SDOF systems of two representative system types. Further work is needed to evaluate the variability of the exponents for a wider variation in structural systems.

Chapter 4

EFFECTS OF DEEP BASINS ON STRUCTURAL COLLAPSE DURING LARGE SUBDUCTION EARTHQUAKES

This chapter is based on the following reference:

Marafi, Nasser A., Marc O. Eberhard, Jeffrey W. Berman, Erin A. Wirth, and Arthur D. Frankel (2017). "Effects of Deep Basins on Structural Collapse during Large Subduction Earthquakes". In: *Earthquake Spectra* 33.3, pp. 963–997. ISSN: 8755-2930. DOI: [10.1193/071916EQS114M](https://doi.org/10.1193/071916EQS114M)

4.1 Chapter Overview

Chapter 3 identified ground-motion characteristics that are known to affect structural response. This chapter shows how those characteristics are modified by deep sedimentary basins during large subduction earthquakes. This is important because much of the Puget Sound region overlies deep basins and the effects of deep sedimentary basins are only implicitly considered in seismic hazard maps used in U.S. building codes. This chapter evaluates the effects of basins on spectral accelerations, ground-motion duration, spectral shape, and structural collapse using subduction earthquake recordings from basins in Japan that have similar depths as the basins within the Puget Lowland region. For three of the Japanese basins and the basins surrounding the Puget Lowland region, the spectral accelerations were amplified by a factor of 2 to 4 for periods above 2.0 s. The long-duration subduction earthquakes and the effects of basins on spectral shape combined, lower the spectral accelerations at collapse for a set of building archetypes relative to other ground motions. For the hypothetical case in which these motions represent the entire hazard, the archetypes would need to increase up to 3.3 times its strength to compensate for these effects.

4.2 Introduction

Sedimentary basins are known to increase the intensity of ground motions and the resulting damage (e.g., Kawase, 1996; Graves et al., 1998; Hatayama et al., 2007; Frankel et al., 2009). These amplifications are generally attributed to: (1) impedance contrasts between basin layers, (2) focusing of shear-waves at the surface, and (3) conversion of shear-waves into surface waves at the basin edges (Choi et al., 2005). The basin amplification phenomenon is consistent with the increased levels of damage observed within basins during earthquakes, including in the 1987 Michoacan (Hall and Beck, 1986), 1994 Northridge (Graves et al., 1998), 1995 Kobe (Kawase, 1996), 2001 Nisqually (Frankel et al., 2009), and 2003 Tokachi-Oki (Hatayama et al., 2007) earthquakes. Heaton et al. (2006) demonstrated with numerical analysis that the Tokachi-Oki motions would have hypothetically caused larger-than-expected damage to steel moment-resisting frame buildings at several basin locations. Furthermore, Celebi et al. (2016, 2016) and others used seismic instrumentation data to show that tall structures in Tokyo were excited by the Kanto basin during the 2011 Tohoku earthquake.

Although basins are known to affect ground motions for crustal earthquakes (Choi et al., 2005), the effects of basins may be different for large-magnitude subduction earthquakes. The seismic velocity structure of subduction zones (e.g., accretionary wedge, down-going slab, serpentinized mantle) differs from that for crustal earthquakes. The differences in velocity structure may affect the generation of surface waves and alter shear-wave propagation that is then amplified by sedimentary basins. In addition, Choi et al. (2005) noted differences in basin amplification between earthquake sources that are distant from basins and sources that coincide with basins, as is more likely for crustal earthquakes.

Subduction earthquakes are particularly important in the Pacific Northwest (PNW), where they can dominate the seismic hazard, particularly for long-period structures. For example, in downtown Seattle, subduction interface earthquakes contribute 47% of the total hazard for the 2.0-s spectral acceleration corresponding to a mean return time of 2,475 years (USGS (United States Geological Survey), 2008). Subduction intraslab earthquakes contribute another 22%. Seattle and much of the Puget Sound region is underlain by a deep, sedimentary basin.

The National Seismic Hazard Maps (NSHM), used by the ASCE 7-16 (2017) seismic design procedures, do not explicitly account for the effects of basins on spectral accelerations (Petersen et al., 2014; Frankel et al., 2007). The NSHM spectral accelerations are computed for a reference site condition with an average shear-wave velocity in the upper 30 meters (V_{S30}) equal to 760 m/s, which corresponds to the boundary between site classes B and C (BSSC 2009). For crustal earthquakes, these values are computed with Ground-Motion Models (GMMs) using a generic basin depth corresponding to this value of V_{S30} , because fine-scale, seismic-wave velocity maps are currently unavailable for much of the US. For subduction earthquakes, the GMMs used in the hazard maps do not include terms that explicitly account for basins.

For both crustal and subduction earthquakes, the effects of basins are only indirectly accounted for by the correlation between basin effects and V_{S30} (Abrahamson et al., 2014; Campbell and Bozorgnia, 2014). This correlation also affects the ASCE 7-10 site coefficients, which assume different values of basin depth for each site class. This correlation is weak for sites with high V_{S30} values (> 360 m/s) located in deep basins, such as those in the Seattle basin (Chang et al., 2014). In addition, these site coefficients, which are only provided at periods of 0.2 s and 1.0 s, cannot account for the long-period amplification that is observed in basins.

It would be possible to account for these effects by conducting a site-specific hazard analysis that accounts for basin amplification, combined with nonlinear time history analysis using motions that are consistent with the seismic hazard, including large-magnitude, subduction earthquakes measured in basins. However, most structures are designed using equivalent lateral-force procedures. These procedures do not explicitly account for the effects of ground-motion duration and spectral shape, which also affect structural response (Bommer et al., 2004; Hancock and Bommer, 2007; Raghunandan and Liel, 2013; Chandramohan et al., 2016b, and Chapter 3 herein).

Some researchers have used physics-based ground-motion simulations to quantify how ground motions in basins differ from other motions (e.g., Graves et al., 2011; Skarlatoudis et al., 2015). This chapter characterizes the effects of the Yufutsu, Kosen, Kanto, and Niigata basins in Japan on spectral accelerations, ground-motion durations, and spectral shapes for motions measured during subduction earthquakes. The chapter focuses on these basins because they

have been subjected to large-magnitude megathrust earthquakes, they have similar depths to the basins underlying the Puget Sound region, including Seattle (Blakely et al., 2002), and numerous ground-motion records are available. The scope of this chapter is limited to basin effects quantified using ground motions from earthquake recordings resulting from subduction earthquakes.

To evaluate the effects of these motions on structural collapse, ground-motion recordings from inside and outside three of the basins are used to perform incremental dynamic analyses of 30 archetypical building frame models (Haselton et al., 2011b). For each archetype, the variations in collapse fragilities among the ground-motion sets are compared with measures of ground-motion duration and spectral shape. The basin spectral acceleration amplification factors and changes in collapse fragilities for inside- and outside-basin motions are then combined to develop basin design-strength amplification factors, DF_{basin} . The long-duration of the large-magnitude earthquakes further contributes to the severity of the ground motions. Design-strength factors are also developed to compensate for differences in collapse performance between ground motions measured in basins during large-magnitude earthquakes, and crustal ground motions typically considered to evaluate structural systems (e.g., FEMA, 2009).

4.3 Current Treatment of Basin Effects

Ground-motion models (GMMs) that include basin-amplification terms for crustal earthquakes (Abrahamson et al., 2014; Boore et al., 2014; Chiou and Youngs, 2014; Campbell and Bozorgnia, 2014) have been developed. These terms depend on the depth at which a particular shear-wave velocity (V_S) is measured. The selected shear-wave velocity varies among the GMMs. This chapter characterizes the basin depth using the depth to very stiff bedrock material with a shear-wave velocity (V_S) of 2.5 km/s, denoted as $Z_{2.5}$. This relatively high velocity is a better indicator of basin depth than lower velocities for the basins within the Puget Lowland region, because much of this region has a top layer of glacial till with V_S near 1 km/s (Chang et al., 2014).

The Campbell and Bozorgnia (2014) GMM for crustal earthquakes, referred to here as CB14, expresses the effect of a basin on spectral acceleration in terms of $Z_{2.5}$. CB14 predicts the natural logarithm of the spectral accelerations ($\ln S_a$) by summing the basin term, $f_{\text{basin}}(Z_{2.5})$, with other

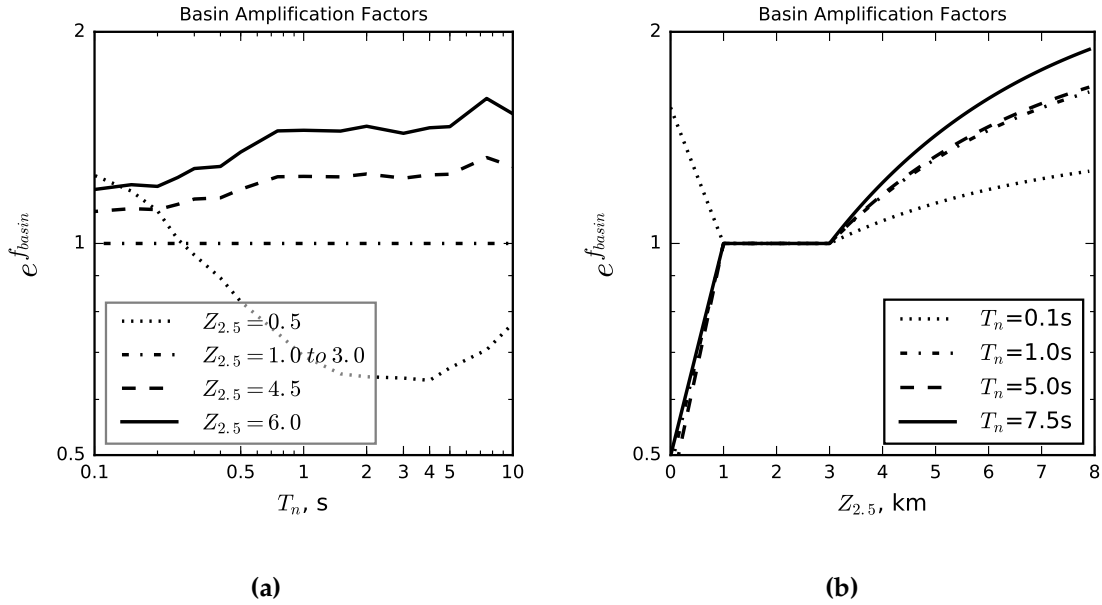


Figure 4.1: Basin amplification factors from the Campbell and Bozorgnia (2014) GMM with respect to (a) structural period and (b) $Z_{2.5}$.

terms that depend on parameters known to affect spectral acceleration (i.e., $\ln S_a = f_{M,R} + f_{local-site} + \dots + f_{basin}$). The exponential of the basin term, f_{basin} , therefore corresponds to an amplification factor to account for the effects of basins. Figure 4.1 shows the variation of the basin amplification factor with respect to period and $Z_{2.5}$. For shallow basins (e.g., $Z_{2.5} = 0.5$ km), the factor is larger than 1 at short periods and is less than 1 at longer periods. For values of $Z_{2.5}$ between 1 and 3 km, S_a values are unchanged, regardless of period. For values of $Z_{2.5}$ deeper than 3.0 km, spectral accelerations are amplified at all periods. The amplification factor reaches a maximum value of 1.3 for $Z_{2.5} = 4.5$ km and 1.6 for $Z_{2.5} = 6$ km at a period of 7.5 s.

The subduction GMMs used in current hazard maps (Atkinson, 2003; Zhao, 2006; Atkinson and Macias, 2009; Addo et al., 2012) do not include basin terms. In addition, the standards referenced by U.S. model building codes (e.g., ASCE, 2013) may not account for many ground-motion characteristics that correlate with structural damage, especially when force-based

seismic design procedures are only used. In particular, Bommer et al. (2004) and Hancock and Bommer (2007) have shown that duration influences engineering demand measures. Chandramohan et al. (2016a), and Raghunandan et al. (2015) found that ground-motion duration can affect the minimum design strength needed to provide sufficient probability against collapse. Similarly, Haselton et al. (2011a), Eads et al. (2015), and Chapter 3 herein have shown that spectral shape influences the collapse probabilities of structures. These ground-motion characteristics are known to influence structural response; therefore, it is important to evaluate how they are affected by the presence of deep basins.

4.4 Seismic Stations in or Near Basins

Most of the Puget Sound region is founded on glacial deposits that overlay sedimentary rocks, which fill the troughs between the Olympic Mountains and The Cascades to form the basins within the Puget Lowland region. Figure 4.2 shows the $Z_{2.5}$ contour map of the Puget Sound, extracted from seismic-wave velocity models generated by Stephenson et al. (2017). This basin reaches depths in terms of $Z_{2.5}$ of up to 8 km. The Puget Sound region is prone to earthquakes due to the subduction of the Juan de Fuca plate beneath the North American plate, and earthquakes due to crustal deformations. The Cascadia subduction zone is capable of producing M_w 8-9 earthquakes along the plate interface (known as interface earthquakes) and deeper M_w 6-7 earthquakes within the slab (intraslab earthquakes). In 2001, this region was subjected to a deep intraslab earthquake with M_w 6.8 (Nisqually). Geologic and historic evidence indicates that the Cascadia region has been subjected to subduction-zone interface earthquakes up to M_w 9 (Atwater et al., 1995; Goldfinger et al., 2012) and that future great earthquakes are inevitable.

Recordings are not available for magnitude 8 or 9 interface events in the PNW, so instead, four Japanese basins are considered here. These basins were selected because they are deep, they have been subjected to a large number of subduction earthquakes, and numerous recordings are available (KiK-net and K-NET seismic networks). Figure 4.3 shows the location of the basins, whose extents are illustrated using the contour line of $Z_{2.5}$ equal to 3.0 km and extracted from the Japan Integrated Velocity Structure Model (Koketsu et al., 2009). The Yufutsu basin, which is partly offshore, is located in Hokkaido, Japan (Figure 4.4a) and has $Z_{2.5}$ values up to almost 8 km

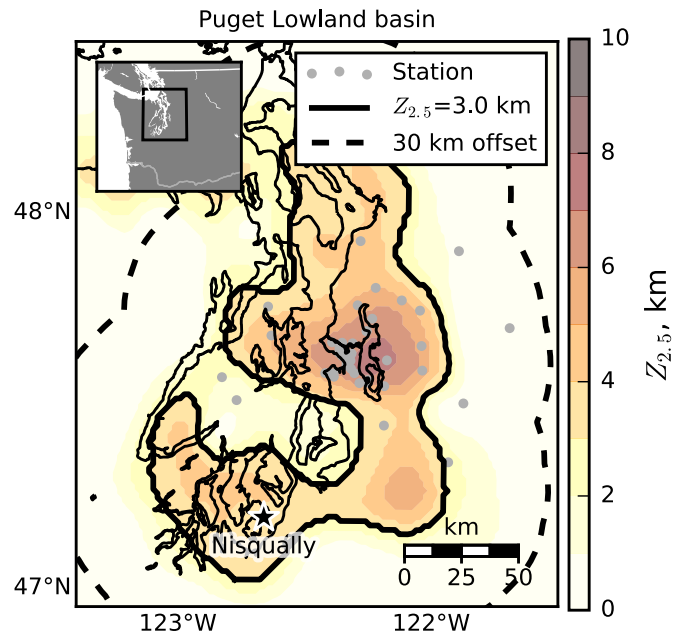


Figure 4.2: $Z_{2.5}$ contour map of the Puget Sound region.

onshore. Figure 4.4b shows the Konsen basin, located in Eastern Hokkaido, and Figure 4.4c shows the Kanto basin, located beneath Tokyo City. Both of these basins reach depths of almost 5 km. Figure 4.4d shows the Niigata basin located on the west coast of Honshu Island, with $Z_{2.5}$ values reaching 8 km.

This chapter considers ground-motion recordings from two large-magnitude, subduction interface earthquakes (2003 M_w 8.3 Tokachi-Oki earthquake, 2011 M_w 9.0 Tohoku earthquake) and four lower-magnitude (M_w 6.7-7.9) subduction interface earthquakes. The epicenters of the large-magnitude earthquakes are denoted with a star in Figure 4.3. These events were determined to be subduction events following the methodology developed by Frohlich (2001), which identifies the earthquake focal mechanism. For the Yufutsu, Konsen, and Kanto basins, the motions selected were the largest three subduction earthquakes whose closest distance to rupture (R_{CD}) was within 100-200 km from the basin. For the Niigata basin, the subduction plate interface is further away, so the selected subduction earthquakes were the three largest within 200-300 km of the basin.

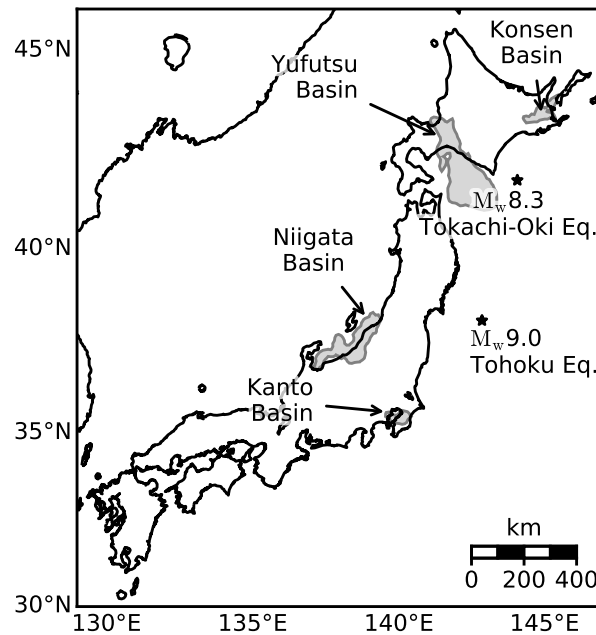


Figure 4.3: $Z_{2.5}$ contour map of Japan showing epicenters of two large magnitude earthquakes.

Numerous ground motions near and inside the four basins have been recorded by the KiK-net and K-NET seismic networks. Each recording's horizontal components were zeroth-ordered baseline corrected and have a usable period range between 0.01 s to 20 s (Stewart et al., 2013). Stations were selected for analysis if they were located within 30 km of the $Z_{2.5} = 3$ km contour line for each basin, shown in Figure 4.4. This distance was selected to provide a balance between the need to select stations near the basin (to limit path-specific effects) and the need to have a sufficient number of recordings for each basin. Stations were excluded if they had evidence of liquefaction during the Tohoku earthquake as per Cox et al. (2013). To reduce the effects of soft-soil amplification, the analyses considered only onshore surface recordings from stations with average shear-wave velocity in the upper 30 meters, V_{S30} , that exceeds 180 m/s, which corresponds to the NEHRP site class D/E boundary BSSC (2009). The values of V_{S30} were computed from the soil profile data available on the K-NET/KiK-net database. K-Net station soil profiles do not extend down to 30 m, so values of V_{S30} were estimated following the recommendations of Boore et al. (2011).

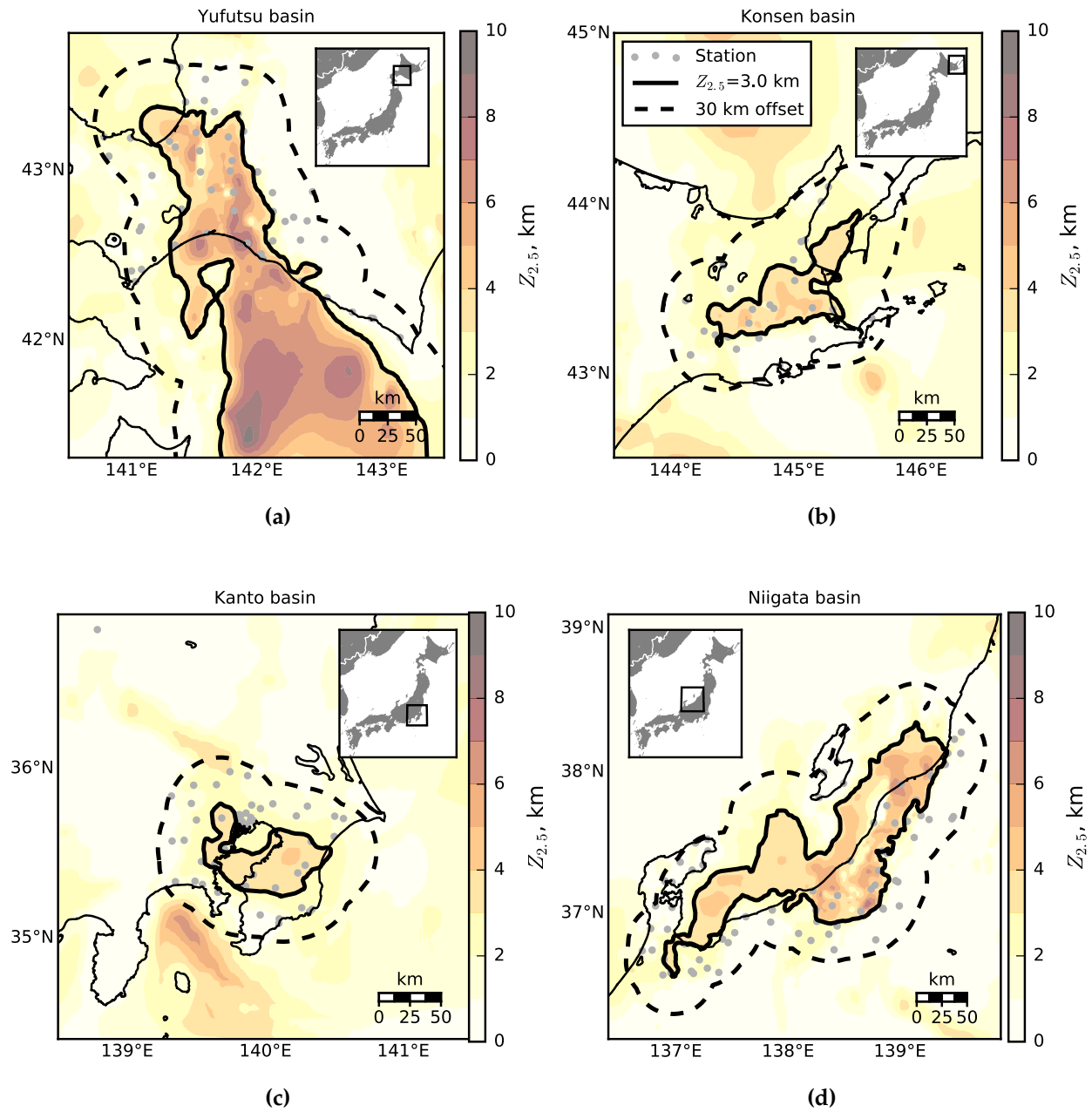


Figure 4.4: $Z_{2.5}$ contour maps of the (a) Yufutsu basin, (b) Konsen basin, (c) Kanto basin, and (d) Niigata basin.

As reported in Table 4.1 (and Figure 4.4), depending on the particular basin, 6 to 20 basin stations met the screening criteria and had values of $Z_{2.5}$ of at least 3 km. In comparison, 7 to 35 stations had values of $Z_{2.5}$ less than 1.5 km. Table 4.1 also reports the event's moment magnitude (M_w), depth, geometric mean of the source-to-site distance (\tilde{R}) for stations within each $Z_{2.5}$ bin (retrieved from ShakeMap, USGS 2018), and the geometric mean of $Z_{2.5}$ for stations within each basin. These source-to-site distances ranged from 45 km to 285 km for Yufutsu, Kosen, and Kanto basins, and from 168 km to 422 km in the Niigata basin. For each event (three per basin), the geometric mean for source-to-site distances (\tilde{R}) are within 85 km for each $Z_{2.5}$ bin. As expected, the log-normal standard deviations (σ_{\ln}) for distance were larger for smaller values of $Z_{2.5}$, because the stations with lower values of $Z_{2.5}$ tended to surround the basin edges. Therefore, since ground motion intensities tend to attenuate with distance, the bins with lower values of $Z_{2.5}$ would tend to have higher variability in ground-motion intensity.

4.5 Effects of Basin on Spectral Acceleration

The spectral accelerations at each period are important because earthquake loads are usually computed from the design spectral acceleration at the fundamental period of a structure. Figure 4.5 shows the geometric mean of S_a (\tilde{S}_a) with respect to period for all ground-motions in each $Z_{2.5}$ bin, including the contributions of both horizontal components at each station. For the Yufutsu and Kosen basins, the values of \tilde{S}_a are shown for the Tokachi-Oki earthquake. For the Kanto and Niigata basins, the values are plotted for the Tohoku earthquake. The values are plotted for $Z_{2.5}$ ranges of: 1.5 – 3 km, 3 – 4.5 km, and > 4.5 km for periods (T_n) from 0.1 to 10 seconds. The values of \tilde{S}_a for the bins can be compared directly because the values of \tilde{R}_{CD} are similar among the bins (Table 4.1).

For all four basins and for a wide range of periods, \tilde{S}_a consistently increases with $Z_{2.5}$ but the ratios of \tilde{S}_a among bins varies with basin and period. For example, for the Yufutsu basin (Figure 4.5a), the ratio of \tilde{S}_a between the deepest ($Z_{2.5} > 4.5$) and shallowest ($Z_{2.5} < 1.5$) bins is 1.5 (0.24 g/0.16 g) at 0.5 s. This ratio increases to 2.1 (0.12 g/0.056 g) at 2 s and increases further to 3.8 (0.065 g/0.017 g) at 5 s. The trends in ratios are similar for the Kosen basin (Figure 4.5b) and Niigata basin (Figure 4.5d). Note that the magnitudes of S_a in the Niigata basin are much lower (< 0.05

Table 4.1: Statistics on station recordings for each $Z_{2.5}$ bin

| Basin | M_w | Event Name | Event Date | Depth (km) | $Z_{2.5} < 1.5\text{km}$ | | | $1.5\text{km} \leq Z_{2.5} < 3.0\text{km}$ | | | $3.0\text{km} \leq Z_{2.5} < 4.5\text{km}$ | | | $4.5\text{km} \leq Z_{2.5}$ | | | | | | |
|----------------------|-------|----------------------------|------------|------------|--------------------------|------------------|-------------------------|--|----------------|------------------|--|-------------------|----------------|-----------------------------|-------------------------|-------------------|----------------|------------------|-------------------------|-------------------|
| | | | | | # ¹ | \tilde{R}_{CD} | $\sigma_{\text{In}(R)}$ | $\tilde{Z}_{2.5}$ | # ¹ | \tilde{R}_{CD} | $\sigma_{\text{In}(R)}$ | $\tilde{Z}_{2.5}$ | # ¹ | \tilde{R}_{CD} | $\sigma_{\text{In}(R)}$ | $\tilde{Z}_{2.5}$ | # ¹ | \tilde{R}_{CD} | $\sigma_{\text{In}(R)}$ | $\tilde{Z}_{2.5}$ |
| Yufutsu ^c | 8.3 | Tokachi-Okai | 2003-09-25 | 27.0 | 21 | 125 | 0.49 | 0.39 | 15 | 143 | 0.33 | 2.03 | 8 | 139 | 0.34 | 3.51 | 12 | 136 | 0.16 | 5.46 |
| | 7.4 | Hokkaido ⁶ | 2003-09-25 | 33.0 | 21 | 1763 | 0.43 | 0.35 | 14 | 203 ³ | 0.24 | 2.06 | 8 | 205 ³ | 0.26 | 3.51 | 11 | 205 ³ | 0.12 | 5.29 |
| | 6.8 | Hokkaido ⁶ | 2008-09-11 | 25.0 | 21 | 156 | 0.5 | 0.4 | 15 | 189 | 0.27 | 2.03 | 8 | 186 | 0.28 | 3.51 | 12 | 184 | 0.13 | 5.46 |
| Konsen ^b | 8.3 | Tokachi-Okai | 2003-09-25 | 27.0 | 9 | 102 | 0.26 | 0.6 | 11 | 97 | 0.31 | 2.19 | 6 | 108 | 0.13 | 3.49 | - | - | - | - |
| | 6.8 | Hokkaido ⁶ | 2008-09-11 | 25.0 | 9 | 178 | 0.17 | 0.6 | 13 | 182 | 0.22 | 2.21 | 6 | 185 | 0.08 | 3.49 | - | - | - | - |
| | 6.7 | East Hokkaido ⁶ | 2003-10-08 | 32.0 | 7 | 100 ³ | 0.29 | 0.46 | 13 | 111 ³ | 0.25 | 2.21 | 6 | 102 ³ | 0.09 | 3.49 | - | - | - | - |
| Kanto ^b | 9.0 | Tohoku | 2011-03-11 | 29.0 | 8 | 187 | 0.04 | 0.76 | 294 | 148 ⁴ | 0.15 ⁴ | 2.30 ⁴ | 12 | 152 | 0.09 | 3.24 | - | - | - | - |
| | 7.9 | Tohoku AF | 2011-03-11 | 42.6 | 8 | 178 ³ | 0.08 | 0.76 | 30 | 142 ³ | 0.18 | 2.30 | 12 | 143 ³ | 0.11 | 3.24 | - | - | - | - |
| | 6.9 | East Honshu ⁶ | 2008-05-07 | 27.0 | 7 | 189 | 0.08 | 0.79 | 294 | 150 ⁴ | 0.18 ⁴ | 2.304 | 12 | 151 | 0.11 | 3.24 | - | - | - | - |
| Niigata ^c | 9.0 | Tohoku | 2011-03-11 | 29.0 | 35 | 265 | 0.29 | 0.46 | 17 | 270 | 0.24 | 2.14 | 12 | 235 | 0.15 | 3.6 | 4 | 208 | 0.05 | 5.25 |
| | 7.9 | Tohoku AF | 2011-03-11 | 42.6 | 25 | 301 ³ | 0.21 | 0.38 | 15 | 310 ³ | 0.14 | 2.10 | 11 | 284 ³ | 0.11 | 3.57 | 3 | 264 ³ | 0.03 | 5.0 |
| | 6.9 | East Honshu ⁶ | 2008-05-07 | 27.0 | 20 | 296 | 0.20 | 0.38 | 10 | 302 | 0.14 | 2.24 | 10 | 278 | 0.05 | 3.64 | 3 | 267 | 0.02 | 5.0 |
| Puget ^b | 6.8 | Nisqually ^a | 2001-02-28 | 51.9 | 4 | 91 ² | 0.21 | 0.665 | 3 | 67 ² | 0.15 | 2.51 | 5 | 77 ² | 0.20 | 3.82 | 35 | 79 ² | 0.08 | 6.07 |

Notes: BC-Hydro GMM event and location terms: ^aintraslab, ^bforearc, ^cbackarc. ¹# signifies the number of stations per bin. ²Hypocentral distances (R_{hyp}) shown for intraslab events. ³ R_{CD} is unavailable, therefore R_{hyp} is shown. ⁴ R_{CD} missing for station code CHB027, therefore, this station's recording is not used. ⁵Excluded one value of $Z_{2.5}$ equal to 0 in the calculation of geometric mean, because the seismic-wave velocity model is inaccurate at shallow depths. ⁶Event location is used as the event is unnamed.

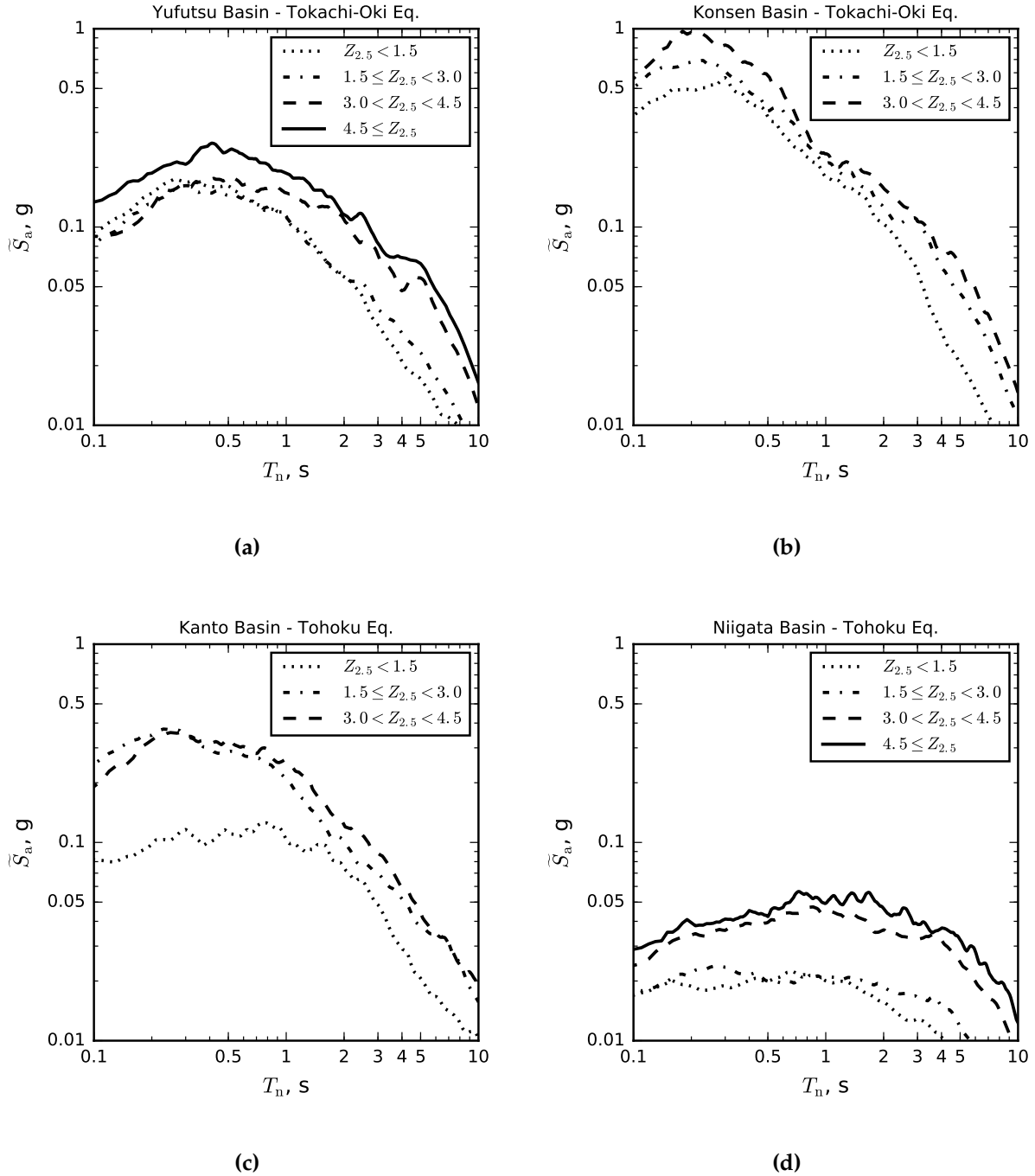


Figure 4.5: Geometric mean of response spectrum of recordings binned in terms of $Z_{2.5}$ for the (a) Yufutsu basin, (b) Konsen basin, (c) Kanto basin, and (d) Niigata basin.

g), because the source-to-site distances are larger. The trends (with respect to period) in the ratios of spectral accelerations differ for the Kanto basin (Figure 4.5c). The corresponding ratios for the Kanto basin generally decrease with period, from 3.0 (0.33 g/0.11 g) at 0.5 s, to 1.6 (0.12 g/0.074 g) at 2 s and to 2.1 (0.044 g/0.021 g) at 5 s. The possible causes of the differences in ratios between the Kanto basin and the other basins are discussed in the following section.

4.6 Relating GMM Residuals to $Z_{2.5}$

Although the source-to-site distances were similar for each $Z_{2.5}$ bin, they were not identical, and recordings also vary due to local site properties, such as V_{S30} . To account for these variations, the measured accelerations were normalized by the accelerations predicted from GMMs that account for effects other than basins. The normalization is not perfect because some GMMs include the effect of V_{S30} , which can be a proxy for basin amplification in situations where V_{S30} correlates with basin depth parameters (e.g., $Z_{1.0}$ and $Z_{2.5}$), especially at stations with low basin depths (e.g., Campbell and Bozorgnia, 2014). However, this chapter only relies on recordings from site class C and D stations, and for this dataset, V_{S30} and $Z_{2.5}$ were only weakly correlated ($R^2 < 0.03$) for all four basins (Figure 4.6). The low R^2 indicates that variations in V_{S30} among $Z_{2.5}$ bins would not significantly affect variations in the computed \tilde{S}_a among $Z_{2.5}$ bins.

GMMs include a series of terms that account for properties that correlate with ground-motion intensity measures. For GMMs that do not account for basins, the spectral acceleration is commonly predicted with an expression that has the following general form:

$$\ln S_{a,GMM} = f_{M,R}(M, R) + f_{\text{local-site}}(\dots) \quad (4.1)$$

where $f_{M,R}$ is the term that accounts for the effects of magnitude (M) and source-to-site distance (R). $f_{\text{local-site}}$ accounts for local site effects, often expressed in terms of V_{S30} . The GMM residuals provide a convenient way of identifying the effects of basins on S_a . The GMM residual, ϵ , is computed as the difference between the natural logarithm of the recorded S_a ($\ln S_{a,rec}$) and the natural logarithm of the predicted S_a ($\ln S_{a,GMM}$):

$$\epsilon = \ln S_{a,rec} - \ln S_{a,GMM} = \epsilon_{\text{basin}}(\dots) + \epsilon_{\text{other}}(\dots) \quad (4.2)$$

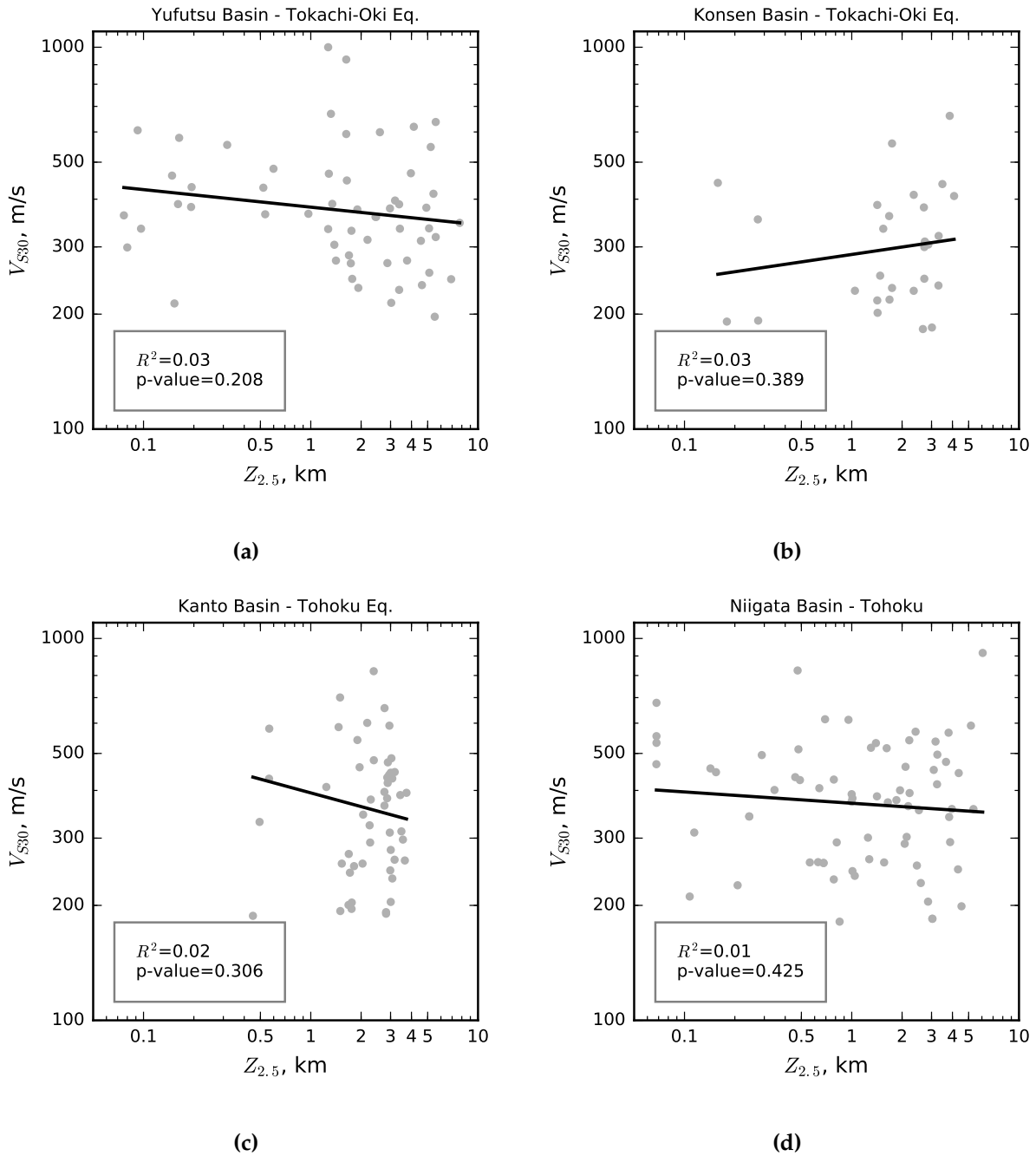


Figure 4.6: The selected station's V_{S30} parameter with respect to $Z_{2.5}$ for the (a) Yufutsu basin, (b) Konsen basin, (c) Kanto basin, and (d) Niigata basin.

where ϵ_{basin} is the residual due to sedimentary basin effects not included in the GMM, and ϵ_{other} is the residual due to other effects not captured by the GMM. These "other" effects that contribute to ϵ_{other} include path-specific and local-site effects that are influenced by crustal heterogeneity, and near-surface layering that is not captured by averaging the shear-wave velocity profile to compute V_{S30} (Atik et al., 2010). In this chapter, the mean residual for the recordings in a particular $Z_{2.5}$ bin is denoted as $\hat{\epsilon}_Z$. The difference in mean residual between a particular bin to the shallowest bin ($Z_{2.5} < 1.5$) is denoted as $\Delta\hat{\epsilon}_Z$ and expressed as,

$$\Delta\hat{\epsilon}_Z = \hat{\epsilon}_Z - \hat{\epsilon}_{Z < 1.5} = [\hat{\epsilon}_{Z,\text{basin}} + \hat{\epsilon}_{Z,\text{other}}] - [\hat{\epsilon}_{Z < 1.5,\text{basin}} + \hat{\epsilon}_{Z < 1.5,\text{other}}] \quad (4.3)$$

where $\epsilon_{Z < 1.5}$ is defined as the mean residual for recordings with $Z_{2.5} < 1.5$. Ideally, $\tilde{\epsilon}_{Z < 1.5}$ would equal zero only if all of the GMM predictions were exactly equal to all of the measured values outside the basin (i.e., the GMM had no uncertainty in its prediction). To isolate the effect of the basins, the mean within-event GMM residuals due to non-basin effects ("other") are assumed to be similar inside and outside the basin, so $\Delta\hat{\epsilon}$ can be approximated as:

$$\Delta\hat{\epsilon}_Z \approx \hat{\epsilon}_{Z,\text{basin}} - \hat{\epsilon}_{Z < 1.5,\text{basin}} \quad (4.4)$$

In this chapter, the effect of the basin on spectral accelerations is quantified in terms of the basin amplification factor, BAF_{S_a} , which is defined as the exponential of $\Delta\hat{\epsilon}_Z$.

$$\text{BAF}_{S_a}(Z) = e^{\Delta\hat{\epsilon}_Z} = e^{\Delta\hat{\epsilon}_{Z,\text{basin}}} / e^{\Delta\hat{\epsilon}_{Z < 1.5,\text{basin}}} = \frac{\left(\prod_{y=1}^Y \frac{S_{a,Z,\text{basin}}^y}{S_{a,Z,\text{GMM}}^y}\right)^{\frac{1}{Y}}}{\left(\prod_{x=1}^X \frac{S_{a,Z < 1.5,\text{basin}}^x}{S_{a,Z < 1.5,\text{GMM}}^x}\right)^{\frac{1}{X}}} \quad (4.5)$$

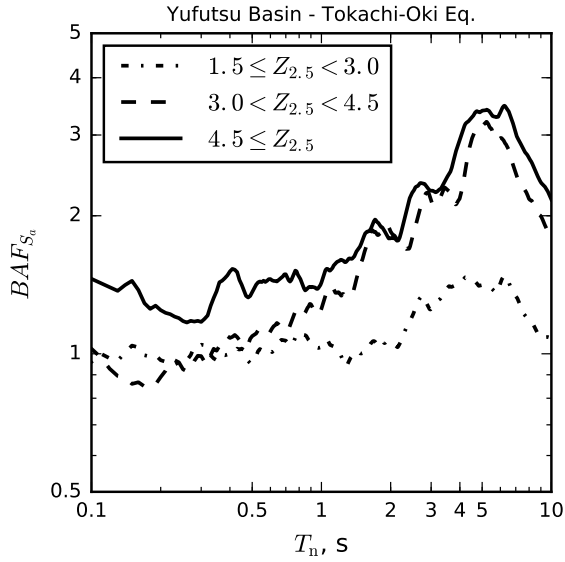
where X is the number of ground-motions with $Z_{2.5} < 1.5$ and Y is the number of ground-motion within a particular $Z_{2.5}$ range. BAF_{S_a} can be interpreted as the geometric mean of the ratio of the measured to predicted spectral accelerations inside the basin, normalized by the same quantity outside the basin ($Z_{2.5} < 1.5$).

Although several subduction GMMs are used in the U.S. hazard maps, this chapter considers only the most recent version of the (Abrahamson et al., 2016). The BC-Hydro GMM uses terms that distinguish between stations located in the forearc (between the subduction trench and the volcanic fronts) and the backarc region (beyond the volcanic fronts). Stations used in the Yufutsu and Niigata basin were located in the back-arc region, whereas both the Kosen and Kanto station were located in the forearc region.

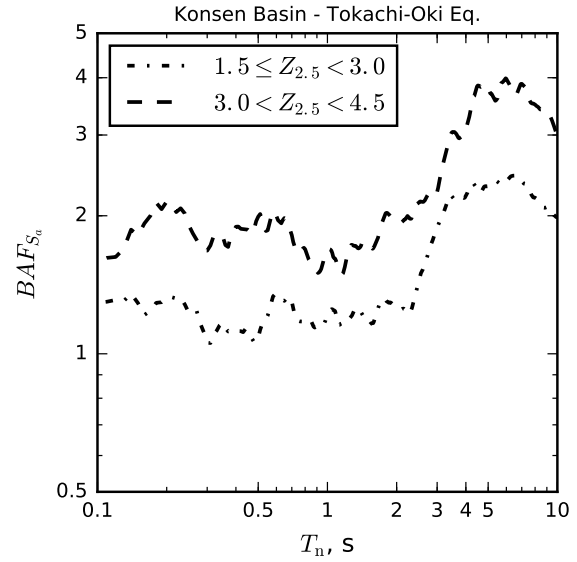
Figure 4.7 shows values of $BAF_{S\alpha}$ computed for the Yufutsu and Konsen basins during the Tokachi-Oki earthquake, and the Niigata and Kanto basin during the Tohoku earthquake. For the Yufutsu, Konsen, and Niigata basins, the $BAF_{S\alpha}$ values exceed one for nearly all bins and periods. For these three basins, $BAF_{S\alpha}$ values generally increase with $Z_{2.5}$, varying between values of 2 to 4 for all periods larger than 2 s. For the Kanto basin, $BAF_{S\alpha}$ values exceed one for periods less than 1.4 and larger than 3.0 s. For this basin, the maximum $BAF_{S\alpha}$ values of 2 to 3 occurred at short periods (< 0.3 s).

The Kanto basin appears to amplify motions differently than the other basins. The work presented here does not provide the basis for explaining why this basin behaves differently. Numerical studies have attributed amplitude variations to the aspect ratio of a basin (Bard and Bouchon, 1985) and its overall shape (MezaFajardo et al., 2016) which are not captured by $Z_{2.5}$. In addition, Denolle et al. (2014) and Frankel et al. (2009) found that differences in basin amplification may be attributable to the azimuthal angle of the earthquake (angle between the vector pointing north at the basin to the earthquake epicenter). For example, Denolle et al. (2014) found that the Kanto basin amplifications were largest for seismic waves traveling eastwards towards Kanto, whereas basin amplifications were smallest for waves traveling from the southern and northwest directions, the latter being the azimuth direction to the seismic waves from the Tohoku event. Similarly, for the Seattle basin (the deepest portion of the basins within the Puget Lowland region), Frankel et al. (2009) found that the basin amplifications were largest from events located to the south and southwest of the basin, which is in a similar direction to the Cascadia subduction plate interface. This high amplification may be caused by the abrupt change in shear-wave velocity at the southern edge of the basin formed by the Seattle fault zone.

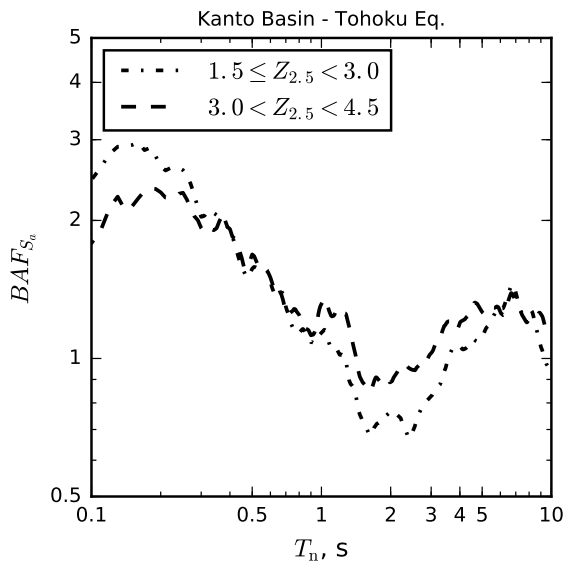
The significance of the basin effect can also be quantified by evaluating the correlation between the within-event residual and the $Z_{2.5}$ basin parameter. As shown in Figure 4.8a, the standard deviation of the GMM residuals for a given period and event exceeds the within-event standard deviation expected for the BC-Hydro GMM ($\tau = 0.43$) (Abrahamson et al., 2016). These residuals are shown in Figure 4.8b to correlate with $\ln Z_{2.5}$. For all four basins, the coefficient of determination, R^2 , generally increases with period, reaching maximum values of 0.36 (6.3 s) for the Yufutsu basin, 0.66 (5.0 s) for the Konsen basin, 0.29 (at 6.7 s) for the Kanto basin, and 0.52 (at



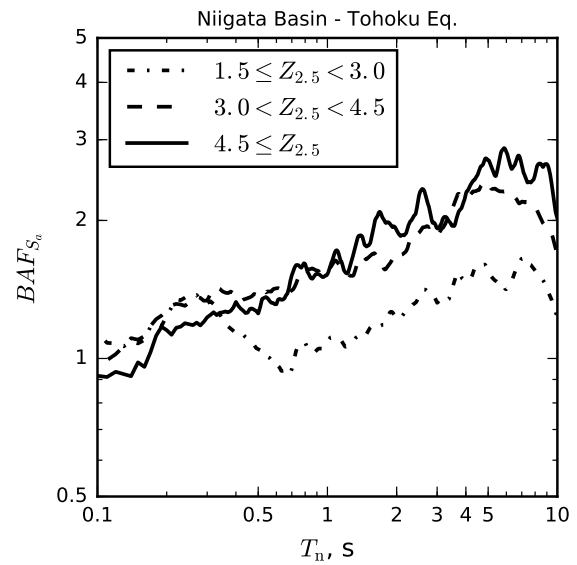
(a)



(b)



(c)



(d)

Figure 4.7: Basin amplification factors with respect to period for the (a) Yufutsu basin, (b) Kosen basin, (c) Kanto basin, and (d) Niigata basin.

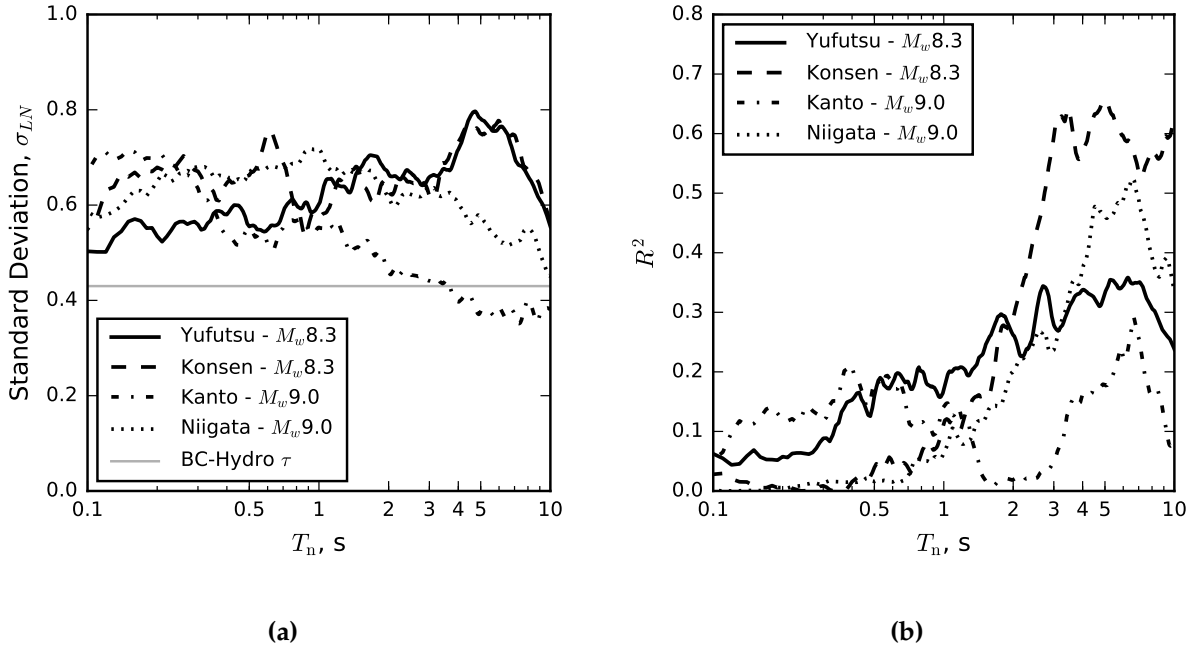


Figure 4.8: (a) Standard deviation of the GMM residual of S_α with respect to period and (b) R^2 statistic with respect to period for the GMM residual of S_α vs. $Z_{2.5}$.

6.6 s) for the Niigata basin. At the periods of maximum BAF_{S_α} , R^2 is smaller for the Kanto basin (0.12 at 0.16 s) than for the Yufutsu basin (0.36 at 6.3 s), Kosen basin (0.60 at 6.0 s) and Niigata basin (0.48 at 5.9 s). These results indicate that the variability of GMM residual is large (Figure 7a) and $\ln Z_{2.5}$ can explain much of this variability at long-periods (Figure 4.8b).

4.7 Effect of Earthquake Magnitude

For crustal earthquake GMMs (e.g., Campbell and Bozorgnia, 2014), the basin terms are independent of earthquake magnitude. To evaluate the effects of magnitude for subduction earthquakes, Figure 4.9 compares BAF_{S_α} values computed using three earthquakes of varying magnitudes for each basin. To facilitate the comparison, a single $Z_{2.5}$ bin is considered for each event, in which the BAF_{S_α} values are computed for recordings from all of the stations that have $Z_{2.5} \geq 3$ km. For some of the lower-magnitude earthquakes, the closest distance to rupture was

not available for all stations on ShakeMap (USGS, 2018), therefore hypocentral distances (shown in Table 4.1) were used in the BC-Hydro GMM predictions. These events have similar azimuths as their rupture plane on the subduction plate interface is in a similar location relative to each basin. In addition, the $Z_{2.5}$ bins between events have similar geometric means of $Z_{2.5}$ and numbers of recordings (listed in Table 4.1).

For all four basins, the BAF_{S_a} plotted in Figure 4.9 are independent of earthquake magnitude for period ranges in which the BAF_{S_a} is the largest. Moreover, at periods where the BAF_{S_a} differs significantly among earthquakes, the amplification does not increase or decrease consistently with increasing magnitude. Skarlatoudis et al. (2015) also found that the amplification factors for a particular basin were similar for several earthquakes.

4.8 Comparison with the Puget Lowland Basin

For the basins within the Puget Lowland region, the largest earthquake for which a significant number of recordings are available is the 2001 Nisqually earthquake. Nisqually earthquake motions were recorded by the Pacific Northwest Seismic Network (PNSN) and the U.S. Geological Survey (USGS) Seattle Urban Seismic Array Stations. These recordings were downloaded from the Incorporated Research Institutions for Seismology (IRIS) Wilber database (2013) and USGS (2001). To reduce the effects of local site conditions, recordings were only considered for sites with V_{S30} equal to at least 180 m/s (as per PNSN V_{S30} maps and Yong, 2015). Stations that triggered during Nisqually were selected if they were located within a 30-km offset (in the outside basin direction) of the $Z_{2.5} = 3$ km contour line. The epicenter of the Nisqually earthquake is underneath the southern basin edge (shown in Figure 4.3). To isolate basin effects and limit effects from rupture directivity during intraslab earthquakes (Adams and Halchuk, 2002), stations located within the same vicinity (city of Seattle) were used. Effects of rupture directivity during Nisqually was noted by Booth (2004) which showed larger Modified Mercalli intensity at locations South-West and South-East of the epicenter. Furthermore, Frankel et al. (2009) used 3D physics-based simulations that confirmed the effects of rupture directivity, radiation pattern, and deep path effects would be azimuthally dependent. For these reasons, stations with similar azimuths from the epicenter were used by further filtering for stations that

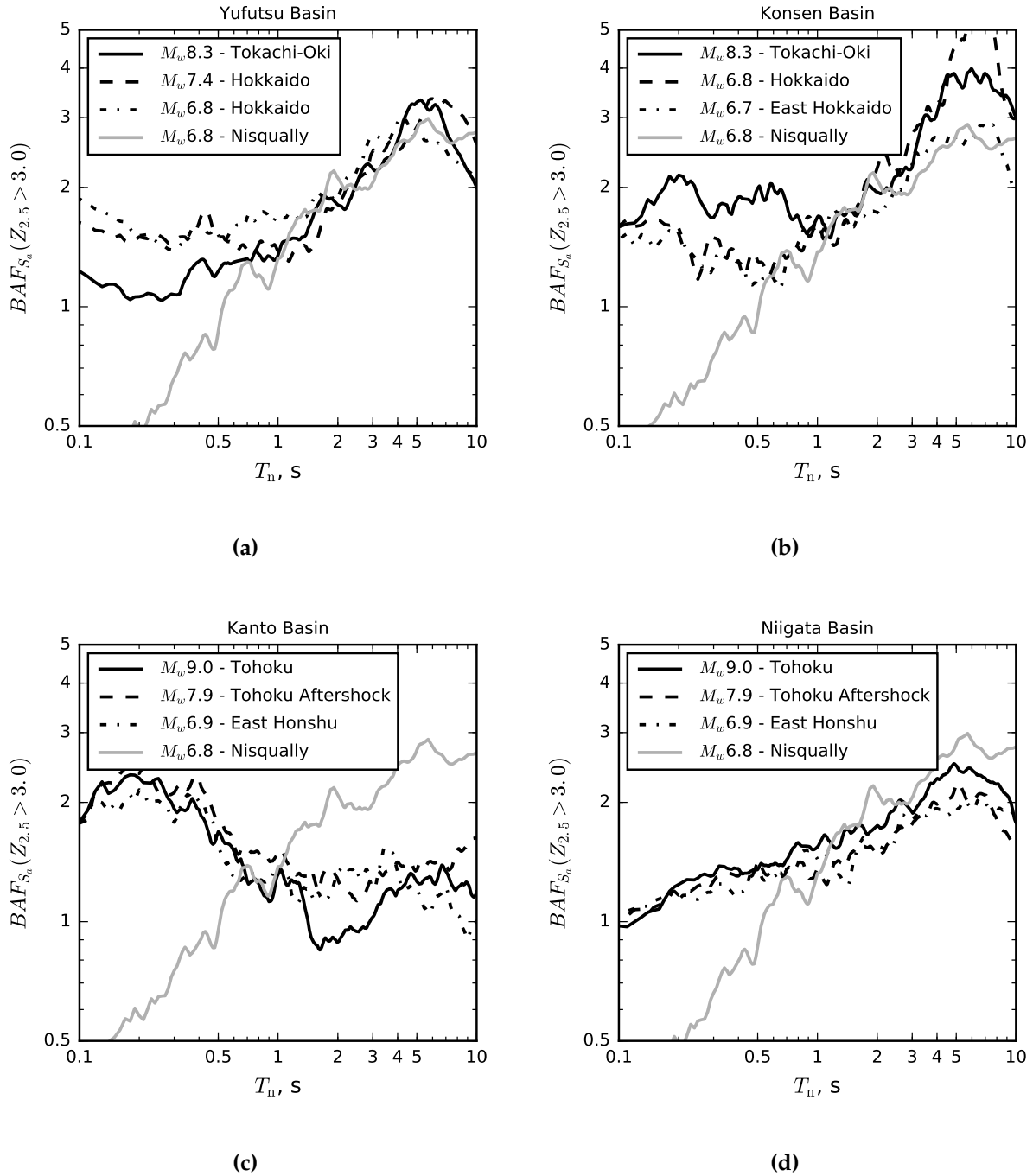


Figure 4.9: Basin amplification factors for earthquakes of varying magnitudes for the (a) Yufutsu basin, (b) Kosen basin, (c) Kanto basin, and (d) Niigata basin. BAF_{S_a} for the basin within the Puget Lowland region during the 2001 Nisqually earthquake is shown for comparison.

are located north of $47^{\circ}15\text{N}$. The number of records from stations having $Z_{2.5} < 1.5$ (4 stations) or $Z_{2.5} \geq 3$ (40 stations) are similar to the four Japanese basins. Table 4.1 shows that the geometric mean of the hypocentral distances for each $Z_{2.5}$ bin are smaller than for the Japanese earthquakes.

The BAF_{S_a} values for the Nisqually earthquake are shown in Figure 4.9, along with similar values for the four Japanese basins. Unlike the four basins in Japan, the basins in the Puget Lowland region during Nisqually appeared to deamplify the spectral accelerations at periods less than 0.5 s. This difference could be due to path effects because the Nisqually hypocenter was deep (≈ 52 km) and located directly underneath the basins within the Puget Lowland region (Figure 4.3), whereas most of the subduction interface events were shallower and further away from the basins. Above periods of 1 s, the BAF_{S_a} for the basins within the Puget Lowland region has similar trends and magnitudes as the Yufutsu, Kosen, and Niigata basins. Again, the Kanto basin behaved differently, as discussed earlier. For long periods, the Nisqually basin amplification was larger than that observed for the Kanto basin.

4.9 Evaluation of Existing Basin Terms

The CB14 basin terms (Figure 4.2) were developed considering crustal earthquake recordings. One strategy for accounting for basins during subduction earthquakes would be to add the CB14 basin term to the BC-Hydro GMM prediction, as has been recommended by Chang et al. (2014). This approach neglects the fact that both the BC-Hydro and the Campbell and Bozorgnia (2014) GMMs include a V_{S30} term, which might indirectly account for basin effects. However, this approximation is adopted for this dataset, because $Z_{2.5}$ did not correlate with V_{S30} .

For the Yufutsu and the basins within the Puget Lowland region, Figure 4.10 shows the BAF_{S_a} normalized by CB14 predictions. These values were computed by subtracting the basin term in CB14 (using the Japan region-specific values for both basins) from the GMM residual computed from BC-Hydro. In this figure, values close to 1.0 indicate that the CB14 factor predicts basin amplifications well, and values above 1.0 indicate that CB14 underestimates the basin effect.

For the Yufutsu basin, the BAF_{S_a} exceed the CB14 basin term by more than 25% for periods above 2.6 seconds and at periods shorter than 0.3 s (shown in Figure 4.10). For the basins within the Puget Lowland region, BAF_{S_a} values are within 25% of the CB14 amplification for periods

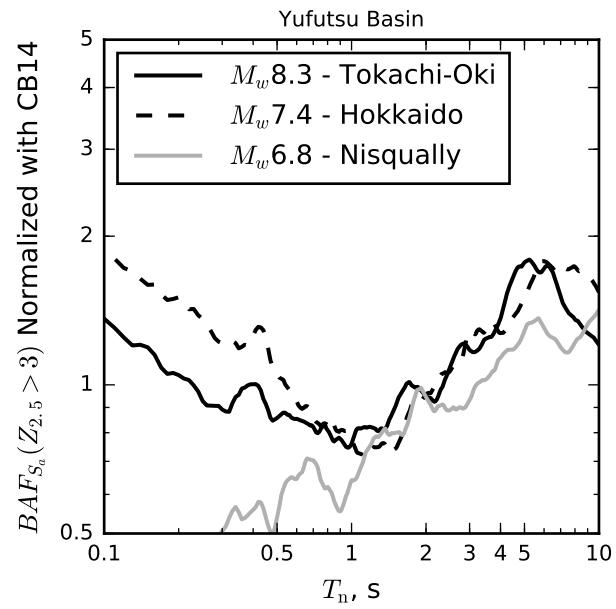


Figure 4.10: Basin amplification factors for spectral acceleration normalized with the amplification predicted using the CB14 basin terms.

between 1.2 to 4.9 s. Below 1.2s, BAF_{S_a} values are smaller than the CB14 amplification. The comparison of the BAF_{S_a} with the CB14 basin term was similar for the other basins and events (Figure 4.11).

For the four basins, the CB14 basin term was shown to account for basin amplifications at periods close to 1 s. However, at short periods the BAF_{S_a} was found to be larger than the CB14 basin term (by at least 25%) for the Yufutsu, Kosen, and Kanto basins. At long periods, BAF_{S_a} was also found to be larger than CB14 for the Yufutsu and Kosen basins.

The BC-Hydro GMM is one of the newer GMMs used to compute the subduction hazard in the national seismic hazard maps USGS (2014). For this reason, BAF_{S_a} values were computed using the BC-Hydro, however, there are other GMMs, that can predict S_a expected from subduction interface earthquakes. The Morikawa and Fujiwara (2013), abbreviated as MF13, GMM was formulated using earthquakes recorded in Japan from crustal, intraslab, and interface events. For the previously shown earthquakes and basins, BAF_{S_a} was computed using MF13 (Figure 4.12) and found to have similar trends and intensities to the BAF_{S_a} values shown in Figure 4.9. Moreover, the MF13 includes an "optional" basin term which is a function of $Z_{1.4}$ (corresponding to the depth to material with a shear-wave velocity equal to 1.4 km/s) that can also be used to account for basin effects. Figure 4.13 shows the BAF_{S_a} computed using the MF13 GMM with the basin term included. The values BAF_{S_a} which include the basin term (Figure 4.13) are closer to 1.0 than the values which exclude the basin term (Figure 4.12), however, the inclusion of the basin term still does not fully account for the basin amplifications as indicated with the large BAF_{S_a} values at short or long periods for four basins and the basins within the Puget Lowland region during Nisqually. These results indicate that the existing basin terms would need to be calibrated for each specific basin, or additional basin and source parameter terms (e.g., basin aspect ratio, shape value, or source azimuthal angle) would need to be included in the basin term.

4.10 Effects of Basin on Significant Duration

Large-magnitude, subduction earthquakes tend to have long durations. Bommer et al. (2004) found that the effects of durations are pronounced in structures that are susceptible to low-cycle

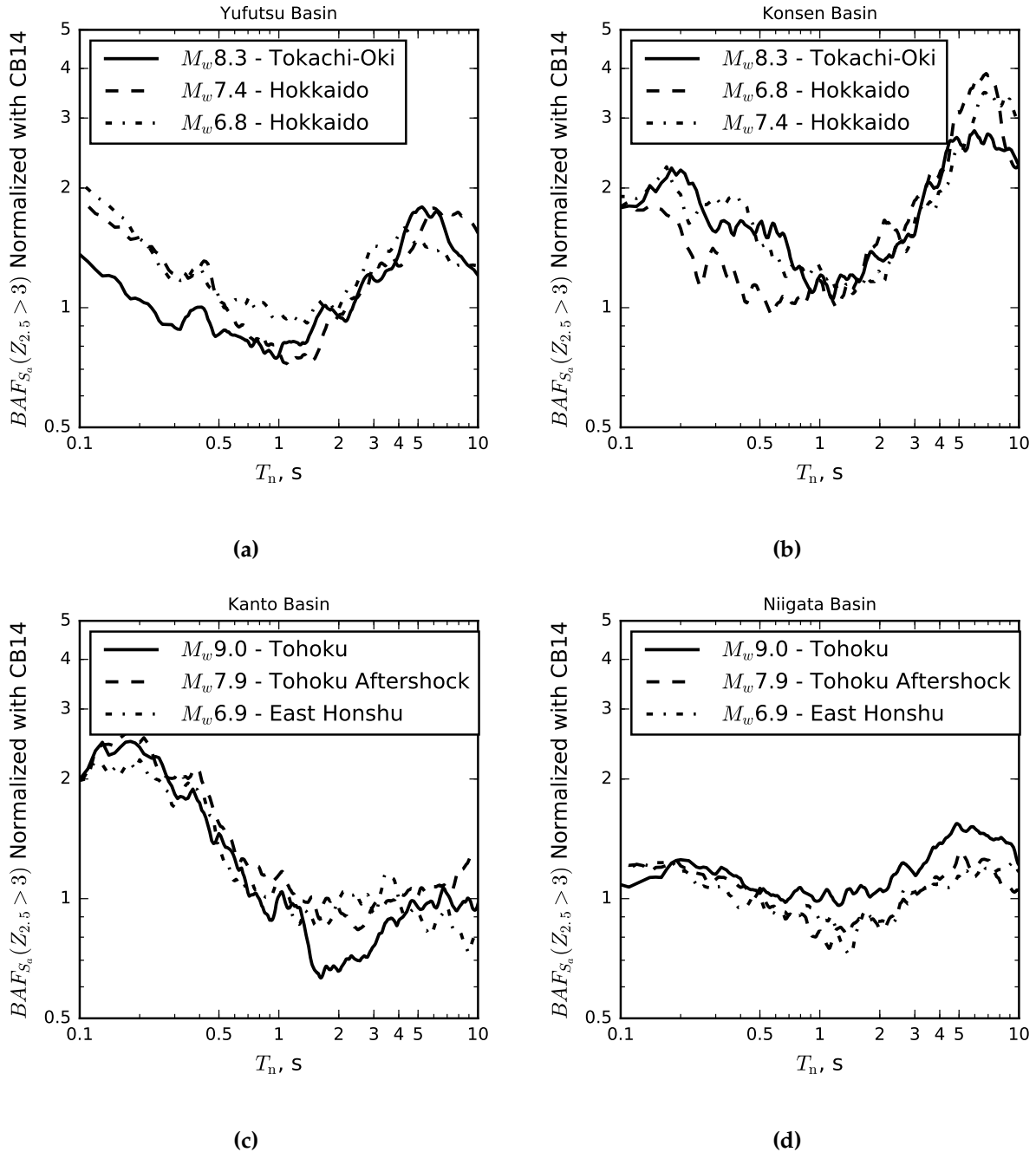


Figure 4.11: Basin amplification factors for spectral acceleration normalized with the amplification predicted using the CB14 basin terms for the (a) Yufutsu basin, (b) Kosen basin, (c) Kanto basin, and (d) Niigata basin.

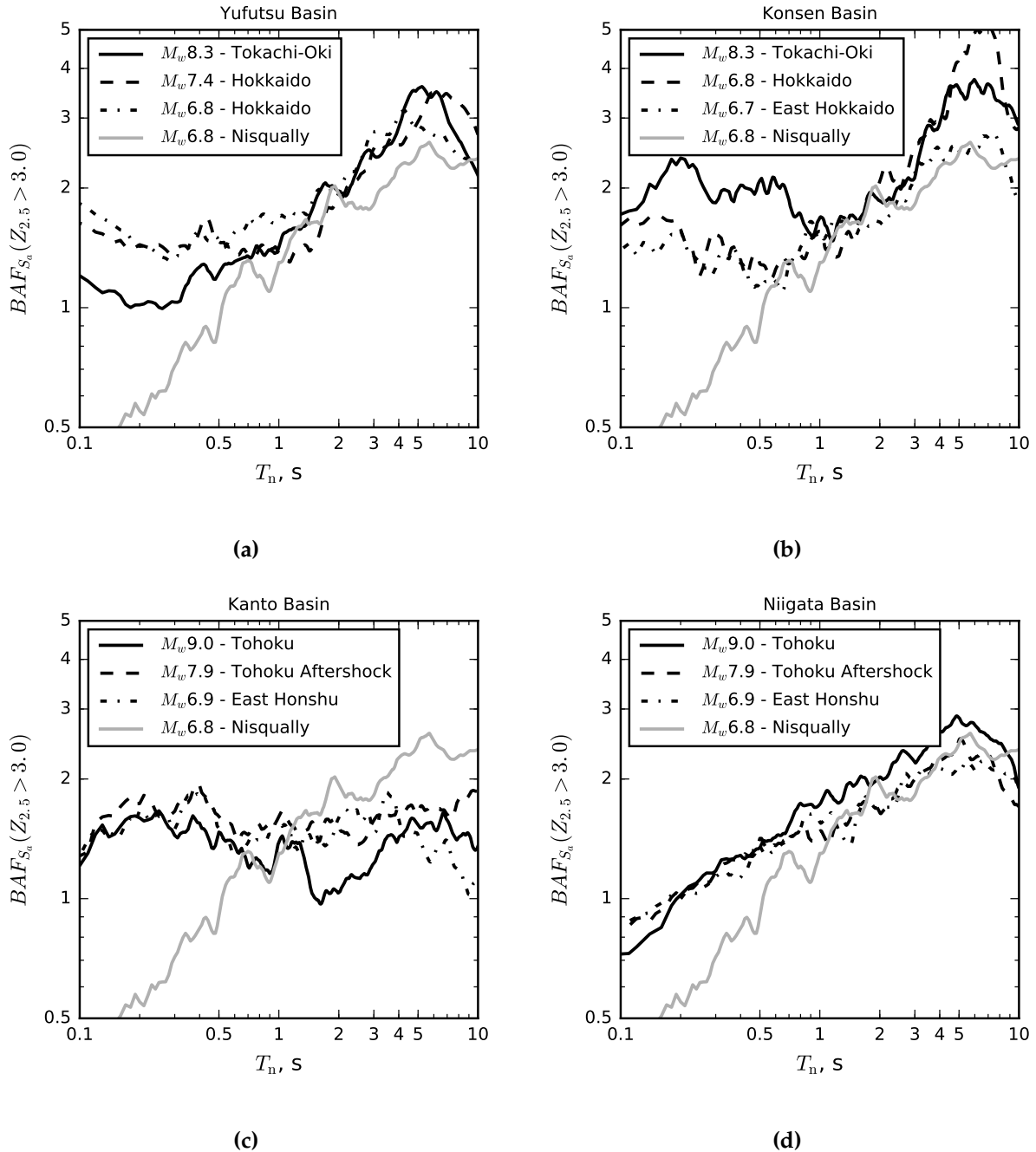


Figure 4.12: Basin amplification factors for spectral acceleration (computed using MK13 residuals without the optional basin term) for the (a) Yufutsu basin, (b) Kosen basin, (c) Kanto basin, and (d) Niigata basin. BAF_{S_n} for the basins within the Puget Lowland region during the 2001 Nisqually earthquake is shown for comparison.

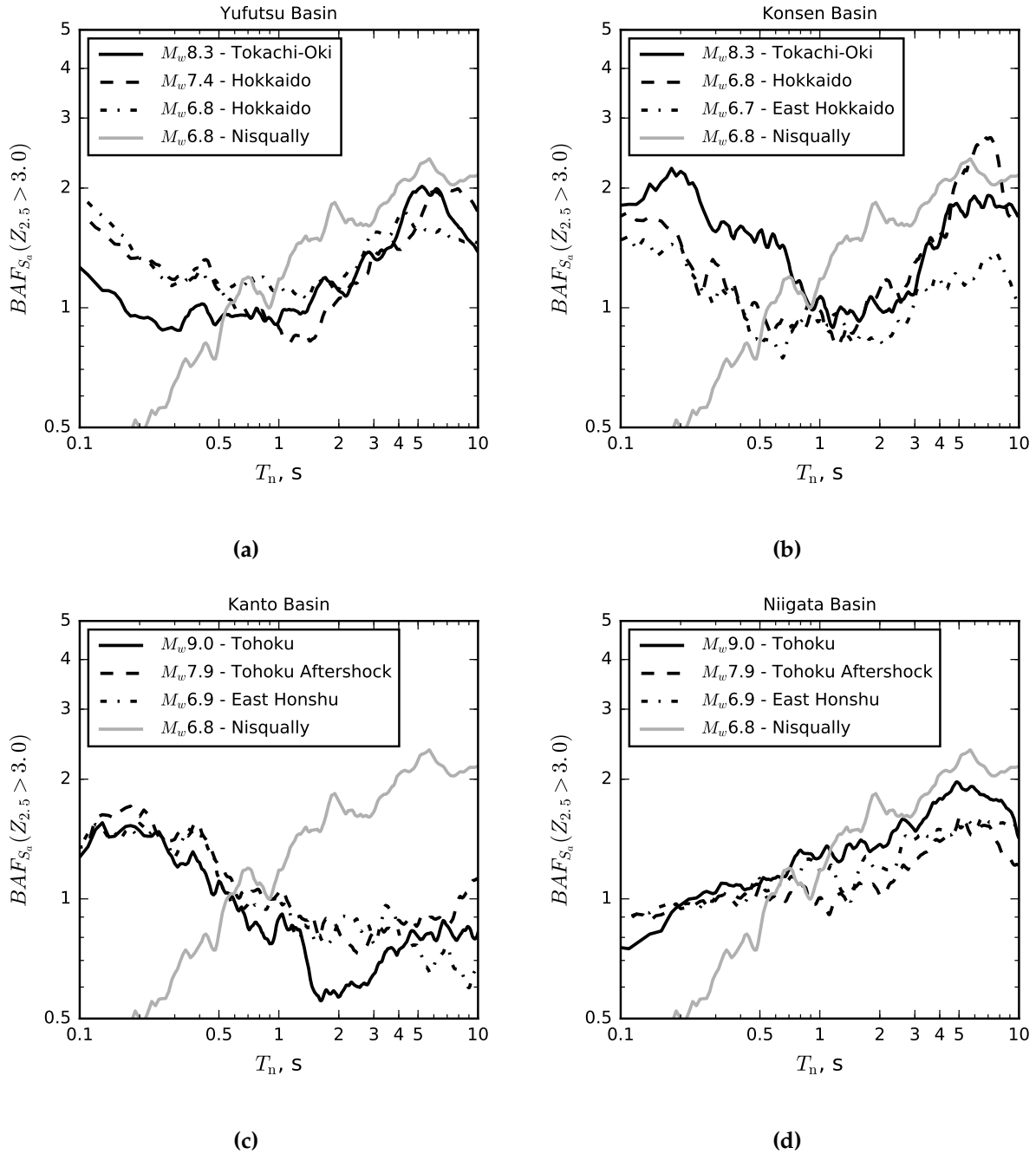


Figure 4.13: Basin amplification factors for spectral acceleration (computed using MK13 residuals with the optional basin term) for the (a) Yufutsu basin, (b) Kosen basin, (c) Kanto basin, and (d) Niigata basin. BAF_{S_n} for the basins within the Puget Lowland region during the 2001 Nisqually earthquake is shown for comparison.

fatigue, and undergo strength and stiffness degradation with cyclic loading. Hancock and Bommer (2007), and Chandramohan et al. (2016a) correlated structural response with various duration IMs. Chandramohan et al. (2016a) found that significant duration, D_s , was most suitable, correlates well with structural collapse, and used to show the impact of duration on structural collapse risk. Here, significant duration is defined as the time between two target values of the integral, $\frac{\int_0^t a_g(t)^2 dt}{\int_0^{t_{max}} a_g(t)^2 dt}$, where a_g is the ground acceleration and t_{max} is the total duration of the record. This chapter uses significant duration computed at the 5-95% threshold, $D_{s,5-95\%}$.

For each basin, the effects of the basin on duration can be seen in Figure 4.14, which shows $D_{s,5-95\%}$ with respect to $Z_{2.5}$. The durations for the subduction zone earthquakes were much longer (> 30 s) than those typically used to assess structural systems using FEMA P695. By comparison, the geometric mean $D_{s,5-95\%}$ was approximately 13 s for motions used in FEMA P695. This figure also shows the results of a simple linear regression analysis in log-scale for each basin for the largest magnitude earthquake. The resulting R^2 is 0.22 for the Kosen basin and 0.31 for the Niigata basin indicating that a significant portion of the variability in $D_{s,5-95\%}$ can be explained by $Z_{2.5}$. However, the low value of $R^2 = 0.13$ for the Yufutsu basin indicates that this relationship is not as strong as previously computed for long-period S_a (using GMM residuals, Figure 7). The Kanto basin also has a small R^2 , equal to 0.04, which indicates that no strong correlation exists between $Z_{2.5}$ and $D_{s,5-95\%}$.

Several duration GMMs (e.g., Abrahamson and Silva, 1996; Kempton and Stewart, 2006; Bommer et al., 2009) recognize that significant duration increases with distance. These GMMs were developed using crustal earthquakes. They are used here, because the authors are unaware of any significant duration GMMs for subduction earthquakes. Table 4.2 shows the R^2 and p-values for the correlation between GMM duration residuals and $\ln Z_{2.5}$ for the three events for each basin.

For a single comparison, a threshold p-value of 0.05 is conventionally used to reject the null hypothesis (corresponding to no basin effect on duration). In this case, multiple comparisons are performed (3 events for the 4 basins in Japan and 1 for the basins within the Puget Lowland region, resulting in a total of 13 comparisons). Therefore, the likelihood of incorrectly rejecting the

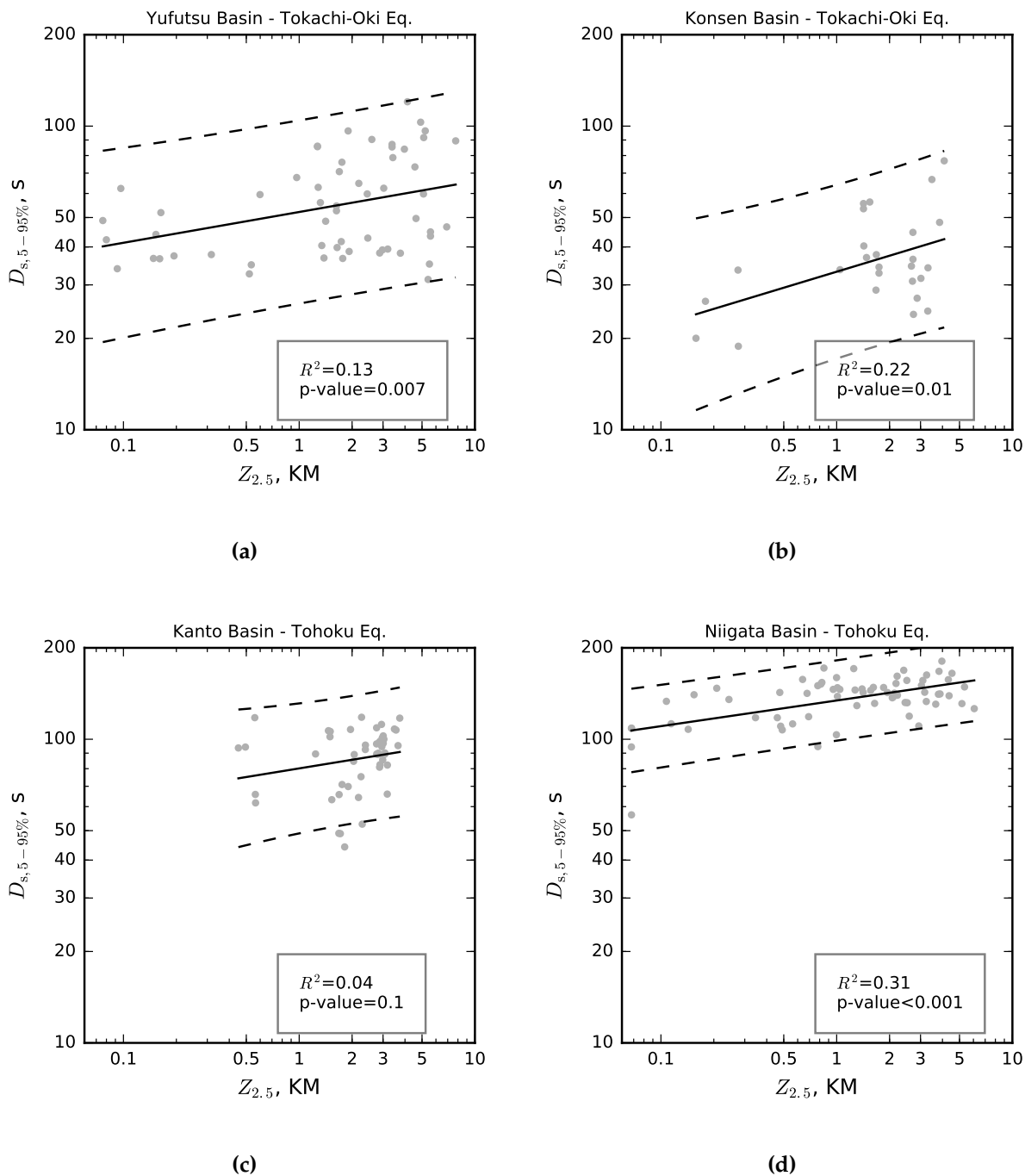


Figure 4.14: Significant Duration with respect to $Z_{2.5}$ for the (a) Yufutsu basin, (b) Konsen basin, (c) Kanto basin, and (d) Niigata basin.

Table 4.2: Statistics on significant duration GMM residual.

| Basin | Eq. | M_w | Abrahamson and Silva (1996) | | Kempton and Stewart (2006) | | Bommer et al. (2009) | |
|---------|-------------------|-------|--------------------------------|---------|-------------------------------|---------|----------------------|---------|
| | | | R^2 | p-value | R^2 | p-value | R^2 | p-value |
| Yufutsu | Tokachi-Okii | 8.3 | 0.05 | 0.09 | 0.08 | 0.03 | 0.08 | 0.04 |
| | Hokkaido | 7.4 | 0.02 | 0.4 | 0.04 | 0.2 | 0.10 | 0.07 |
| | Hokkaido | 6.8 | 0.10 | 0.02 | 0.11 | 0.01 | 0.11 | 0.01 |
| Konsen | Tokachi-Okii | 8.3 | 0.20 | 0.02 | 0.21 | 0.02 | 0.22 | 0.02 |
| | Hokkaido | 6.8 | 0.28 | 0.004 | 0.28 | 0.003 | 0.31 | 0.002 |
| | East Hokkaido | 6.7 | 0.50 | 0.002 | 0.54 | 0.001 | 0.56 | 0.001 |
| Kanto | Tohoku | 9.0 | 0.09 | 0.04 | 0.06 | 0.08 | 0.00 | 0.7 |
| | Tohoku Aftershock | 7.9 | 0.01 | 0.4 | 0.00 | 0.7 | 0.00 | 0.7 |
| | East Honshu | 6.9 | 0.16 | 0.005 | 0.15 | 0.008 | 0.08 | 0.05 |
| Niigata | Tohoku | 9.0 | 0.18 | <0.001 | 0.25 | <0.001 | 0.24 | <0.001 |
| | Tohoku Aftershock | 7.9 | 0.00 | 0.7 | 0.00 | 0.7 | 0.01 | 0.6 |
| | East Honshu | 6.9 | 0.05 | 0.2 | 0.05 | 0.2 | 0.07 | 0.09 |
| Puget | Nisqually | 6.8 | 0.11 | 0.03 | 0.10 | 0.04 | 0.10 | 0.04 |

null hypothesis (Type 1 error) increases. To decrease the likelihood of this error, the Bon-ferroni correction (Miller, 1981) was used. According to this correction, to reject the null hypothesis, the minimum p-value would need to be less than 0.0038 (i.e., $0.05/13$, corresponding to the set level of significance divided by the number of comparisons). Table 4.2 shows that null hypothesis can be rejected and the statistical inferences found were similar regardless of the GMM used.

Based on the R^2 statistic, it appears that the significant duration residual most strongly correlated ($R^2 \geq 0.20$ for all three events) with $\ln Z_{2.5}$ for the Konsen basin. The R^2 statistic for the basins within the Puget Lowland region during the Nisqually earthquake was small, varying from 0.10 to 0.11, depending on the GMM.

4.11 Effects of Basin on Spectral Shape

The effects of the shape of the response spectrum are not typically considered in conventional design. However, Haselton et al. (2011b) and Eads et al. (2015), among others, have shown that spectral shape influences collapse probabilities for structures. Chapter 3 developed an intensity

measure, SS_a that accounts for spectral shape and for differences in period elongation between brittle and ductile structures. This IM was found to correlate well with structural response for crustal and subduction earthquake ground motions (Chapter 3). This intensity measure can be used to evaluate the effects of basins on spectral shape (by relating SS_a to $Z_{2.5}$).

SS_a , is defined using the integral of the ground-motion response spectrum (damping ratio of 5%) between the fundamental period of the building (T_n) and the nominal elongated period (αT_n). To make SS_a independent of the ground-motion amplitude, the integral is then normalized by the area of a rectangle with a height of $S_a(T_n)$ and width of $(\alpha - 1)T_n$.

$$SS_a(T_n, \alpha) = \frac{\int_{T_n}^{\alpha T_n} S_a(T) dT}{S_a(T_n)(\alpha - 1)T_n} \quad (4.6)$$

where αT_n accounts for the period elongation of the structure. The factor α is computed as where $C_\alpha = 1.3$ was selected such that the intensity measure best correlated with structural response in Chapter 3. A C_α of 1.3 was found to correlate to collapse using the ground-motions and archetypes used in this chapter. The value of μ is the system's displacement ductility factor which, in practice, can be taken as the response modification coefficient (R) prescribed in ASCE 7-10 (Chapter 3). A value of R equal to 8 is used here, which corresponds to the value used for special reinforced concrete moment frame (SRCMF) systems and for other seismic force-resisting systems used in seismic design category D (ASCE, 2017). SS_a values larger than 1.0 indicate that the spectral ordinate increases with increasing period, on average. Values of SS_a smaller than 1.0 indicates that the spectral ordinate decreases with increasing period.

For μ equal to 8, Figure 4.15 shows SS_a values computed for periods ranging from 0.1 s to 5 s. As is typical of most ground motions (and design spectra), SS_a tends to decrease with increasing period. At low periods, SS_a does not vary consistently with $Z_{2.5}$. However, at longer periods (1 s to 4 s) the SS_a values for the Yufutsu and Kosen basins increase consistently with $Z_{2.5}$. There are no clear relationships between SS_a and $Z_{2.5}$ for the Kanto and Niigata basins.

As a comparison, SS_a values for a well-studied set of crustal ground motions are also shown in Figure 4.15. This set of motions, compiled by Haselton et al. (2011b), consists of 39 record pairs of earthquakes with M_w ranging from 6.5 to 7.6. These motions were recorded at moderate source-to-site distances (10-45 km) and were located on sites with V_{S30} more than 180 m/s. This set is an expanded version of the far-field ground motion set used in FEMA P695 (2009), and in

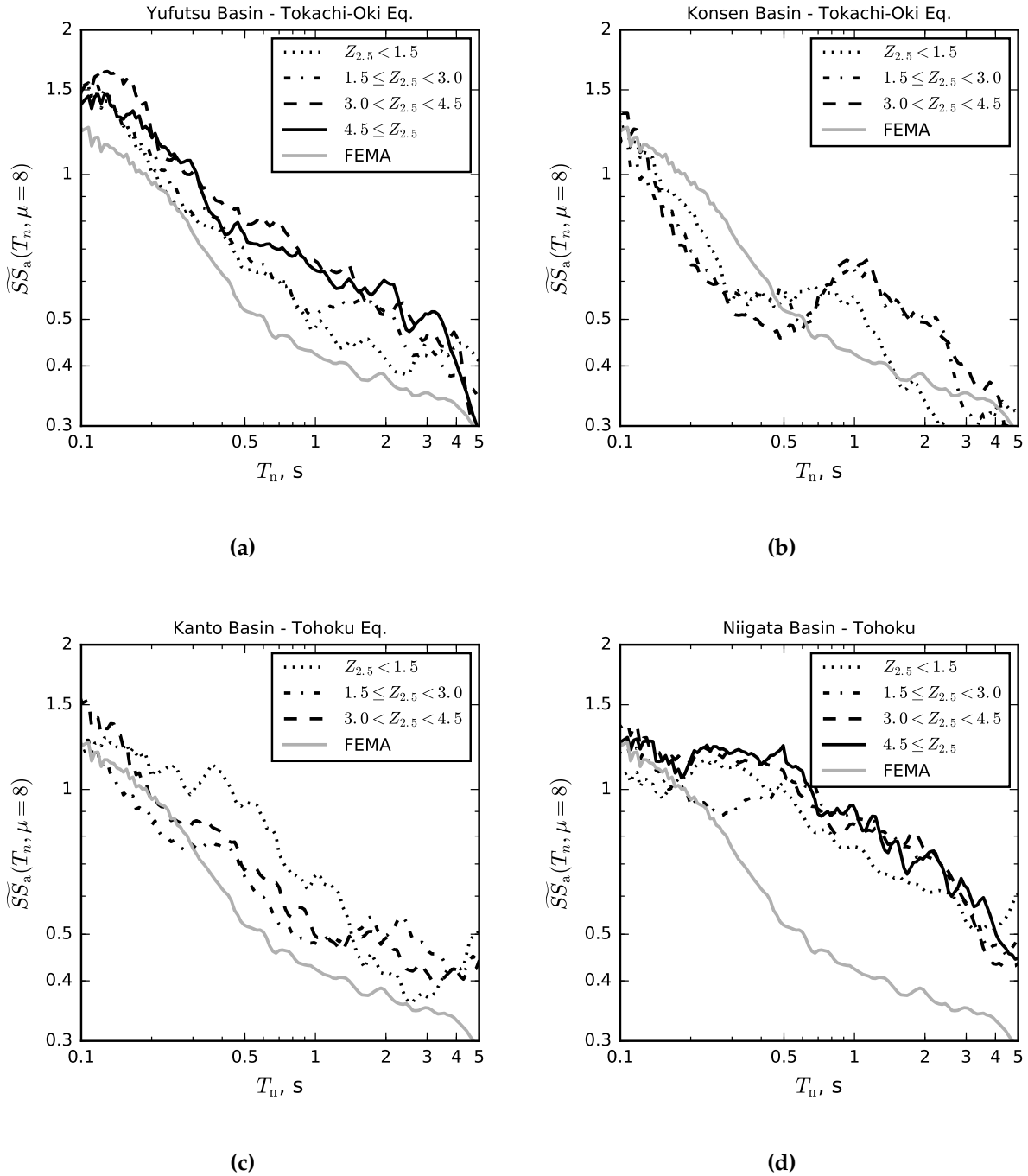


Figure 4.15: Geometric mean of SS_a for various $Z_{2.5}$ bins with respect to period for the (a) Yufutsu basin, (b) Kosen basin, (c) Kanto basin, and (d) Niigata basin. The geometric mean of SS_a for the FEMA motions are also shown for comparison.

this chapter, this set is referred to as the FEMA ground motion set. Some of these motions are recorded on sites located inside basins (e.g., Los Angeles basin) and would, therefore, have some inside basin characteristics. For the FEMA motions recorded in California (23/39), the $Z_{2.5}$ values are listed in the PEER NGA-West-2 flatfile (2014). Only 11% of these motions have a value of $Z_{2.5}$ above 3 km, with a geometric mean of $Z_{2.5}$ equal to 1.8 km; for the remaining FEMA recordings, the $Z_{2.5}$ values were unavailable.

The geometric mean of SS_a values with respect to period for recordings in the expanded FEMA set are shown for comparison in Figure 4.15. For bins with $Z_{2.5} \geq 3$ km, all four basins have larger values of SS_a (more damaging) than the FEMA set at periods longer than 0.5 s. At shorter periods the SS_a of the FEMA and basin motions are more similar. The differences between the SS_a values for the Niigata basin motions and the FEMA motions are particularly large at long periods. This difference is likely due to the long source-to-site distance, which is known to attenuate high-frequency seismic waves, resulting in a flatter response spectrum (and larger SS_a). In addition, the values of SS_a for the FEMA motions may be particularly low for long periods, because large-magnitude interface earthquakes have more low-frequency content than crustal earthquakes and the maximum usable period range for these recordings (FEMA motions) varies from 4 s to 25 s.

The variability of the IM due to non-basin effects was accounted using GMMs, however, there are no current GMMs for SS_a and the authors are unaware of subduction GMMs for spectral shape. Alternatively, the effects of basins on SS_a can be verified directly by taking the coefficient of determination (R^2) between $\ln SS_a$ and $\ln Z_{2.5}$ for a given period. Figure 4.16 shows the R^2 with respect to period for the three events in each basin. The R^2 significantly varies with short period (0 to 0.3) and are largest in the Kosen and Niigata basins with a mean R^2 around 0.1 for periods between 0.5 s to 2 s for the three events. The mean R^2 are much lower in the Yufutsu and Kanto basins, 0.03 and 0.02 respectively. While the geometric mean of the SS_a between bins was shown to increase (Figure 4.15), the variability in SS_a in each bin is large as is confirmed with the low R^2 especially in the Yufutsu and Kanto basin.

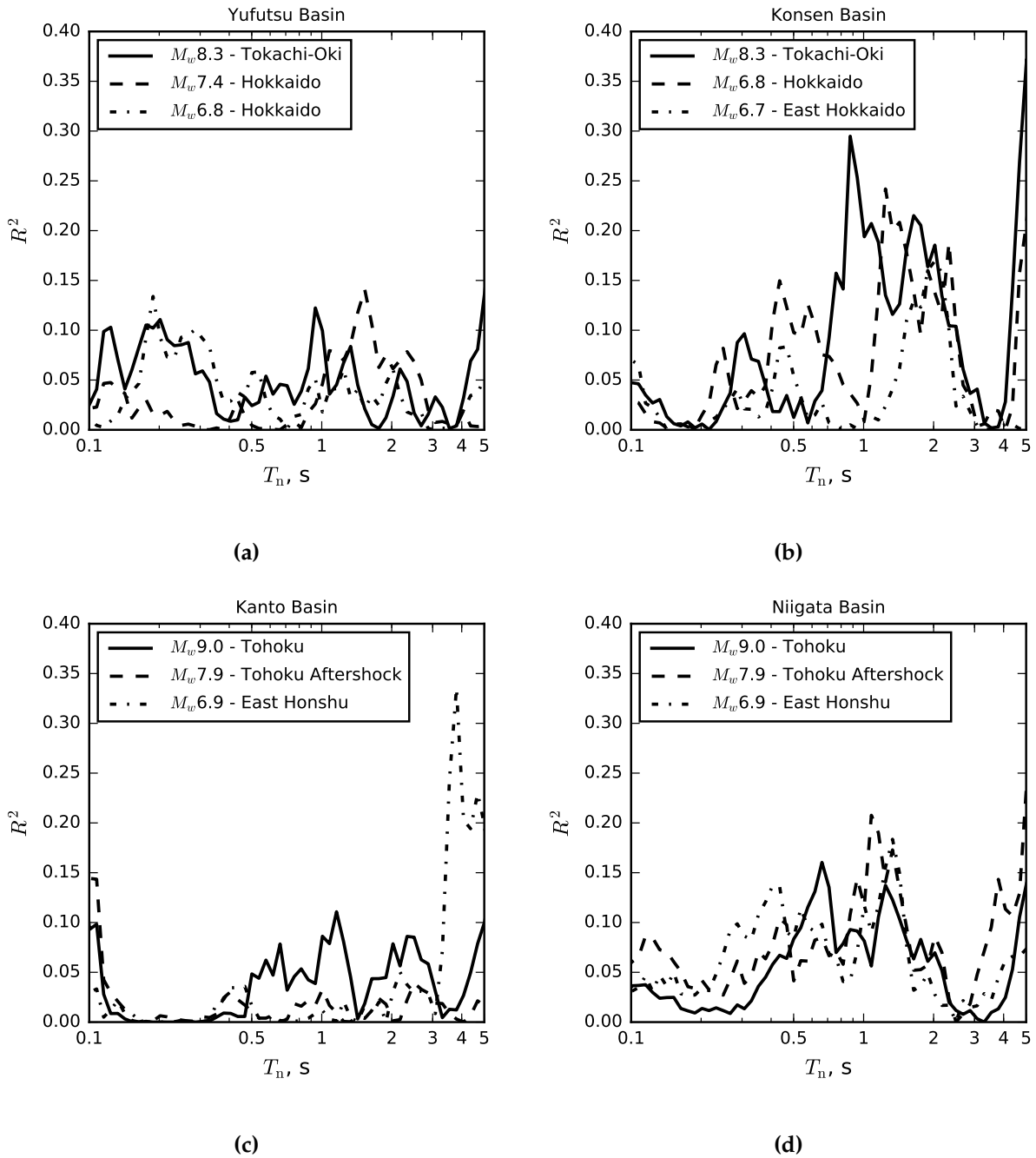


Figure 4.16: R^2 statistic for SS_a with respect to period for the (a) Yufutsu basin, (b) Kosen basin, (c) Kanto basin, and (d) Niigata basin.

4.12 Effects on Structural Collapse

One means of evaluating the damage potential of ground motions is to compute the intensity of the ground motion at which archetype structures collapse. To evaluate the effects of basins and large-magnitude subduction earthquakes on structural collapse, dynamic collapse analyses were performed for 30 MDOF archetypical reinforced concrete special moment frame buildings, developed by Haselton et al. (2011b), in *OpenSees* (2016). These buildings have been used in numerous studies on the effects of ground motions (e.g., Eads et al., 2015).

The archetypes were designed for a site in northern Los Angeles, with a short period MCE S_a equal to 1.5 g and a 1-sec MCE S_a equal to 0.6 g. The maximum considered earthquake spectral acceleration at each archetype's fundamental period, S_{MT} , was computed using the MCE response spectrum defined in FEMA P695. These models were originally evaluated using the expanded FEMA ground motion set, so for comparison purposes the collapse analysis results for the FEMA set are also shown here. These archetypes were subjected to the inside-basin ($Z_{2.5} \geq 3$) and outside-basin ($Z_{2.5} < 1.5$) motions from three basins. This chapter uses Haselton et al. (2011b) definition of collapse which corresponds to the point of dynamic instability, where the lateral story drifts of the building increase without bounds. Structural collapse was not evaluated for the weaker Niigata basin ground motions because it would have been necessary to apply large scale factors to these motions to cause structural collapse.

4.13 Relative Collapse Capacity

The FEMA P695 guidelines quantifies the collapse capacity of structures using the geometric mean of the spectral acceleration that caused the structure to collapse ($\tilde{S}_{a,c}$). The value of $\tilde{S}_{a,c}$ among the ground-motion sets varies due to the characteristics of the recordings in the sets. In this chapter, the ratio of $\tilde{S}_{a,c}$ for the outside-to-inside basin sets is computed to quantify the differences in ground-motion characteristics that affect structural collapse which are not captured by S_a alone. The ratio of collapse capacities between two ground-motion sets is known as the relative collapse capacity. The relative collapse capacity is also computed using FEMA-to-inside motions to quantify the differences between crustal motions and inside-basin subduction motions on structural collapse.

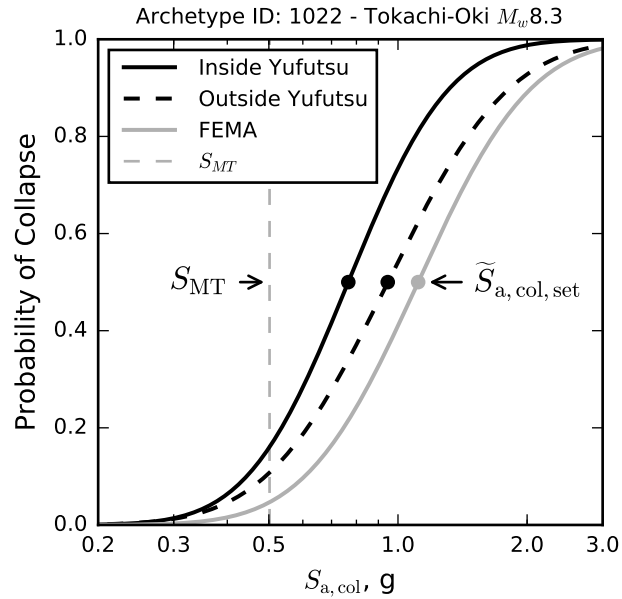


Figure 4.17: Collapse fragility functions for three ground-motion sets computed using spectral acceleration.

As an example, the collapse fragility functions for the Yufutsu-basin ground-motion sets are shown in Figure 4.17 for an eight-story reinforced concrete frame with an initial period of 1.79 s (archetype 1022). This structure was designed for an S_{MT} equal to 0.5 g. The geometric mean of spectral acceleration at collapse ($\tilde{S}_{a,c}$) was 0.77 g for the inside-Yufutsu-basin set, 0.95 g for the outside basin set, and 1.11 g for the FEMA set. For this archetype, the relative collapse capacity between the outside- and inside-basin motions can be defined as the geometric mean of $S_{a,c}$ for outside-basin motions, normalized by the geometric mean of $S_{a,c}$ for inside-basin motions (i.e., $\tilde{S}_{a,c,outside}/\tilde{S}_{a,c,inside}$). For this archetype, the relative collapse capacity of outside-to-inside motions is equal to 1.24, which means that the inside motions are more damaging at the same level of spectral acceleration.

The concept of relative collapse capacity can be extended to all 30 archetypes and all three basins. The relative collapse capacity of outside-to-inside basin motions is shown in Figure 4.18a. $\tilde{S}_{a,c,outside}$ exceeds $\tilde{S}_{a,c,inside}$ for nearly all structures in the Yufutsu basin (29/30 with geometric

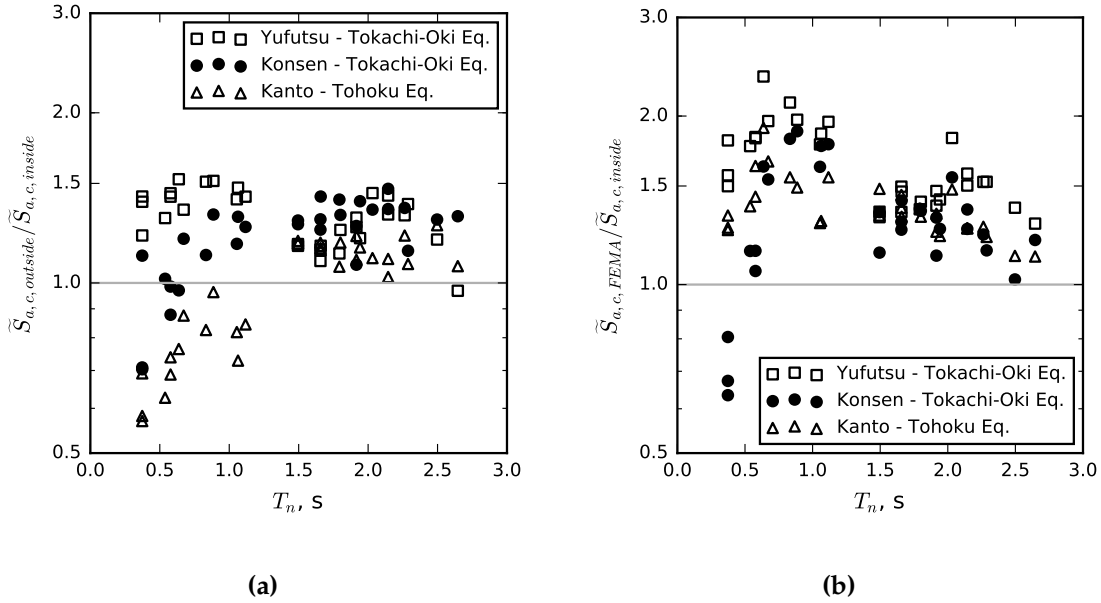


Figure 4.18: Ratio of geometric mean of spectral accelerations at collapse for the (a) outside-basin to inside-basin set (b) FEMA to inside-basin set for all archetypes.

mean of 1.30) and Konsen basin (25/30 with geometric mean of 1.18). These differences in the relative collapse capacity indicate that the inside-basin motions are more damaging at the same level of S_a for the Yufutsu and Konsen basins for nearly all the archetypes. For the Kanto basin, all 17 structures with a period above 1.5 s have a relative collapse capacity above 1.0 (geometric mean equal to 1.14). For all 13 structures with a period below 1.5 s, this ratio is below 1.0 (geometric mean = 0.72).

These differences are consistent with differences in duration and spectral shape for all three basins. The differences are quantified in Table 4.3 using the geometric mean of D_s , SS_a , and $S_{a,c}$ intensities for inside- and outside-basin ground-motion sets from the Yufutsu, Konsen, and Kanto basins. The geometric means are split into two groups, one for archetypes with periods less than 1.5 s (short-period archetypes) and the other for archetypes with periods more than 1.5 s (long-period archetypes). For the short-period archetypes subjected to Yufutsu- and Konsen-basin ground motions, and long-period archetypes subjected to all three basin ground motions,

the $\tilde{S}_{a,c,inside}$ was smaller $\tilde{S}_{a,c,outside}$ because both the \tilde{D}_s and \tilde{SS}_a were smaller for outside than inside basin ground motions (values are shown in online Table 4.3). For the short-period structures in the Kanto basin, the $\tilde{S}_{a,c,outside}$ was smaller $\tilde{S}_{a,c,inside}$ because SS_a was much smaller for inside- (0.62) than outside-basin (0.80) ground motions whereas the differences in \tilde{D}_s were subtle (94 s to 89 s for inside-to-outside basin).

The relative collapse capacity can also be used to compare the FEMA motions with the motions recorded inside basins. Figure 4.18b shows the relative collapse capacity for the FEMA and inside-basin motion sets ($\tilde{S}_{a,c,FEMA}/\tilde{S}_{a,c,inside}$) for all 30 frames and three basins. This figure shows that $\tilde{S}_{a,c,FEMA}$ is larger than $\tilde{S}_{a,c,inside}$ for all 30 archetypes for the Yufutsu- and Konsen-basin motions, and 90% of the archetypes (27/30) subjected to the Kanto basin motions. The geometric mean for all 30 archetypes and three basins is 1.41. This is because both \tilde{D}_s and \tilde{SS}_a intensities for short- and long-period archetypes are smaller in the FEMA set than the inside-basin set for all three basins (shown in online Table 4.3). Similar to the collapse capacities computed here, Liel et al. (2015) estimated that the relative collapse capacity of crustal-to-subduction (short-to-long duration) ground-motion sets is 1.6 for SRCMF archetypes designed in Seattle and Portland.

Figure 4.18 shows that, at a given level of spectral acceleration, (1) the FEMA motions are the least likely to cause collapse, (2) the outside-basin motions are more damaging than the FEMA ones, and (3) the inside-basin motions are even more damaging.

4.14 Combined Intensity Measure

The differences in $\tilde{S}_{a,c}$ among the ground-motion sets were expected, because structural collapse depends not only on S_a , but also on other ground-motion characteristics, such as duration and spectral shape. The effects of spectral acceleration, ground-motion duration, and spectral shape can be accounted for by an intensity measure that combines spectral acceleration at the period of a structure, significant duration, and SS_a (Chapter 3). The combined IM is computed as:

$$IM_{[comb]} = S_a(T_n) \times D_{s,5-95\%}^{C_{dur}} \times SS_a^{C_{shape}} \quad (4.7)$$

where the empirical exponent C_{dur} is equal to 0.11 and accounts for the structure's sensitivity to $D_{s,5-95\%}$. The C_{shape} exponent is equal to 0.54 and accounts for the structure's sensitivity to SS_a . The values of these exponents were selected to minimize the log-normal standard deviation of

Table 4.3: Geometric mean of various measures

| Set A/B | Measure | $T_n < 1.5s(13Archetypes)$ | | | | | | $T_n \geq 1.5s(17Archetypes)$ | | | | | | | | | |
|----------------|---|----------------------------|------|---------|------|--------|------|-------------------------------|------|------|------|---------|------|--------|------|-------|------|
| | | FEMA | | Yufutsu | | Konsen | | Kanto | | FEMA | | Yufutsu | | Konsen | | Kanto | |
| | | Out | In | Out | In | Out | In | Out | In | Out | In | Out | In | Out | In | Out | In |
| - | $\tilde{D}_s [s]$ | 13 | 48 | 63 | 73 | 33 | 43 | 89 | 94 | 94 | 13 | 48 | 63 | 33 | 43 | 89 | 94 |
| | \tilde{SS}_a | 0.49 | 0.60 | 0.73 | 0.56 | 0.55 | 0.56 | 0.80 | 0.62 | 0.37 | 0.42 | 0.56 | 0.34 | 0.50 | 0.42 | 0.47 | 0.47 |
| | $\tilde{S}_{a,c} [g]$ | 2.72 | 2.01 | 1.44 | 2.21 | 2.21 | 2.10 | 1.37 | 1.90 | 0.83 | 0.71 | 0.56 | 0.85 | 0.64 | 0.74 | 0.65 | 0.65 |
| | BAF _{sa} | - | 1.33 | | 1.77 | | 1.49 | | 1.86 | | 1.94 | | 1.03 | | 1.01 | | 1.01 |
| Outside/Inside | $\tilde{D}_{s,B}^{dur} / \tilde{D}_{s,A}^{dur}$ | - | 1.03 | | 1.03 | | 1.01 | | 1.03 | | 1.03 | | 1.03 | | 1.03 | | 1.01 |
| | $\tilde{SS}_{a,B}^{Cshape} / \tilde{SS}_{a,A}^{Cshape}$ | - | 1.11 | | 1.01 | | 0.87 | | 1.17 | | 1.23 | | 1.27 | | 1.06 | | 1.06 |
| | $\tilde{D}_{s,B-A}^{dur} / \tilde{SS}_{a,B-A}^{Cshape}$ | - | 1.15 | | 1.04 | | 0.88 | | 1.20 | | 1.27 | | 1.33 | | 1.07 | | 1.07 |
| | $S_{a,c,A} / S_{a,c,B}$ | - | 1.40 | | 1.05 | | 0.72 | | 1.27 | | 1.33 | | 2.52 | | 1.14 | | 1.14 |
| | DF _{basin} | - | 1.88 | | 1.82 | | 1.10 | | 2.27 | | 2.52 | | 1.14 | | 1.04 | | 1.04 |
| FEMA/Inside | $\tilde{D}_{s,B}^{dur} / \tilde{D}_{s,A}^{dur}$ | - | 1.19 | | 1.14 | | 1.24 | | 1.19 | | 1.14 | | 1.14 | | 1.24 | | 1.24 |
| | $\tilde{SS}_{a,B}^{Cshape} / \tilde{SS}_{a,A}^{Cshape}$ | - | 1.24 | | 1.07 | | 1.14 | | 1.24 | | 1.01 | | 1.01 | | 0.98 | | 0.98 |
| | $\tilde{D}_{s,B-A}^{dur} / \tilde{SS}_{a,B-A}^{Cshape}$ | - | 1.48 | | 1.23 | | 1.41 | | 1.49 | | 1.15 | | 1.15 | | 1.22 | | 1.22 |
| | $S_{a,c,A} / S_{a,c,B}$ | - | 1.89 | | 1.30 | | 1.43 | | 1.48 | | 1.30 | | 1.30 | | 1.28 | | 1.28 |
| | DF _{basin+sub.} | - | 2.47 | | 2.22 | | 2.17 | | 2.68 | | 2.45 | | 2.45 | | 1.18 | | 1.18 |

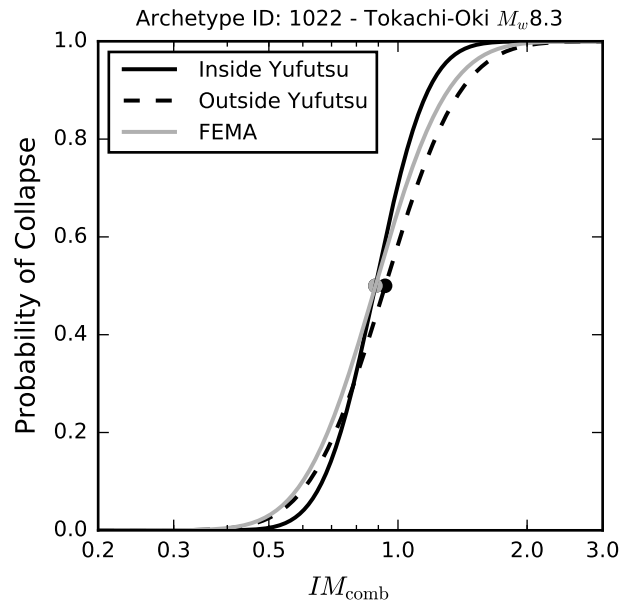


Figure 4.19: Collapse fragility function for three ground-motion sets computed using IMcomb.

the intensity measure at collapse for the full set of archetypes and ground motions. Figure 4.19 shows the collapse fragility curves computed using IM_{comb} for the eight-story frame (archetype 1022). In this calculation, the SS_a intensity measure was computed with a μ equal to 8 and quantifies the spectral shape between the period range of T_1 to $3.68T_1$, where T_1 is the first-mode period of the structure. Unlike the curves shown in Figure 12 for spectral acceleration, the fragility curves computed using IM_{comb} values are now nearly identical for the three datasets. In addition, the new intensity measure decreases the coefficient of variations computed in log scale for each dataset. For example, for the motions measured inside the Yufutsu basin, the coefficient of variation in log scale decreases from 35% for spectral acceleration to 20% for IM_{comb} . For this archetype, the differences in spectral acceleration at collapse are attributable to differences in ground-motion duration ($D_{s,5-95\%}$) and spectral shape (SS_a).

Similarly, the combined IM can be used to show that the differences in spectral accelerations at collapse for each of the 30 structures are attributable mainly to differences in ground-motion duration and spectral shape. For each archetype and basin, the relative collapse capacity ratios of

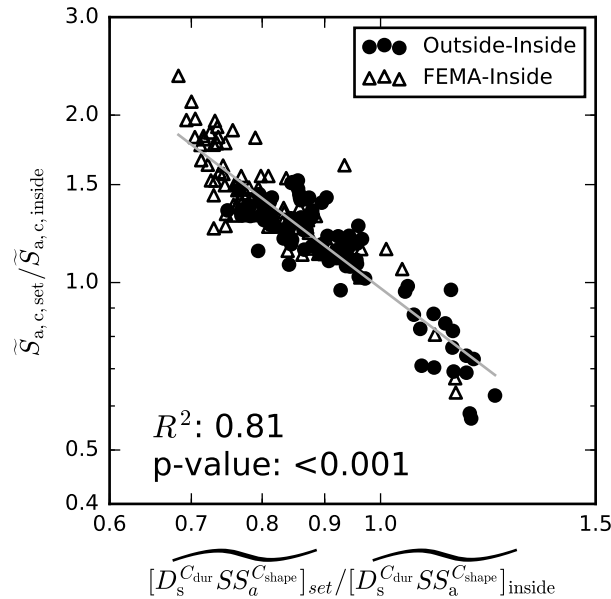


Figure 4.20: Ratio of $\tilde{S}_{a,c}$ of a ground-motion set to the $\tilde{S}_{a,c}$ for the inside-basin set with respect to the ratio of $D_s^{C_{dur}} \widetilde{SS}_a^{C_{shape}}$ geometric mean of $D_s^{C_{dur}} \widetilde{SS}_a^{C_{shape}}$ for a ground-motion set to the geometric mean of for the inside-basin set computed for the 30 archetypes using both the outside-basin set and the FEMA set.

outside-to-inside basin motions are plotted in Figure 4.20 (as solid circles) versus the ratio of geometric mean of $D_s^{C_{dur}} \widetilde{SS}_a^{C_{shape}}$ for the outside-basin motions to inside-basin motions (i.e., $[\widetilde{D}_s^{C_{dur}} \widetilde{SS}_a^{C_{shape}}]_{outside} / [\widetilde{D}_s^{C_{dur}} \widetilde{SS}_a^{C_{shape}}]_{inside}$). The relative collapse capacity is also plotted (as a hollow triangles) in Figure 4.20 to compare the FEMA motions and the inside-basin motions. As the normalized duration and spectral-shape intensity terms increase (x-axis), the normalized spectral acceleration at collapse decreases (y-axis) consistently, resulting in a value of R^2 equal to 0.81.

This high correlation indicates that the differences in $\tilde{S}_{a,c}$ among ground-motion sets are in large part attributable to the variations in ground-motion duration and spectral shapes. The independent effects of duration and spectral shape can be evaluated by considering the duration and spectral shape terms separately. Table 4.3 shows the relative intensity due to duration

($D_s^{C_{dur}}$) and spectral shape ($SS_a^{C_{shape}}$) between inside-to-outside and inside-to-FEMA ground-motion sets. These relative intensities correspond to the amplification on $\tilde{S}_{a,c,inside}$ due to duration and shape separately so that it equals $\tilde{S}_{a,c,outside}$ or $\tilde{S}_{a,c,FEMA}$. For example, long-period archetypes subjected to FEMA motions relative to inside-Yufutsu-basin motions would see an $\tilde{S}_{a,c}$ increase of 19% from duration, 24 % from spectral shape, and 49% altogether. The separated effects of duration and spectral shape on $\tilde{S}_{a,c}$ for short- and long-period archetypes for the three basins can be found Table 4.3.

4.15 Design Factors

The collapse risk for a structure at a particular location depends on the contributions of a variety of earthquake mechanisms, magnitudes, and distances, each having their own duration and spectral shape. In practice, one could include the effects large-magnitude earthquakes and basins within the combination of a site-specific hazard analysis and nonlinear, time-history analysis using motions consistent with the various sources contributing to the hazard at that site.

For illustrative purposes, the influence of subduction earthquakes exciting basins is evaluated for the hypothetical case in which the seismic hazard is attributable entirely to a single subduction zone earthquake at a particular distance away (i.e., the motions considered in this chapter). In this ideal situation, two structures of the same configuration (e.g., similar structural system, seismic mass, number of stories, story height) would be designed to have the same risk-targeted collapse probability, whether it was located inside or outside a basin and subjected to a large-magnitude subduction earthquake. To account for the influence of basins on collapse, it is necessary to consider: (1) the amplification of spectral acceleration (BAF_{S_a}) in the basin, and (2) the reduction of $\tilde{S}_{a,c}$ between motions inside and outside basins (shown in Figure 13). These two effects can be taken into account by multiplying the strength of structures located inside the basin by the following factor:

$$DF_{basin} = BAF_{S_a} \times \frac{\tilde{S}_{a,c,outside}}{\tilde{S}_{a,c,inside}} \quad (4.8)$$

where the BAF_{S_a} values (Figure 4.9) account for the increase spectral acceleration due to basin effects. The ratio of the two values of $\tilde{S}_{a,c}$ accounts for the differences in ground-motion duration and spectral shape, which affect the spectral acceleration at collapse. Figure 4.21 shows (solid

circles) the DF_{basin} values with respect to period for all 30 archetypes for the three basins. In this figure, the BAF_{S_a} values used for the Yufutsu and Kosen basins are from the M_w 8.3 Tokachi-Oki earthquake, and values used for the Kanto basin are from the M_w 9.0 Tohoku earthquake. This design factor (specifically the ratio of $\tilde{S}_{a,c}$) assumes that design S_a of structures inside and outside basins are similar, as expected for an idealized seismic hazard that does not include basin effects and considers a single earthquake. For periods ≥ 1.5 s, the geometric mean of DF_{basin} is 2.3 for the Yufutsu basin, 2.5 for the Kosen basin, and 1.0 for the Kanto basin.

It is also possible to estimate a design factor, DF , that accounts not only for the effects of deep basins but the combined effects of basins and large-magnitude subduction earthquakes. This factor is derived relative to the expanded 39-motion FEMA set compiled by Haselton et al. (2011b) and used by other researchers. The design factor can be computed as:

$$DF_{\text{basin+sub.}} = BAF_{S_a} \times \frac{\tilde{S}_{a,c,FEMA}}{\tilde{S}_{a,c,inside}} \quad (4.9)$$

where the BAF_{S_a} values are again shown in Figure 4.9. Figure 4.21 (hollow triangles) also shows the $DF_{\text{basin+sub.}}$ values with respect to period for all 30 archetypes. For periods ≥ 1.5 s, the geometric mean of $DF_{\text{basin+sub.}}$ is 2.7 for the Yufutsu basin and 2.5 for the Kosen basin. For periods below 1.5s, the geometric mean of $DF_{\text{basin+sub.}}$ is 2.2 for the Kanto basin which is largely attributable to the BAF_{S_a} values being larger at shorter periods (shown in Figure 4.9c). These basin design factors were computed for archetypical buildings with periods that are shorter (Yufutsu and Kosen basins) or longer (Kanto basin) than where the maximum BAF_{S_a} values occur. The expected design factors would be larger for structures with periods closer to 5-7 s for the Yufutsu and Kosen basins and at periods smaller than 0.4 s for the Kanto basin.

Increases in design spectral accelerations to account for the effects of subduction earthquakes have been recommended by other researchers. Liel et al. (2015) estimated that crustal earthquake (short-duration) motions would have a 60% larger $\tilde{S}_{a,c}$ than subduction earthquakes (long-duration) motions. These differences in collapse fragilities resulted in an 34 % increase in the risk-targeted MCE S_a at 1s for Seattle (Liel et al., 2015). More recently, Chandramohan (2016, Chapter 6) proposed adjustment factors that target uniform collapse risk for structures in earthquake prone regions. These adjustment factors are also hazard consistent (i.e., considering contributions from subduction interface, in-slab, and crustal earthquake sources that are

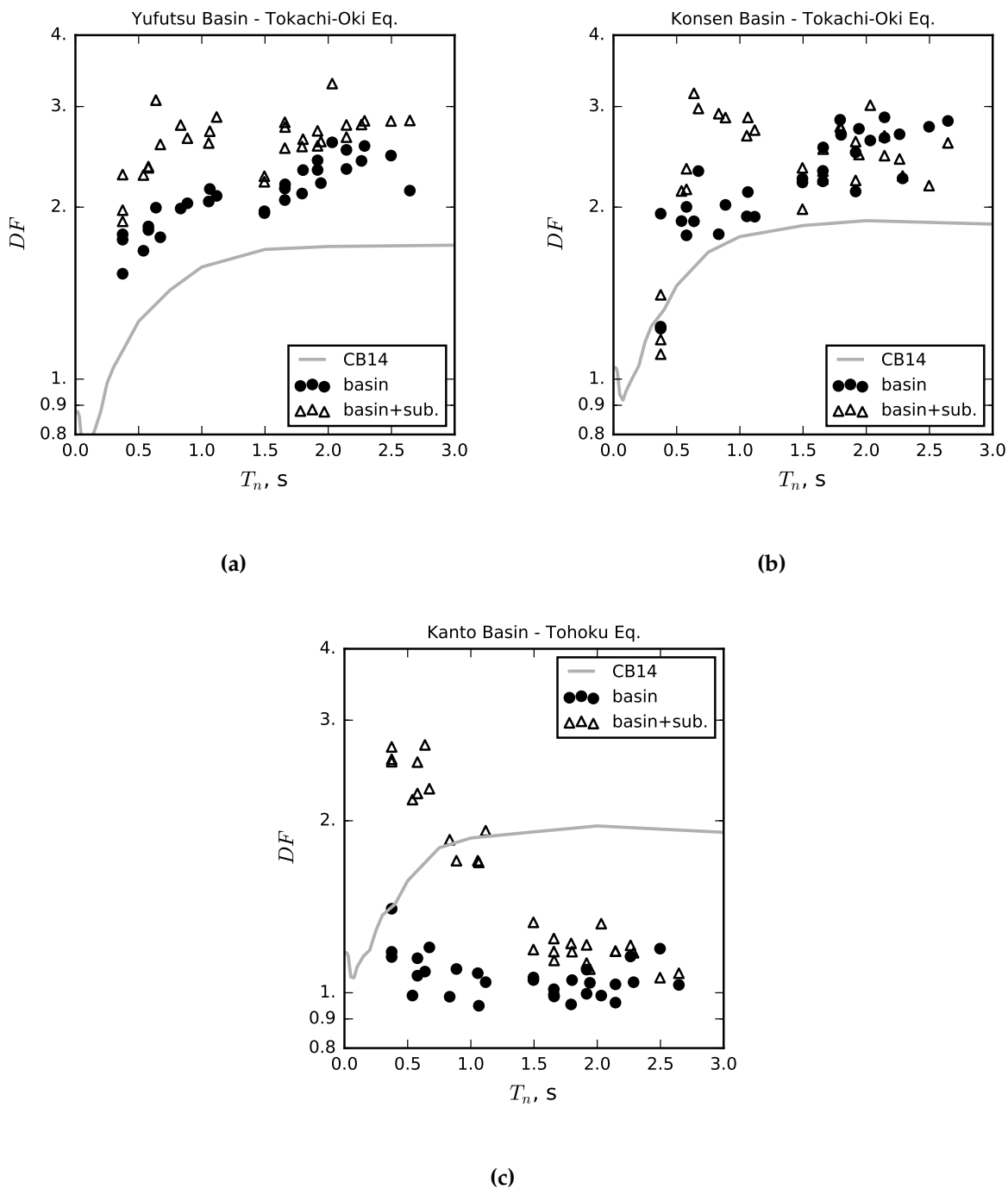


Figure 4.21: Basin design factor with respect to period for the (a) Yufutsu basin, (b) Konsen basin, and (c) Kanto basin.

consistent with the seismic hazard deaggregation) and account for the effects of duration and spectral shape but do not explicitly account for the effects of basins. The adjustment factors result in design strengths that are around 20-29% for 0.2-2 s structures in Seattle relative to structures in Los Angeles. The adjustment factors by Chandramohan (2016) and Liel et al. (2015) are lower because they consider multiple sources (both from crustal and subduction earthquakes) and do not explicitly account for basin amplifications on S_a (BAF_{S_a}).

The DF values computed in this chapter are for situations in which the seismic hazard is controlled by the single subduction earthquake considered here (2001 Tokachi-Oki and 2011 Tohoku). In reality, the appropriate design factor would need to be adjusted considering all possible source mechanisms, magnitudes, and distances that significantly contribute to the seismic hazard (e.g., Liel et al., 2015; Chandramohan, 2016). A site-specific hazard-consistent design factor could be computed using the results from a probabilistic seismic hazard analysis that considers basin effects and multiple intensity measures (e.g., S_a , D_s , and SS_a) which is outside the scope of this chapter.

In addition, this design factor assumes that increasing the design force would proportionally increase the spectral acceleration at collapse. The strength increase might not be proportional if an increase in minimum design strength significantly alters the dynamic properties of the structure. Additionally, the collapse capacity of a structure can be increased using other methods that do not change the structure's strength, such as increasing damping, reducing cyclic deterioration, or altering the stiffness so that the building's period is not amplified by the basin. These design factors have only been computed using SRCMF archetypes and their applicability to other structural systems needs to be evaluated.

4.16 Compariosn with CB14

Recently, Chang et al. (2014) developed design recommendations for tall buildings in the Puget Sound region. These recommendations account for basin effects by amplifying the S_a in the hazard response spectrum using the CB14 basin term (Figure 4.21). To evaluate whether the CB14 basin term would account for the observed effects, the DF_{CB14} basin design factors are computed

using CB14 as:

$$DF_{CB14} = e^{f_{basin}(\tilde{Z}_{2.5,inside})} / e^{f_{basin}(\tilde{Z}_{2.5,outside})} \quad (4.10)$$

where f_{basin} is the basin term (in log-scale) in CB14 and $\tilde{Z}_{2.5,inside}$ is the geometric mean of $Z_{2.5}$ for inside basin records and $\tilde{Z}_{2.5,outside}$ is the geometric mean of $Z_{2.5}$ for outside basin recordings. Figure 16 shows that DF_{CB14} are smaller than both DF_{basin} and $DF_{basin+sub.}$ for almost all structures in the Yufutsu and Kosen basins. For the Kanto basin, almost all values are below DF_{CB14} except at short periods where $DF_{basin+sub.}$ values are larger than DF_{CB14} . Assuming that the Yufutsu and Puget Lowland basins have similar characteristics (based on their similar $Z_{2.5}$, and BAF_{S_a} trends with period), these results suggest that the CB14 basin amplification term may underestimate the effects of the basins within the Puget Lowland region at long periods.

4.17 Chapter Conclusions

The effects of the Yufutsu, Kosen, Kanto, and Niigata basins during large-magnitude subduction interface earthquakes were evaluated in terms of the spectral acceleration, significant duration, and spectral shape. The effects of the basins on structural collapse of a set of archetype structures were computed for the three basins with the strongest shaking.

For all four basins, spectral accelerations consistently increased with increasing basin depth, as characterized by $Z_{2.5}$. This correlation was apparent in the measured spectral accelerations (Figure 4.5) and basin-amplification factors (Figure 4.7) computed from GMM residuals. These factors exceeded 2.0 at periods above 2 s for the Yufutsu, Kosen, and Niigata basins. In contrast, the basin amplification factor for the Kanto basin exceeded 2.0 for periods below 0.3 s. For all four basins, BAF_{S_a} values were insensitive to earthquake magnitude (Figure 4.9).

The spectral acceleration amplification of the basins within the Puget Lowland region during the 2001 Nisqually earthquake was similar for periods above 1.0 s to the amplification observed for the Yufutsu, Kosen, and Niigata basins. Unlike the Japanese basins, the basins within the Puget Lowland region appeared to deamplify spectral accelerations at periods less than 1.0 s.

The correlation between the GMM residual for $D_{s,5-95\%}$ and $Z_{2.5}$ was significant for the Kosen basin (R^2 from 0.20 to 0.56, Table 2), but the correlations were much weaker for the other Japanese basins (R^2 from 0.00 to 0.25).

The shape of the acceleration response spectrum is important because ground motions with acceleration spectra that increase with period tend to be more damaging (Chapter 3). Compared to motions measured outside the basins, spectral shapes (quantified using SS_a) tended to be more damaging (i.e., had larger SS_a values) for motions measured inside the Yufutsu and Kosen basins for a wide range of periods (0.5-4 s; Figure 11). For all four basins, the values of SS_a tended to be larger than those computed for the FEMA set of motions for most periods and basin depths.

For nearly all of the 30 building archetypes (variations of reinforced concrete moment frames), the computed geometric mean of the spectral acceleration at collapse, $\tilde{S}_{a,c}$, was smaller for motions measured within the Yufutsu and Kosen basins than for motions measured outside the basins (Figure 4.20). This reduction in $\tilde{S}_{a,c}$ was attributed to the differences in significant duration and spectral shape, and could be accounted for using a ground-motion intensity measure, IM_{comb} , developed in Chapter 3.

In practice, the seismic hazard for a particular building depends on the contributions of all possible earthquake mechanisms, magnitudes, and distances. For illustrative purposes, the effects of basin on spectral acceleration and on the reduced collapse capacity are combined for the hypothetical case of a frame building subjected only to the types of motions discussed here. To account for both basins and large-magnitude subduction earthquakes (as compared with crustal ground motions used in FEMA P695), the strengths of the frames would need to be increased by a factor of 1.1 to 3.3, depending on the particular archetype and basin.

Chapter 5

GROUND MOTIONS SIMULATIONS FOR AN M9 CASCADIA SUBDUCTION ZONE EARTHQUAKE

5.1 Chapter Overview

Chapter 4 found similar trends in basin amplification on spectral acceleration among three out of the four basin in Japan during subduction earthquakes. While the observed trends were similar, the amount of amplification differed between the three basins. To quantify the amount of basin amplifications expected in the Puget Sound region and address the paucity of recorded interface earthquakes (Chapter 2), Frankel et al. (2018b) and Wirth et al. (2018) simulated a wide range of possible M9 CSZ earthquake rupture scenarios using physics-based ground-motion simulations. This chapter provides a short summary of the physics-based simulations and then characterizes the ground-motion produced from the simulations in terms of spectral acceleration and compares them to spectral acceleration predicted using ground-motion models (i.e., GMM residuals). The variations in spectral accelerations residuals from sites inside and outside the basin are then explained using several basin proxies.

5.2 Ground-Motion Generation

Physics-based ground-motion simulations of an M9 Cascadia subduction zone earthquake were performed by collaborators for a wide range of possible earthquake rupture scenarios. Figure 5.1 shows the research steps that generated the M9 CSZ ground-motions. Prior to generating the ground-motions, a suite of possible M9 rupture scenarios was selected by the seismology team on the M9 Project (discussed in 5.2.1). These simulations were run using a finite-difference code using high-performance computers (discussed in 5.2.2). The results from these simulations were used to generate broadband ground motions (discussed in 5.2.3) which were then studied in terms of several ground motions intensity measures that are known to affect structure response (Sections

5.2.2-5.2.3). Where ground-motion models (GMM) exist, the ground-motion intensity measures were compared to values predicted by the GMM.

5.2.1 *Identifying Rupture Scenarios*

A series of scenarios representing potential M9 CSZ earthquakes were simulated to reflect the uncertainty in rupture characteristics. These scenarios varied in terms of down-dip rupture extent, hypocenter location, rupture slip distribution, and subevent locations. Figure 5.2 shows an illustration for each of the rupture parameters varied within the suite of possible scenarios.

The hypocenter location was varied such that they occurred in the northern, middle, and southern portion of the rupture plane. The variation of the hypocenter location was proportioned so that it was similar to the logic trees used in the CSZ recurrence models to create the United States National Seismic Hazard Maps (Petersen et al., 2015).

The M9 simulations also include areas of high-stress drop along the fault rupture plane. These high-stress drop areas are referred to as $M_w 8$ sub-events and were necessary to generate strong ground shaking, especially at shorter periods (<10 s). Each of the 30 simulations used 5 sub-events that were distributed randomly along the deeper portion of the rupture zone. The sequencing of the subevents varied depending on the hypocenter location.

The long-period shaking (>10 s) was dominated by the background slip along the fault plane. Rupture parameters that affected the back slip were also varied between the simulations, for example, the extent of the rupture plane, and the slip distribution along the rupture plane which both varied (randomly) the travel distance at a particular point along the rupture plane and velocity of the slip. More information about the 3D simulations, the parameters considered and their justification can be found in (Frankel et al., 2018b).

5.2.2 *Finite-Difference Simulations*

Once the rupture parameters are selected, a finite-difference code from Liu and Archuleta (2002) was used by the M9 Seismology Team to simulate scenarios of magnitude-9 Cascadia Subduction zone (CSZ) earthquakes. The simulation used the seismic velocity model of the Pacific Northwest

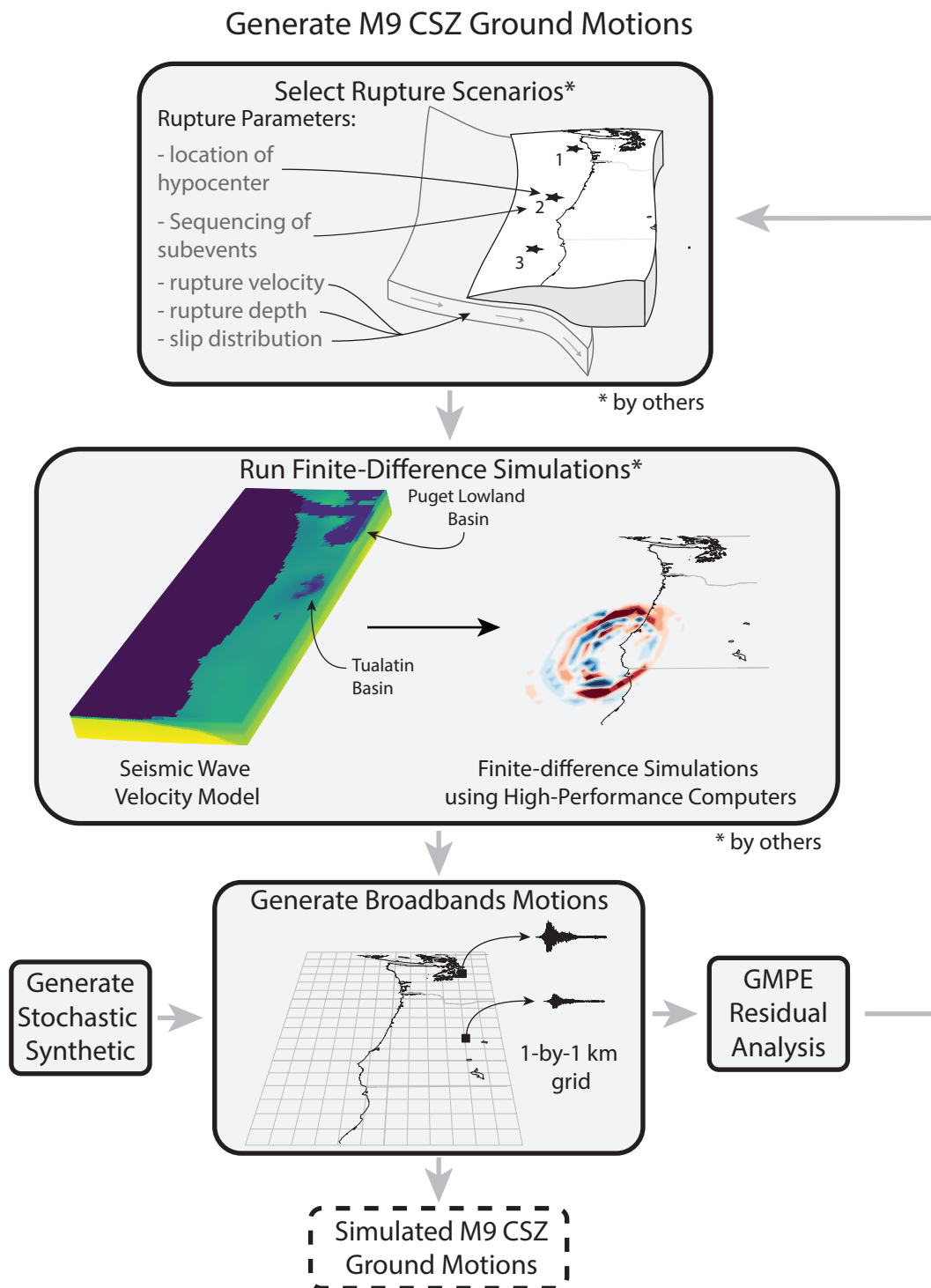


Figure 5.1: M9 CSZ ground-motion generation research plan.

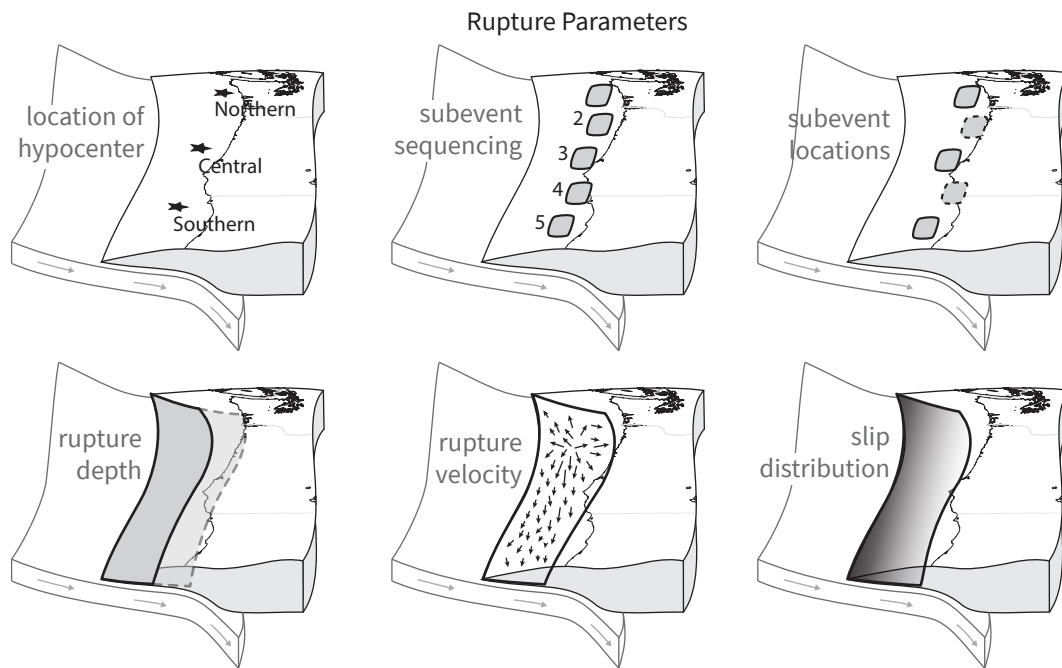


Figure 5.2: Illustration of M9 CSZ rupture variables.

from Stephenson et al. (2017), which includes deep sedimentary basins that underlie Seattle and Portland.

The simulations were performed using high-performance computers at the Pacific Northwest National Laboratory and the Texas Advanced Computing Center (TACC through DesignSafe-CI, 2017). Each simulation generated 500,000 motions on a 1-by-1 km grid spacing for a region from Northern California North to Vancouver Island and from off the West Coast to as far inland as central Washington and Oregon. These recordings were generated deterministically up to a 1hz frequency and generated stochastically at frequencies above 1hz.

5.2.3 Generate Broadband Ground-Motions

The broadband generation procedure combines a high-frequency stochastic signal with the deterministic time series to compensate for the frequency content that is not generated reliably by the finite-difference simulations. This procedure is summarized in Figure 5.2 and is discussed in

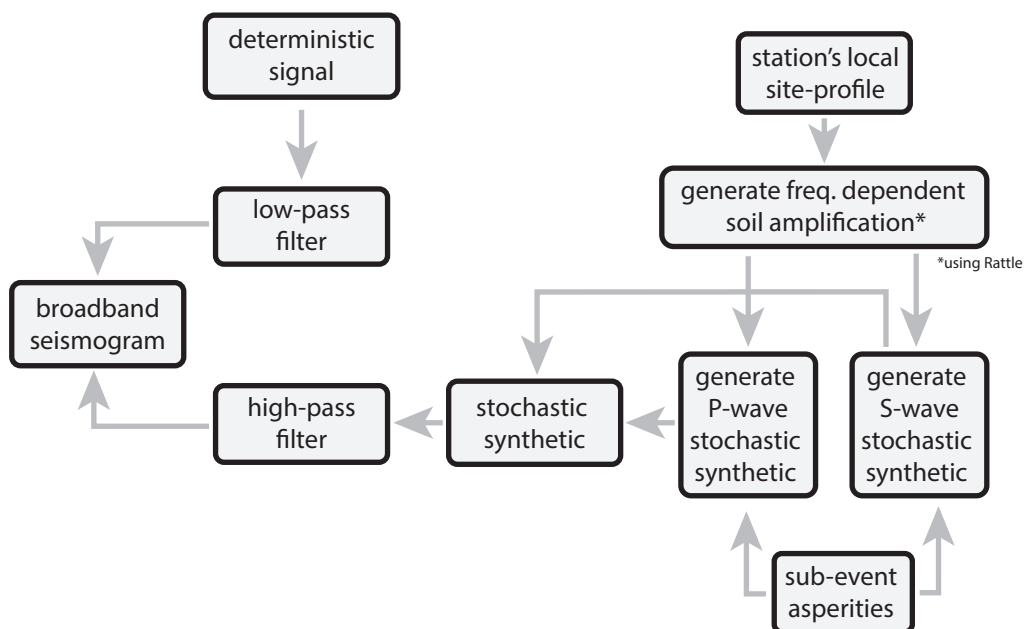


Figure 5.3: Procedure for generating broadband ground motions from the simulated deterministic time series.

more detail by Frankel (2009). The simulated ground motions were generated assuming that all stations are located on a site with the same local-soil profile corresponding to a site class C (NEHRP site classification) with a V_{S30} equal to 600 m/s.

The stochastic synthetics are generated using a method developed by Boore (1983) and implemented using the SMSIM program (Boore, 1996). This program generates the stochastic synthetic by accounting for the site's distance to the rupture plane, the sub-event asperities along the fault rupture plane, and many other parameters that are not discussed here for brevity. The generated stochastic synthetic is then amplified to account for local soil amplifications using frequency-dependent amplification factors determined using the Fortran code Rattle (Boore and Joyner, 1997). These amplifications were determined here using a generic western-US soil profile that corresponds to the site's V_{S30} . The stochastic signals for S- and P-waves were generated separately and then added together to form the stochastic synthetic.

The deterministic and stochastic synthetics were combined by first passing the deterministic synthetic through a phaseless low-pass Butterworth filter, whereas the stochastic synthetic was passed through a similar but high-pass filter. Both filters have a corner frequency at 1hz and are third-order. The filtered synthetics were then summed to create the broadband ground motion. For a single location, generating a broadband ground motion from the simulation results takes several minutes on a single processor, therefore high-performance computers (Hyak) at the University of Washington and the Texas Advanced Computing Center (through DesignSafe-CI) were used to scale-up the broadband generation process to produce ground motions quickly for each realization.

5.3 Spectral Acceleration

In United States building and bridge specifications (e.g., ASCE 7-16, AASHTO 2017) design seismic loads are derived from the spectral acceleration (for a damping ratio of 5%) at the fundamental period of a structure. The suite of thirty simulations were evaluated in terms of spectral acceleration by computing the response spectra for selected locations (5.3.1), evaluating the regional variation in S_a (5.3.2), and comparing the observed S_a from the simulations to that predicted by the GMMs (5.3.3).

5.3.1 Response Spectra

Figure 5.4a shows the geometric mean of the spectral acceleration (S_a) for both horizontal components with respect to period for all 30 realizations for a site in downtown Seattle. At each period, the lognormal mean is denoted with a solid black line, and the dashed black lines denote one standard deviation above and below the mean. For comparison, the design spectrum corresponding to the ASCE 7-16 (2017) risk-adjusted maximum considered earthquake (MCE_R) (assuming Site Class C) is shown with a solid red line.

Figure 5.4b shows the same information as Figure 1a but for a site 73 km south of Seattle (near La Grande, Washington). Ground-motion models (e.g., Abrahamson et al., 2016) predict similar spectral accelerations for the Seattle and La Grande sites for an interface earthquake, because both locations have similar values of closest-distance to the fault-rupture plane (R_{CD}). The differences

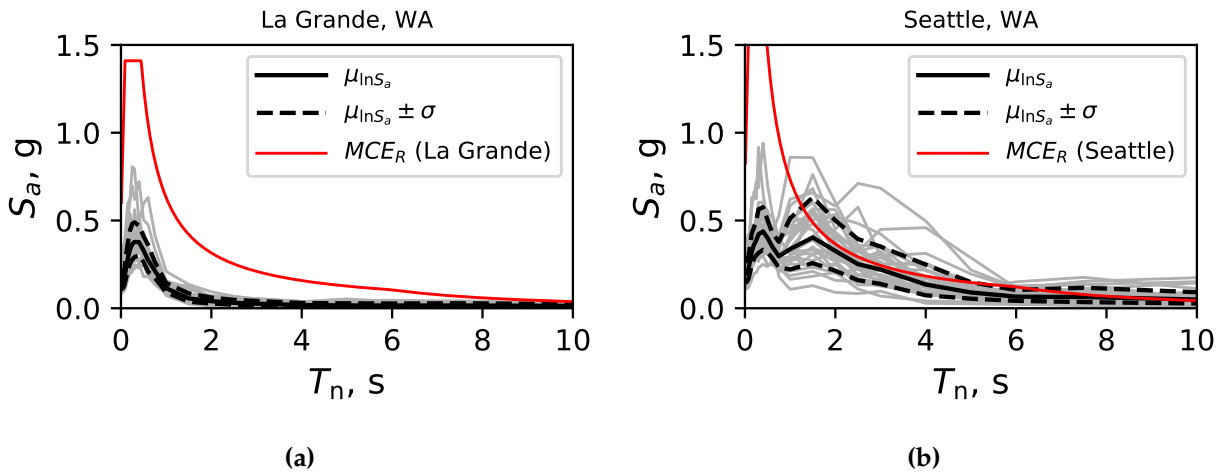


Figure 5.4: Spectral acceleration for both horizontal components for all thirty M9 simulations for (a) Seattle and (b) La Grande. Response spectra corresponding to the risk-targeted maximum considered earthquake for Seattle and La Grande (using the 2014 USGS NSHM) are shown in red.

between the motions simulated for Seattle and La Grande can be attributed mainly to the effects of the deep sedimentary basin that underlies Seattle.

5.3.2 Regional Variation in Spectral Acceleration

This increase in spectral acceleration due to basin effects can also be observed for many locations within the Puget Sound region. Figure 5.5 shows the spectral acceleration with respect to closest distance to rupture (R_{CD}) for (a) 1-second, (b) 3-second, and (c) 5-second period for a particular realization. As expected, the mean intensity of spectral acceleration attenuates with distance as indicated by the negative slope of the black solid line. However, at sites located inside basins (sites with $Z_{2.5} > 3$ km denoted with a plus symbol) their spectral intensity is much larger than the average spectral intensity for stations within a similar R_{CD} (black solid line). This increase in S_a is largely attributed to basin effects.

The regional attenuation due to source-to-site distance and amplification in spectral acceleration due to basin within the Puget Sound region can also be observed through a contour

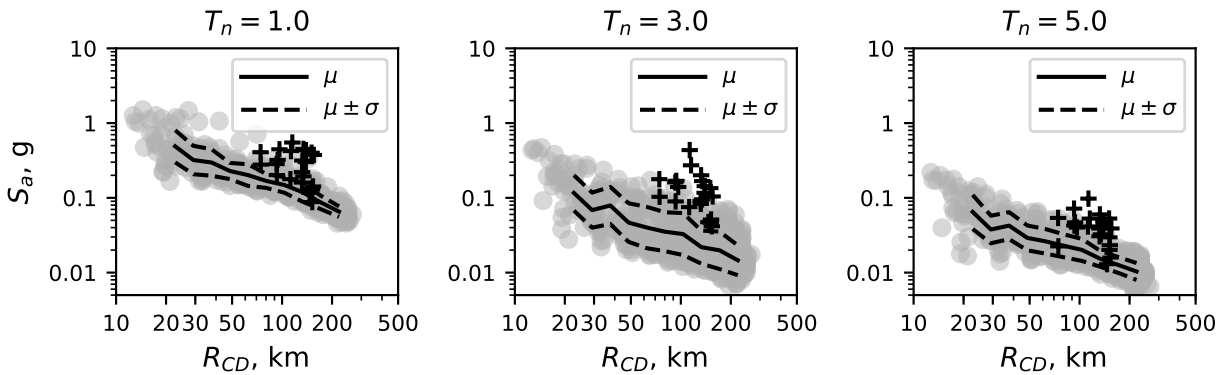


Figure 5.5: Spectral acceleration with respect to distance for non-basin (designated with a grey dot) and basin (designated with a plus symbol) sites for (a) 1.0-second, (b) 3.0-second, and (c) 5-second oscillator periods for a particular realization (*csz006*).

map of S_a . Figure 5.6 shows a contour map of geometric mean of S_a at 0.5-second period and 2.0-second period for all thirty M9 CSZ realizations. As expected, short period spectral accelerations are not amplified by the basin and therefore only reduce in intensity as sites move away from the fault rupture plane. In contrast, at longer periods (2.0-second) the spectral acceleration intensifies near Seattle which is located in the deepest part of the basin (Figure 5.6).

Ground Motion Models (GMM) were used to evaluate whether the simulated ground motions are comparable to recordings from similar earthquakes. These simulations were compared to GMMs by: (1) examining the differences between the simulated spectral acceleration to the GMM prediction for a set of locations, this difference is known as the GMM residual; (2) computing the average residual for the group of locations around the Pacific Northwest (known as the simulation bias); and (3) evaluating the variability of the residuals between-events and within-event and comparing this variability to that observed in GMMs.

5.3.3 Regional Variation in Residual

The GMM residual for spectral acceleration quantifies the difference, in log-scale, between the simulated ground motions and the GMM prediction. For some subduction GMMs, the residual is

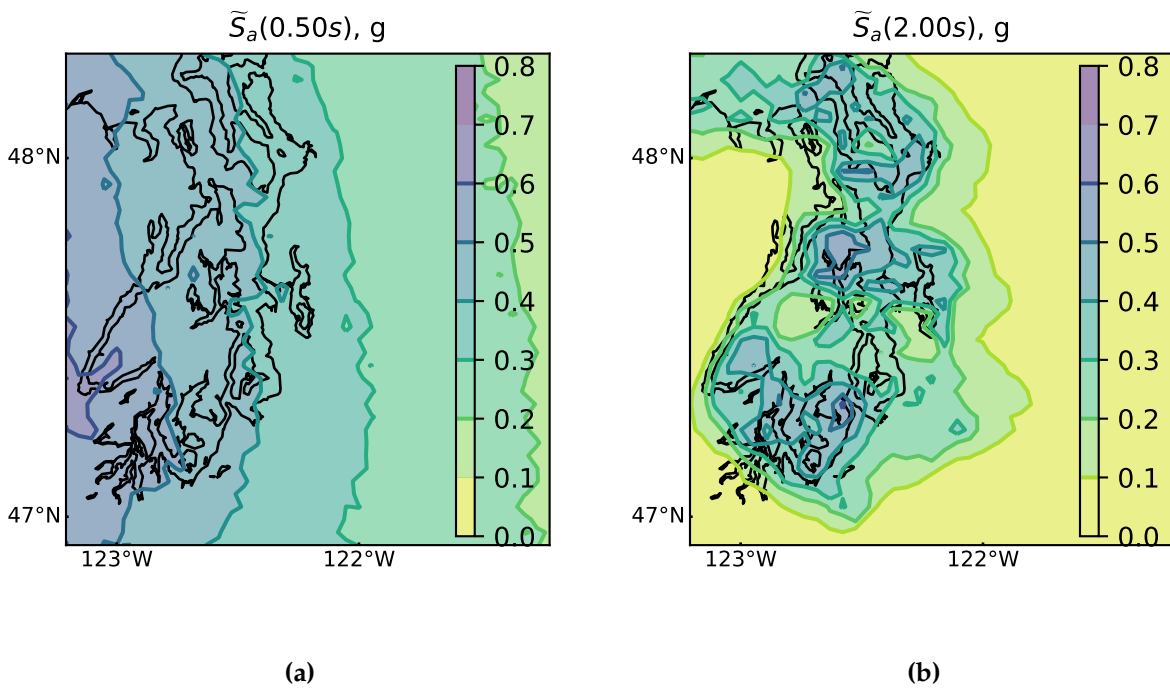


Figure 5.6: Contour map of the geometric mean of the spectral acceleration for all thirty realizations at (a) 0.5-second and (b) 2.0-second period.

always large because the GMM used does not include terms which account for basin amplifications that are known to increase spectral accelerations (e.g., Choi et al., 2005). Here, the BC-Hydro Subduction GMM (2016) is used, which does not include a term to differentiate between inside and outside basin locations. Therefore the inside basin spectral accelerations as computed from the simulation results are expected to be larger than the GMM predictions.

As an example, Figure 5.7 shows a contour map of the average GMM residual for (a) 0.5-second and (b) 2-second spectral acceleration computed using the thirty M9 CSZ realizations. At 0.5-second periods, the GMM residuals are within 0.5 (in terms of $\ln S_a$) for locations with $R_{CD} < \sim 120$ km (i.e., West of -122.5 degree Longitude). However, at long source-to-site distances, the GMM is found to underpredict spectral accelerations M9 simulations. Frankel et al. (2018b) attributes this to the (a) shallow depth of the Cascadia sub-event and (b) the frequency independent Q (quality factor that describes the damping of an oscillator). At 2.0-second periods, the GMM residuals are larger (reaching 2.0) in the Puget Lowland region and Portland region than the surrounding regions. This is due to the basins that underlie the Puget Sound Region (for e.g., Seattle basin) and the Tualatin basin (shown previously in Figure 2.10). Figure 5.8 shows a similar plot to Figure 5.6 but for the Puget Sound region. The maximum residuals are located in areas where the basin is deepest such as the downtown Seattle area.

The mean of the GMM residuals from motions outside the basin was computed for each realization. The mean residual is expressed as the realization bias and is computed using all onshore stations not in sedimentary basins ($Z_{2.5} < 2$ km). The bias can be expressed as,

$$\text{bias} = \frac{1}{N} \sum_{i=1}^N (\ln S_{a,\text{sim},\text{sta}.i} - \ln S_{a,\text{GMM},\text{sta}.i}) \quad (5.1)$$

where N is the number of considered stations, $S_{a,\text{sim},\text{sta}.i}$ is the spectral acceleration computed from the simulated ground motions at a particular station, i, and $S_{a,\text{GMM},\text{sta}.i}$ is the spectral acceleration GMM prediction for a particular station, i. The bias is then computed for several periods and for several realizations for comparison. Figure 5.9a shows the bias with respect to period for each realization. For almost all realizations, the bias are on average within 0.5 (in terms of $\ln S_a$) up to to ~ 7 seconds. At long periods (> 7 s), the bias is constantly larger than 0 for all realizations. The values for bias within simulation were found to be similar with other GMMs. For example, Figure 5.9b shows bias computed with the Morikawa and Fujiwara (2013) GMM.

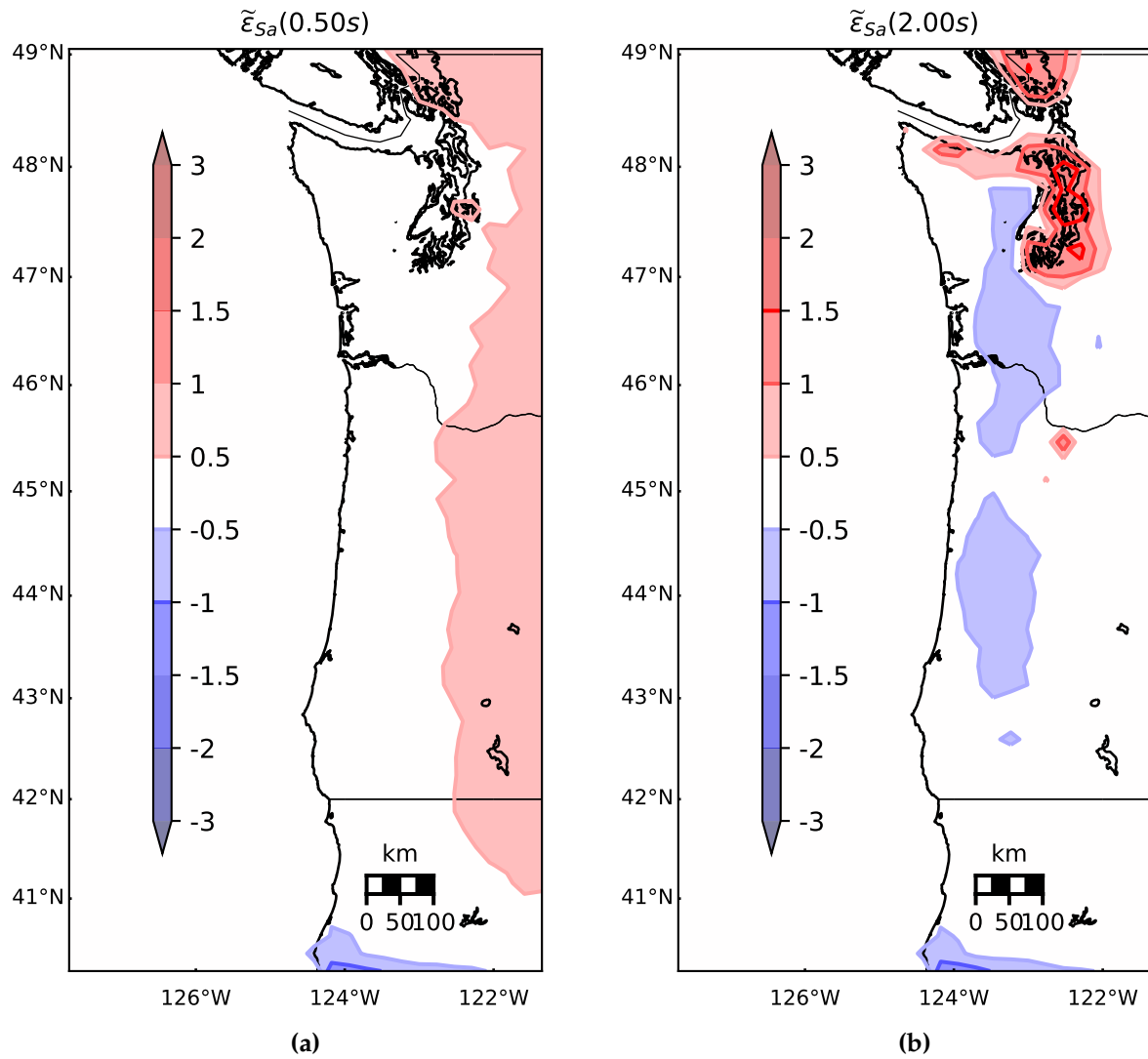


Figure 5.7: Contour map of average GMM residual for S_a at 0.5-second and 2-seconds for all thirty M9 CSZ realizations.

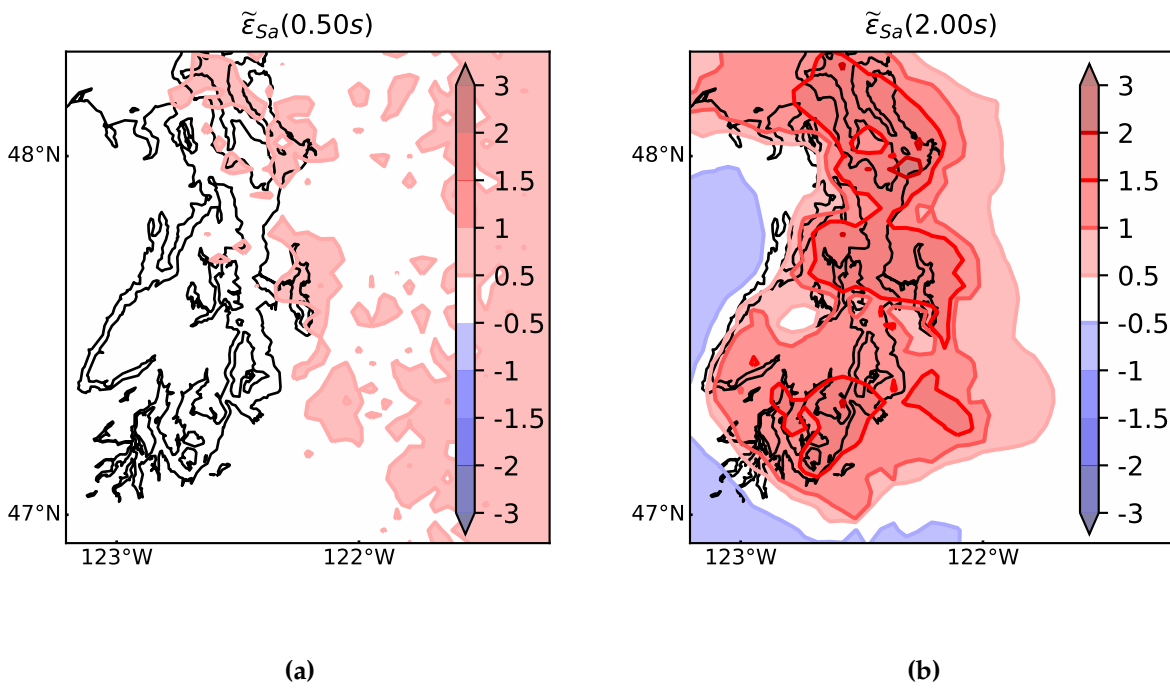


Figure 5.8: Mean GMM (BC-Hydro 2016) residual for all thirty realizations at (a) 0.5-second and (b) 2.0-second period.

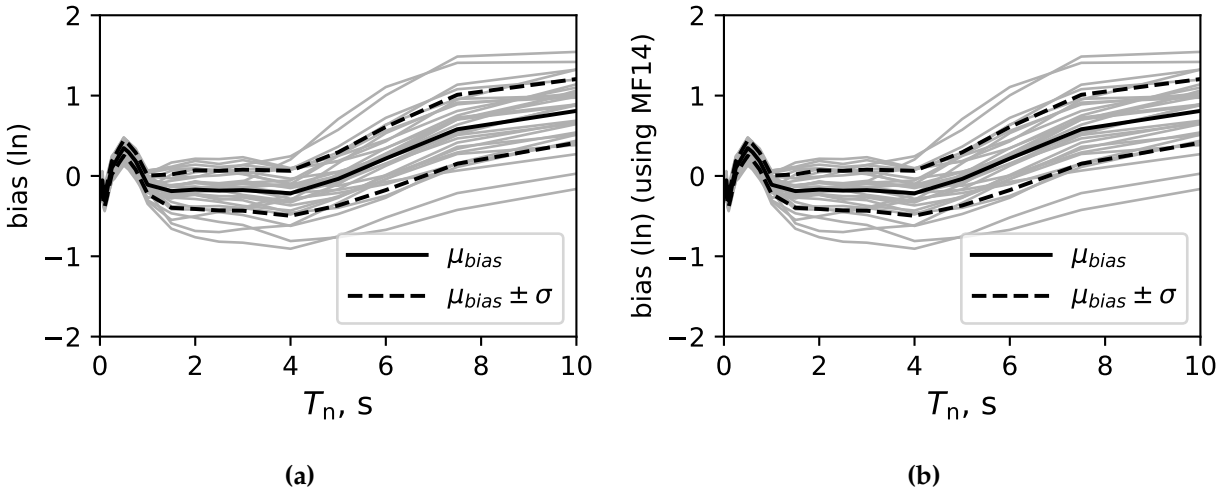


Figure 5.9: Bias (mean residual in natural-log) with respect to period for multiple realizations computed using (a) Abrahamson et al. (2016) and (b) Morikawa and Fujiwara (2013) GMM.

5.3.4 Variation in Within- and Between-Event Residuals

In probabilistic seismic hazard analysis, the variability in S_a prediction in the GMM is important and used to capture uncertainty. Here, the variability in the GMM residual is quantified and compared to the standard deviations observed in BC-Hydro GMM. Figure 5.10 plots the total, within-event (intra-event), and between-event (inter-event) standard deviation in spectral acceleration for the thirty M9 CSZ simulations for all outside basin sites (where $Z_{2.5} < 1.5$ km). Consistent with most GMMs, the within-event standard deviation is smaller than the between-event standard deviations up to 6-seconds. At longer periods, the within-event standard deviation is only slightly larger than the between-event residual. The total standard deviation ranges from 0.42 (at 0.01 s) to 0.79 (at 2 s). The standard deviations are similar to those predicted by BC-Hydro (2016) shown in red on Figure 5.10. For example, at long periods (> 1 s) the standard deviations are in the same range observed in recordings. However, at shorter periods (< 1 s) the standard deviations are much smaller, which is because the same soil profile was used for all sites to generate the stochastic signal (> 1 Hz) portion of the broadband motions (discussed in Section 5.2.3).

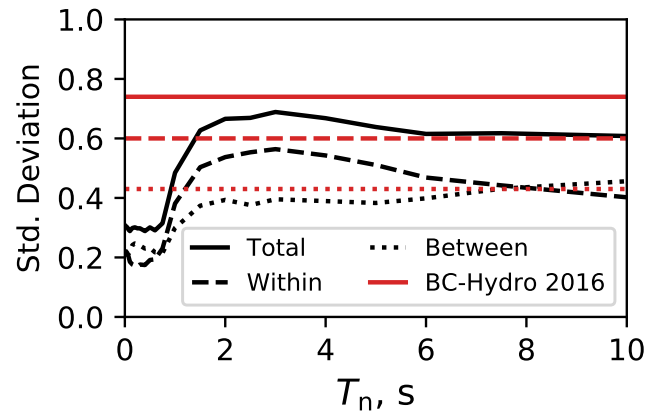


Figure 5.10: Standard deviation of GMM residual for sites that are outside the basin ($Z_{2.5} < 1.5$ km). Total, within, and between event standard deviation as predicted by the Abrahamson et al., 2016 (BC-Hydro 2016) GMM is shown in red.

5.3.5 Correlation coefficients GMM residuals and $Z_{2.5}$, $Z_{1.5}$, and $Z_{1.0}$.

Chapter 4 used the depth to rock with shear-wave velocity (V_S) equal to 2,500 m/s, denoted $Z_{2.5}$, to characterize basin response because that was found to adequately describe the depths of four deep basins in Japan. Here, the variation in GMM residuals is explained using three basin proxies that describe the basin depth. This section uses the three basin proxies, (a) $Z_{2.5}$, (b) depth to rock with $V_S = 1,500$ m/s, denoted $Z_{1.5}$, and (c) depth to rock with $V_S = 1,000$ m/s, denoted as $Z_{1.0}$.

Both $Z_{1.0}$ and $Z_{2.5}$ are featured in four out of the five NGA-West-2 GMMs (Gregor et al., 2014) to predict basin amplifications observed in ground-motion recordings. Others (e.g., Choi et al., 2005; Day et al., 2008) use $Z_{1.5}$ to characterize basin response in California from recordings and 3D physics-based simulations. The regional variation of $Z_{2.5}$, $Z_{1.5}$, and $Z_{1.0}$ within the Puget Sound region is visualized in the contour plots shown in Figure 5.11. The plots show that the both $Z_{1.5}$ and $Z_{1.0}$ outline the Seattle basin, whereas $Z_{2.5}$ outlines the deeper basin that surrounds the Puget Lowland region. Through these contour maps, it is evident that the Seattle basin sits within the deeper basin that surrounds the Puget Sound region.

To find the best predictor of basin amplification observed in the M9 simulations, simple linear regression is used. For all sites within the Puget Sound region (Figure 5.11), the within-event residuals are related to $Z_{2.5}$ (Figure 5.12), $Z_{1.5}$ (Figure 5.13), and $Z_{1.0}$ (Figure 5.14) for 1-second, 3-second, and 5-second periods. The regressed coefficients corresponding to the intercept (β_0) and slope (β_1) for the line of best fit (“trend line”) are also summarized in each figure. The coefficient of determination, R^2 , indicates the percentage of variation of the within-event GMM residual that can be explained with each basin proxy (summarized for each trend line shown in Figure 5.12-5.13).

This regression analyses shown in Figure 5.12 to Figure 5.14 were repeated for a range of periods (0.01-10s), and the regressed coefficients β_0 and β_1 are summarized with respect to period for the three basin proxies on Figure 5.15. As expected, the figure shows that the slope (β_1) of the trend line is positive for all periods above 1-seconds, indicating that the residuals are generally larger as the basin proxy increases. The slopes (β_1) are larger for $Z_{1.0}$ than $Z_{2.5}$ because for the same inside basin region (e.g., Seattle) the values of $Z_{1.0}$ are about ~ 7 times smaller than the $Z_{2.5}$ values, therefore, the slope would need to be ~ 7 times larger to predict the same increase in residual. As expected, the y-axis intercept (β_0) of the trend line is always below zero for periods larger than 0.75s indicating that the default BC-Hydro (2016) prediction is for a site that includes some basin amplification (i.e., the GMM is centered on a site with $Z_{2.5}$, $Z_{1.5}$, and $Z_{1.0}$ greater than zero). The coefficients β_0 , β_1 , and R^2 for all the basin proxies $Z_{2.5}$, $Z_{1.5}$, and $Z_{1.0}$ are summarized in Table 5.1.

More importantly, the amount of variation that can be explained by each basin proxy is captured by the coefficient of determination, R^2 . For most periods corresponding to building structures, the R^2 are large enough to indicate the importance of including basin amplifications in the GMM prediction. The R^2 for each trend line as a function of period is shown in Figure 5.16. For all periods above 1.0-second, the R^2 are larger (up to 0.58 at 2.5 seconds) for $Z_{2.5}$ than $Z_{1.5}$ and $Z_{1.0}$ indicating that $Z_{2.5}$ maybe a better measure for basin amplification than $Z_{1.5}$ and $Z_{1.0}$.

The relationship between the basin proxy and the GMM residuals may not be linear. In fact, the functional forms of basin terms used in most GMMs (e.g., NGA-West-2) are not entirely linear. Therefore, adjusting the functional form of the regression model could result in even larger R^2 values. It should also be noted that the linear models determined here are not constrained at the

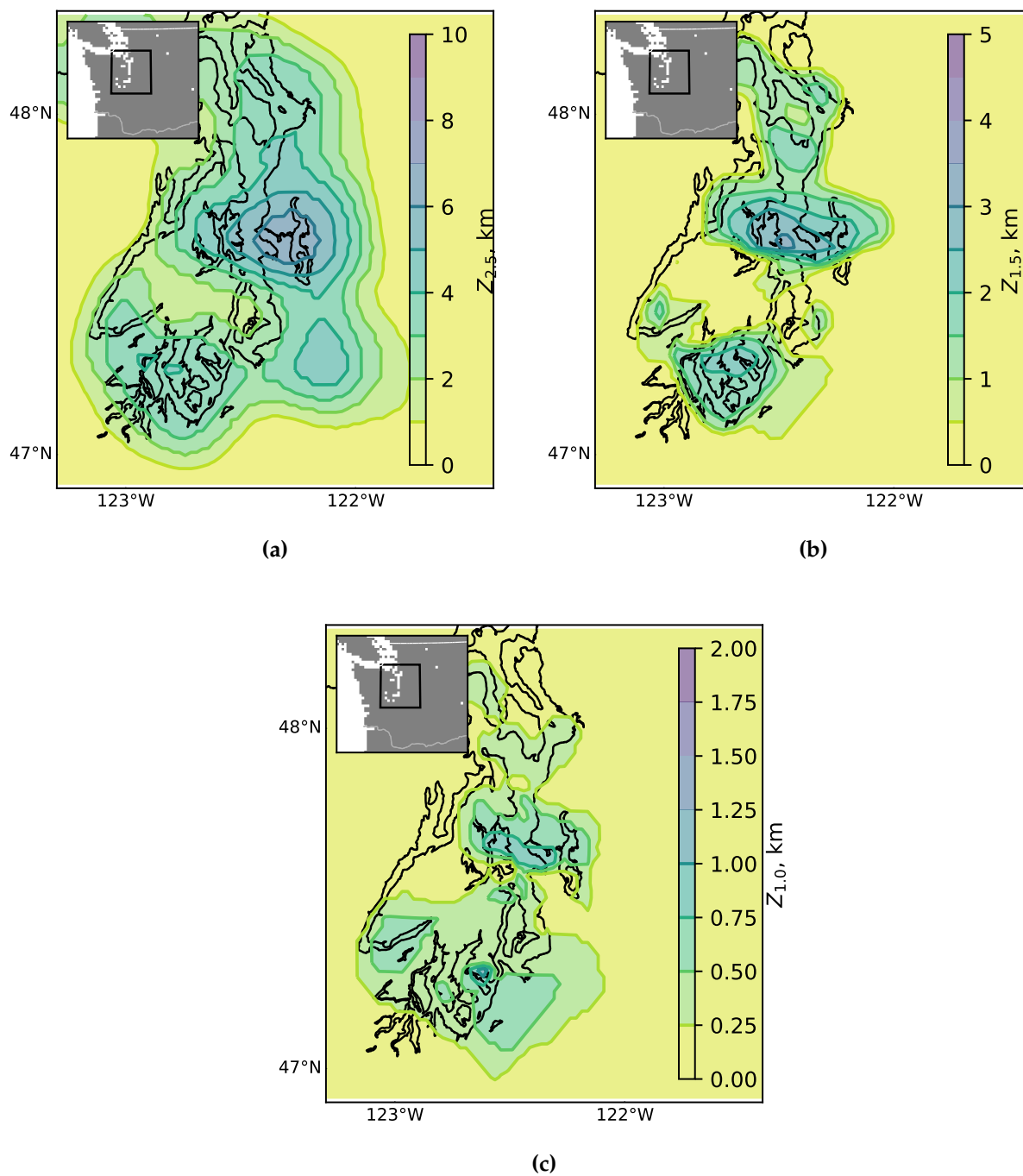


Figure 5.11: Contour map of $Z_{2.5}$, $Z_{1.5}$, and $Z_{1.0}$ for the Puget Sound Region.

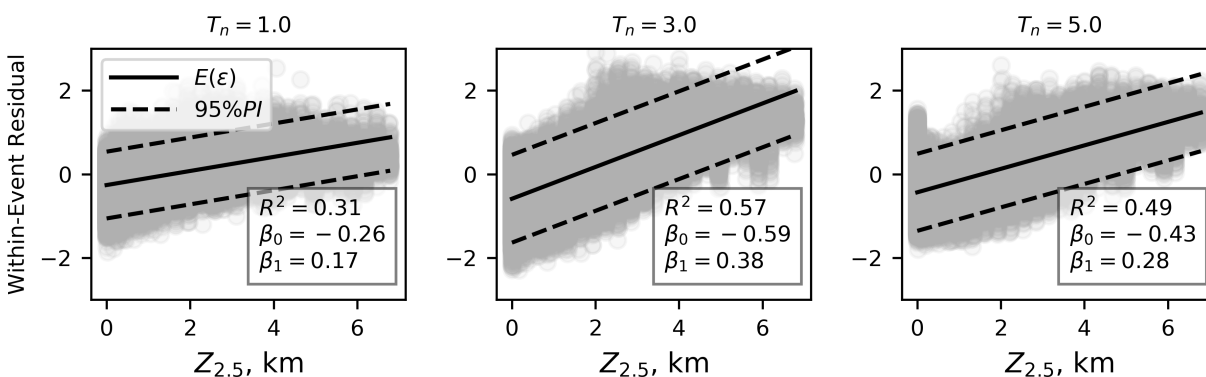


Figure 5.12: Residual with respect to $Z_{2.5}$ for (a) 1.0-second, (b) 3-second, and (c) 5-second periods

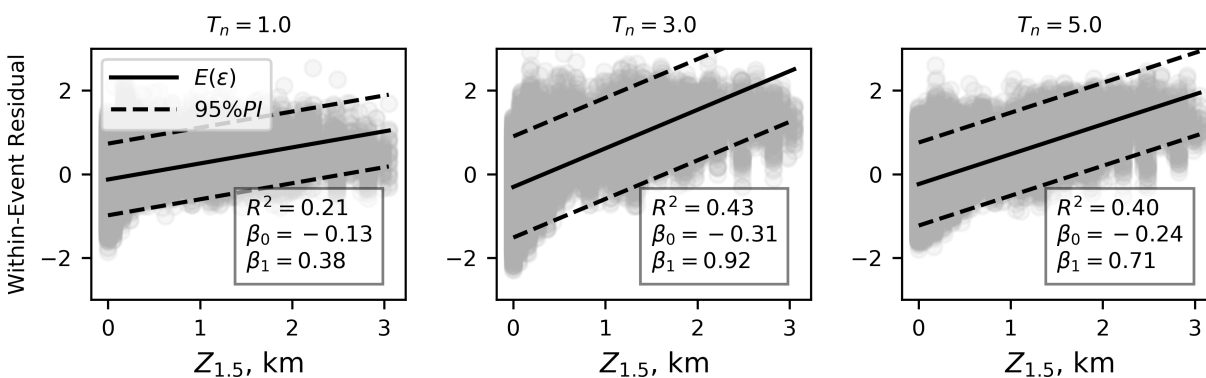


Figure 5.13: Residual with respect to $Z_{1.5}$ for (a) 1.0-second, (b) 3-second, and (c) 5-second periods

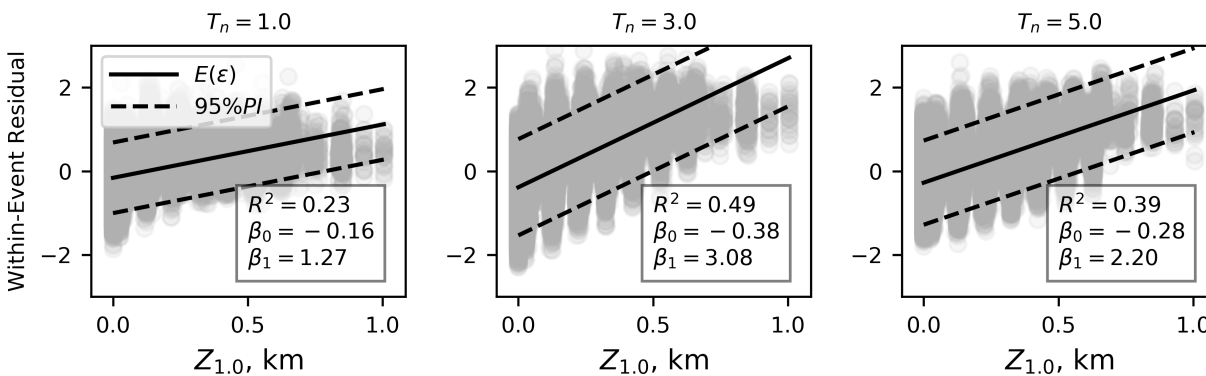


Figure 5.14: Residual with respect to $Z_{1.0}$ for (a) 1.0-second, (b) 3-second, and (c) 5-second periods

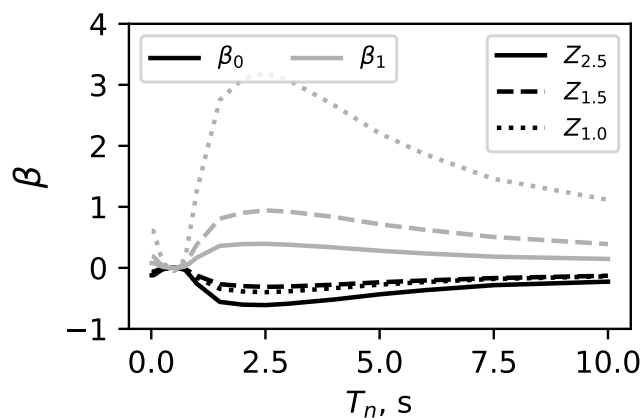


Figure 5.15: The regression coefficients of β_0 and β_1 with respect to period for $Z_{2.5}$, $Z_{1.5}$, and $Z_{1.0}$

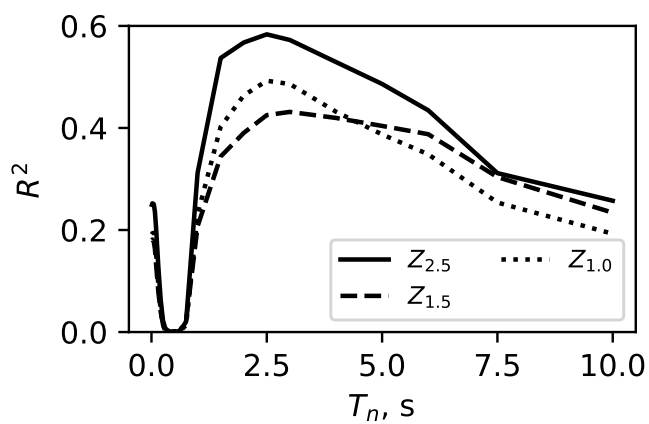


Figure 5.16: The coefficient of determination, R^2 , for the simple linear regression analyses conducted for $Z_{2.5}$, $Z_{1.5}$, and $Z_{1.0}$

extreme ends. For example, Figure 5.14c shows the basin term is over-predicting amplification for all pints with a $Z_{1.0}$ near 1 km. Nonetheless, the data indicate that $Z_{2.5}$ correlates best with basin amplification.

Table 5.1: Results of Simple Linear Regression Analysis.

| Period (s) | Z _{2.5} | | | Z _{1.5} | | | Z _{1.0} | | |
|------------|------------------|-----------|----------------|------------------|-----------|----------------|------------------|-----------|----------------|
| | β_0 | β_1 | R ² | β_0 | β_1 | R ² | β_0 | β_1 | R ² |
| 0.01 | -0.12 | 0.08 | 0.25 | -0.06 | 0.19 | 0.18 | -0.08 | 0.61 | 0.19 |
| 0.02 | -0.12 | 0.08 | 0.25 | -0.06 | 0.19 | 0.18 | -0.08 | 0.61 | 0.19 |
| 0.05 | -0.12 | 0.08 | 0.25 | -0.06 | 0.18 | 0.18 | -0.08 | 0.60 | 0.19 |
| 0.08 | -0.11 | 0.07 | 0.24 | -0.05 | 0.16 | 0.16 | -0.07 | 0.55 | 0.18 |
| 0.10 | -0.10 | 0.06 | 0.20 | -0.05 | 0.14 | 0.13 | -0.06 | 0.49 | 0.15 |
| 0.15 | -0.07 | 0.05 | 0.13 | -0.03 | 0.10 | 0.08 | -0.04 | 0.34 | 0.09 |
| 0.20 | -0.05 | 0.03 | 0.06 | -0.02 | 0.07 | 0.04 | -0.03 | 0.22 | 0.04 |
| 0.25 | -0.03 | 0.02 | 0.02 | -0.01 | 0.04 | 0.01 | -0.01 | 0.12 | 0.01 |
| 0.30 | -0.02 | 0.01 | 0.01 | -0.01 | 0.02 | 0.00 | -0.01 | 0.06 | 0.00 |
| 0.40 | 0.00 | 0.00 | 0.00 | 0.00 | 0.01 | 0.00 | 0.00 | -0.01 | 0.00 |
| 0.50 | 0.01 | 0.00 | 0.00 | 0.00 | 0.00 | 0.00 | 0.01 | -0.05 | 0.00 |
| 0.60 | 0.00 | 0.00 | 0.00 | 0.00 | 0.01 | 0.00 | 0.00 | 0.00 | 0.00 |
| 0.75 | -0.04 | 0.02 | 0.02 | -0.02 | 0.07 | 0.02 | -0.02 | 0.18 | 0.01 |
| 1.00 | -0.26 | 0.17 | 0.31 | -0.13 | 0.38 | 0.21 | -0.16 | 1.27 | 0.23 |
| 1.50 | -0.56 | 0.36 | 0.54 | -0.27 | 0.81 | 0.34 | -0.34 | 2.75 | 0.40 |
| 2.00 | -0.60 | 0.39 | 0.57 | -0.30 | 0.90 | 0.39 | -0.39 | 3.10 | 0.46 |
| 2.50 | -0.61 | 0.39 | 0.58 | -0.31 | 0.94 | 0.43 | -0.40 | 3.19 | 0.49 |
| 3.00 | -0.59 | 0.38 | 0.57 | -0.31 | 0.92 | 0.43 | -0.38 | 3.08 | 0.49 |
| 4.00 | -0.52 | 0.34 | 0.53 | -0.28 | 0.83 | 0.42 | -0.33 | 2.67 | 0.43 |
| 5.00 | -0.43 | 0.28 | 0.49 | -0.24 | 0.71 | 0.40 | -0.28 | 2.20 | 0.39 |
| 6.00 | -0.37 | 0.24 | 0.43 | -0.21 | 0.62 | 0.39 | -0.23 | 1.86 | 0.35 |
| 7.50 | -0.28 | 0.18 | 0.31 | -0.17 | 0.51 | 0.30 | -0.18 | 1.46 | 0.25 |
| 10.00 | -0.23 | 0.15 | 0.26 | -0.13 | 0.39 | 0.23 | -0.14 | 1.11 | 0.19 |

Notes: Changes in collapse probability above 100% are shown in bold.

5.4 Summary

The thirty scenarios of M9 Cascadia Subduction Zone earthquake were generated using physics-based ground-motion simulations. Frequency content below 1 Hz was generated deterministically using 3D simulations, whereas, frequency content above 1 Hz were generated stochastically. The resulting motions from these simulations were evaluated by computing the spectral acceleration values at a range of periods and comparing them to the BC-Hydro (2016) ground-motion model (GMM) predictions. For sites located outside of the basin, the simulations were within 0.5 ($\ln S_a$) of the GMM prediction whereas sites located inside the basin the GMM residuals were much larger because BC-Hydro does not currently include a basin term.

The variation in GMM residuals is large in regions where basins are present (e.g., Puget Sound). This variation was explained using simple linear regression by relating the GMM residual with the three basin proxies, $Z_{2.5}$, $Z_{1.5}$, and $Z_{1.0}$, individually. The $Z_{2.5}$ proxy was found to explain the largest amount of GMM residual variations (i.e., largest R^2 values) for all periods. This indicates that $Z_{2.5}$ best characterizes basin amplification in the Puget Sound region observed from the 3D simulation results.

Chapter 6

IMPACTS OF SIMULATED M9 CASCADIA SUBDUCTION ZONE MOTIONS ON IDEALIZED SYSTEMS

This chapter is based on the following reference:

Marafi, N. A., M. O. Eberhard, J. W. Berman, E. A. Wirth, and Frankel A. D. (2018a). "Impacts of Simulated M9 Cascadia Subduction Zone Motions on Idealized Systems". In: *Earthquake Spectra, In-review*

6.1 Chapter Overview

The previous [chapter](#) showed that the spectral accelerations observed within the simulated magnitude-9 CSZ scenarios are similar to those predicted using ground-motion models for sites located outside basins. For sites located inside basins, the motions were found to be much more damaging in terms of spectral acceleration than expected from ground-motion models. In addition to spectral acceleration, other ground-motion characteristics are important to quantify structural performance ([Chapter 3](#)). The first half of this chapter quantifies the (1) basin amplification factor expected in the Puget Lowland region (similar to [Chapter 4](#)), (2) spectral shape, and (3) ground-motion duration and then compares these characteristics to ground-motions consistent with those used in structural evaluations.

The second half of the chapter studies the effects of the simulated M9 CSZ motions on four sets of deteriorating single-degree-of-freedom oscillators that are representative of idealized systems. The resulting deformation demands and collapse likelihood are studied using a normalized version of the combined-intensity measure from [Chapter 3](#) (effective spectral acceleration, denoted as $S_{a,eff}$) which was found to explain the variability in response between the 30 simulated M9 scenarios and motions that correspond to the risk-adjusted maximum

considered earthquake (using a conditional mean spectra). Finally, the regional variation of damage was estimated by combining probabilistic characterizations of the seismic resistance of structures and of $S_{a,eff}$, which accounts for the effects of spectral accelerations, spectral shape, and ground-motion duration.

6.2 Introduction

Geologic evidence indicates that the Cascadia Subduction Zone (CSZ) is capable of producing large-magnitude, megathrust earthquakes at the interface between the Juan de Fuca and North American plates (Atwater et al., 1995; Goldfinger et al., 2012). Similar subduction regions in Indonesia, Chile, and Japan have produced devastating earthquakes and tsunamis (e.g., Okazaki et al. (2013), Sengara et al. (2006), and Wallace et al. (2012)). The most recent large-magnitude, interface earthquake on the CSZ occurred in 1700 A.D. (Atwater et al., 1995), and according to Petersen et al. (2002), there is a 10-14% chance that a magnitude-9 earthquake will occur along the Cascadia Subduction Zone within the next 50 years.

There is much uncertainty about the characteristics of the ground motions that would result from a large-magnitude, interface CSZ earthquake, because no seismic recordings are available from such an event. Based on motions recorded in other regions, the ground motions are expected to have long durations, and they are likely to be modified by the deep sedimentary basins that underlie the Puget Sound region. The effects of these long durations and the modification of the ground motions by the deep basins are not taken into account by the National Seismic Hazard Maps (NSHMP, 2002 and NSHMP, 2014) that are used in the ASHTO (2017) and ASCE 7-16 (2017) seismic loading provisions.

To compensate for the paucity of recorded interface events, Frankel et al. (2018b) and Wirth et al. (2018) simulated the generation and propagation of magnitude-9 CSZ earthquakes for a range of rupture scenarios. In this chapter, the motions from these simulations (denoted herein as the M9 simulations) are characterized using three intensity measures (spectral acceleration, ground-motion duration and spectral shape) that are known to correlate with structural response (Chapter 4). The ductility demands and potential for causing structural collapse are estimated using four sets of single-degree-of-freedom (SDOF) systems with ductile or brittle properties, and

either high or low strengths. The ductility demands and collapse performance of these SDOF systems are interpreted in terms of a scalar ground-motion intensity measure, $S_{a,eff}$, which combines spectral acceleration, spectral shape, and duration (Chapter 3). Fragility curves developed using this intensity measure are then combined with the simulation results and estimates of structural strength to compute collapse probabilities and ductility demands for idealized structures located throughout the Puget Sound region considering the CSZ hazard.

6.3 Simulations of M9 Cascadia Subduction Zone Earthquake

Frankel et al. (2018b) report the results of 30 physics-based magnitude-9 (M9) CSZ earthquake simulations that were developed as part of a collaboration between the United States Geological Survey and the University of Washington with the support of the National Science Foundation. The 30 realizations represent a variety of magnitude-9 full CSZ rupture scenarios and include variations in hypocenter location, inland extent of the rupture plane, and the location of high stress drop subevents along the fault plane. The extent of the down-dip rupture was varied to be consistent with the logic tree branches for a full-length rupture of the CSZ used in the U.S. National Seismic Hazard Maps (Petersen et al., 2014).

For frequencies up to 1 Hz, the motions were generated using a finite-difference code (Liu and Archuleta, 2002) that uses a 3D seismic velocity model (Stephenson et al., 2017) that reflects the geological structure of the CSZ and the Puget Sound region. This region is founded on glacial deposits that overlay sedimentary rocks that fill the troughs between the Olympic Mountains and the Cascade Mountains. The model also includes several deep sedimentary basins within the Puget Lowland region, including the deepest one which underlies Seattle. Each scenario generated 500,000 motions on a 1-by-1 km grid spacing for a region ranging from Northern California to Vancouver Island, and from off the West Coast to as far inland as central Washington and Oregon. For frequencies above 1 Hz, the motions were generated with a stochastic procedure (Frankel, 2009) assuming a generic rock site profile (Boore and Joyner, 1997) without considering the effects of the basins. To create a broadband motion, the low-frequency and high-frequency components of the simulated motions were combined using a third-order,

low-pass and high-pass Butterworth filter at 1 Hz, respectively. These motions can be retrieved from the following web link: <https://doi.org/10.17603/DS2WM3W>.

Frankel et al. (2018b) generated the ground-motions throughout the Pacific Northwest with the assumption that all grid point locations were located on a site with a time-averaged 30 m shear-wave velocity (V_{S30}) equal to 600 m/s. Most of downtown Seattle is underlain by glacially compacted sediments with V_{S30} equal to approximately 500 m/s. To provide site-specific motions for a representative site in Seattle, the simulated motions were propagated up a one-dimensional soil column with an equivalent-linear, ground response analysis (ProShake, EduPro Civil Systems Inc., 2018). The soil column was comprised of 30, 1-m-thick soil layers, in which the top layer had a shear-wave velocity of 235 m/s and the shear-wave velocity of the deeper layers varied with the 4th root of the depth to the layer. This propagation affected mainly the ground-motion components for frequencies above 1 hz (1 s). For example, at a period of 0.5 s the ratio of spectral acceleration of the propagated motions to that of the input motion was 1.12. At 2.0 s periods, this ratio was equal to 1.02.

6.4 Spectral Accelerations

In United States building and bridge specifications (e.g., ASCE 7-16, 2017, and ASHTO, 2017) design seismic loads are derived from the spectral acceleration (for a damping ratio of 5%) at the fundamental period of a structure. Figure 6.1a shows the geometric mean of the spectral acceleration (\tilde{S}_a) for both horizontal components with respect to period for all 30 realizations for a site in downtown Seattle. At each period, the lognormal mean is denoted with a solid black line, and the dashed black lines denote one standard deviation above and below the mean. For comparison, the design spectrum corresponding to the ASCE 7-16 risk-adjusted maximum considered earthquake (MCE_R) (assuming Site Class C) is shown with a solid red line.

For Seattle, \tilde{S}_a of the M9 simulations are much smaller than the MCE_R design values for periods below 1 second. However, for periods ranging from 1 to 4 s, the geometric mean of the M9 spectral accelerations are just slightly below the MCE_R design values, and the spectral accelerations for many of the simulated motions exceed the MCE_R design values. For example, 43% (13 of the 30) of the M9 CSZ motions exceed the MCE_R values at a period of 2 s. This

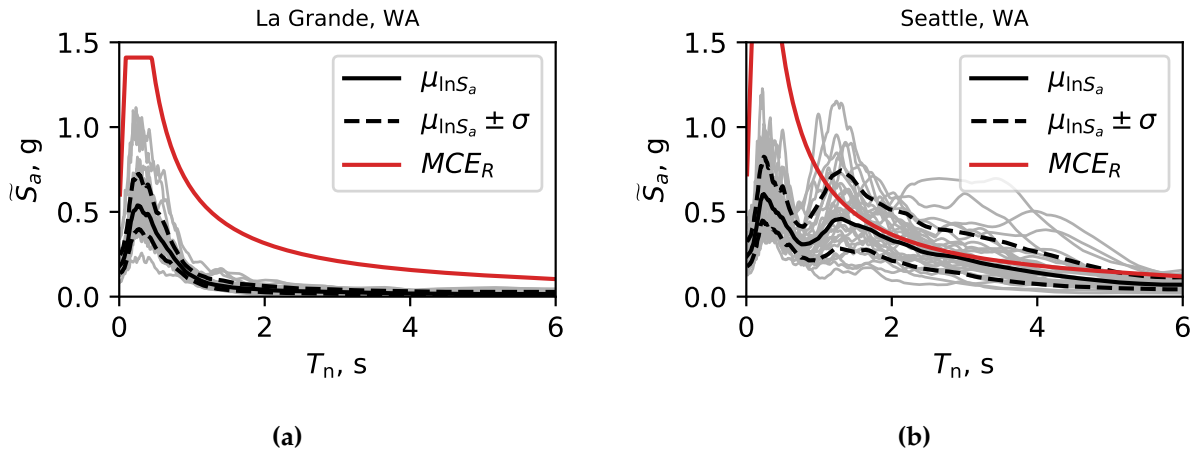


Figure 6.1: Geometric mean of the spectral acceleration for both horizontal components for all thirty M9 simulations for (a) Seattle and (b) La Grande. Response spectra corresponding to the risk-targeted maximum considered earthquake for Seattle and La Grande (using the 2014 USGS NSHM) are shown in red.

exceedance is important, because magnitude-9 interface earthquakes represent only part of the seismic hazard in Seattle, which has large contribution from the Seattle Fault. For example, at a period of 0.5 s, the CSZ full-rupture earthquake (M8.8 to 9.3) contributes 20% of the seismic hazard, and at a period of 2.0 s, it contributes 43%. In addition, the return period for the M9 earthquake is around 500 years, not the 2475 years used in the MCE or even the approximately 2000 years in the MCE_R at a 2 s period USGS (2008). Assuming a Poisson distribution, there would be a 55% chance that five or more M9 earthquakes would occur during the 2475-year design period.

Figure 6.1b shows the same information as Figure 6.1a but for a site that lies outside the basin is 73 km south of Seattle (near La Grande, Washington) for $V_{S30} = 500$ m/s. Ground-motion models predict similar spectral accelerations for the Seattle and La Grande sites for an interface earthquake, because both locations have similar values of closest-distance to the fault-rupture plane (R_{CD}). Indeed, the design spectra (accounting for all sources) for the two locations are within 15% for periods less than 0.5 s. In contrast, for periods greater than 0.5 s, the simulated

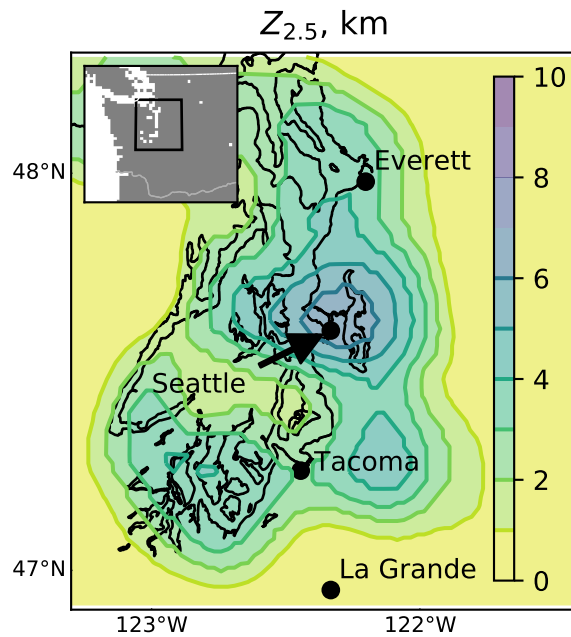


Figure 6.2: Map of $Z_{2.5}$ for the Puget Lowland Region

values of S_a are much lower in La Grande than the motions simulated for Seattle and than the MCE_R values (0 out of the 30 exceed the MCE_R).

The differences between the motions simulated for Seattle and La Grande can be attributed mainly to the effects of the deep sedimentary basin that underlies Seattle. A one-dimensional measure of the basin depth is the depth to very stiff bedrock material with a shear-wave velocity (V_s) of 2.5 km/s, denoted as $Z_{2.5}$. Campbell and Bozorgnia (2014) used this measure of basin depth in their ground-motion model (GMM) for crustal earthquakes. Figure 6.2 shows the variation of $Z_{2.5}$ within the Puget Lowland region in which $Z_{2.5}$ reaches values of 4 to 5 km over a wide area. Seattle and many of its surrounding cities are located in the Seattle basin, a region where $Z_{2.5}$ reaches values up to 7 km. The map shows that there are also shallower basins near Everett (north of Seattle) and Tacoma (southwest of Seattle). In contrast, $Z_{2.5}$ is equal to 0.5 km for the location near La Grande.

The effects of the basin on ground-motion intensity can be visualized by comparing the map of $Z_{2.5}$ (Figure 6.2) with the regional variation of the geometric mean of the spectral acceleration

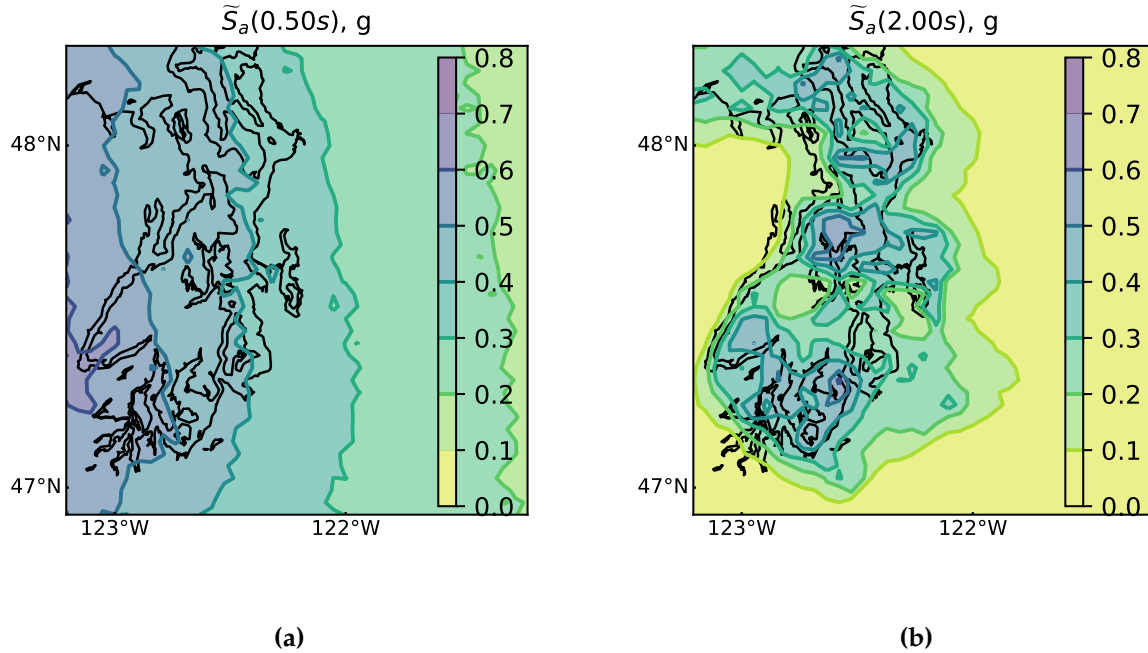


Figure 6.3: Regional variation of geometric mean of S_a for all M9 realizations of the spectral accelerations at periods of (a) 0.5 seconds and (b) 2.0 seconds.

for the two horizontal components (\tilde{S}_a) for the thirty M9 simulations (Figure 6.3) across the Puget Sound region. Figure 6.3a shows that, as expected, the short-period (0.5s) spectral accelerations attenuate consistently with distance from the fault rupture plane (smaller \tilde{S}_a going eastward). In contrast, Figure 6.3b shows that at longer periods (e.g., 2.0 s) the spectral accelerations increase within the Puget Sound Lowland compared to nearby locations, and the spectral accelerations are particularly high for locations in the deepest part of the Seattle basin. \tilde{S}_a is also higher for the Everett and Tacoma basins.

To isolate the impact of the basins on spectral acceleration from the effects of site-to-source attenuation, it is necessary to account for the attenuation of the ground motion with increasing R_{CD} . This was done by normalizing S_a at each site and for each realization by the spectral acceleration calculated with the BC-Hydro (Abrahamson et al. 2016) GMM, $S_a/S_{a,GMM}$. The mean natural log of these ratios (for 30 scenarios), defined as the residuals (ϵ), are plotted in

Figure 6.4 for periods of 0.5 s and 2.0 s. Figure 6.4 shows that the simulated values of S_a at 0.5 s are on average within 0.5 natural logarithm units of the BC-Hydro model predictions over a wide area. In contrast, the values of the spectral accelerations at 2.0 s for the simulations greatly exceed the BC-Hydro GMM values where the basin is the deepest (e.g., Seattle). This large difference (up to a value of $\epsilon = 2.08$, which corresponds to a factor of 8.0) is attributed to the fact that the BC-Hydro GMM does not explicitly account for the effects of basins on S_a . Instead, it takes into account basin depth only to the extent that the basin effects are correlated with V_{S30} . This correlation is significant in some other regions of the U.S. but not in the Puget Sound because much of this region is founded on glacially compacted sediment with high V_{S30} (> 360 m/s) located in deep basins ($Z_{2.5} > 5$ km). It should also be noted that $Z_{2.5}$ is only a crude indicator of basin effects, in reality basin amplifications due to focusing and surface-wave conversion (Choi et al., 2005) may not always occurs in areas with high values of $Z_{2.5}$.

The effect of the basin on spectral accelerations can be quantified (accounting for ground-motion attenuation) in terms of the basin amplification factor, BAF_{S_a} , which is defined as:

$$BAF_{S_a}(Z_{2.5,i}, Z_{2.5,o}) = \left(\prod_{y=1}^Y \frac{S_{a,Z_{2.5,i}}^y}{S_{a,Z_{2.5,i},GMM}^y} \right)^{1/Y} / \left(\prod_{x=1}^X \frac{S_{a,Z_{2.5,o}}^x}{S_{a,Z_{2.5,o},GMM}^x} \right)^{1/X} \quad (6.1)$$

where X is the number of ground-motions for locations with $Z_{2.5}$ approximately equal to (within 0.25 km) the reference value, $Z_{2.5,o}$, and Y is the number of ground-motions where $Z_{2.5}$ approximately equals $Z_{2.5,i}$, and $S_{a,GMM}$ is the spectral acceleration predicted by the GMM at each location. BAF_{S_a} can be interpreted as the geometric mean of the ratio of the measured to predicted spectral accelerations inside the basin (for a particular value of $Z_{2.5}$), normalized by the same quantity for locations with the shallower reference depth to stiff material ($Z_{2.5,o}$).

Figure 6.5 shows the variation of BAF_{S_a} with respect to period for the Puget Lowland region using motions from all thirty M9 CSZ Simulations (shown in grey). The figure shows the geometric mean of BAF_{S_a} (solid black line) and 16th and 86th percentile of BAF_{S_a} (dashed black lines) assuming a lognormal distribution. The values of the basin-amplification term depends on the reference value for $Z_{2.5}$ ($Z_{2.5,o}$). The 2014 USGS NSHM do not explicitly account for variations in $Z_{2.5}$ across the U.S, and many of the GMM models do not have explicit basin terms (e.g., Abrahamson et al., 2016; Atkinson and Boore, 2006). For the Campbell and Bozorgnia (2014)

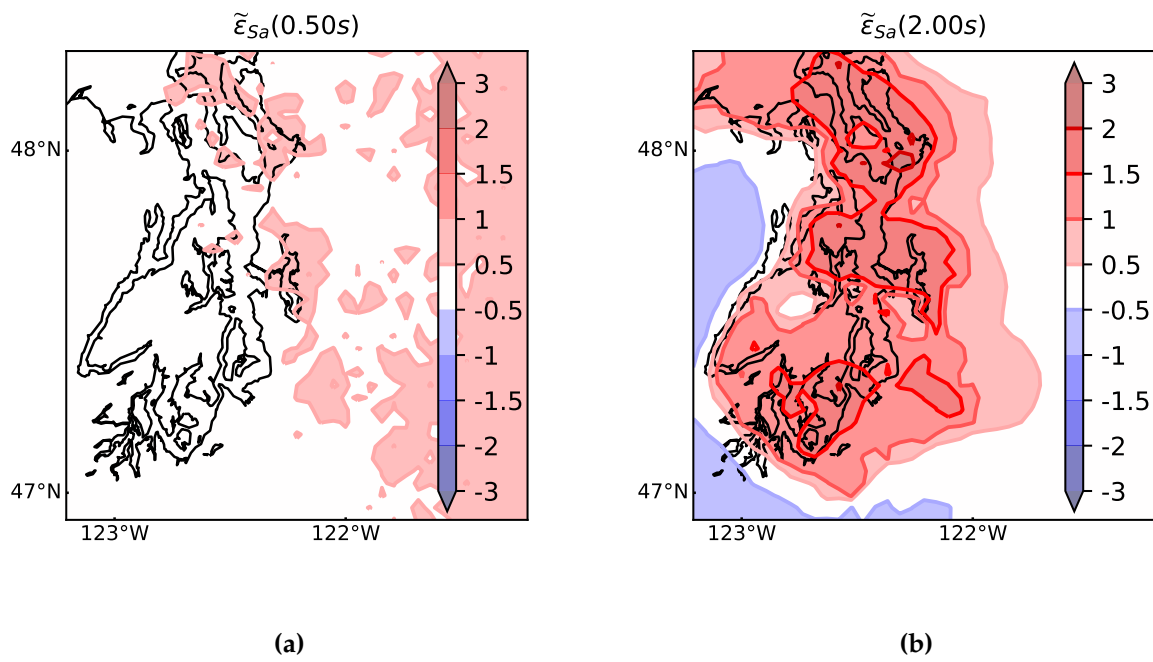


Figure 6.4: Regional variation residual of spectral accelerations (BC-Hydro) at periods of (a) 0.5 seconds and (b) 2.0s seconds for all M9 realizations.

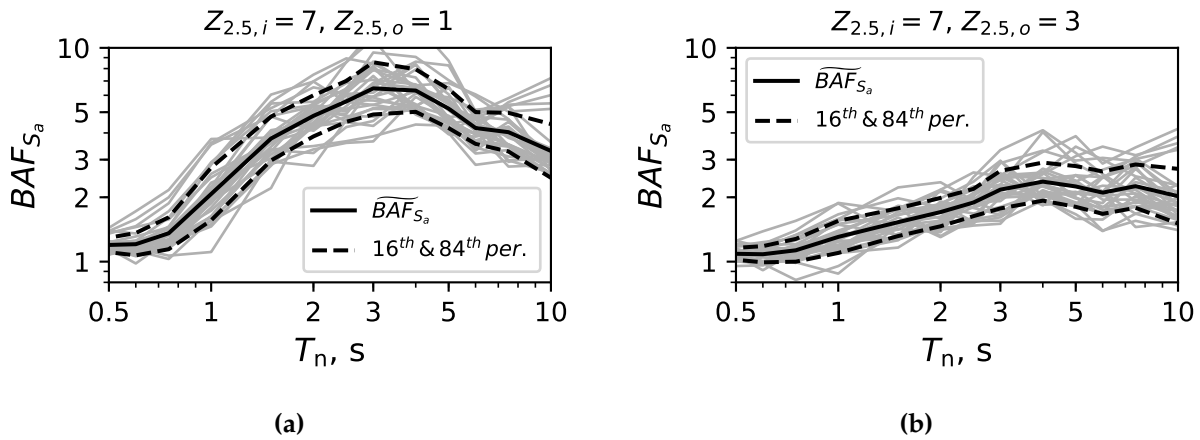


Figure 6.5: BAF_{S_a} for Seattle basin locations within 2 km of the $Z_{2.5,i} = 7$ km contour computed using different reference $Z_{2.5,o}$: (a) locations on the $Z_{2.5}$ contour line equal to 1 km and (b) locations on the $Z_{2.5}$ contour line equal to 3.0 km

GMM for crustal sources, which accounts for $Z_{2.5}$ in their basin term, the basin amplification is equal to 1.0 for $Z_{2.5}$ ranging from 1 to 3 km.

For a $Z_{2.5,o}$ of 1 km (Figure 6.5a), the geometric mean of BAF_{S_a} increases with period reaching a maximum value of 6.5 at 3 s period. For a $Z_{2.5,o}$ of 3 km (Figure 6.5b), the BAF_{S_a} also increases with period but reaches a maximum value of 2.4 at 4 s, around 62% lower than the maximum basin amplification computed assuming a reference $Z_{2.5} = 1$ km.

To demonstrate the combined effects of basin depth and period, Figure 6.6 shows the variation of BAF_{S_a} with period (for constant values of $Z_{2.5,o} = 2$ km/s) and the variation of BAF_{S_a} with $Z_{2.5,i}$ (for constant values of period) for locations within the Puget Lowland (mapped in Figure 6.2). The BAF_{S_a} consistently increases with period up to a period of 5.0 s for $Z_{2.5,i}$ values between 3 and 7 km (Figure 6.6a). The maximum BAF is equal to 3.5 for $Z_{2.5,i} = 7$ km and $T_n = 5$ s. Figure 6.6b shows that BAF_{S_a} increases nearly linearly with $\ln Z_{2.5,i}$ for $Z_{2.5,i}$ exceeding 1.5 km.

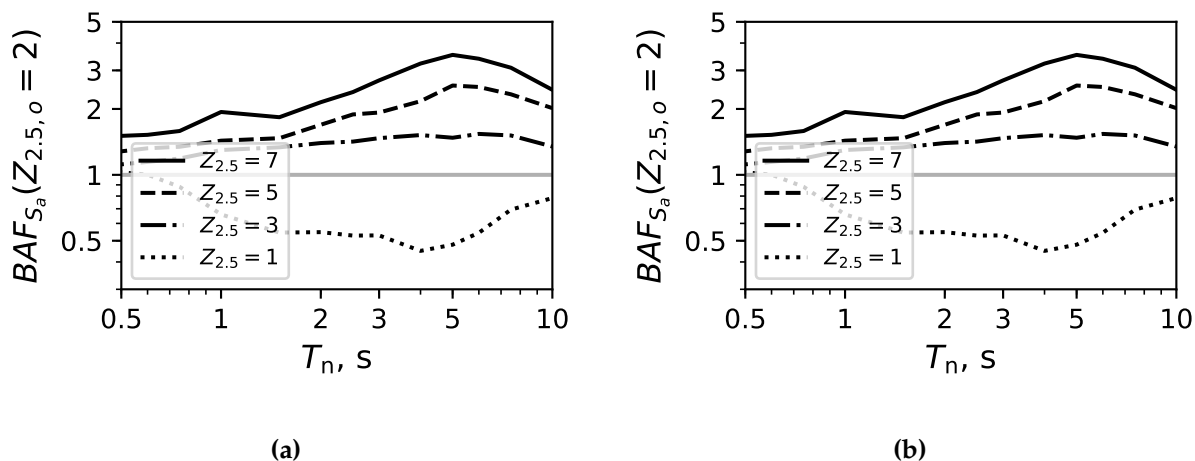


Figure 6.6: Basin Amplification Factors with $Z_o = 2\text{km}$ (a) with respect to period for various $Z_{2.5}$ and (b) with respect to $Z_{2.5}$ for various periods for the Puget Sound region computed using the thirty M9 CSZ simulations.

6.5 Spectral Shape

The effects of the shape of the response spectrum are not typically considered in conventional design. Nonetheless, numerous researchers have found that the shape of the spectrum at periods near the fundamental period of the structure affects the response of nonlinear systems. For example, Newmark and Hall (1982) long ago developed “equal energy” and “equal displacement” rules that recognized that the relationship between elastic and inelastic displacements varies depending on whether the period is in the constant acceleration, velocity, or displacement ranges of the spectrum. More recently, Haselton et al. (2011a) and Eads et al. (2015) and Chapter 3 have shown that spectral shape influences collapse probabilities for structures. Similarly, Deng et al. (2018) developed an intensity measure that accounts for the effects of shape on the ductility demand of a bilinear SDOF system.

Chapter 3 developed a measure of spectral shape, SS_a , that accounts for ductility demand, and the differences in period elongation between brittle and ductile structures. This measure correlated well with the collapse performance for recorded crustal and subduction earthquake

ground motions. The form of the shape measure also makes it possible to evaluate the effect of spectral shape on displacement demands below the collapse level. This measure can be used to evaluate the effects of basins on spectral shape by relating SS_α to $Z_{2.5}$.

SS_α is defined using the integral of the ground-motion response spectrum (damping ratio of 5%) between the fundamental period of the building (T_n) and the nominal elongated period (αT_n). To make SS_α independent of the spectral amplitude at the fundamental period, the integral is normalized by the area of a rectangle with a height of $S_\alpha(T_n)$ and width of $(\alpha - 1)T_n$.

$$SS_\alpha(T_n, \alpha) = \frac{(\int_{T_n}^{\alpha T_n} S_\alpha(T) dT)}{S_\alpha(T_n)(\alpha - 1)T_n} \quad (6.2)$$

where αT_n accounts for the period elongation of the structure. For evaluating the likelihood of collapse, α is taken as $\sqrt{\mu_{50}}$, where μ_{50} is a measure of the system's ductility capacity and is taken as the ductility at the onset of 50% strength loss under monotonic loading. This can be calculated as, $(\delta_c + \delta_u)/(2\delta_y)$, where δ_y , δ_u , and δ_c are the displacements at yield, capping, and ultimate strength, respectively. For evaluating the likelihood of exceeding a target displacement ductility, μ_{target} , the upper limit of the period range is taken as equal to the period derived from the secant stiffness; therefore α is taken as $\sqrt{\mu_{target}}$. Values of SS_α larger than 1.0 indicate that the spectral accelerations increase with increasing period, on average, which is likely to make the ground motion more damaging. Values of SS_α smaller than 1.0 indicate that the spectral accelerations decrease with increasing period.

Figure 6.7 plots the regional variation of the geometric mean of SS_α (computed with $\alpha = \sqrt{13.4}$, as recommended in Chapter 3, and is representative of a ductile system that is discussed in further detail later) for all 30 realizations and both horizontal components for periods of 0.5 s (Figure 6.7a) and 2.0 s (Figure 6.7b). The spectral shapes in Seattle are more damaging (SS_α larger) are more damaging at shorter periods than at longer periods (> 2 s). This is also shown in the response spectra in Figure 6.1a, in which the spectral acceleration in Seattle reaches a maximum at a period of about 1.5s. Periods above that value have lower spectral accelerations on average, which decreases the spectral shape intensity, SS_α . Therefore, SS_α is more likely to be large inside the basin at medium periods (0.5 - 1.0 s) than at longer periods.

The effect of basin depth on spectral shape can be interpreted in terms of the variation of SS_α with $Z_{2.5}$. Figure 6.8 shows the geometric mean of SS_α with respect to period for locations in and

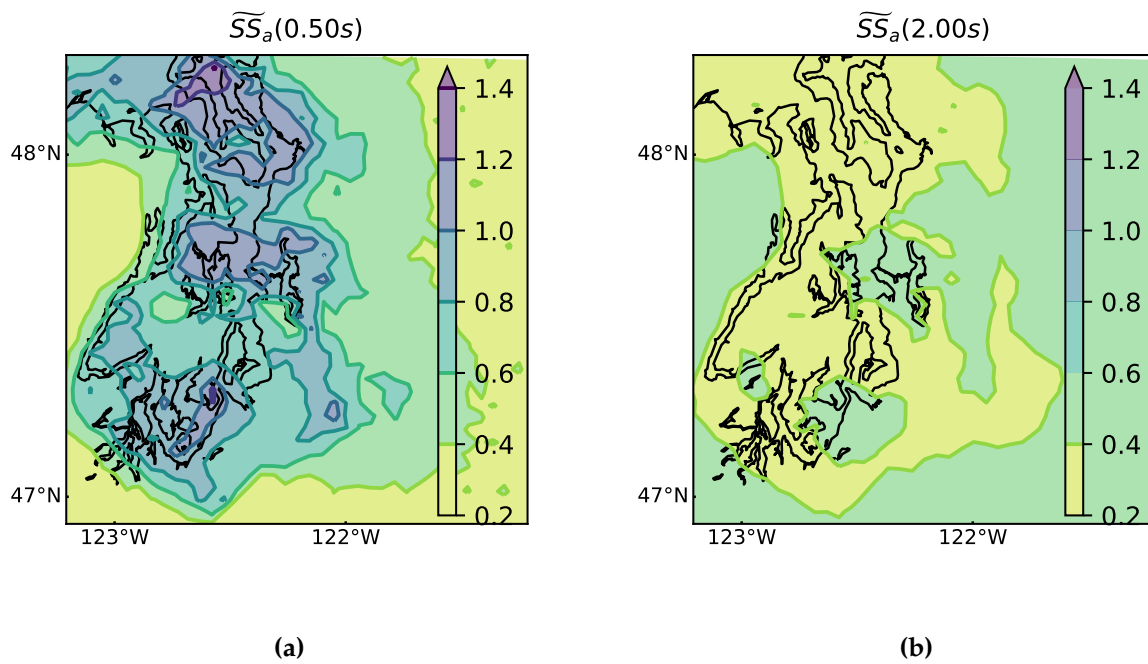


Figure 6.7: Regional Variation of SS_a for a period of (a) 0.5s and (b) 2.0s where α is taken as $\sqrt{13.4}$ and is representative of a ductile system.

around the Seattle basin selected to have $Z_{2.5}$ values equal to: 1.0 km, 3.0 km, 5.0 km, and 7.0 km. To control for the effects of ground-motion attenuation with source-to-site distance, only sites that are within 105 and 125 km (Seattle is around 115 km) from the fault rupture plane (R_{CD}) are included in the values plotted in Figure 6.8. For periods between 0.5 to 1.3 s, SS_a was on average larger in the regions in which $Z_{2.5}$ exceeded 3.0 km in the Puget Lowland region than at locations for which $Z_{2.5}$ was lower ($Z_{2.5} < 3.0$ km). At periods of engineering interest (> 0.1 s), SS_a was largest at 0.75s reaching values of 1.25 for the $Z_{2.5} = 7.0$ km bin.

In performance-based design, nonlinear time history analysis of the structure is typically performed using ground-motions selected to match the conditional mean spectrum (CMS) of the MCE_R earthquake (Baker, 2011). Appendix A discusses the calculation of the conditional mean spectrum. The CMS is meant to represent the expected ground motion spectra conditioned on occurrence of a target S_a (taken as the MCE_R) value at the period of interest (Baker, 2011). In Figure 6.8, the spectral shapes observed in the M9 motions are compared with the corresponding shapes for motions expected in MCE_R , by calculating SS_a from the conditional mean spectrum. The simulated M9 CSZ motions inside the basin ($Z_{2.5} > 3$ km) have larger values of SS_a for all periods up to 5 s. These differences indicate that the spectral shapes of the M9 CSZ motions in Seattle are likely more damaging than motions selected to match the CMS. This could be attributed to the prediction equations for the correlations of spectral accelerations values (Baker and Jayaram, 2008) used to compute the CMS were derived solely from shallow crustal records from a database that consists largely of non-basin sites and sites on shallower basins.

6.6 Duration

Researchers have shown that the duration of the ground motion can affect structural response (e.g., Marsh and Gianotti, 1995; Bommer et al., 2004; Raghunandan et al., 2015; Chandramohan et al., 2016a). For example, Bommer et al. (2004) found that the effects of duration are pronounced in structures that are susceptible to low-cycle fatigue, and undergo strength and stiffness degradation with cyclic loading. Hancock and Bommer (2007) and Chandramohan et al. (2016a) found that significant duration, D_s , correlated well with structural collapse and had the advantage of being scale independent. Significant duration is defined as the time between two target values of the

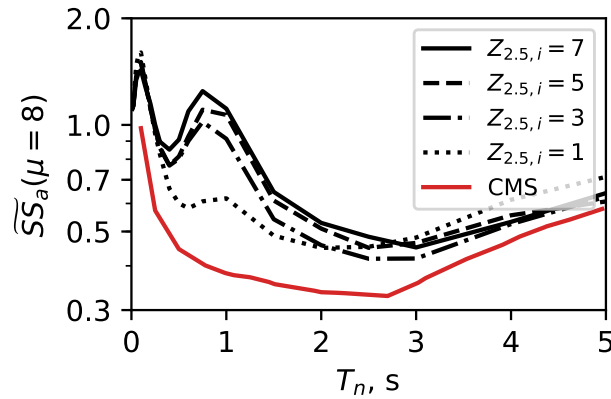


Figure 6.8: The geometric mean of SS_a for various $Z_{2.5}$ bins with respect with period.

integral, $\frac{\int_0^t a_g(t)^2 dt}{\int_0^{t_{\max}} a_g(t)^2 dt}$, where a_g is the ground acceleration and t_{\max} is the total duration of the record. This chapter uses significant duration computed at the 5-95% thresholds, $D_{s,5-95\%}$.

For subduction interface earthquakes, GMMs are not available for $D_{s,5-95\%}$. However, $D_{s,595\%}$ is known to increase with earthquake magnitude, extent of rupture plane and site-to-source distance (Afshari and Stewart, 2016). Figure 6.9 shows the regional variation of the geometric mean of $D_{s,5-95\%}$ for all thirty M9 realizations. As expected, $D_{s,5-95\%}$ increases with distance from the fault rupture plane (moving eastwards). The duration does not vary consistently with $Z_{2.5}$. For example, both the Seattle and La Grande ground-motion sets had $D_{s,5-95\%}$ geometric mean values near 110 s, for the full broadband motions, and for the deterministic motions (long-period) component of the motions. The effects of basins on other duration metrics (e.g., bracketed duration) were not considered here and need to be studied.

6.7 Representative SDOF Systems

Four sets of single-degree-of-freedom systems were used to evaluate the impacts of the M9 CSZ motions on structural collapse and deformation demands. Each of the system sets had combinations of the ductility at maximum force, μ_{cap} , and the force reduction factor, R , corresponding to: (1) low-strength and brittle, (2) high-strength and brittle, (3) low-strength and

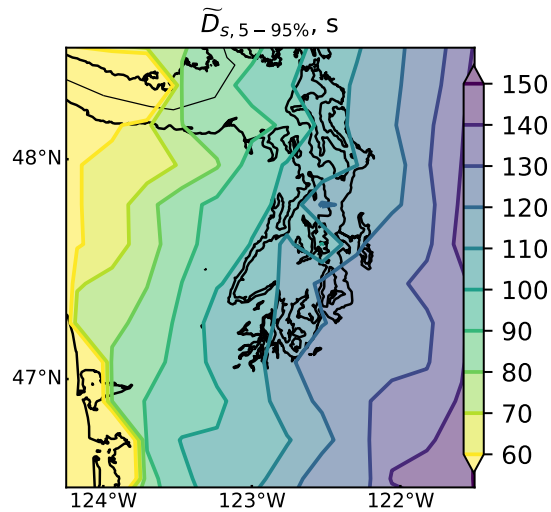


Figure 6.9: Regional variation of the geometric mean of the $D_{s,5-95\%}$ for all thirty M9 CSZ realizations.

ductile, and (4) high-strengths and ductile. A value of μ_{cap} equal to 3 was selected for the brittle systems, and 8 for the ductile systems. Similarly, R was equal to 3 for the high-strength systems, and R was 8 for the log-strength systems. Fourteen periods, varying from 0.25 to 5s, were considered for each of the four system sets.

The systems were modeled using a nonlinear spring with 5% Rayleigh damping (*OpenSees*, McKenna, 2016). The spring material model used the Modified Ibarra-Medina-Krawinkler Deterioration Model with the Peak-Oriented Hysteretic Response (abbreviated as the IMK model, Ibarra et al. 2005). Figure 6.10 illustrates the backbone and cyclic properties of the spring. The normalized yield strength, η , is computed as,

$$\eta = F_y/m = \Omega S_{a,DBE}/R \quad (6.3)$$

where Ω accounts for design and material overstrength typically observed in buildings, taken as 1.5 (Luco et al., 2007, 2009 NEHRP provisions). $S_{a,DBE}$ is the design spectral acceleration at each site determined in ASCE 7-16 (which references the 2014 USGS NSHM) for NEHRP Site Class C, m is the system's mass, and R is the design response modification factor.

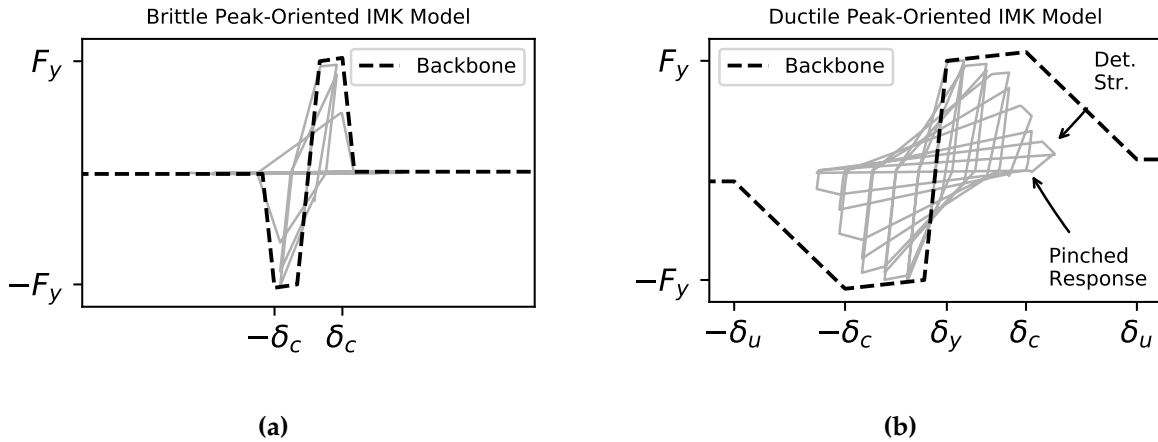


Figure 6.10: Deteriorating SDOF system backbone and cyclic force-displacement response for (a) brittle and (b) ductile system.

The post-yield stiffness of the system was assumed equal to 1% of the elastic stiffness. The system reached capping strength at μ_{cap}/δ_y (denoted as δ_c in Figure 6.10). After reaching the capping strength, the systems had a negative stiffness of $\alpha_{PC}k$, where α_{PC} was equal to 0.1 and 0.5 for ductile and brittle system sets, respectively. The backbone flattened" (i.e., zero stiffness) once the descending branch reached κF_y where κ is taken as near-zero. The IMK model material parameters that control cyclic deterioration α_s , α_c , and α_a were set to $100\delta_y$ for the ductile systems and $25\delta_y$ for the brittle systems, similar to the ranges considered in Ibarra and Krawinkler (2011). For both the brittle and ductile systems, the deterioration parameter α_k was set equal to $2\alpha_s$.

The material model has a pinched hysteretic response that is typically observed in reinforced concrete frames and walls, and steel braced frames. The force-displacement response of the system after cycling can be much lower than the non-deteriorated" backbone (shown as black-dashed line in Figure 6.10), because the system strength deteriorates based on the amount of energy dissipated in previous cycles (Ibarra and Krawinkler, 2011) as controlled by the α parameters above.

6.8 Drift Demands

The four system sets (variations of μ_{50} and R) with fourteen initial periods were subjected to the 30 pairs of ground motions from the M9 simulations for Seattle and La Grande. To compare these motions to those expected from the MCE_R design earthquake, the systems were also subjected to 100 motions selected to match the Seattle CMS for each system period. The CMS set includes ground-motions from crustal, intraslab, and interface earthquakes, all of which control a portion of the seismic hazard for Seattle. Appendix A summarizes the procedure used to select and scale the ground-motions to match the CMS for Seattle.

At each period, Figure 6.11 shows the median ductility demand for each combination of system set and motion set. For all four sets of systems, the median deformation demands for Seattle motions exceeded the CMS demands for all periods above 1s. At a period of 2s, the difference in demands ranged from about 40% (both low-strength- and high-strength-ductile systems) to about 44% (high-strength-brittle systems). The difference in ductility demands between the CMS and Seattle motions for the weak-brittle system was extremely large ($> 100\%$), because the majority of the systems collapsed.

As expected, the deformations of the high-strength-ductile ($R = 3$, $\mu_{cap.} = 8$) systems were far smaller than their deformation capacities for all motion sets. This combination of structural properties, e.g., high strength and ductility, would be rare. At the other extreme ($R = 8$, $\mu_{cap.} = 3$), the weak-brittle systems reached ductility demands larger than $\mu_{cap.}$ for all periods below 2.0-2.5s for both the CMS motions and the Seattle M9 motions. These systems would not be representative of modern practice, because structures with low ductility capacities (e.g., without ductile detailing) would not be designed with large force-reduction factors (e.g., $R = 8$). However, such combinations might be expected for some older structures.

The high-strength-brittle ($R = 3$, $\mu_{cap.} = 3$) and weak-ductile ($R = 8$, $\mu_{cap.} = 8$) system sets are more representative of modern practice. For the high-strength-brittle set, the ductility demand exceeded the capacity only near a period of 1.25 s, but for periods ranging from 1.5-2.5s, the demands were near the capacity. The median demands for low-strength-ductile system set greatly exceeded their capacities for periods between 0.5s and 1.5s.

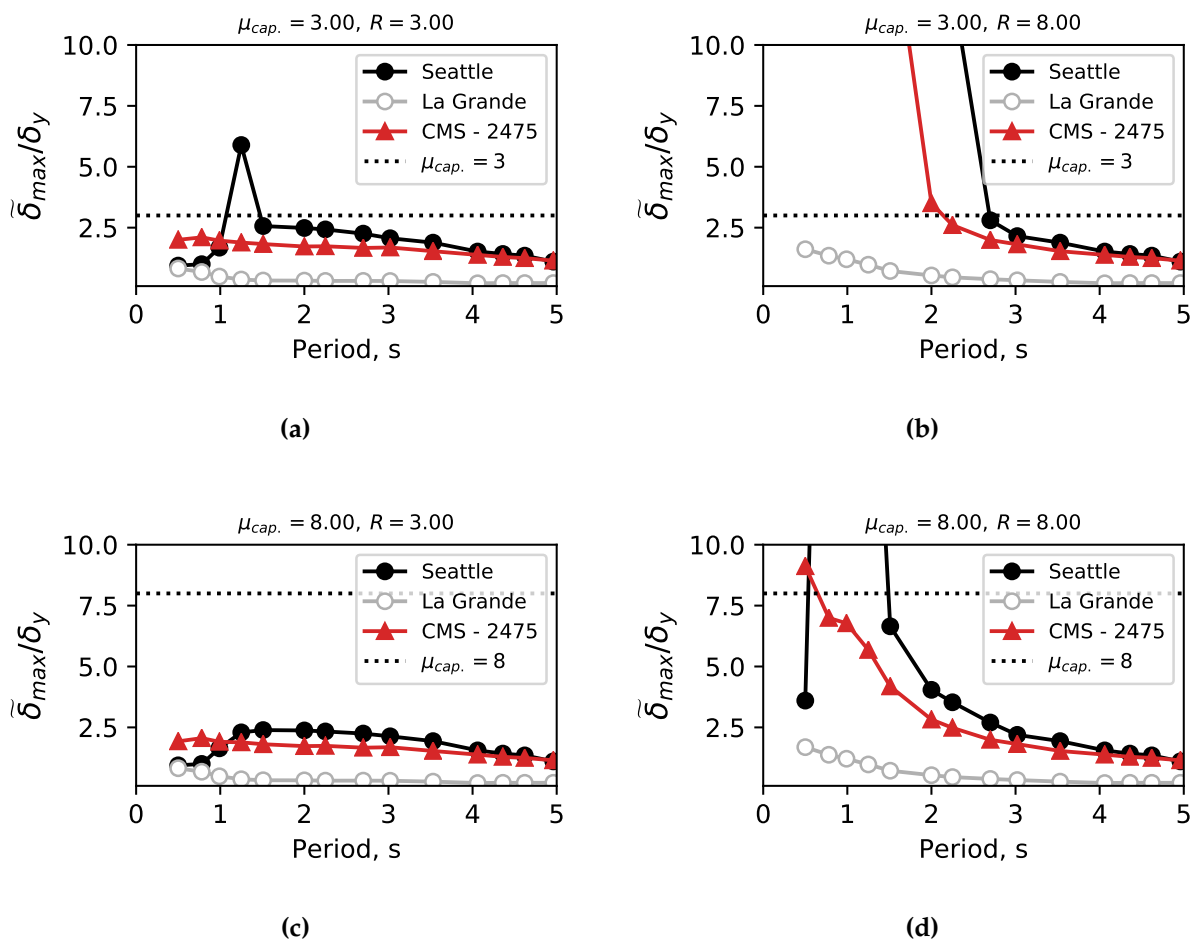


Figure 6.11: Drift demands for SDOF systems with response to period subjected to M9 Motions at Seattle and La Grande and motions selected to match the CMS for (a) low-strength-brittle, (b) high-strength-brittle, (c) low-strength-ductile, and (d) high-strength-ductile deteriorating SDOF systems.

In contrast, the motions simulated for La Grande imposed ductility demands much smaller than $\mu_{cap.}$ for all periods for all four system sets, even the low-strength-brittle combination. This result indicates that structures with a wide range of force-deformation properties would likely be capable of withstanding the expected M9 shaking in La Grande and similar sites outside the basins.

6.9 Collapse Potential of Ground Motions

The potential of the Seattle M9 and CMS motions to cause collapse differed greatly. To evaluate the collapse potential of each ground-motion set, each ground-motion was scaled in increments of $0.1S_a/\eta$ (where $\eta = F_y/m$) until each of the systems collapsed (i.e., incremental dynamic analysis). Figure 6.12 shows the resulting fragility functions that predict the probability of collapse for brittle and ductile systems conditioned on S_a/η (the ratio of the elastic demand to capacity). The fragility functions computed for the Seattle-M9 and CMS ground-motion sets are shown separately.

For both the brittle and ductile systems, the fragility curves for the two motion sets differed greatly. For example, the value of S_a/η that corresponds to a 50% likelihood of collapse of the brittle system set (Figure 6.14a) is 4.1 for the CMS motions and 2.2 for the Seattle-M9 motions, corresponding to a decrease of 46%. Similarly, the value of S_a/η that corresponds to a 50% likelihood of collapse of the ductile system set (Figure 6.14b) is 6.8 for the CMS motions and 2.6 for the Seattle-M9 motions, corresponding to a 62% decrease. At any particular value of S_a/η , the simulated Seattle-M9 motions are more likely to cause collapse. At any given intensity, the maximum absolute differences in probability between the two ground-motion sets, also known as the two-sample Kolmogorov-Smirnov test (KS-statistic), are 34% for the brittle system and 87% for the ductile system.

6.10 Accounting for Effects of Spectral Acceleration, Duration and Shape

Much of the variation in response among the individual ground motions and the ground-motions sets (i.e., Seattle, CMS) is attributable to the combination of spectral accelerations, spectral shape and ground-motion duration. A scalar intensity measure, developed in Chapter 3, made it possible to explicitly identify the contributions of each of these ground-motion characteristics to the structural demands. A normalized version of this intensity measure, $S_{a,eff}$, can be computed as:

$$S_{a,eff}(T_n) = S_a(T_n)\gamma_{dur}\gamma_{shape} \quad (6.4)$$

where γ_{dur} and γ_{shape} are non-dimensional parameters that account for the influence of duration and spectral shape on ground-motion intensity. For duration, $\gamma_{dur} = (D_s/(12T_n))^{C_{dur}}$ and the

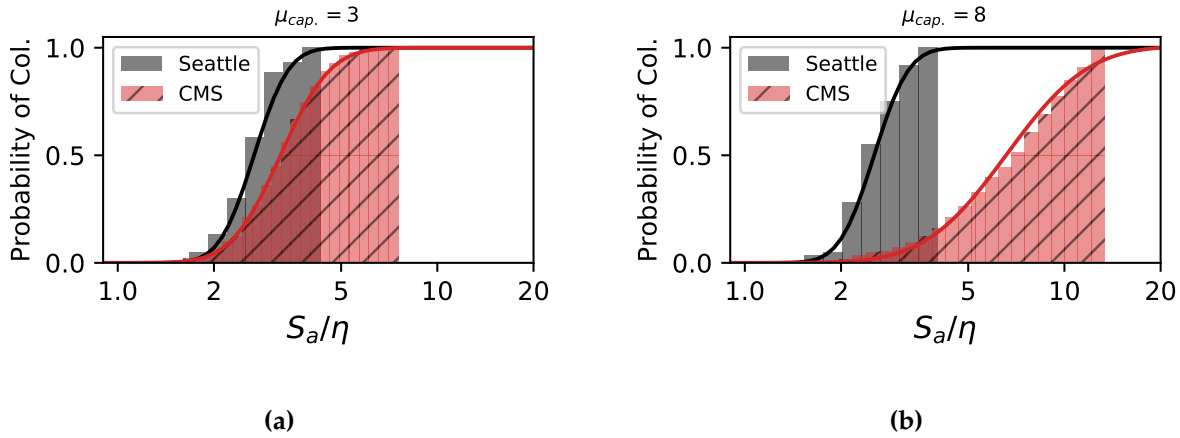


Figure 6.12: Fragility function prediction probability of collapse for (a) brittle and (b) ductile systems using S_a

quantity D_s/T_n is related to the number of system force-deformation cycles. The normalization constant of 12 corresponds to a nominal significant duration of 12s (the geometric mean for a commonly used crustal ground motion set in FEMA P695), divided by a nominal period of 1s. The exponent C_{dur} accounts for the structure's sensitivity to the duration. In general, this exponent varies with the ductility demand and the details of the force-deformation cyclic deformation. The optimal values of C_{dur} can be determined using regression analyses (see Chapter 3), and can be approximated as 0.10 for collapse calculations and 0.00 for estimates of deformation demand.

For the influence of spectral shape on ground motion intensity, $\gamma_{shape} = \left(\frac{SS_a(T_n, \alpha)}{SS_{a,0}}\right)^{C_{shape}}$ where the value of SS_a is normalized by $SS_{a,0}$ which is taken as $\ln\alpha/(\alpha - 1)$. This relationship can be derived from Eq. 6.2 with the assumption that $S_a(T_n)$ varies as $1/T_n$, as is the case for much of the design spectrum. The C_{shape} exponent accounts for the structure's sensitivity to spectral shape. This exponent increases with the ductility demand and can be approximated as $0.65\sqrt{\mu - 1}$ with a lower limit of 1.0 where μ is either taken as $\mu_{cap.}$ or μ_{target} .

Much of the differences in the system performances for the CMS and M9 ground-motion sets can be attributed to differences in spectral shape and duration. Figure 6.13 shows the geometric means and their variation (one standard deviation above and below) of γ_{shape} and γ_{dur} for a

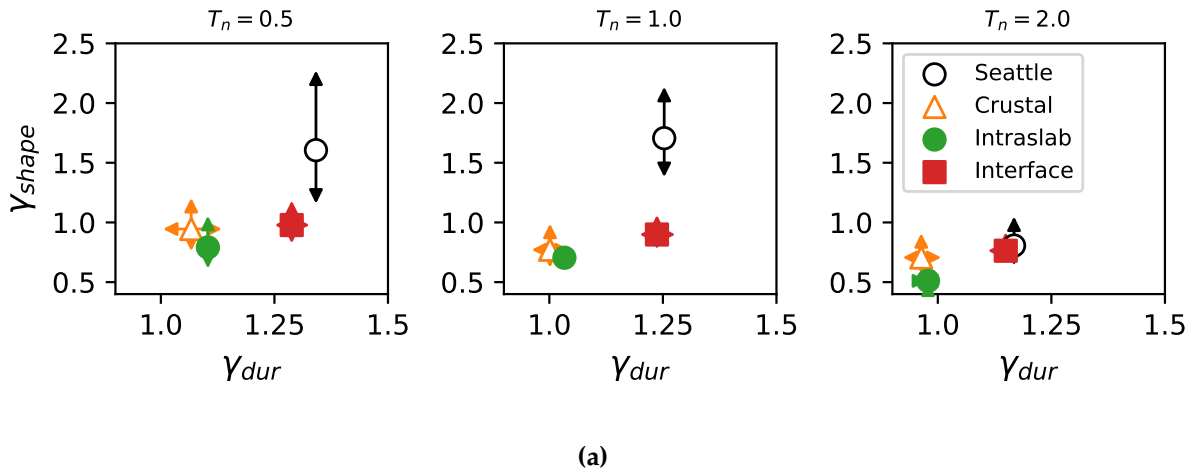


Figure 6.13: Mean and standard deviation of the γ_{shape} and γ_{dur} parameters for ductile (a) 0.5-second, (b) 1.0-second, and (c) 2-second systems for μ equal to 8. One standard deviation above and below the mean is indicated using the arrows.

ductility capacity of 8 at periods of 0.5, 1.0 and 2 s for the components of the CMS set and the Seattle M9 set. For all three periods, the duration factors for the crustal and intraslab earthquake motions from their CMS set are near 1.0, as expected, whereas the factor increases to 1.1 to 1.3 for the interface earthquakes in the CMS set and the simulated M9 motions, both of which are based on large-magnitude earthquakes. The shape factors for the Seattle M9 motions, which include the effect of the basin for the longer periods, are larger than those for any of the CMS set components for all three periods. This effect is particularly large at periods between 0.5-1.0 s, where γ_{shape} has a mean value of 1.66.

The differences in structural performance for ground-motions with different duration and spectral shape can be accounted for with $S_{a,eff}$. Figure 6.14 shows the collapse fragility curves expressed in terms of $S_{a,eff}/\eta$. The figure shows that using $S_{a,eff}$ nearly eliminates the difference in performance at a given ground motion intensity. The values of $S_{a,eff}/\eta$ at a collapse probability of 50% differs between the two motion sets by only 6% for the brittle system set and by 3% for the ductile system set. The collapse fragilities derived using $S_{a,eff}$ resulted in 35% and 78% reductions in the KS-statistic, for the brittle and ductile systems, respectively. In addition,

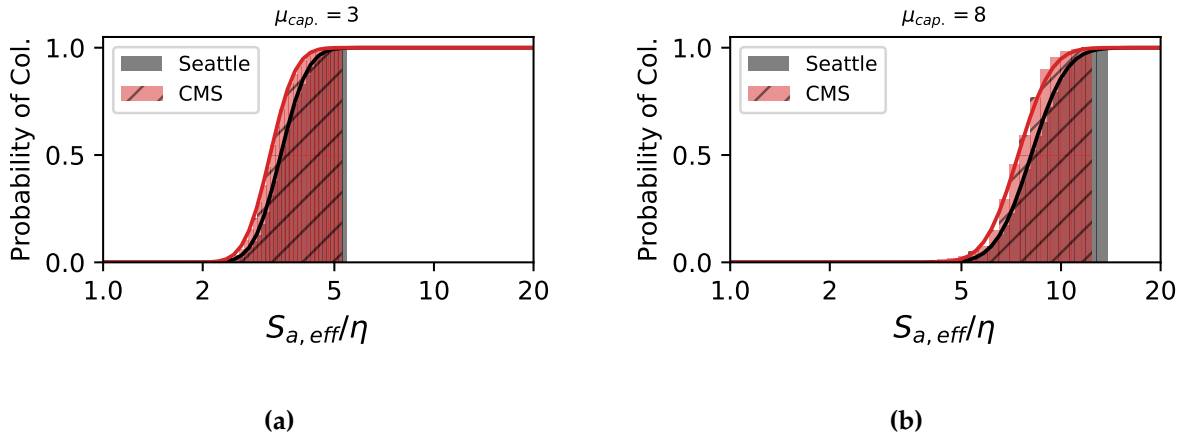


Figure 6.14: Fragility function prediction probability of collapse for (a) brittle and (b) ductile systems using $S_{a,eff}/\eta$.

the values of $S_{a,eff}/\eta$ that correspond to a 50% chance of collapse (4.0 for brittle set and 7.9 for ductile set) are approximately equal to $\mu_{cap.}$.

More formally, the efficiency of the intensity measures in predicting collapse can be compared by examining the lognormal statistics of the intensity measures at collapse. Table 6.1 shows the geometric mean and lognormal standard deviation, σ_{ln} , for both S_a and $S_{a,eff}$ at collapse for the four sets of motions: Seattle M9 simulated, La Grande M9 simulated, CMS and the combination of all the motions. For every set, the values of σ_{ln} are reduced in going from S_a to $S_{a,eff}$. Combining all of the motions, σ_{ln} reduces from 0.53 to 0.18 (66% reduction) for the ductile systems and from 0.30 to 0.16 (47% reduction) for the brittle ones.

These results demonstrate that the key differences in collapse potential are attributable to differences in motion duration and spectral shape, and these differences can be accounted for with $S_{a,eff}$.

6.11 Ductility Demands

The S_a and $S_{a,eff}$ ground-motion intensity measures can also be used to evaluate the likelihood of exceeding a target deformation demand. Fragility relationships were computed for a deformation

Table 6.1: Location and scale parameters for fragility curves conditioned on $\ln S_a$ and $\ln S_{a,eff}$.

| System | GM Set | Probability of $\mu > \mu_{cap.}/2$ | | | | Probability of Collapse | | | |
|-----------------------------|--------------|-------------------------------------|----------|-----------------|----------|-------------------------|----------|-----------------|----------|
| | | $\ln S_a$ | | $\ln S_{a,eff}$ | | $\ln S_a$ | | $\ln S_{a,eff}$ | |
| | | e^μ | σ | e^μ | σ | e^μ | σ | e^μ | σ |
| Brittle ($\mu_{cap} = 3$) | CMS | 1.67 | 0.14 | 1.65 | 0.13 | 3.32 | 0.28 | 3.25 | 0.15 |
| | Seattle-M9 | 1.52 | 0.09 | 1.55 | 0.08 | 2.74 | 0.20 | 3.53 | 0.15 |
| | La Grande-M9 | 1.44 | 0.09 | 1.52 | 0.08 | 2.06 | 0.23 | 3.66 | 0.15 |
| | All | 1.64 | 0.14 | 1.63 | 0.13 | 3.14 | 0.30 | 3.66 | 0.15 |
| Ductile ($\mu_{cap} = 8$) | CMS | 4.14 | 0.30 | 3.87 | 4.14 | 6.78 | 0.46 | 7.64 | 0.20 |
| | Seattle-M9 | 2.15 | 0.21 | 4.13 | 2.15 | 2.61 | 0.20 | 7.84 | 0.11 |
| | La Grande-M9 | 2.28 | 0.21 | 3.77 | 0.13 | 3.80 | 0.28 | 8.25 | 0.13 |
| | All | 3.73 | 0.37 | 3.88 | 3.73 | 5.82 | 0.53 | 7.12 | 0.18 |

Notes: The table shows the location (μ) and scale (σ) parameters for a normally distributed intensity measures $\ln S_a$ and $\ln S_{a,eff}$ for various ground-motion sets.

demand of $\mu_{cap.}/2$, which corresponds to ductility demand of 1.5 for the brittle system set and 4.0 for the ductile set. Figure 6.15 shows the resulting fragility relationships in terms of S_a , and Figure 6.16 shows the corresponding relationships for $S_{a,eff}$. As was the case for the collapse calculations, accounting for the effects of spectral shape ($C_{dur} = 0$, $C_{shape}=0.46$ for brittle, and $C_{shape} = 0.65$ for ductile) with $S_{a,eff}$ resulted in much smaller KS-statistics, less than 7% for both. As shown in Table 6.1, for the combination of all of the motions considered, σ_{ln} reduces from 0.37 to 0.22 (41% reduction) for the ductile systems and from 0.14 to 0.13 (10% reduction) for the brittle ones. The smaller reduction in σ_{ln} for the brittle system was expected, since the target deformation is only 50% larger than than yield deformation, so spectral shape effects are smaller than for larger ductility demands.

The prediction of expected damage is important for pre-event scenario planning (e.g., Detweiler and Wein, 2018) and post-event emergency response using recorded ground motions (e.g., USGS, 2018). For example, Hazus (2018) uses scalar measures of ground-motion intensity (e.g., PGA, PGV, or S_a at a single period) with damage fragility relationships to provide probabilistic estimates of the impacts of an earthquake.

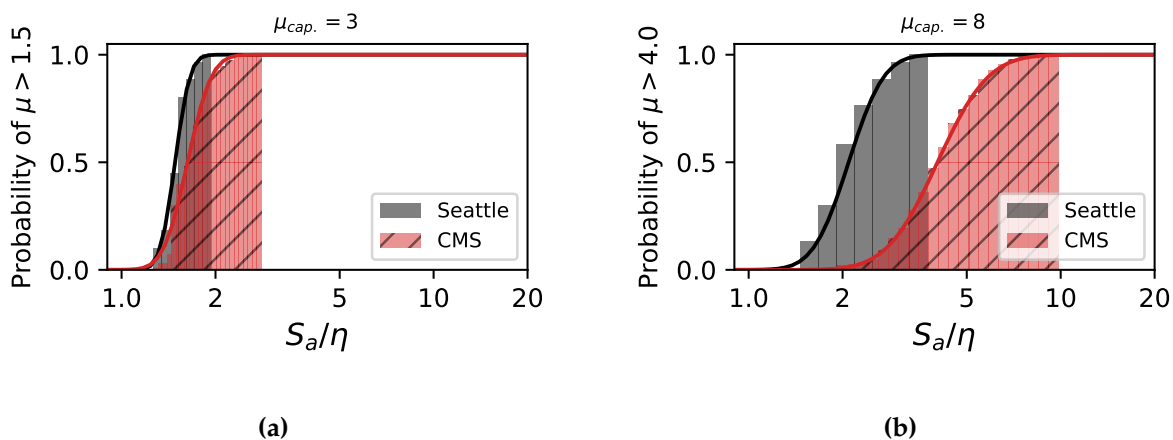


Figure 6.15: Fragility function predicting probability of ductility demand exceeding half the ductility capacity for (a) brittle and (b) ductile systems using S_a/η .

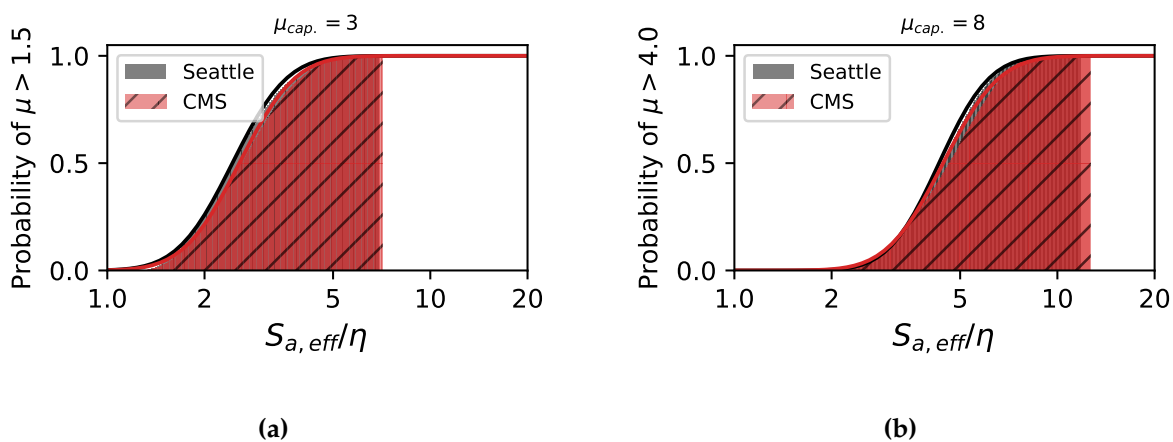


Figure 6.16: Fragility function predicting probability of ductility demand exceeding half the ductility capacity for (a) brittle and (b) ductile systems using $S_{a,eff}/\eta$. Regional Variation of Collapse Probability

As shown previously, estimates of collapse and deformation demands based on S_a alone are inadequate to characterize the impacts of the simulated M9 motions. $S_{a,eff}$ provides a more efficient means of estimating the likelihood of collapse and exceeding $\mu_{cap}/2$ (Table 6.1). The collapse probability of a new structure at each location within the Puget Sound region (for $V_{S30} = 600$ km/s) was estimated by combining (1) the probabilistic characterization of the seismic resistance of new structures (including material, design, and model uncertainties); (2) the mean and record-to-record variability of the estimates of $S_{a,eff}$ from the 30 realizations, β_{RTR} ; and (3) the fragility curves described in Table 6.1.

The design spectral accelerations varied within the Puget Sound region because of variations in distance to local crustal faults (e.g., Seattle Fault, South Whidbey Island Fault) and distance to the Cascadia Subduction Zone fault rupture plane. For each location, the normalized design strength, η , was computed using the ASCE 7-16 design values that were retrieved from the USGS (2018) for Site Class C and Risk Category II. Similar to the systems previously used, an overstrength factor of 1.5 was assumed in η for all locations (Luco et al., 2007).

The system properties vary due to material, design, and modelling uncertainties (FEMA P695). These effects are accounted for by assuming η varies with a lognormal standard deviation, $\sigma_{\ln\eta}$, is taken as 0.45. The variability of the IM for a given damage state (collapse is considered here) is explicitly accounted for here in the fragility functions (defined in Table 6.1). Therefore, the record-to-record variability was subtracted from the total variability assumed in ASCE 7-16. This expression can be written as $\sqrt{\beta_{tot}^2 - \beta_{RTR}^2}$, where β_{tot} is the total variability of the IM at collapse considering material, design, modelling, and record-to-record variability, and β_{RTR} is due to record-to-record variation of the IM at collapse. The value of β_{tot} is taken as 0.6 as per ASCE 7-16 (Section 21.2.1.2) and β_{RTR} is 0.4 (FEMA P695).

The value of η varies over the Puget Sound region. For a low-strength-ductile structure ($R = 8$) representing modern design, the median value of η decreases moving eastwards and ranges from 0.22 to 0.09g for 0.5 s periods. The values are lower at 2.0 s period, ranging from 0.09 to 0.03g.

The lognormal probability density function for $S_{a,eff}$ for collapse ($S_{a,eff,col.}$) was generated from the two horizontal components of the 30 simulations at each grid point for a ductile structure where $C_{dur} = 0.10$ and $C_{shape} = 1.0$. The resulting regional variation of the geometric

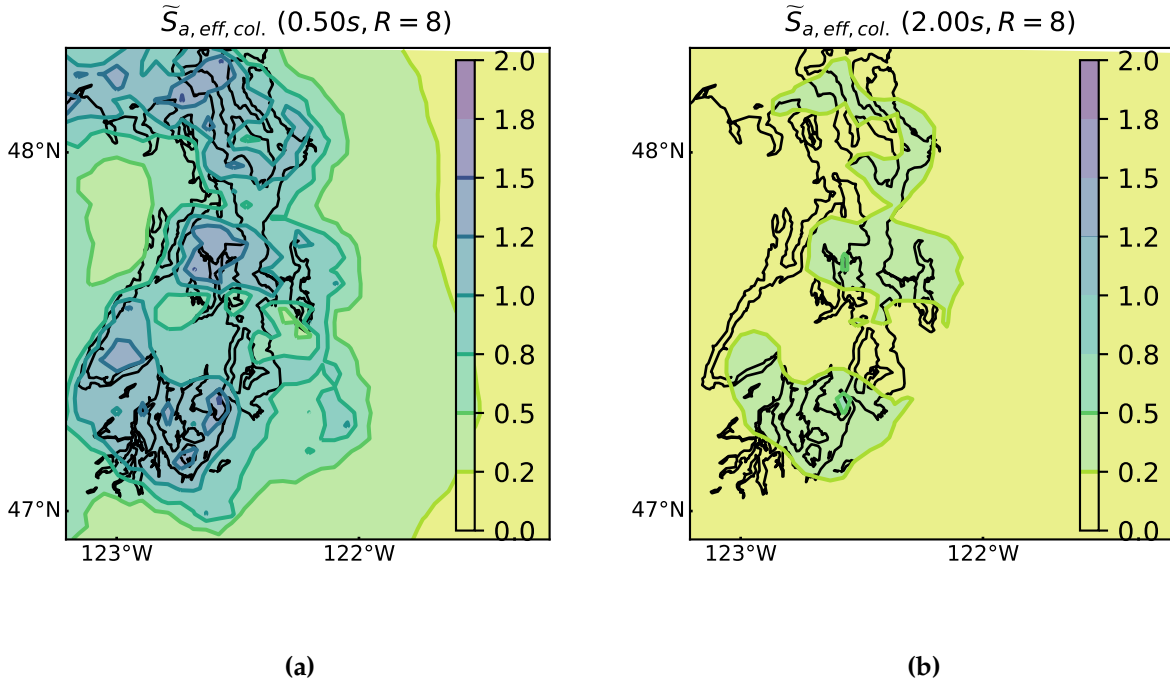


Figure 6.17: Regional variation of geometric mean of $S_{a,eff}$ for (a) 0.5-second and (b) 2.0-second for the suite of M9 earthquakes for a low-strength-ductile structure.

mean of $S_{a,eff,col.}$ is plotted in Figure 6.17 for periods of 0.5 s and 2.0 s for low-strength-ductile structure ($R = 8$). As expected, the demands are largest near the deepest part of the basins. At 0.5 s periods, $S_{a,eff,col.}$ reaches up to 1.5 g for high-strength-brittle systems. However at longer periods, $S_{a,eff,col.}$ is smaller and reaches values of 0.5 g at locations corresponding to the deepest part of the basin.

For a given site, the probability of collapse under a simulated M9 CSZ earthquake was computed considering the uncertainty due to record-to-record variation among the M9 scenarios, and uncertainty in system resistance. The collapse probability for each location can be computed as,

$$P[\text{col.}|M9] = \iint P[\text{col.}|\frac{S_{a,eff}}{\eta}] f_{S_{a,eff}}(S_{a,eff}|M9) f_{\eta}(\frac{1}{\eta}) d\frac{1}{\eta} dS_{a,eff} \quad (6.5)$$

where $f_{S_{a,eff}}$ is the lognormal probability density of $S_{a,eff}$ for the thirty M9 scenarios for a single location, f_{η} is the lognormal probability density of $1/\eta$ (also accounts for uncertainty in material strength, design, and modelling), and $P[COL|S_{a,eff}/\eta]$ is the collapse fragility function (defined in Table 6.1) that is conditioned on $\ln S_{a,eff}/\eta$.

Figure 6.18 and Figure 6.19 show the regional variation of the collapse probability for the M9 motions for high-strength-brittle and low-strength-ductile systems (i.e., most representative of new systems) with periods of 0.5, 1.0, and 2.0 seconds. As expected the collapse probability for the high-strength-brittle structures is always less than 10% for an initial period of 0.5s, because these structures have low spectral accelerations compared with the design acceleration (Figure 6.1a). For structures with longer periods, the collapse probability is much higher, especially for regions that coincide with the deeper basins. For example, high-strength-brittle systems in locations where $Z_{2.5} > 6$ km (i.e., Seattle) have a mean collapse probability of 14% and 18% at 1.0 s and 2.0 s periods, respectively. For low-strength-ductile systems, the mean collapse probability for $Z_{2.5} > 6$ km is largest at a period of 1.0 s, around 18%. In contrast, for periods shorter and longer than 1 s the mean collapse probability reduces to a value of around 7% on average.

At a period of 1 s, the extent of larger collapse probabilities for the low-strength-ductile system is larger than that for high-strength-brittle systems, because low-strength-ductile systems have more period elongation and are more affected by the unfavorable spectral shape at this period (Figure 6.8). In contrast, at a period of 2 s, the high-strength-brittle system is more likely to collapse than its low-strength-ductile counterpart, because the larger period elongation of the ductile system allows it to take advantage of the favorable spectral shape beyond 2s (Figure 6.8).

These collapse analyses were computed assuming that: (i) the structural response can be represented with deteriorating single-degree-of-freedom systems with 5% damping, (ii) the system strengths were based on ASCE 7-16 provisions for NEHRP site class C, and (iii) the analyses were conditioned on the occurrence of a M9 interface earthquake. Despite these limitations it is instructive to compare these collapse probabilities with the intended collapse risk.

ASCE 7-16 targets a 1% chance of collapse due to an earthquake during the buildings assumed 50-year lifespan. Assuming an average 500-year return period (Poisson distribution), the M9 CSZ earthquake would have 9.5% chance of occurring in 50 years. Neglecting the

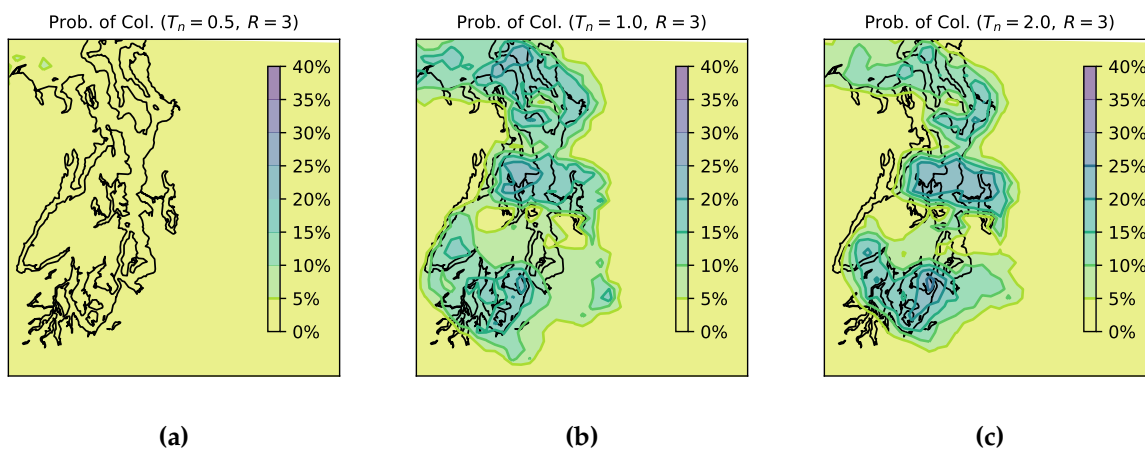


Figure 6.18: Regional variation of the collapse probability for a high-strength-brittle system at (a) 0.5 s, (b) 1 s, and (c) 2.0 s period.

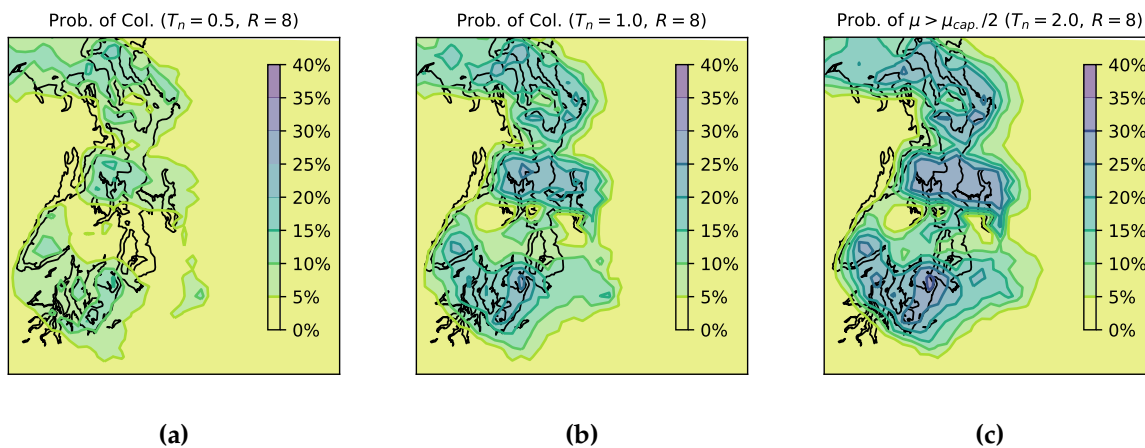


Figure 6.19: Regional variation of the collapse probability in a M9 CSZ earthquake for a low-strength-ductile system at (a) 0.5 s, (b) 1 s, and (c) 2.0 s period.

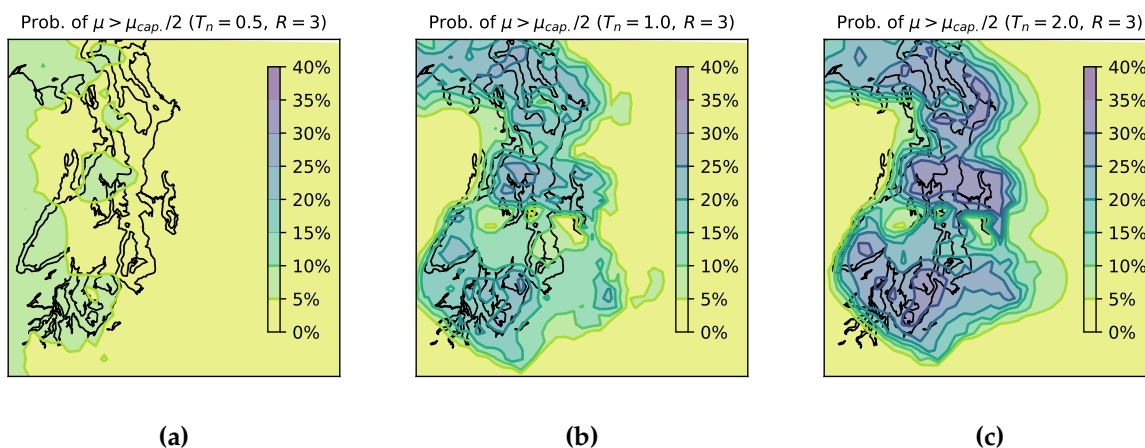


Figure 6.20: Regional variation of the probability of exceeding $\mu_{cap.}/2$ for a high-strength-brittle system at (a) 0.5 s, (b) 1 s, and (c) 2.0 s period.

contribution of collapse risk from other earthquake sources and magnitudes, the acceptable collapse probability from an M9 CSZ earthquake would be 10.5% (0.01/0.095). Figures 6.20 and 6.21 shows that the target collapse probability will be exceeded for structures with periods over a broad region corresponding to the deepest part of the basins that include the cities of Seattle, Bellevue, and Everett. Of course, the actual collapse risk would increase if other sources contributing to the seismic hazard were considered.

6.12 Regional Variation of Ductility Demands

The probability of exceeding a ductility demand that exceeds $\mu_{cap.}/2$ can also be computed following the same procedure used to assess collapse risk, but with fragility functions that predict probability of exceeding $\mu_{cap.}/2$ (listed in Table 6.1). Figure 6.20 and Figure 6.21 show the regional variation for the probability of exceeding $\mu_{cap.}/2$ for 0.5-, 1.0-, and 2.0-second systems. The results show, with the exception of the high-strength-brittle, low-period structures, all the systems over a large region would be very likely to exceed this target displacement during an M9 event. In some locations, the likelihood would be as high as 34%.

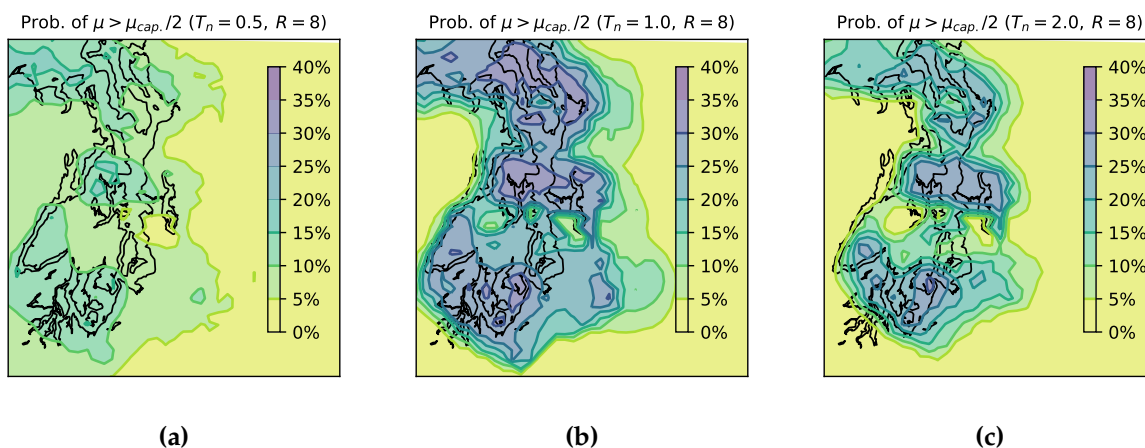


Figure 6.21: Regional variation of the probability of exceeding $\mu_{cap.}/2$ for a low-strength-ductile system at (a) 0.5 s, (b) 1 s, and (c) 2.0 s period.

6.13 Chapter Conclusions

Thirty physics-based ground motion simulations provided an opportunity to evaluate the impacts of an M9 earthquake on the Pacific Northwest. The low-frequency component of the motions was computed with a deterministic finite-difference solution that accounted for several deep sedimentary basins. The high-frequency components of the motions were computed with a stochastic procedure (Frankel, 2009) that did not account for the basins. Outside the Puget Lowland region, the spectral accelerations of this set of simulated ground motions were similar to those predicted by with the BC-Hydro GMM (Abrahamson et al., 2016). However, within the Puget Lowland region, and in particular, within the Seattle basin, the effect of the sedimentary basin dominated the regional variation of the ground-motion intensities.

The sedimentary layers that underlie much of the Puget Lowland, and Seattle in particular, tend to amplify ground motion spectral accelerations at longer periods. As a result, the simulated motions, which have a return period of about 500 years, produced spectral accelerations that are in many scenarios larger than the MCE_R design earthquake that has a return period of about 2000

years for Seattle. The amplification of the motions within the basin correlated well with $Z_{2.5}$, the depth to a shear-wave velocity of 2.5 km/s.

The period-dependent variation in the spectral amplification led to ground motions with spectral shapes that further increased the impacts of the ground motions on long-period structures. In addition, the simulated ground motions had long durations (significant duration geomean of about 110 s in Seattle, compared to a geomean of 12 s for the FEMA P695 motions), because the earthquake magnitude is large. As a result, the ductility demands and the probability of collapse of SDOF systems with varying strength and ductility capacity were significantly higher for the simulated M9 ground motions than for motions selected and scaled to a CMS representing the MCE_R hazard.

The effects of the simulated motions on structural response could not be explained well in terms of spectral acceleration alone. Instead, the results of nonlinear SDOF analyses correlated better with $S_{a,eff}$, a ductility dependent intensity measure that explicitly accounts for spectral acceleration (S_a), ground-motion duration (γ_{dur}) and spectral shape (γ_{shape}). For example, at a period of 1.0s, a low-strength ($R = 8$) and ductile ($\mu = 8$) single-degree freedom had M9 Seattle spectral accelerations that were 60% lower than the CMS motions at MCE_R (0.35g vs 0.56g), but its duration factor was 17% higher (1.25 vs 1.08) and its shape factor was 117% higher (1.71 vs. 0.79) of the CMS motion.

On a regional basis, the probability of collapse and of exceeding a target ductility were estimated based on (1) the probabilistic characterization of the seismic resistance of new structures (accounting for material, design, and modelling uncertainties); (2) the mean and record-to-record variability of the estimates of $S_{a,eff}$ from the 30 realizations; and (3) the derived fragility curves for $S_{a,eff}$. The results suggest that the probability of structural collapse is unacceptably high for many structures within the Seattle, Tacoma and Everett basins, particularly for those with periods around 1.0 s. Moderate damage (corresponding to a ductility demand of about half of its capacity) would be widespread throughout the Puget Lowland region.

Chapter 7

VARIABILITY IN SEISMIC COLLAPSE PROBABILITIES OF SOLID AND COUPLED-WALL BUILDINGS

This chapter is based on the following reference:

Marafi, Nasser A., Kamal A. Ahmed, Dawn E. Lehman, and Laura N. Lowes (2018c). "Variability in Seismic Collapse Probabilities of Solid and Coupled-Wall Buildings". In: *Journal of Structural Engineering, In-review*

7.1 Chapter Overview

Chapter 6 quantified the collapse risk of idealized SDOF systems for the simulated M9 motions. These idealized systems are computationally efficient and provide robust predictions of collapse because these models are simple. These simplifications make these systems more convenient for research, but they only provide rough estimates of structural performance. This chapter improves the collapse prediction for more complicated multiple-degree-of-freedom analytical models of reinforced concrete walls that are a common lateral load resisting system for buildings.

Common wall configurations are solid planar or solid flanged (i.e., H, I, T, L or C-shaped cross sections) and coupled planar or flanged walls. Previous modelling methodology often provides highly varying predictions of collapse in RC walls due to element non-convergence in the analytical models. This chapter mitigates the non-convergence issues by enhancing the modelling methodology by Pugh et al. (2015) using displacement-based beam-column elements. The second part of the chapter studies the sensitivity of collapse and other damage states to modeling decisions and model parameters for both solid and coupled wall archetypes. This is done using a nonlinear incremental dynamic analysis with the suite of ground motions developed for the FEMA P695 procedure and a set of six idealized wall buildings of varying

heights. The collapse risk between solid and coupled wall archetypes are also compared and design decisions are identified that can reduce the earthquake collapse risk. The methodology presented in this chapter is also later implemented in Chapter 8 to study the effect of the simulated M9 motions on a series of RC core wall archetypes.

7.2 Introduction

Reinforced concrete structural walls are used commonly as the lateral force resisting system for buildings in regions of high seismicity. Design codes are intended to result in a walled building that (i) develops a desirable plastic mechanism under earthquake loading, (ii) has a low probability of collapse when subjected to the maximum considered earthquake (MCE), and (iii) has a flexural strength and stiffness that are large enough so that the walled building meets serviceability requirement under design-level earthquake loading. This is accomplished primarily through prescriptive detailing requirements intended to achieve adequate deformation capacity as well as limits on shear demand.

With publication of the FEMA P695 (2009) document, which provides a methodology for assessing the collapse risk posed by buildings designed using a particular design code or set of design specifications, questions have arisen as to the collapse risk posed by walled buildings designed using current US codes and standard practice as well as the relative collapse risk posed by solid versus coupled walls. To date, several studies have investigated the collapse risk posed by buildings with solid walls (e.g., Pugh, 2012; Gogus and Wallace, 2015, and others), but investigation of the collapse risk posed by coupled wall buildings has been limited. Previous studies addressing collapse risk assessment for buildings with solid walls provide a basis for the current study and are reviewed below.

Gogus and Wallace (2015) employed the FEMA P695 methodology to assess the collapse risk of walled buildings designed using current ASCE 7 (2017) strength reduction factors (i.e., R factors) that either meet ACI 318 (2014) Code requirements for detailing of special walls or not (ordinary walls). Walled buildings considered in the study were 1-, 2-, 4-, 8-, and 12-stories and employed independent solid rather than coupled walls. Nonlinear dynamic analyses of walled buildings were conducted using the *OpenSees* software platform (McKenna, 2016) through the

computational resources provided by DesignSafe-CI (Rathje et al., 2017). Walls were modeled using displacement-based distributed plasticity beam-column elements, supplemented with shear and rotational springs to simulate shear flexibility and deformation due to bar pull-out at the base of the wall. Building models included beam-column elements and springs to represent concrete wall response as well as an axially loaded P-delta column to represent the gravity-load carrying system. For walls, loss of lateral strength was not explicitly modeled; instead, simulation data were post-processed to determine the onset of "collapse". Criteria used to define onset of collapse were (i) magnitude of compressive strain for unconfined concrete exceeding 0.01 or for confined concrete exceeding 0.06, (ii) steel tensile strain exceeding 0.05, which is defined less than the fracture strain under monotonic loading to account for low-cycle fatigue, (iii) magnitude of shear strain exceeding 0.015, and (iv) inter-story drift exceeding 5%, which was intended to represent failure of the gravity load resisting system. The results of the Gogus and Wallace study indicate that to achieve the desired collapse risk the R-factor used for wall design should depend on building height, with $R=6$ (current ASCE 7 R factor for non-bearing walls) being suitable for the 4-story building, and larger values suitable for shear-demand-limited 8- and 12-story buildings. These results are consistent with those of Hsiao et al. (2013) who recommend height-dependent R-factors for steel braced frames. However, Gogus and Wallace recommend the use of the current R factor for all walls as high shear demands are common in walls in regions of high seismicity.

Pugh (2012) and Pugh et al. (2017) also employed the FEMA P695 methodology to evaluate the collapse risk posed by walled buildings designed using current US code requirements, including ASCE 7 strength reduction factors and ACI 318 detailing requirements for special walls. However, in Pugh's study, wall heights ranged from 6 to 30 stories and lateral strength loss in walls was explicitly modeled. To simulate lateral strength loss, Pugh et al. used OpenSees with force-based beam-column elements and an approach for simulating material response that had been demonstrated, using a large experimental data set, to provide accurate and mesh-independent simulation of onset of strength loss (Pugh et al., 2015). Specifically, the model developed by Pugh et al. achieves accurate prediction of strength loss with minimal mesh dependence by (i) defining the post-peak concrete compression response using the concrete

crushing energy, calibrated for unconfined and for confined concrete, and a measure of mesh size and by (ii) defining onset of steel compressive strength loss due to buckling at the strain at which concrete reaches residual compressive strength. Similar to Gogus and Wallace (2015), walled buildings were considered to "collapse" due to failure of the gravity load carrying system if inter-story drift exceeded 5%. Results of the study indicate that (i) reduced R factors are required to achieve desired collapse risk at MCE for walled buildings with solid walls and (ii) under moderate to severe earthquake loading, inelastic response and flexural over-strength of walls results in shear demands that are two to four times those determined from elastic design and used for design and, thus, the potential for reduced flexural deformation capacity due to flexure-shear failure. The magnitude of shear amplification observed by Pugh et al. is consistent with the results of many other studies (e.g., Priestley et al., 2007; Boivin and Paultre, 2012).

Collapse analysis of coupled wall systems are limited, however, researchers Kim, 2016, e.g., have investigated the variability in engineering demand of coupled core-walls during MCE-level ground shaking. Kim's study used both (1) two-dimensional *OpenSees* models that were based on the modelling methodology developed by Kolozvari et al. (2015a) and Kolozvari et al. (2015b) and (2) three-dimensional non-linear models using CSI Perform 3D (2018). Kim, however, focused on tall (20- and 30-story) coupled core-wall buildings and sought to quantify (1) the variability in predicted building response resulting from ground motion variability, (2) variation in design parameters such as seismic mass, dead and live loads and (3) variation in modeling assumptions such as concrete compressive strengths, reinforcing steel yield strengths, concrete shear modulus, and coupling beam strength. Through Monte Carlo simulations, Kim concluded that uncertainty in simulated demand measures (story drifts, roof drifts, beam rotations, and wall axial strains) was due primarily to ground motion record-to-record variability and that other factors (uncertainty in design parameters and modeling assumptions) resulted in significantly less variability. Kim (2016) recommended a minimum coefficient of variation (COV) of 20% be used to account for uncertainty in ground motion and 5% COV be used to represent uncertainty in design and/or model parameters when evaluating the reliability of structural walls used in high-rise construction.

7.2.1 Research Objectives

The research presented in this chapter i) quantifies and compares the MCE collapse risk posed by solid versus coupled wall buildings designed using current US code requirements and standard practice, ii) quantifies the uncertainty in collapse risk resulting from modeling assumptions, and iii) assesses the impact on collapse risk of design requirements that limit axial load in walls. This is accomplished using the FEMA P695 methodology and a modeling approach that extends that proposed by Pugh et al. (2015) to provide an accurate simulation of strength loss as well as a high level of numerical robustness.

Specifically, the current study advances previous work by others as follows: Pugh et al. (2015) investigated the collapse risk of solid walled buildings using the fiber-type force-based beam-column elements available in *OpenSees* (2016). While the force-based element formulation provides an accurate simulation of response, it requires an intra-element solution at each step in the analysis. If this intra-element solution fails, which is not uncommon during simulation of strength loss, the numerical simulation of the building fails to converge. If this failure to converge is interpreted as building collapse (Vamvatsikos and Cornell, 2002), which has been done in past studies, then collapse risk is incorrectly increased. The current study advances wall modeling work by Pugh et al. (2015) by using the regularization method proposed by Coleman and Spacone (2001) for displacement-based elements, to achieve accurate and mesh-objective simulation of wall response using the displacement-based element formulation. The current study then employs displacement-based elements to simulate wall response and demonstrates that using this element formulation, walled-building collapse risk is reduced in comparison with results generated using the force-based element.

The three numerical simulation studies selected (Gogus and Wallace, 2015; Pugh et al., 2015; Kim, 2016) used different modeling parameters. It is postulated that selected values of salient modeling parameters could impact the damage potential at the maximum considered earthquake (MCE) and collapse. Specifically, this study investigates the impact of modeling of the steel and concrete on performance looking at a range of assumptions in the constitutive modelling of the concrete and reinforcing steel and varies them within reason to study their impact on collapse. The constitutive modelling parameters considered are: (1) confined concrete stress, (2) residual

strength, (3) crushing energy of the confined and unconfined concrete, and the effects of reinforcing steel due to ultimate strain.

Similarly, it is postulated that design parameters such as system configuration (e.g., solid & coupled walls), axial load ratio, and gravity system drift capacity would also impact the building response. These parameters are also included in the study by studying changes in collapse risk with system design variations that affect the wall axial load, the drift capacity of the gravity system, adjustments to wall thickness to study the effects of axial load ratio due to coupling action.

7.3 Archetype Models

The above research results were realized through activities described in the following sections, including (1) design of a series of idealized walled buildings, (2) development of a reference model for each walled building, and (3) creation of a suite of simulation models defined by plausible variations on model parameters included in the reference models. The resulting archetype designs and base modeling approach is described below.

7.3.1 Design of archetypes

Collapse vulnerability of mid-height wall buildings was investigated using idealized models of 4-, 8-, and 12-story solid wall and coupled wall building archetypes. All six archetypes were designed using the equivalent lateral force (ELF) procedure in ASCE 7-10 (2013). The archetypes are located on a NEHRP Site Class C in Los Angeles (L.A.) with a short-period spectral acceleration, S_S , and 1-s spectral acceleration, S_1 , of 1.5 g and 0.6 g respectively. For all archetypes, an occupancy Risk Category I was assumed, which corresponded to ASCE 7-10 Seismic Design Category D designation for this particular site.

Figure 7.1 shows a typical floor plan for the archetypes. The floor plate is 36.6 m (120 ft.) long by 36.6 m (120 ft.) wide with four 9.15 m (30 ft.) bays of slab-column gravity framing in each orthogonal direction. The 4- and 8-story archetype had two walls in each direction, and the 12-story wall had four walls in each direction.

Table 7.1: Properties of the solid and coupled wall archetypes.

| Design ID | $C_u T_a$ (s) | Building Design Base Shear | MRSA Period (s) (Cracked) | Shear Stress Demand (V_u/V_c) | Axial Load Ratio ($P_g/f'_c A_g$) |
|-----------|---------------|-------------------------------|------------------------------|--------------------------------------|--|
| 4SW | 0.56 | 0.25W | 0.47 | 1.32 | 2.6% |
| 8SW | 0.93 | 0.11W | 1.14 | 0.96 | 5.0% |
| 12SW | 1.25 | 0.08W | 1.68 | 0.53 | 7.6% |
| 4CW | 0.56 | 0.25W | 0.58 | 1.76 | 3.5% |
| 8CW | 0.93 | 0.11W | 1.44 | 1.28 | 6.7% |
| 12CW | 1.25 | 0.08W | 1.92 | 0.70 | 10.1% |

In addition to the self-weight, superimposed dead and live loads were included. The total dead loads for typical floors and the roof were 8.38 kPa (175 psf) and 6.70 kPa (140 psf), respectively. The live loads for typical floors and the roof were 3.11 kPa (65 psf), and 0.96 kPa (20 psf), respectively. The seismic weight of the archetype was computed by considering all the dead load (self-weight and super-imposed) and an additional 0.48 KPa (10 psf) for partition walls (which is typically considered part of the live load in the gravity frame design). The resulting seismic weights of the 4-, 8-, and 12-story archetypes were 2.32 MN (10,300 kips), 4.80 MN (21,300 kips), and 7.25 MN (32,200 kips), respectively.

All archetypes used a seismic force reduction factor (R) of 6, which requires walls to be designed and detailed per Chapter 18 of ACI 318-14 (2014) for special reinforced concrete shear walls. The upper-bound limit on design period ($C_u T_a$) and the elastic period with cracked concrete properties are listed in Table 7.1. The total seismic base shear as a fraction of the effective seismic weight (i.e., the seismic response coefficient, variable C_s in ASCE 7-10 §12.8) were 0.25, 0.11, 0.08 for the 4-, 8- and 12-story archetypes, respectively. The archetypes were all designed using concrete with a design compressive strength (f'_c) of 34.5 MPa (5,000 psi) and reinforced with ASTM A706 steel that has a yield stress (f_y) of 414 MPa (60 ksi).

7.3.2 Solid Wall Design

For the solid-wall archetypes, the wall thickness and length were constant through the height of the archetype and designed to meet the following criteria: (1) base shear stress demand resulting from the ELF demands are less than $0.334f'_c$ MPa ($4f'_c$ psi) to mitigate the reduction in flexural drift capacity due to flexural-shear failure, (2) flexural strength such that $\phi M_n > M_u$ where $\phi = 0.9$ per ACI; M_n corresponds to the flexural strength as per ACI, M_u is based on moment demand due to ELF per ASCE 7-10 12.8, and (3) elastic stiffness to meet the drift limit states according to §12.12 in ASCE 7-10 using an effective stiffness of $0.5E_c I_g$, as permitted in ACI 318-14.

Wall geometry and reinforcing steel configuration for solid wall designs are provided in Table 7.3; the cross-sectional reinforcement layout is shown in Figure 7.4. The 4-story archetype with solid walls (4SW) had two 610 mm (2-ft) thick by 7.32 m (24-ft) long walls in each direction and the 8-story archetype (8SW) had two 610 mm (2 ft.) thick by 9.1 m (30 ft.) long walls in each direction. The 12-story archetypes (12SW) required additional wall area which resulted in four 610 mm (2 ft.) by 9.1 m (30 ft.) walls in each direction. Torsion was not considered.

The resulting ratio of horizontal shear force (due to seismic loads) to the concrete shear capacity, V_u/V_c , ranged from 0.53 to 1.32 and is summarized in Table 1. These values are much lower than the limit of $4V_c$ per ACI 318-14. The resulting axial load ratio ($P_g/(l_w b 4f'_c)$, where P_g is computed using the 1.0D + 0.5L load combination, l_w and b is the wall length and thickness respectively) of the interior walls are 2.6%, 5.0%, and 7.6% for the 4-, 8- and 12- story solid wall archetypes, respectively. The gravity load P_g was computed assuming a wall tributary area of 9.1 m (30 ft) by 11.6 m (38 ft) for the 4-story archetype, and 9.1 m (30 ft) by 13.4 m (44 ft) for the 8- and 12-story archetype.

The web and boundary element (shown and labelled as BEA in Figure 7.4) of the wall were detailed according to the requirements in ACI 318-14 §18.10. The variation in boundary element reinforcement layout along the wall height was optimized to balance efficiency (the required versus the provided reinforcement) and constructability (the number of variations in the section reinforcement layout). Table 7.3 summarizes the boundary element: (1) length, l_{be} , (2) size and number of longitudinal reinforcement, l_r , and (3) longitudinal reinforcement ratios, ρ_l for all

solid wall archetypes. Figure 7.2 shows the moment demand and capacity of the wall for each story.

7.3.3 Coupled Wall Design

The coupled wall archetypes were designed to have the same wall thickness and overall length (including the coupling beam length, l_{cb} in Figure 7.4) as their solid wall counterparts and placed in the same location in plan (shown in Figure 7.1). However, the coupled walls include openings located at the center of the wall at each story which result in a reduction in stiffness. This opening was 1.98 m (6.5 ft.) wide by 3.05m (10 ft.) tall for the 4-story archetype (4CW) and 2.29 m (7.5 ft.) wide by 3.05m (10 ft.) tall for the 8- and 12-story archetype (8CW and 12CW). The dimensions of the coupling beams for coupled wall archetypes are summarized in Table 7.2.

For the coupled wall, pier shear stress ratios are larger than for the solid walls (V_u/V_c) and ranged from 0.70 to 1.76 (up to a $0.44V_u/V_c$ increase from the solid wall counterpart). Similarly, pier axial load ratios resulting from gravity load ($P_g/(l_w b f'_c)$) are larger than the solid walls and are 3.5%, 6.7%, and 10.1% for the 4-, 8-, and 12- story archetypes, respectively (up to a $0.025f'_c A_g$ increase from the solid wall counterpart). The design shear forces and moments on the coupling beams and wall piers were determined by applying the ELF forces to an elastic model using an effective stiffness of $0.5E_c I_g$ for both the wall piers and coupling beams.

All of the coupling beams have span-to-depth ratios that are less than 2.5 and are diagonally reinforced, per ACI 318-14 §18.10.7.4; designs are summarized in Table 7.2 (column d_r for diagonally reinforced). Horizontal bars (labelled as hbr in Figure 7.4) along the coupling beam perimeter are provided, per ACI 318-14 §18.10.7.4, and are restrained using #4 crossties (transverse reinforcement, labelled as tr in Figure 7.4) spaced at 64 mm (2.5 in.) along the length of the coupling beam.

The wall piers required special boundary elements (BE_A and BE_B in Figure 7.4) to meet the flexural demands under ELF (same loading to their solid walls counterpart) using elastic modeling. The length of the boundary elements, longitudinal, and confinement reinforcement for all three coupled wall archetypes are summarized in Table 7.4 (columns labelled l_{be} , l_r , and c_r , respectively). The moment capacity under maximum (tensile) and minimum (compressive)

Table 7.2: Coupling beam dimensions and reinforcement layout.

| Archetype | Stories | h | b | l_{cb} | dr | hbr | tr |
|-----------|---------|---------------|--------------|---------------|--------------|-------------------|--------------------|
| 4SCW | 1 | 1524mm (60in) | 610mm (24in) | 1.83 m (72in) | 8-#11 (2x4) | #4@152mm (6in) | #4@64mm (2.5in) |
| | 2-3 | 914mm (36in) | 610mm (24in) | 1.83 m (72in) | 8-#11 (2x4) | #4@152mm (6in) | #4@64mm (2.5in) |
| | 4 | 914mm (36in) | 610mm (24in) | 1.83 m (72in) | 8-#8 (2x4) | #4@152mm (6in) | #4@64mm (2.5in) |
| 8CW | 1 | 1524mm (60in) | 610mm (24in) | 2.29 m (90in) | 12-#10 (3x4) | #4@152mm (6in) | #4@64mm (2.5in) |
| | 2-4 | 914mm (36in) | 610mm (24in) | 2.29 m (90in) | 12-#11 (3x4) | #4@152mm (6in) | #4@64mm (2.5in) |
| | 5-6 | 914mm (36in) | 610mm (24in) | 2.29 m (90in) | 12-#10 (3x4) | #4@152mm (6in) | #4@64mm (2.5in) |
| | 7-8 | 914mm (36in) | 610mm (24in) | 2.29 m (90in) | 8-#10 (2x4) | #4@152mm (6in) | #4@64mm (2.5in) |
| 12SCW | 1 | 1524mm (60in) | 610mm (24in) | 2.29 m (90in) | 8-#10 (2x4) | #4@152mm (6in) | #4@64mm (2.5in) |
| | 2-5 | 914mm (36in) | 610mm (24in) | 2.29 m (90in) | 8-#11 (2x4) | #4@152mm (6in) | #4@64mm (2.5in) |
| | 6-8 | 914mm (36in) | 610mm (24in) | 2.29 m (90in) | 8-#10 (2x4) | #4@152mm (6in) | #4@64mm (2.5in) |
| | 9-12 | 914mm (36in) | 610mm (24in) | 2.29 m (90in) | 6-#10 (2x3) | #4@152mm (6in) | #4@64mm (2.5in) |

Notes: h is the coupling beam height, b is the coupling beam thickness, dr is the diagonal reinforcement, and hbr is the horizontal beam reinforcement, and tr is the transverse reinforcement.

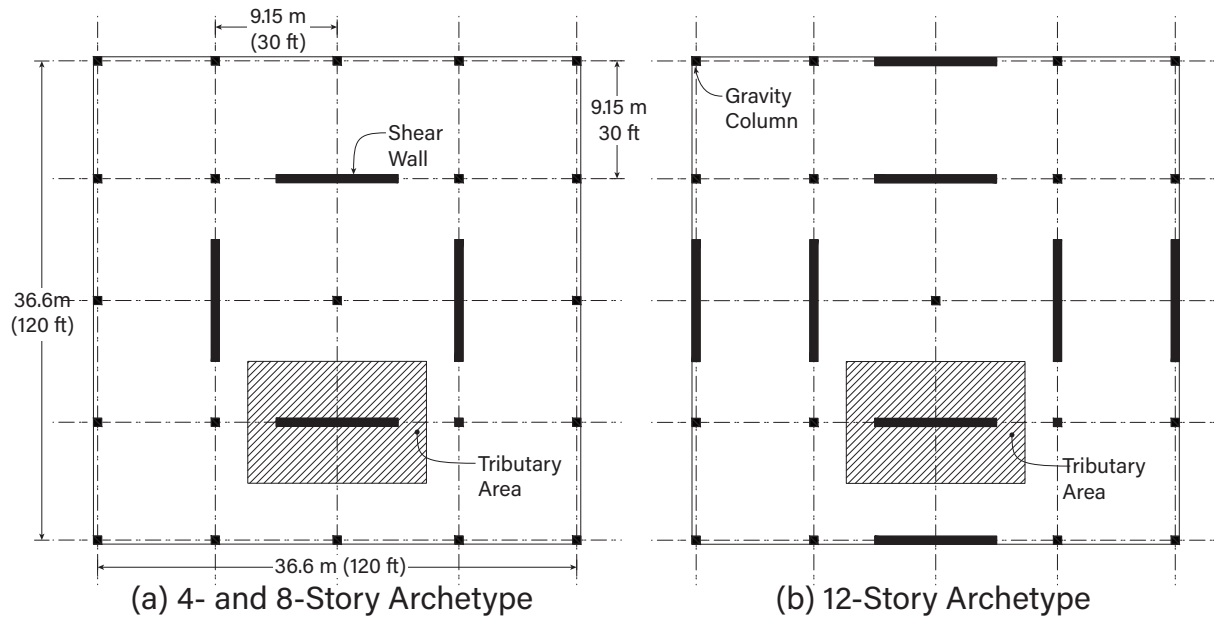


Figure 7.1: Typical floor plan for the (a) 4- and 8-story archetypes and (b) 12-story archetype.

factored axial forces (determined from an elastic static analysis) with respect to each story are shown in Figure 7.3 for all three coupled wall archetypes.

7.4 Nonlinear Modelling Methodology

7.4.1 Improving Numerical stability

The initial model was based on work by Pugh et al. (2015) using *OpenSees* (McKenna, 2016). The Pugh methodology used: (1) fiber-section force-based distributed-plasticity elements (FBE) and (2) experimentally calibrated values for unconfined and confined concrete compressive energy.

One of the primary differences between this research effort and the research conducted by Pugh was the definition of collapse. Where Pugh defined collapse based on loss of lateral resistance, this effort defined collapse as loss of the gravity system which exceeded the collapse limit that was used by Pugh (2012). As such, the analyses were terminated at a larger drift demand and numerical stability to that drift demand was required.

Table 7.3: Solid Wall Archetype dimensions and reinforcement layout.

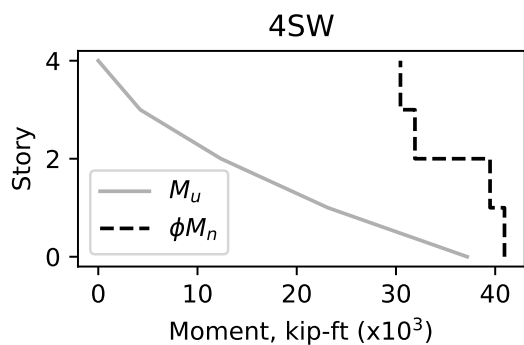
| Boundary Element A (BE _A) | | | | | | | | | |
|---------------------------------------|---------|---------------|--------------|----------------|--------------|--------|----------|---------------|--|
| Arch. | Stories | l_w | b | vwr & hw_r | l_{be} | l_r | ρ_l | c_r | |
| 4SW | 1-2 | 7.32m (24 ft) | 610mm (24in) | #4@6in (152mm) | 1.17m (46in) | 24-#9 | 2.20% | #4@76mm (3in) | |
| | 3-4 | 7.32m (24 ft) | 610mm (24in) | #4@6in (152mm) | 0.97m (38in) | 18-#9 | 2.00% | #4@76mm (3in) | |
| 8SW | 1-3 | 9.15m (30 ft) | 610mm (24in) | #4@6in (152mm) | 1.83m (72in) | 34-#10 | 2.50% | #4@76mm (3in) | |
| | 4-6 | 9.15m (30 ft) | 610mm (24in) | #4@6in (152mm) | 0.91m (36in) | 18-#10 | 2.60% | #4@76mm (3in) | |
| | 7-8 | 9.15m (30 ft) | 610mm (24in) | #4@6in (152mm) | - | - | - | - | |
| 12SW | 1-3 | 9.15m (30 ft) | 610mm (24in) | #4@6in (152mm) | 1.83m (72in) | 28-#10 | 2.10% | #4@76mm (3in) | |
| | 4-6 | 9.15m (30 ft) | 610mm (24in) | #4@6in (152mm) | 1.07m (42in) | 18-#10 | 2.30% | #4@76mm (3in) | |
| | 7-8 | 9.15m (30 ft) | 610mm (24in) | #4@6in (152mm) | 0.76m (30in) | 12-#8 | 1.30% | #4@76mm (3in) | |
| | 9-12 | 9.15m (30 ft) | 610mm (24in) | #4@6in (152mm) | - | - | - | - | |

Notes: l_w is the wall length, b is the wall thickness, vwr is the vertical web reinforcement, hw_r is the horizontal web reinforcement, l_r is the longitudinal reinforcement in the boundary element, c_r is the confinement reinforcement. *Reinforcement is placed across three layers in the boundary element.

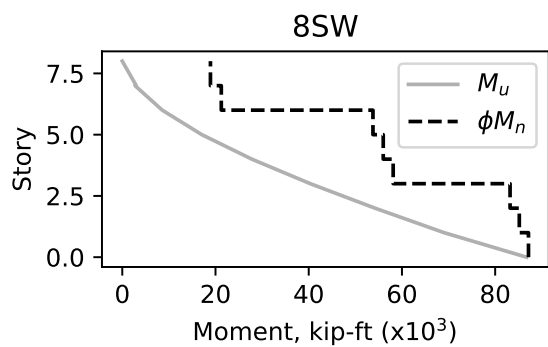
Table 7.4: Coupled Wall Archetype dimensions and reinforcement layout.

| Arch. | Stories | l_w | b | v_{wr} & hwr | Boundary Element A (BE _A) | | | | Boundary Element B (BE _B) | | | |
|-------|---------|------------------|-----------------|-------------------|---------------------------------------|---------|----------|--------------------|---------------------------------------|--------|----------|--------------------|
| | | | | | l_{be} | l_r | ρ_l | cr | l_{be} | l_r | ρ_l | cr |
| 4CW | 1-2 | 7.32m (24in) | 610mm (24in) | #4@6in (152mm) | 1.37m (54in) | 22-#11 | 2.60% | #4@89mm (3.5in) | 0.76m (30in) | 12-#8 | 1.30% | #4@76mm (3in) |
| | | | | | | | | | | | | |
| 8CW | 1-3 | 9.15m (30 ft) | 610mm (24in) | #4@6in (152mm) | 1.83m (72in) | 42-#11* | 3.80% | #4@89mm (3.5in) | 0.76m (30in) | 12-#11 | 2.60% | #4@76mm (3in) |
| | | | | | | | | | | | | |
| 12CW | 1-3 | 9.15m (30 ft) | 610mm (24in) | #4@6in (152mm) | 0.76m (30in) | 10-#10 | 1.80% | #4@64mm (2.5in) | 0.61m (24in) | 12-#5 | 0.50% | #4@76mm (3in) |
| | | | | | | | | | | | | |
| 6-8 | 4-6 | 9.15m (30 ft) | 610mm (24in) | #4@6in (152mm) | 1.37m (54in) | 39-#9* | 3.00% | #4@76mm (3in) | 0.76m (30in) | 12-#7 | 1% | #4@76mm (3.0in) |
| | | | | | | | | | | | | |
| 8-12 | 4-6 | 9.15m (30 ft) | 610mm (24in) | #4@6in (152mm) | 0.76m (30in) | 16-#9 | 2.20% | #4@76mm (3in) | 0.76m (30in) | 12-#7 | 1% | #4@64mm (2.5in) |
| | | | | | | | | | | | | |

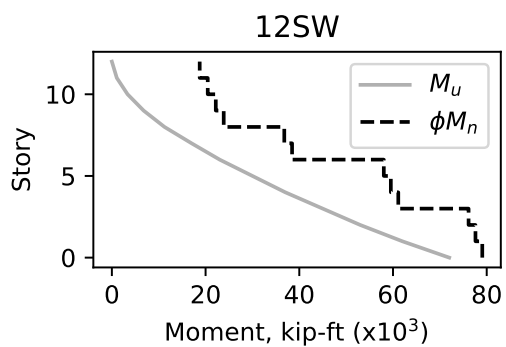
Notes: l_w is the wall length, b is the wall thickness, v_{wr} is the vertical web reinforcement, hwr is the horizontal web reinforcement, l_r is the longitudinal reinforcement in the boundary element, cr is the confinement reinforcement. *Reinforcement is placed across three layers in the boundary element



(a)



(b)



(c)

Figure 7.2: Moment strength and demand (per ELF) along the height of the (a) 4-, (b) 8-, and (c) 12-story solid wall archetype

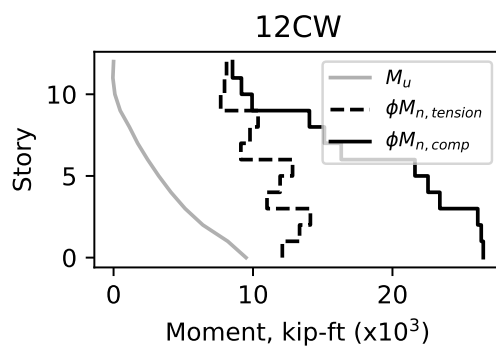
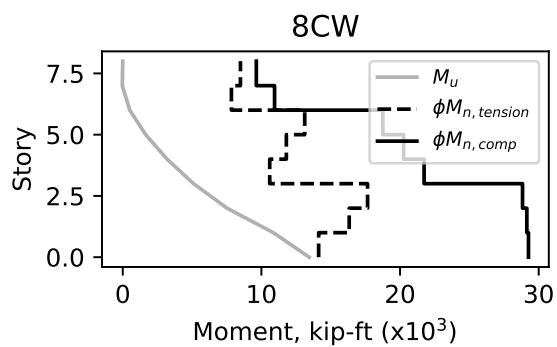
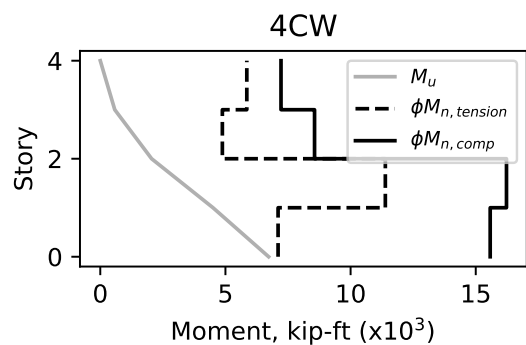


Figure 7.3: Moment strength and demand (per ELF) along the height of the (a) 4-, (b) 8-, and (c) 12-story coupled wall archetype

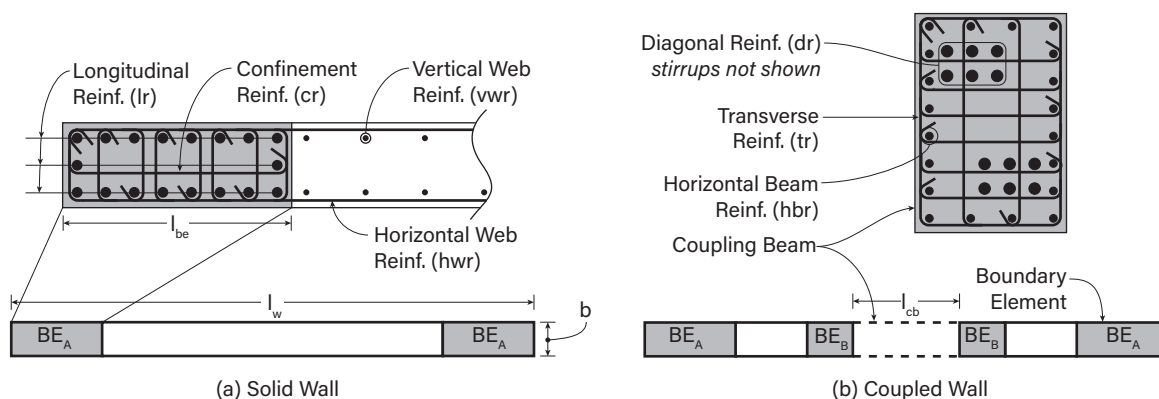


Figure 7.4: Typical detail of (a) solid wall (including boundary element region) and (b) coupled wall (including coupling beam)

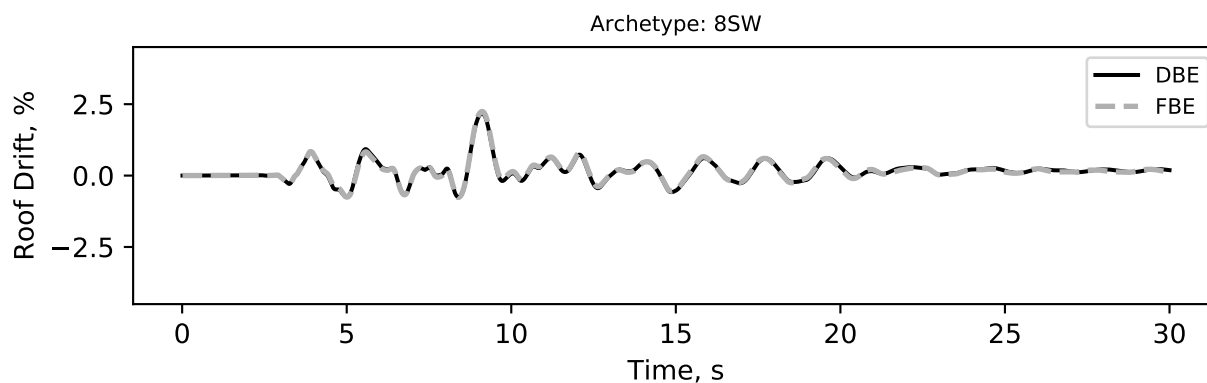


Figure 7.5: Roof-drift time history for the 8-story archetype subjected to ground-motion NGA RSN 953 at $S_a(1s)$ equal to $2g$.

To ensure this was possible, the impact of the element formulation on the instance of numerical instability was investigated. This is critical for collapse evaluation since the methodology assumes numerical instability simulates collapse, but as shown here, numerical instability can result from the element formulation with respect to the nonlinear solution algorithm.

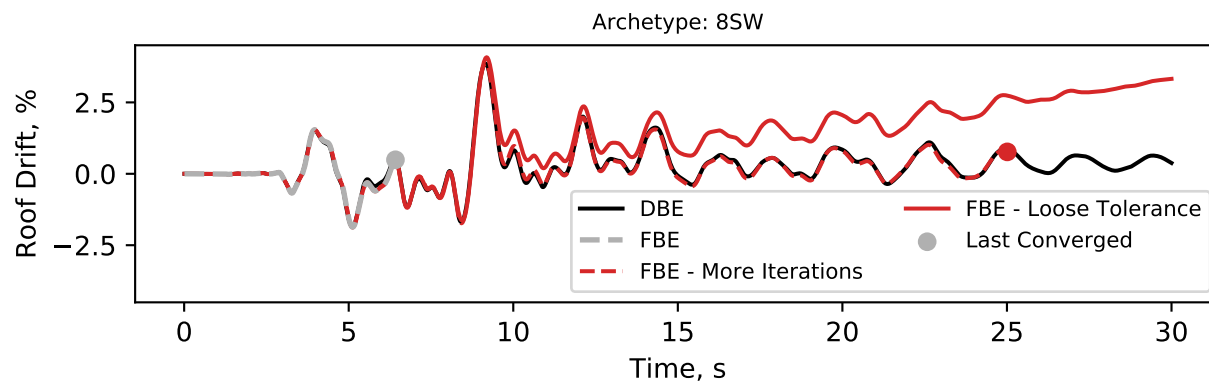


Figure 7.6: Roof-drift time history for the 8-story archetype subjected to ground-motion NGA RSN 953 at $S_a(1s)$ equal to 4g.

Figure 7.5 shows the roof-drift response history for the 8-story (8SW) archetype modelled using FBEs (dashed gray line) and DBEs (solid black line) subjected to a ground motion (NGA RSN 953 from PEER, 2014) with a spectral acceleration at 1s equal to 2g. As shown in the figure, the structural responses are nearly identical. Following the FEMA P695 methodology another analysis is conducted with the ground motion scaled to a higher intensity. Figure 7.6 shows results for analyses conducted at a higher intensity ($S_a(1sec) = 4g$) using DBE, and FBE with different element level solution parameters. The model with DBEs predicted the full response whereas the model with FBEs failed to reach a converged solution after ~6s. The FBEs analysis, either fails or the analysis completed with large errors due to a loose tolerance on the element convergence. Data in Figure 7.5 and Figure 7.6 are for a single ground motion; however similar results are observed for other motions.

Specifically, the data in Figure 7.6 show results for the FBE model with (1) an increased limit on the number of iterations to reach convergence at the element level or by (2) setting a less stringent convergence tolerance solution on the element level. Figure 7.6 shows that increasing the number of iterations (dashed red line) delays the occurrence of instability to ~25s. Increasing the convergence tolerance (less stringent) (shown as a solid red line in Figure 7.6) results in a converged solution for the entire ground motion, however, the predicted roof drifts diverge

significantly from the DBE solution. This difference is not as ideal especially for running a larger number of motions at various intensities, typically required in an incremental dynamic analysis. For these reasons, the displacement-based elements were selected for this research.

7.4.2 Model Configuration

For all walled buildings, collapse risk was assessed using 2D models with earthquake demands applied only in one direction. Figure 7.7 shows a schematic of the models for the solid and coupled walls, respectively. The solid walls and coupled wall piers were modeled using six displacement-based beam-column elements per story, with five integration points per element and applying the Gauss-Lobatto numerical integration scheme. The coupling beams used three elements over their length. The distance between the end of the coupling beam and the centerline model of the wall pier was modeled using rigid end zones. The axial and flexural response of each RC cross-section is modeled using a fiber-based approach at each integration point. Figure 7.7d and e illustrate the fiber cross-section for the walls and fiber cross-section of the coupling beams at various locations along its span.

7.4.3 Constitutive Modeling

Constitutive models are shown in Figure 7.8. Expected concrete and steel material strengths are defined as $f'_{ce} = 1.3f'_c$ and $f_{ye} = 1.17f_y$, respectively, per PEER TBI (2017). The OpenSees Steel02 material model was used to simulate the cyclic response of reinforcing steel; for this model, the stress-strain backbone curve and unload/reload paths are defined using the model by Menegotto and Pinto (1973). Steel material properties were defined as follows: modulus of elasticity, $E_s = 200$ GPa (29,000 ksi), a constant post-yield strain-hardening ratio of 0.6% (shown as parameter b in Figure 7.8), and an ultimate tensile strain of 20%.

The longitudinal reinforcing bars inside RC members exhibit excessive buckling once the surrounding concrete crushes. Pugh developed a simple model to simulate full bar buckling, using the *OpenSees* MinMax wrapper to force the reinforcing steel to lose compression and tension strength once the surrounding concrete reaches residual strain (ϵ_{res} in Figure 7.8). To

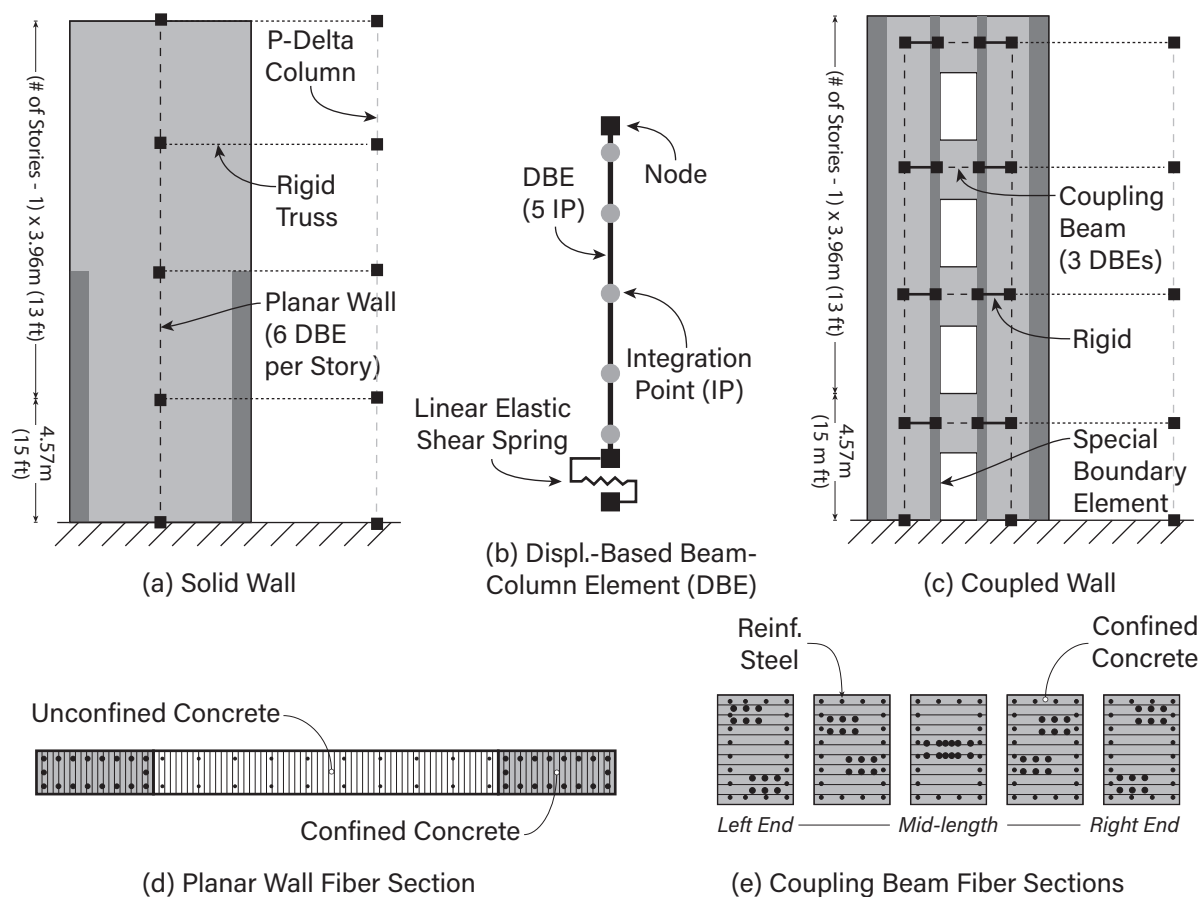


Figure 7.7: Diagram of the *OpenSees* analytical model illustrating the (a) solid wall archetypes (b) displacement-based elements (c) coupled wall archetypes (d) planar wall fiber

simulate tensile fracture of the reinforcing bars, the MinMax wrapper forces the material to lose strength once the strains exceed ϵ_{u} .

The Concrete02 material model (Yassin, 1994) was used to simulate the cyclic response of the concrete, this material model uses the Hognestad (1951) stress-strain relationship to define the pre-peak response in compression, and a linear post-peak response to the residual concrete capacity (f_{res}) as shown in Figure 7.8b. The strain at maximum stress is denoted as ϵ_p . For unconfined concrete, ϵ_p is set as $2f_p/E_c$ where E_c is defined as $4,750f_p$ MPa ($57,000f_p$ psi, as recommended

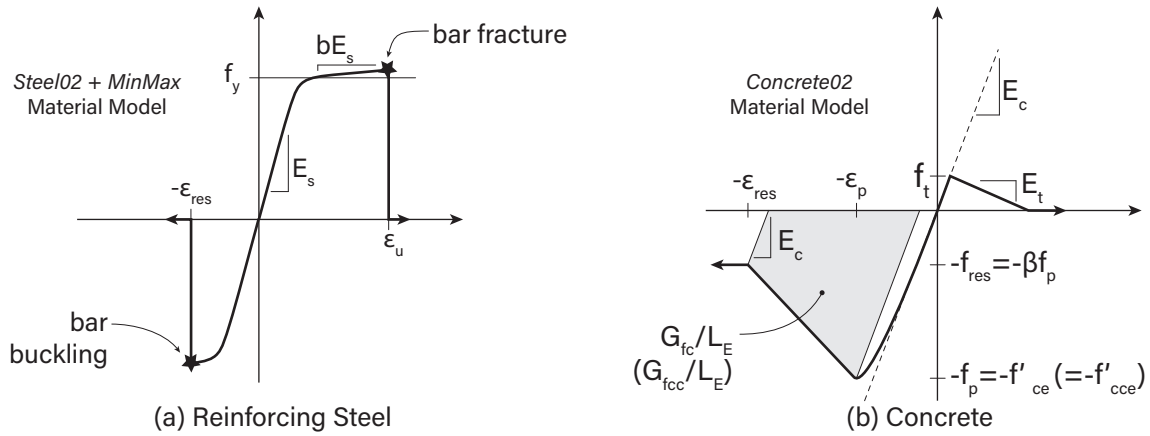


Figure 7.8: Stress-strain relationship for the fiber-section (a) reinforcing steel and (b) concrete. Confined concrete properties are shown in parenthesis.

by ACI 318-14). For the base model, the confined concrete variables $f_p = f'_{cce}$ and ϵ_p were defined using recommendations by Saatcioglu and Razvi (1992). The residual concrete capacity, f_{res} , is taken as βf_p where β is defined as 0.01 for unconfined concrete and 0.2 for confined concrete. The tensile strength is equal to $0.33f'_{ce}$ MPa ($4f'_{ce}$ psi), as per Wong et al. (2013) and a tensile softening stiffness (E_t) equal to $0.05 E_c$ (Yassin, 1994). The parameter Λ in Concrete02 is 0.1, which is the ratio of unloading slope at ϵ_p to E_c .

Birely (2012) showed that the majority of walls sustain a compression-type failure characterized by simultaneous concrete crushing and buckling of the longitudinal reinforcement. Coleman and Spacone (2001) and Pugh et al. (2015) show that when wall failure occurs and accompanying strength loss is simulated, deformations localize in the failing element or section, which results in “mesh-dependent” results if steps are not taken to mitigate this. To minimize mesh dependences, work by Coleman and Spacone (2001) and Pugh et al. (2015) regularize concrete compression softening with post-peak concrete compression stress-strain response using the concrete compressive energy (G_f) and a measure of the element mesh size. Specifically, regularized strain at onset of residual compressive strength, ϵ_{res} , is computed as,

$$\epsilon_{res} = \frac{2G_f}{(\beta + 1)f_p L_E} + \epsilon_p \frac{\beta + 1}{2} \quad (7.1)$$

where G_f is defined as the concrete crushing energy in N/mm (kips per in), is the percentage of f_p corresponding to the residual compressive strength, and L_E is the length over which softening occurs in the model. For the FBE, L_E corresponds to the length of a single integration point because the FBE formulation forces localization over a single integration point; for the DBE, L_E is length of the entire element because the DBE formulations forces localization within a single element (Coleman and Spacone, 2001).

The work by Pugh used the FBE where the modeling here uses the DBE. As such, the compressive energy (G_f) needed to be reexamined. The same approach used by Pugh was used here, with the addition of new data (published after the Pugh work was complete). First, the optimal values of G_f for the confined and unconfined concrete were determined for wall tests; the salient parameters of the specimens selected are presented in Table 7.5 from the following publications: Vallenias et al. (1979), Oh et al. (2002), Liu (2004), Thomsen and Wallace (2004), Dazio et al. (2009), Tran and Wallace (2015), and Shegay et al. (2017). All of these walls sustained a compression-controlled failure. Figure 7.9 shows the geometric mean of the ratio of $u_{pred.}$ (drift at strength loss) as predicted in *OpenSees* to $u_{exp.}$ computed from the experiment, $u_{pred.}/u_{exp.}$, for various values of G_{fc}/f'_c and G_{fcc}/G_{fc} . The resulting values were $2.0f'_{ce}$ N/mm ($0.0134f'_{ce}$ kips/in) for unconfined concrete crushing energy, G_{fc} . The results from the 15 specimens equally, the optimal crushing energy for confined concrete, G_{fcc} , was found to equal $2.2G_{fc}$.

Pugh (2012) found that the optimal confined-concrete crushing energy depends on the amount of confinement. This was explored in Figure 7.10 which plots the ratio of peak compressive stress of confined to unconfined concrete, K_c . For the data investigated, two tests exhibit a large compressive energy relative to the other tests (grey markers in Figure 7.10) and were not included in the statistical tests. The remaining data indicates that confined-concrete compressive energy values increase with K_c ($R^2 = 0.41$). It should be noted that most of the specimens with large K_c in Figure 7.10 (specimens C10, A10, A14, and A20 from Shegay et al. (2017), shown as hollow circles) were detailed with double 180-degree hooks. Due to the lack of highly confined ($K_c > 1.25$) test specimens with 135-degree hooks that are common in US practice, the base model uses a fixed G_{fcc}/G_{fc} ratio of 1.75. In addition to studying different confined concrete constitutive models, a variation of the compressive energy value is also

Table 7.5: Results comparing predicted to experimental results for various wall specimens.

| Wall Specimen ID | Reference | $G_{fcc}/G_{fc} = 1.75$ | | | Optimal G_{fcc}/G_{fc} | | | |
|------------------|----------------------------|------------------------------|------------------------------|--|--------------------------|------------------------------|------------------------------|--|
| | | $\frac{k_{pred.}}{k_{exp.}}$ | $\frac{V_{pred.}}{V_{exp.}}$ | $\frac{\delta_{pred.}}{\delta_{exp.}}$ | $\frac{G_{fcc}}{G_{fc}}$ | $\frac{k_{pred.}}{k_{exp.}}$ | $\frac{V_{pred.}}{V_{exp.}}$ | $\frac{\delta_{pred.}}{\delta_{exp.}}$ |
| S5 | Vallenas et al. (1979) | 0.78 | 1.03 | 0.9 | 2.0 | 0.78 | 1.04 | 0.96 |
| WR20 | Oh et al. (2002) | 1.30 | 0.99 | 0.47 | 4.5 | 1.31 | 0.99 | 0.89 |
| W1 | Liu (2004) | 2.12 | 1.10 | 0.77 | 3.5 | 2.06 | 1.14 | 1.15 |
| RW1 | Thomsen and Wallace (2004) | 1.39 | 1.11 | 1.08 | 1.50 | 1.38 | 1.09 | 1.01 |
| RW2 | Thomsen and Wallace (2004) | 1.65 | 1.04 | 1.21 | 1.25 | 1.82 | 1.02 | 1.09 |
| WSH6 | Dazio et al. (2009) | 1.14 | 0.92 | 0.48 | 6.00 | 1.14 | 0.92 | 0.89 |
| S38 | Tran and Wallace (2015) | 1.18 | 0.91 | 1.16 | 1.50 | 1.18 | 0.9 | 1.00 |
| S51 | Tran and Wallace (2015) | 0.81 | 1.00 | 1.35 | 1.00 | 0.82 | 0.99 | 0.92 |
| S63 | Tran and Wallace (2015) | 1.09 | 1.06 | 0.67 | 2.25 | 1.09 | 1.07 | 1.03 |
| S64 ¹ | Tran and Wallace (2015) | 0.90 | 1.28 | 3.041 | 1.00 | 0.91 | 1.24 | 2.421 |
| S78 | Tran and Wallace (2015) | 0.82 | 1.1 | 1.38 | 1.00 | 0.81 | 1.09 | 1.00 |
| C10 | Shegay et al. (2017) | 0.98 | 0.91 | 0.63 | 4.25 | 0.97 | 0.93 | 1.07 |
| A10 | Shegay et al. (2017) | 0.96 | 0.93 | 0.64 | 3.25 | 0.96 | 0.95 | 1.01 |
| A14 | Shegay et al. (2017) | 0.78 | 0.98 | 0.59 | 3.25 | 0.78 | 0.99 | 1.00 |
| A20 | Shegay et al. (2017) | 0.73 | 0.95 | 0.71 | 2.50 | 0.73 | 0.96 | 1.03 |
| | Geometric Mean | 1.06 | 1.02 | 0.81 | | 1.06 | 1.02 | 1.00 |
| | σ_{ln} | 0.13 | 0.04 | 0.16 | | 0.14 | 0.04 | 0.03 |

Note: $k_{pred.}/k_{exp.}$ is the ratio predicted to experimental initial stiffness, $V_{pred.}/V_{exp.}$ is the ratio of predicted to experimental maximum shear strength, and $\delta_{pred.}/\delta_{exp.}$ is the ratio of the predicted to experimental drift are strength loss. 1 Specimen removed prior to computing the geometric mean and σ_{ln} .

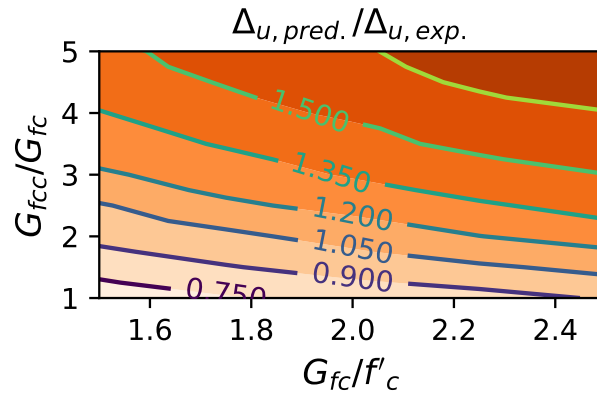


Figure 7.9: Median of the prediction to experimental for various values of G_{fcc}/G_{fc} and G_{fc}/f'_c values for 15 RC wall specimens with a compression-controlled failure mechanism.

investigated as part of the parametric study. Figure 7.11 shows a typical comparison between the measured and simulated response using the selected values of G_{fcc}/G_{fc} equal to 1.75 and G_{fc}/f'_c equal to 2.0; the model predicts the full cyclic response and strength degradation indicating that the assumed values for compressive energy are sufficient.

Shear deformations were modeled using a linear spring, as shown in Figure 7.7. The elastic shear stiffness of a cantilevered column can be estimated as GA_v/L_E where G is the shear modulus, A_v is the effective shear area, and L_E is the length of the wall element. This chapter approximates G as $0.4E_c$, as per ACI 318-14, and A_v is taken as $\frac{5}{6}l_w b$.

7.4.4 Other Modelling Assumptions

The gravity system was not modeled. Instead, a P-Delta column was used, as shown in Figure 7.7, connected to the RC wall using rigid-truss elements at every story. The P-Delta column is a rigid axial element with a pinned support. The vertical load resisted by the P-Delta column at each level is a percentage of the floor area resisted by the gravity system multiplied by the total seismic weight resisted by the wall (i.e., the remainder of the archetype's total vertical load due to gravity not resisted by the wall). The *OpenSees* models include 2% Rayleigh damping where the damping

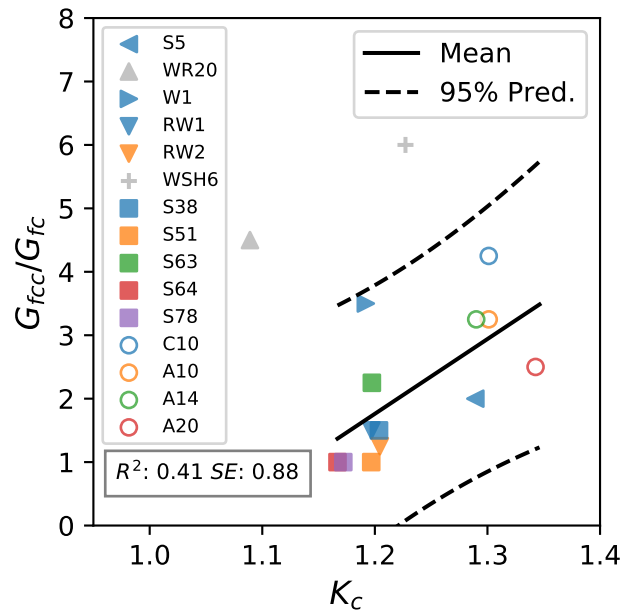


Figure 7.10: Optimal confined to unconfined crushing energy with respect to the ratio of confined to unconfined concrete peak compressive stress as predicted using Saatcioglu and Razvi (1992) for the following wall specimens: S5 from Vallenias et al. (1979), WR20 from Oh et al. (2002), W1 from Liu (2004), RW1 and RW2 from Thomsen and Wallace (2004), WSH6 from Dazio et al. (2009), S38, S51, S63, and S78 from Tran and Wallace (2015), and C10, A10, A14, and A20 from Shegay et al. (2017).

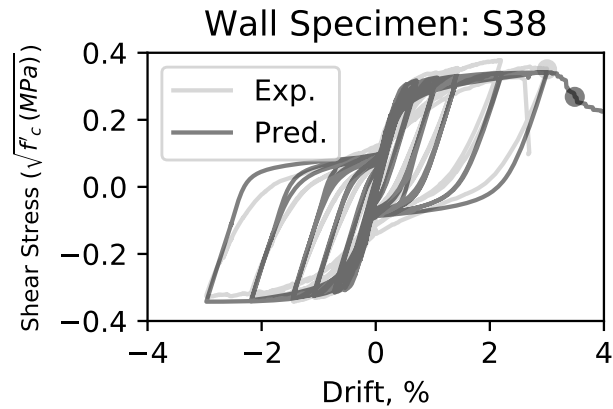


Figure 7.11: Experiment and *OpenSees* prediction (using $G_{fc}/f'_c = 2$ and $G_{fcc}/G_{fc} = 1.75$ for wall specimen S38 from Tran and Wallace (2015) (solid circles indicate the drift at significant strength loss)

coefficients are computed using the first two modes and are assigned to both the mass and initial stiffness matrix in *OpenSees*.

7.5 Collapse Probability at MCE for Archetypes: Base Model and Parametric Study

7.5.1 Method to Determine Probability of Collapse at MCE

The methodology described in FEMA P695 was used to predict the probability of structural collapse at the Maximum Considered Earthquake (MCE) for the walled buildings. The steps are as follows:

Conduct incremental dynamic analyses. For each ground motion, conduct an incremental dynamic analysis (IDA) for all six building archetypes. Use the 22 ground-motion pairs defined by the FEMA P695 (2009) report. An IDA (shown in Figure 7.14) comprises of nonlinear dynamic analyses using ground-motion recordings scaled to increasing intensity levels until structural collapse is simulated (Vamvatsikos and Cornell, 2002).

Quantify collapse. Collapse may occur due to a side-sway mechanism that results in dynamic instability, where the lateral drift of the building increases essentially without bound when



Figure 7.12: Partial building collapse due to failure slab-column connections after the 1994 Northridge Earthquake (photo by NOAA/NGDC, J. Dewey, U.S. Geological Survey).

ground-motion spectral acceleration is increased by a small amount (Haselton et al., 2011b), this is also referred to as the IDA “flat lining”). In addition to this global P-delta instability, structures may exhibit partial collapse due to the failure of components in the gravity system (e.g., Figure 7.12 is an example of partial building collapse after the 1994 Northridge earthquake). For slab-column systems (the most common gravity system) used with RC walls, prior experimental tests can be used to establish their drift capacity (e.g., Hueste et al., 2009; Matzke et al., 2015), and are summarized in Figure 7.13. For lower gravity-shear ratios (ratio of the shear resulting from gravity loads to the shear design capacity), the story drift at which gravity load carrying capacity is lost ranges from 3% to 7%. This dependence on the gravity-shear ratio is not considered here. Instead, a 5% inter-story drift capacity was considered for a base case for all archetypes which corresponds to the median drift capacity for slab-column connections with reinforcement. The parameter study investigates the impact of the drift capacity on collapse risk.

Develop Collapse Fragility Curves. Using the IDA results a fragility curve was computed that predicts the probability of collapse as a function of spectral acceleration, where collapse is defined by an inter-story drift that exceeds 5% as discussed above (Figure 7.14). Instances where the analysis failed to converge and where the previous analysis (previous S_a increment) resulted in a max. inter-story drift less than 5% drift, the structure was deemed to have collapsed due to

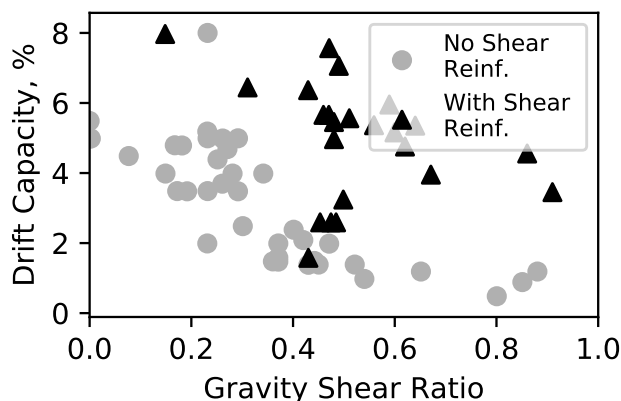


Figure 7.13: Drift capacity of slab-column connections with and without shear reinforcement with respect to gravity shear ratio (data from Matzke et al. 2015).

non-convergence (Vamvatsikos and Cornell, 2002). Note that for all archetypes but 12CW, non-converged analyses occurred at S_a values that are larger than $S_{a,MCE}$, therefore this only slightly impacting the collapse probability at $S_{a,MCE}$. For the 12CW archetype only one analysis failed to converge before S_a . The distribution of spectral acceleration at collapse for each archetype is then fitted to a lognormal distribution to compute the cumulative distribution function of S_a at collapse (i.e., collapse fragility curve).

Determine Collapse Probability. Using the S_a value for MCE (at $C_u T_a$ which is used as an approximate value for the fundamental period of the structure), determine the probability of collapse from the archetype-specific fragility curve (Figure 7.15).

This section presents the results of the base model using this methodology. The remaining sections present the impact on the calculated probability of collapse at MCE if select parameters are changed.

7.5.2 Collapse Probabilities at MCE: Base model

The results of IDAs of the 8-story base models are shown in Figure 7.14. These IDA results are used to compute the collapse fragility as a function of the spectral acceleration resulting in collapse for

the 44 ground-motions (shown with a dot for each analysis in Figure 7.14). Figure 7.15 shows the resulting collapse fragility curves for all archetypes, and the probability of collapse at the MCE spectral acceleration (indicated with a black dot); also listed in Table 7.6. The collapse probability at MCE for the 4-, 8-, and 12-story solid wall archetypes are 2.3%, 0.91%, and 2.9%, respectively. For the coupled walls, the collapse probabilities are 11.6%, 8.7%, and 6.9% for the 4-, 8-, and 12-story archetypes, respectively. Note that the fragility curves between archetypes are not comparable because they are conditioned on different period ($C_u T_a$). However, Figure 7.15 shows that these collapse probabilities are within the target 10% probability of collapse for S_a values corresponding to the maximum considered earthquake (ASCE 7-16), shown as a solid black dot.

The collapse probability of the coupled walls is larger because the coupling action increases the compression loads in the "compression pier", over the gravity-induced compression load carried by the planar wall, and resulted in a compression-controlled failure at a lower ground motion intensity level. Where the axial load ratios, $P/(A_w f'_{ce})$, in the 4-, 8-, and 12-story coupled walls due to gravity and earthquake loadings were 12, 20, and 18% from an elastic analysis under ELF, respectively; compression demands increased to 16, 25, and 28% on average (later discussed in Figure 7.27) when subjected to ground-motion at the MCE S_a intensity. As expected, compressive piers with axial load ratios above 30% will lose significant strength following spalling (Lehman et al., 2013).

7.5.3 Impact of Element Formulation on Collapse Probability

As discussed previously, the probability of collapse depends on the element formulation used, as the FBE formulation may cause a "failure to converge" at the element level that results in an assumed collapse state. For all six archetypes, an IDA was performed using the FBE formulation, as per the recommendations of Pugh et al. (2015). Figure 7.17 shows a comparison of the IDA results for a 4-story coupled wall archetype modelled using DBE (Figure 7.17a) and FBE (Figure 7.17b). The data shows that when the FBE is used, many of the analyses are unable to reach convergence (shown as red dots) at higher drifts and/or intensity levels. At these points, the archetypes are assumed to have collapsed due to non-convergence (Vamvatsikos and Cornell, 2002). This assumption is shown to result in a lower collapse spectral acceleration prediction

Table 7.6: Percentage change in collapse probability for studied values of modelling and design parameters.

| Parameter Type | Parameter Value | Solid | | | Coupled | | |
|--|----------------------------|-------------|--------------|-------------|-------------|-------------|-------------|
| | | 4-Story | 8-Story | 12-Story | 4-Story | 8-Story | 12-Story |
| Base Model - Probability of Collapse | | 2.2% | 0.89% | 2.8% | 11.3% | 8.7% | 6.5% |
| Element | Force-Based Elements | 15% | 1569% | 734% | 66% | 65% | 83% |
| Confined Concrete Model | Mander et al. (1988) | 5% | 9% | 1% | 2% | -1% | 9% |
| | Richart et al. (1928) | 19% | 46% | -3% | 6% | 8% | 26% |
| Concrete Residual Strength | $\beta=0.05$ | 8% | 11% | 19% | 16% | 156% | 143% |
| | $\beta=0.10$ | 6% | 10% | 18% | 8% | 90% | 90% |
| | $\beta=0.05, \beta_w=0.05$ | 6% | 9% | 18% | 13% | 118% | 73% |
| | $\beta=0.10, \beta_w=0.10$ | 0% | 7% | -1% | 4% | 17% | 9% |
| | $\beta=0.20, \beta_w=0.20$ | 0% | -2% | -6% | -9% | -33% | -41% |
| Unconfined Concrete Compressive Energy | $G_{fc}/f'_{ce} = 1.5$ | 1% | 1% | 4% | 5% | 0% | 6% |
| | $G_{fc}/f'_{ce} = 2.5$ | 0% | 0% | -5% | -1% | -7% | -8% |
| Confined Concrete Compressive Energy | $G_{fcc}/G_{fc} = 1.5$ | 0% | 0% | 1% | 1% | -1% | 2% |
| | $G_{fcc}/G_{fc} = 2.5$ | -1% | -1% | -5% | -1% | -6% | -5% |
| | $G_{fcc}/G_{fc} = 3.0$ | -1% | -1% | -6% | -3% | -12% | -14% |
| Ultimate Steel Strain | $\epsilon_{ult}=5\%$ | 157% | 158% | 22% | 64% | 41% | 27% |
| | $\epsilon_{ult} = 10\%$ | 31% | 11% | 2% | 1% | 1% | 3% |
| | $\epsilon_{ult} = 15\%$ | 3% | 1% | 0% | 1% | 0% | 0% |
| Wall Axial Load | x0.5 | 20% | 67% | 15% | 2% | -16% | -31% |
| | x1.5 | -12% | 41% | 22% | -1% | 42% | 55% |
| | x2.0 | -21% | 290% | 139% | 6% | 108% | 178% |
| Wall Thickness | x1.5 | -56% | 25% | -82% | -68% | -67% | -54% |
| | x2.0 | -39% | -7% | -97% | -85% | -79% | -69% |
| | x3.0 | -43% | -54% | -98% | -97% | -89% | -95% |
| Non-simulated Collapse Criteria | Max. ISD = 3% | 240% | 850% | 362% | 139% | 144% | 211% |
| | Max. ISD = 7% | -40% | -52% | -54% | -28% | -16% | -12% |
| | Max. ISD = 10% | -32% | -41% | -57% | -45% | -20% | -20% |

Notes: Changes in collapse probability above 100% are shown in bold.

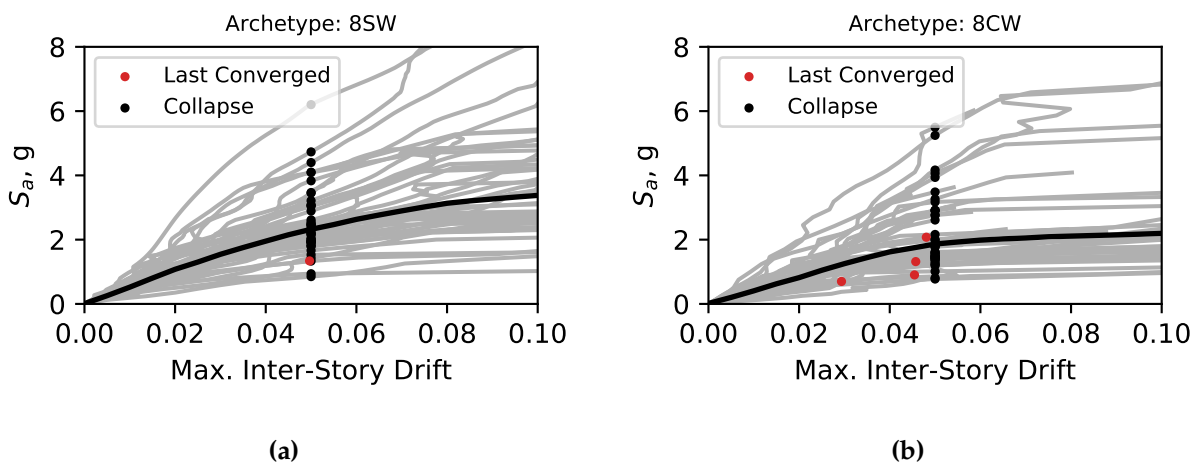


Figure 7.14: Incremental dynamic analysis results for the (a) 8SW and (b) 8CW archetype using the reference modeling approach. The black line indicates the median S_a at a given max. inter-story drift.

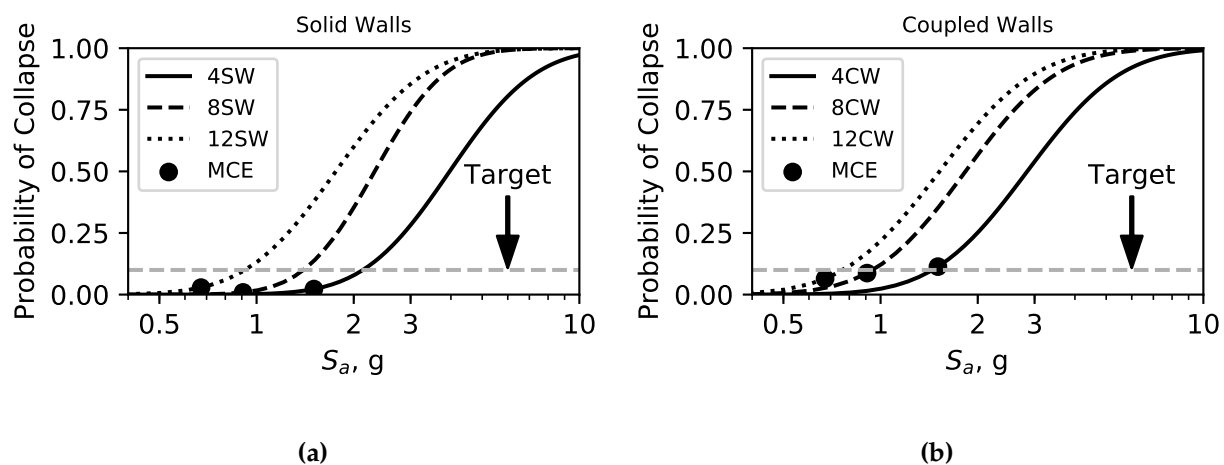


Figure 7.15: Collapse Fragilities for the (a) solid and (b) coupled wall archetypes. using base model.

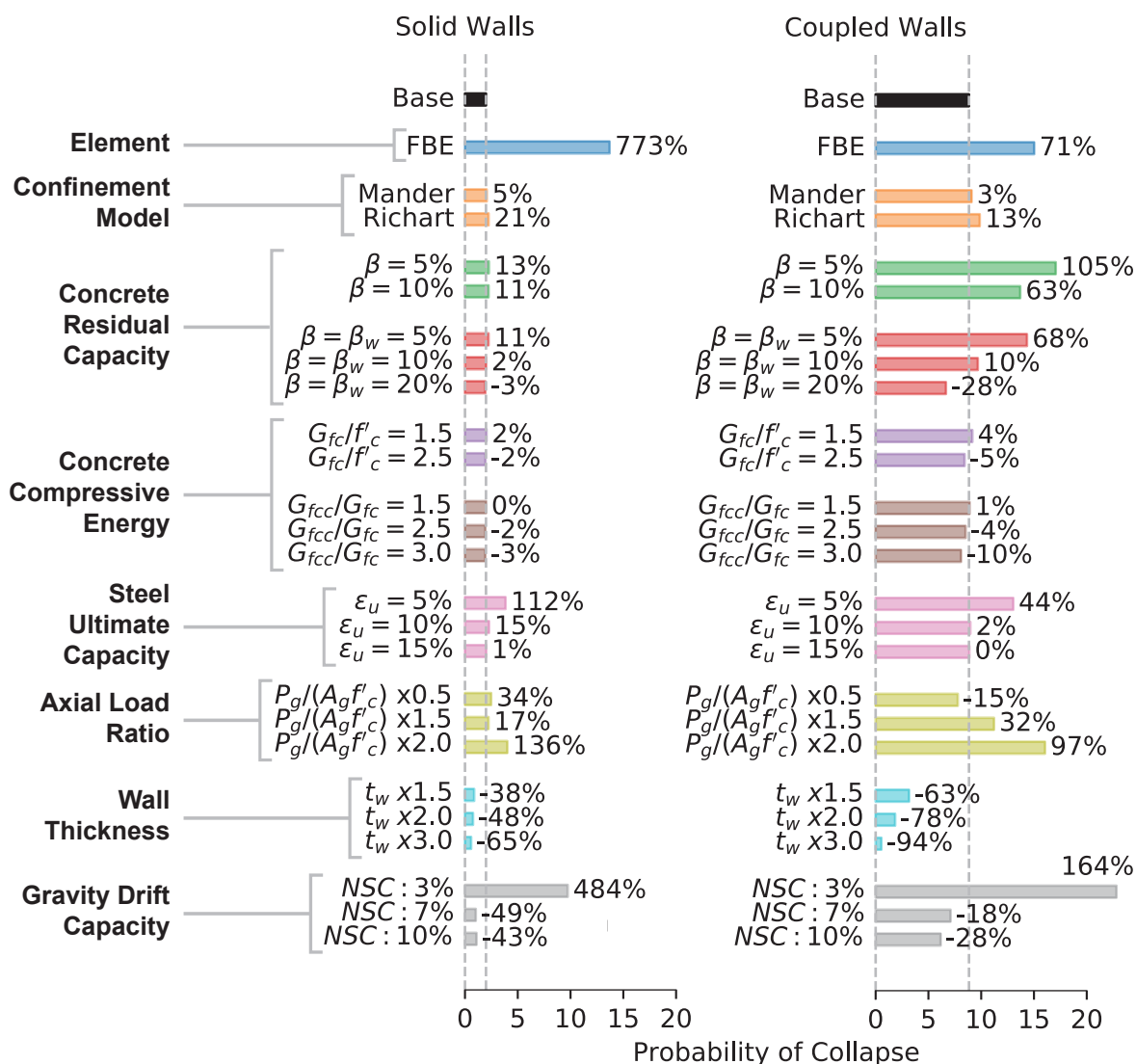


Figure 7.16: The average change in the probability of collapse at MCE for (a) solid wall archetypes and (b) coupled wall archetypes (percentages near the bars indicate the percentage change from the base model). Note that the top bar (solid black) corresponds to the base model and the length of each of the bars corresponds to the probability of collapse.

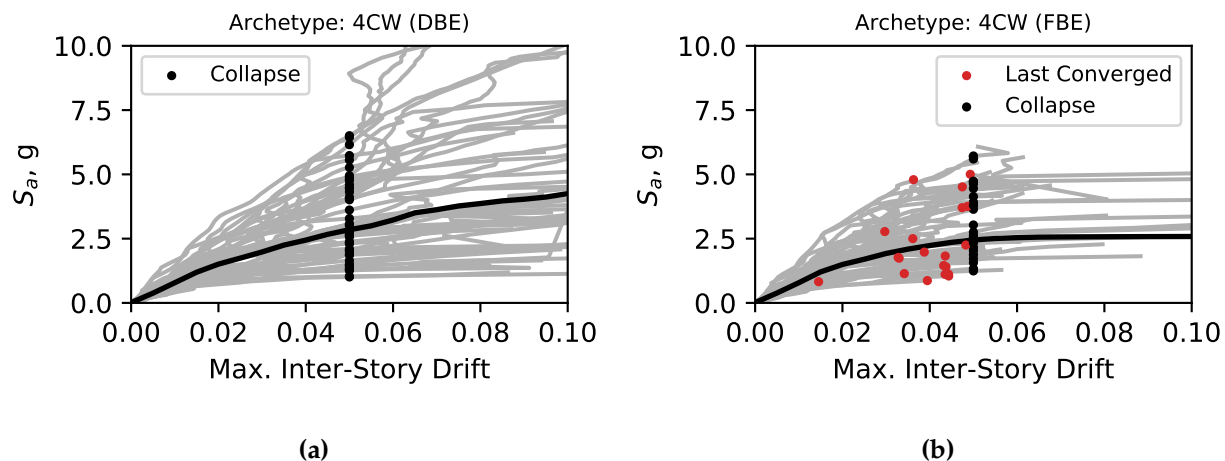


Figure 7.17: Incremental dynamic analysis results for a 4-story coupled core wall (4CW) modelled using (a) displacement-based elements and (b) force-based elements in *OpenSees*.

for the FBE than the DBE formulations (Figure 7.17a), similarly, others (e.g., Chandramohan et al., 2017) have noted similar trends. This reduction in S_a at collapse produces a higher collapse probability at the MCE where the percentage change in collapse probability is listed in Table 7.6.

The three archetypes for each system are taken as a performance group where Figure 7.16 shows the average probability of collapse at MCE for the solid and coupled walls separately. The length of the bar indicates the probability of collapse (corresponding to the value on the x axis) and the number adjacent to the bar indicates the percent change in the probability of collapse relative to the base case. The results show that the collapse probability would significantly increase (> 100%) for both the solid and coupled wall archetypes if FBE is used instead of DBE.

7.5.4 Impact of Concrete Response on Collapse Probability

There are many empirical compressive stress-strain response models for confined concrete. Here three models (the base model and two others) were studied: (1) Richart et al. (1928), (2) Mander et al. (1988), and (3) Saatcioglu and Razvi (1992), which is used in of the base model. Each model was used to predict parameters f_p and ϵ_p (shown in Figure 7.7) for the confined concrete region.

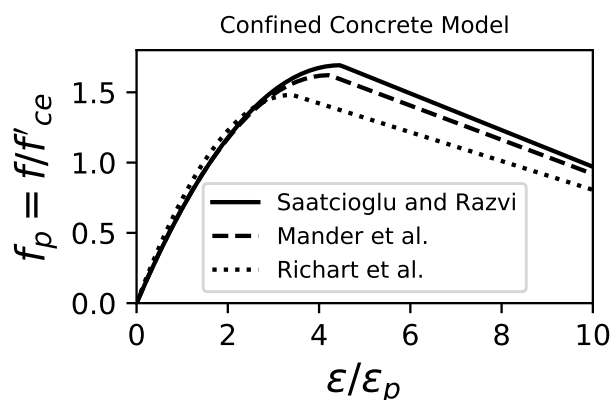


Figure 7.18: Stress-strain relationship of confined concrete using the Saatcioglu and Razvi (1992) model, Mander et al. (1988), and Richart et al. (1928) model to predict the confined concrete stress and strain.

Figure 7.18 compares the stress-strain relationship for the three confined concrete models for the boundary element of the 8-story solid wall. The peak compressive strength and strain predicted using Mander et al. is only 4% lower than that predicted by Saatcioglu and Razvi (base) model, whereas, the Richart et al. model predicts a 12% lower peak strength and a 24% smaller strain than the Saatcioglu and Razvi (base) model.

Figure 7.19 shows normalized base shear with respect to roof drift from a pushover analysis for all three confined concrete models for the two 8-story archetypes. Lateral loads are distributed based on the first mode contribution factor at each story level. The pushover results are shown for the 8-story solid archetype (8SW) and coupled wall archetype (8CW), with the base case shown in red. The onset of strength loss is reduced in the coupled archetype due to concrete crushing and bar buckling that resulted from the increased axial load due to coupling action (also cited in Mahin and Bertero, 1976; Aktan and Bertero, 1987; Lehman et al., 2013). However, the effects of the confined concrete models show: (1) the strength is unchanged, (2) no change in P-delta response prior to the onset of strength loss, and (3) change in response once the onset of strength loss occurs. For 8SW, the drift at strength loss is shown to vary between the three confined concrete

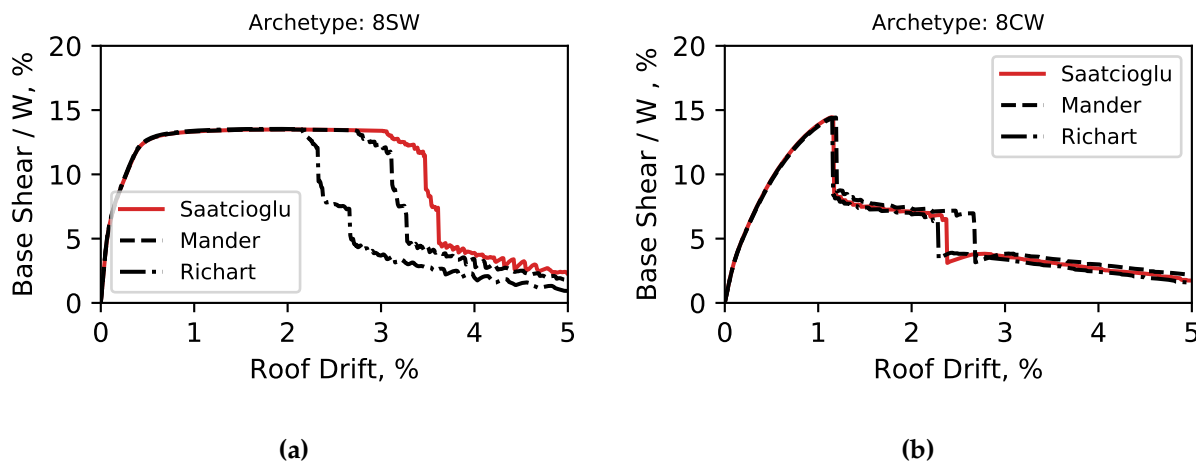


Figure 7.19: Pushover of 8SW using the (a) Saatcioglu and Razvi model and the (b) Mander et al. model to predict the confined concrete stress and strain (red lines show base model).

models (3.3% for Saatcioglu, 3.0% for Mander, and 2.3% for Richart), however, for 8CW, the drifts at strength loss were found to be similar for the three models. This is due to the fact that in a coupled wall system, the compression region extends to the web region in the “compression pier” (illustrated in Figure 7.20) therefore the pushover response is less sensitive to variations in the maximum compressive strength in boundary element region. Similar observations were found for the 4- and 12-story archetypes. The results shown in Figure 7.16 indicate that the probability of collapse increases by 21% for the solid walls and 13% for the coupled walls on average if the Richart model is used.

7.5.5 Impact of Concrete Residual Strength on Collapse Probability

Evaluation of simulation data shows walls can sustain significant lateral loads at large drift demands due to the concrete residual compression capacity (f_{res} in Figure 7.8b). However, most laboratory tests do not continue to full loss of lateral load carrying capacity, so data are not available for calibration of the residual concrete compressive strength. The impact of $f_{res} = \beta f_p$ on collapse probability was explored as part of this study. A review of previous research shows

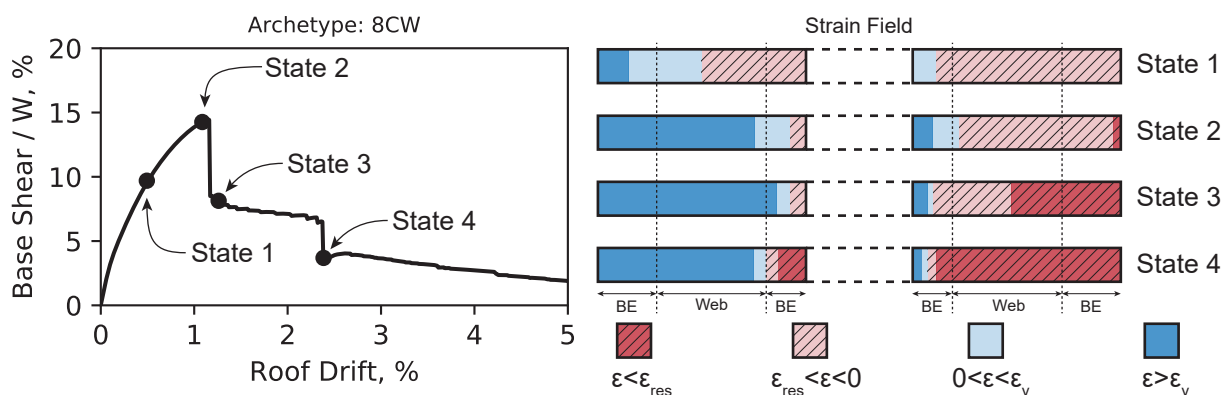


Figure 7.20: Strain field of the coupled wall piers (Archetype: 8CW) at multiple drift states under monotonic loading (boundary element is abbreviated as BE).

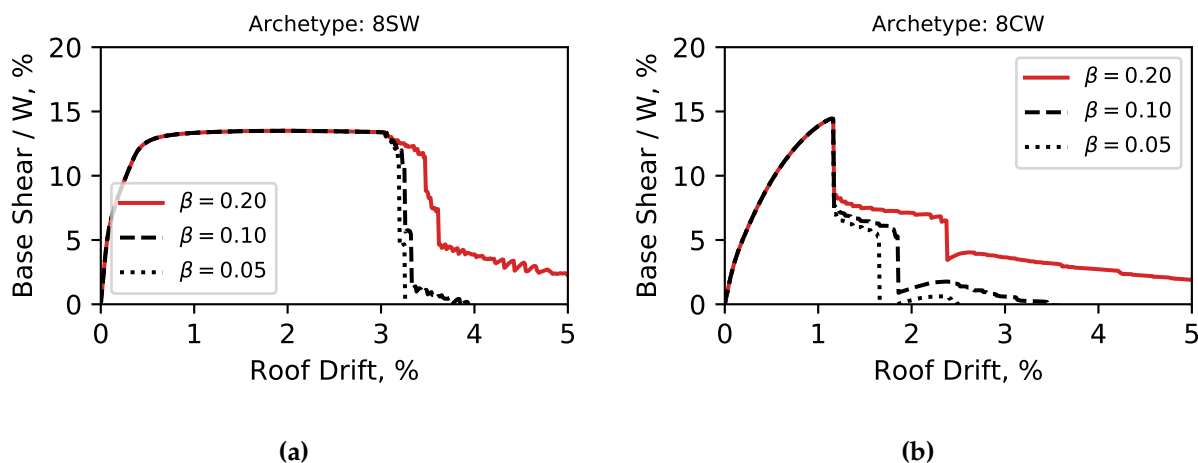


Figure 7.21: Pushover response for the 8-story (a) solid and (b) coupled wall archetype with varying concrete residual strengths.

significant variation in the definition of f_{res} , Park et al. (1982), Saatcioglu and Razvi (1992), and others proposed $\beta=20\%$; others including Vallenias et al. (1979), Shegay et al. (2017) propose $\beta=30\%$. Chang et al. (2014) proposed $\beta=0\%$.

Here, the impact of boundary element (BE) and web concrete f_{res} was investigated. For B.E. concrete, β of 5%, 10%, and 20% (20% is the value used in the base model) and the residual strength of the web concrete β of 1% is considered for all cases. Figure 7.21 shows pushover results for the 8-story archetypes for different β values. As expected, very low values of β result in low residual wall strength past peak. Figure 7.16 shows a reduced β results in an increased collapse probability at MCE. The increase in collapse risk is significant for the coupled wall archetypes, where collapse is determined by compression failure of the compression pier. Again, it is postulated that the dependence on the compression pier for strength and deformability makes this system vulnerable to collapse with poor concrete response.

In addition to considering the impact of residual concrete strength in the boundary element, the residual strength of the web concrete was also investigated. The base model assumes a web concrete has a residual compressive strength of $f_{res} = 0.01f_p$ (i.e., β_w , of 1%). If cross-ties are used in the web, this value may underestimate the residual capacity. Therefore, $\beta_w = 20\%$ and 5% were considered with $\beta = 20\%$ and 5% . Figure 7.22 shows push over curves for the 8-story solid and coupled walls. The data show that for large β in the BE, β_w significantly affects post-peak response. However, for low values of β , all values of β_w result in similar push over curves.

The data in Figure 7.15 show that the average collapse probability was reduced by 3% for the solid walls and 28% for the coupled walls when $\beta_w = \beta = 20\%$. For cases when $\beta = \beta_w = 5\%$, and $\beta = 5\%$ and $\beta_w = 1\%$, the collapse probabilities were found to increase similarly. This indicates that values of residual strength below 5% of f_p would result in similar collapse performance. This outcome is consistent with the changes in drift capacity observed in Figure 7.22. In practice, confining the longitudinal reinforcement in the web may increase the residual compressive strength of the web which would reduce the collapse probability at MCE. Figure 7.15 shows that the β and β_w cause similar trends with respect to collapse probability for the solid and coupled walls, however, β and β_w are much more important for the coupled walls.

7.5.6 Impact of Concrete Compressive Energy on Collapse Probability

Accurate numerical simulation of strength loss in RC systems requires regularization of the concrete compressive response using the concrete crushing energy. Experimental data (Figure

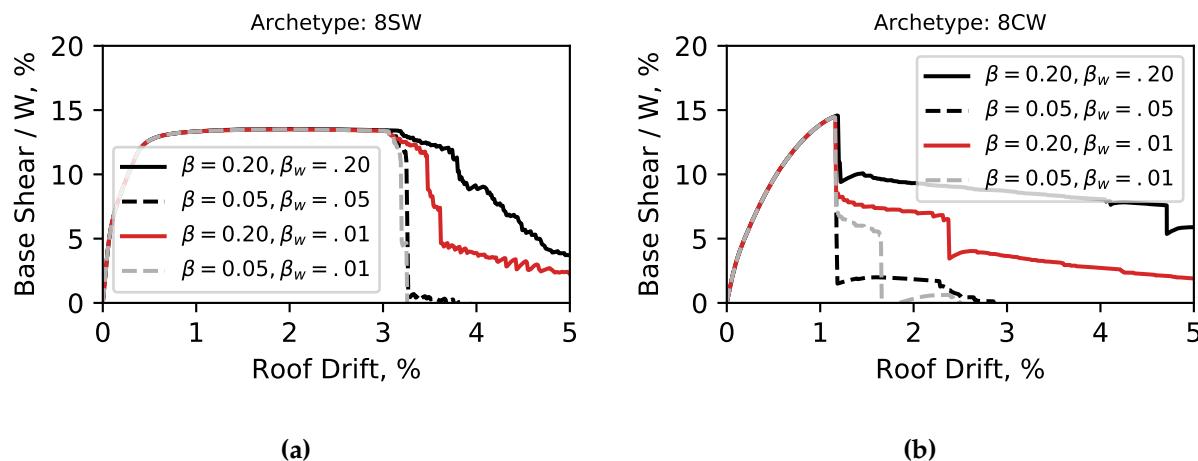


Figure 7.22: Pushover response for the 8-story (a) solid and (b) coupled wall archetype with varying concrete residual strengths in the boundary element and web region (red line shows base model).

7.9) indicate that the ratio of G_{fc}/f'_c ranges from approximately 1.5 to 2.5. In this study, $G_{fc} = 2f'_c$ was used in the base model and impact of G_{fc} varies from $1.5f'_c$ to $2.5f'_c$ was investigated. Figure 7.23 shows that for the solid and coupled 8-story archetype, a 67% increase in crushing energy (1.5 to 2.5) resulted in only a ~11% increase in drift corresponding to loss of lateral load carrying capacity. In addition, data in Table 7.6 show that the collapse probability does not significantly change (within 8%) with varying values of the unconfined compressive energy.

The same analysis was conducted investigating the impact of the confined compressive energy, typically expressed as a ratio of the unconfined compressive energy. To study the sensitivity of the confined crushing energy, G_{fcc}/G_{fc} was given values of 1.5, 1.75 (base model), 2.5, and 3.0 which is the range of optimal values shown in Figure 7.10. Figure 7.24 illustrates the effects in terms of the pushover response of the 8-story continuous and coupled wall archetype. Changing this ratio has a smaller impact on the push-over curves (especially for the coupled walls) and probabilities of collapse (within 14% as shown in Table 7.6) than other parameters thus the analysis results are stable with respect to G_{fcc} and G_{fc} .

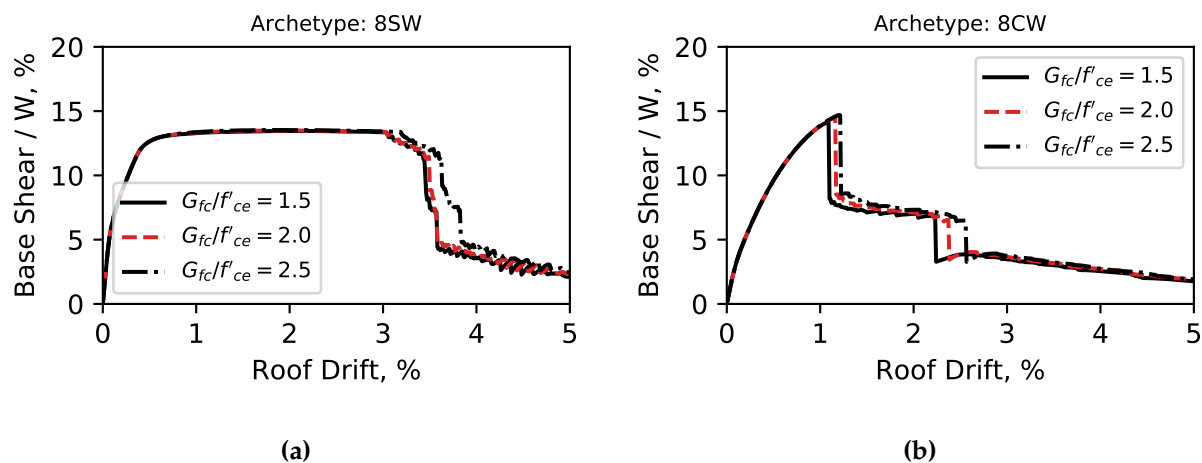


Figure 7.23: Normalized base shear with respect to roof drift for an 8-story (a) continuous wall archetype and (b) coupled wall archetype with varying values of G_{fc}/f'_{ce} (red line shows base model).

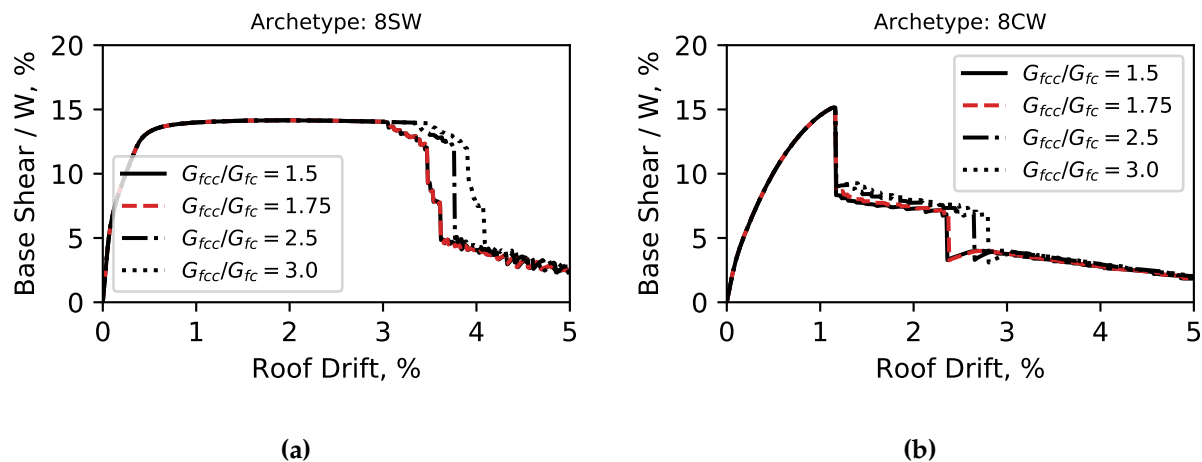


Figure 7.24: Normalized base shear with respect to roof drift for the 8-story (a) continuous and (b) coupled wall archetype assuming various values of G_{fcc}/G_{fc} (red line shows base model).

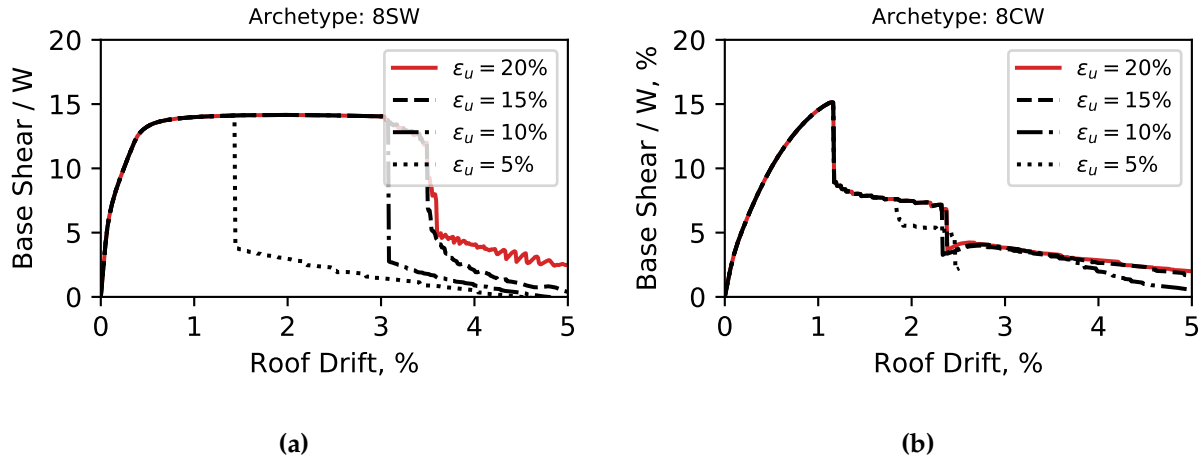


Figure 7.25: Pushover of archetype (a) 8SW and (b) 8CW with varying the ultimate strain of the reinforcing bars (red line shows base model).

7.5.7 Impact of Ultimate Steel Strain on Collapse Probability

ACI 318-14 permits the use of ASTM A615 and A706 reinforcing steel bars in seismic regions. Bournonville et al. (2004) found that under monotonic loading the ultimate strain is, on average, 12.7% (2.5% standard deviation) for ASTM A615 Grade 60 steel and 14.8% (1.8% standard deviation) for ASTM A706 Grade 60 steel. Under cyclic loading, the ultimate strain depends on the applied strain history. For example, Aragon et al. (2017) found that A706 Grade 60 bars fractured at 5% strain due to low-cycle fatigue. The Tall Building Initiative guidelines limit the ultimate strain capacity in reinforcing steel to 5% to account for the effects of low-cycle fatigue.

In this study, the base model employs $\epsilon_u = 20\%$ and the impacts of $\epsilon_u = 5\%$, 10%, 15% and 20% on wall collapse probability was investigated. Data in Figure 7.25 show for the solid wall $\epsilon_u = 5\%$ caused a significant reduction in drift capacity and only a slight reduction for $\epsilon_u = 10\%$ and 15%. These results follow from the fact that wall response is compression controlled for the coupled walls and solid walls with $\epsilon_u = 10\%$ and 20%, so ϵ_u has minimal impact on response. Data in Table 7.6 show that using $\epsilon_u = 5\%$ significantly increase (more than 50%) the collapse probability

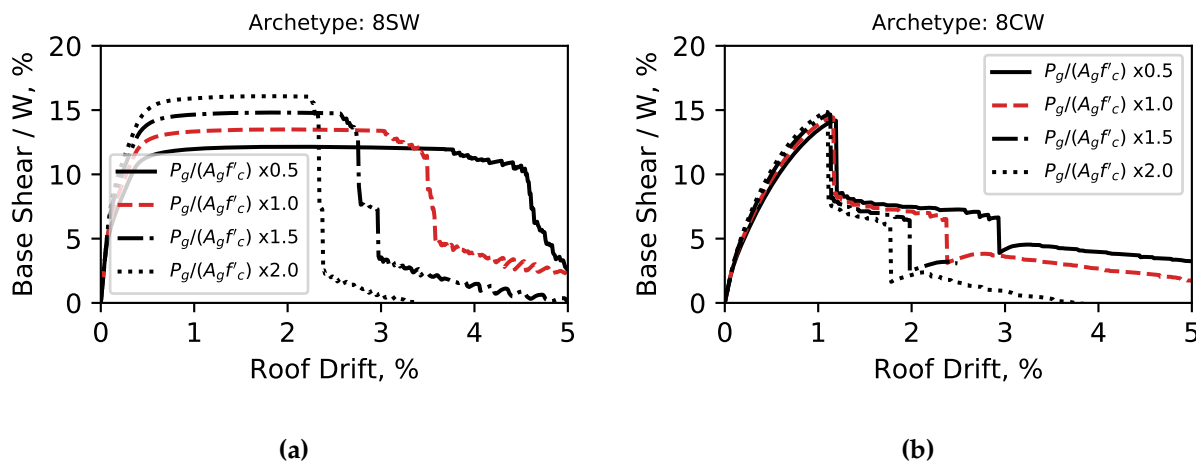


Figure 7.26: Pushover varying axial load ratio due to gravity forces (red line shows base model).

of the shorter building (4SW, 8SW, and 4CW), suggesting that setting $\epsilon_u = 5\%$ changes the failure more from compression to tension failure for these walls.

7.5.8 Impact of Wall Axial Load Ratio on Collapse Probability

Shegay et al. (2017) studied walls with low to moderate axial-load ratios and found that drift capacity was reduced for higher axial load ratios. Although increased compression load is known to reduce drift capacity in RC components, ACI 318 does not limit wall axial load. To study the impact of larger axial load on wall response, wall axial load due to seismic-weight was modified from the base wall by 50%, 150%, and 200%. The pushover response histories for the 8-story archetypes are shown in Figure 7.26. The axial load ratio has a significant impact on the solid wall archetype; for the coupled walls, the impact of axial load ratio on the peak response is minimal and axial load only impacts post-peak degradation at larger drift levels. This is similar to the findings found by Grammatikou et al. (2015). Figure 7.15 and Table 7.6 show that increasing the axial load ratio by a factor of 2 significantly increases the collapse probability for the 8- and 12-story solid and coupled walls. In contrast, reducing the axial load on the 8- and 12-story coupled systems decreases the collapse probability by 16 and 31%, respectively.

7.5.9 Impact of Wall Thickness on Collapse Probability

Current ACI 318 code requirements do not specify limits on wall axial load, however, increased axial load reduces flexural drift capacity. New Zealand building codes (NZS 3101.1&2:2006 A3 §11.4, 2015) recognize this through (1) limits on axial load ratios in walls and (2) account for additional compressive forces that develop in wall piers due to material over-strength in the coupling beams that are not captured in an elastic analysis. As a result of this, coupled wall piers in New Zealand may have a larger cross-sectional area compared with those designed using ACI 318. In this section, the change in collapse probability is computed for a wall with larger cross-sectional areas by increasing wall thicknesses.

The probability of collapse at MCE for the coupled wall was found to be approximately 4 times larger for the coupled archetypes as compared to the solid wall archetypes. This increase is attributed to compression failure of the pier at lower drift levels. Figure 7.27 shows a "box-and-whisker" plot for the maximum axial load ratio at MCE for both the solid and coupled archetypes. In these plots, the box (shown in black) extends to the lower and upper quartile values of the normalized axial load ratio, the single horizontal line within the box (shown in orange) corresponds to the median stress ratio, and the whiskers above and below the box indicate the maximum and minimum axial load ratios. Hollow black circles outside the whiskers are outliers. The median normalized axial load ratio, $P_{max}/(A_w f'_{c,exp})$, increases by a factor of ~5 on average between the solid and coupled walls indicating that large compressive forces develop in the coupled wall piers at an MCE ground-motion intensity.

The archetype wall thickness was increased by 150%, 200%, and 300% to reduce the axial load of the wall under earthquake loading while keeping other variables constant (e.g., reinforcement volume). The pushover responses of the 8-story archetypes are shown in Figure 7.28. For the solid wall, increasing the wall thickness only marginally increased the strength but drastically increases drift at significant strength loss (>5% roof drift). Increasing the wall thickness for the coupled archetype increased the drift capacity and system strength because it added compressive capacity in the "compression pier" thus allowed the tension pier to reach higher tensile stresses.

Figure 7.15 shows that increasing the wall thickness by 200% reduced the collapse probability by 78%, on average, for coupled walls, resulting in a collapse probability that is closer to that of

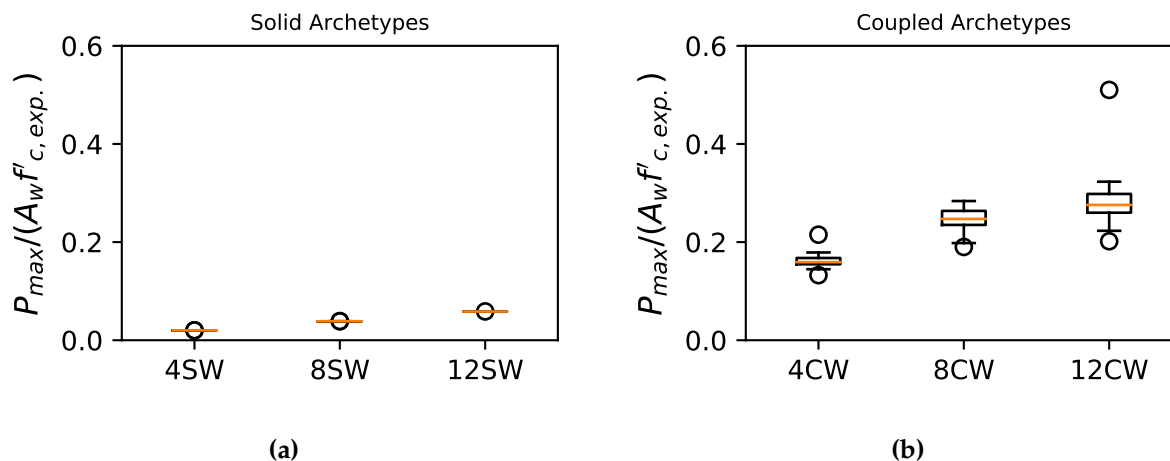


Figure 7.27: Box-and-whisker diagram showing axial ratio in (a) solid walls and (b) coupled walls at the MCE ground-motion spectral acceleration.

the base solid walls (2%). Figure 7.29 shows the variability in the minimum strain (compression) normalized with the residual strain ($\epsilon_{\min}/\epsilon_{res}$) in any of the wall piers at MCE for 8CW with varying wall thickness. Doubling the wall thickness resulted in the majority of the minimum strains from the 44 motions to be less than the concrete crushing strain (ϵ_{res}) and therefore resulted in a reduction in collapse probability at MCE.

7.5.10 Impact of Non-Simulated Collapse Criteria on Collapse Probability

The IDAs are terminated using a non-simulated collapse mechanism based on the maximum inter-story drift (ISD) to simulate failure of the slab-column gravity system (taken as 5% in the base model). Experimental results indicate that drift corresponding to failure of the gravity system varies from 3% to 10% (Figure 7.13). Here, building collapse due to gravity system failure at inter-story drifts of 3%, 5% (base model), 7%, and 10% were considered. The results (Figure 7.15 and Table 7.6) show that decreasing the drift limit has a significant impact on the probability of collapse, in some cases increases by over 800%. Increasing the drift limit to 7% does not have a similar impact, reducing collapse probability by 40-50% for the solid walls, and much less for

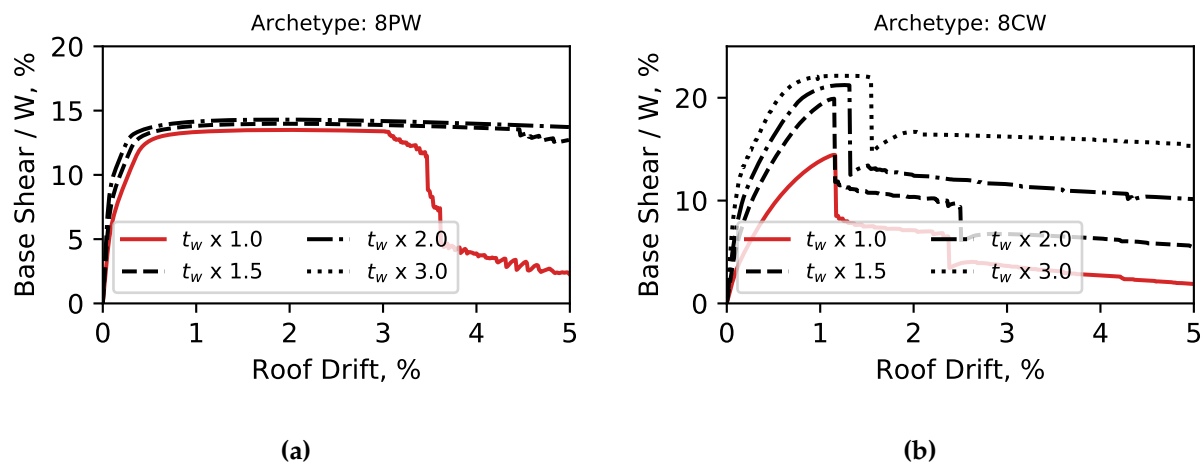


Figure 7.28: Pushover varying wall thickness for archetypes (a) 8PW and (b) 8CW (red line shows base model).

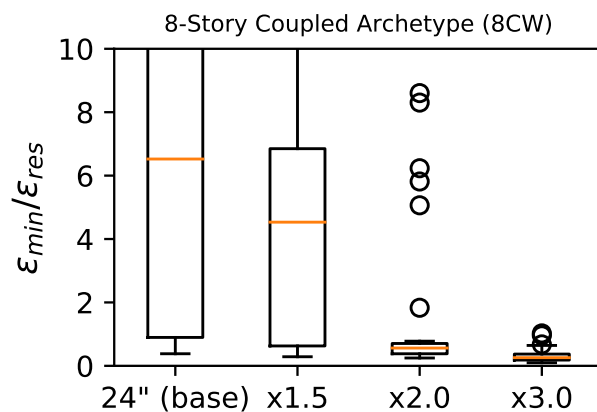


Figure 7.29: Box-and-whisker diagram showing the normalized minimum strain (compression) in any wall pier at MCE for the 8-story coupled wall archetype.

the coupled walls. This is because the IDA curve “flat lined” for most analyses at 5% drift (e.g., Figure 7.14) resulting in a slight increase in collapse S_a with larger gravity system drift capacities. As expected, increasing this limit to 10% only marginally reduced the collapse probability. These results suggest that adequate gravity system drift capacity (at least 5-7%) is needed to ensure that the gravity system does not control the collapse mechanism.

7.6 Shear Amplification

In this study shear failure, $V_{\text{demand}} > V_{\text{capacity}}$, is not considered as a non-simulated collapse limit. However, simulation data show that walls do sustain shear demand greater than the shear capacity. This increase in shear demand is known as dynamic shear amplifications that many building codes (e.g. Canadian, European, and New Zealand) currently consider in design and is being considered for adoption in future U.S. building codes. The amplification of shear demands are primarily due to (1) flexural over-strength and (2) higher-mode effects (e.g., Eibl and Keinzel, 1988; Pugh et al., 2017). Figure 7.30 shows the maximum shear (in the wall/pier) at MCE normalized by the expected shear strength of the wall for all archetypes. The expected shear strengths for each wall/wall pier were calculated as per ACI 318-14 (2014). Although shear amplification is observed for all walls, it is more significant for the coupled walls, which had average amplifications factors of 4 in comparison with average amplification factors of 2.5 for the solid walls. The greater shear amplification in coupled systems is due mainly to the compression pier resisting the majority of the base shear. This redistribution of shear is due to P-M interaction which greatly increases the moment capacity of the compression pier (thus attracts more shear) and greatly reduces the moment capacity of the tension pier. This behavior has been observed in experimental tests of coupled walls (e.g., Aktan and Bertero, 1984; Aktan and Bertero, 1987).

Shear demand in walls predicted by dynamic non-linear analyses is not captured in the linear static analyses typically used in design. For this reason, many researchers (e.g., Paulay and Priestley, 1992; Pugh et al., 2017) have proposed equations for predicting shear demand and design procedures to ensure shear capacity in excess of shear demand observed in nonlinear analysis of walls. Here, a comparison is made between the shear demand determined from

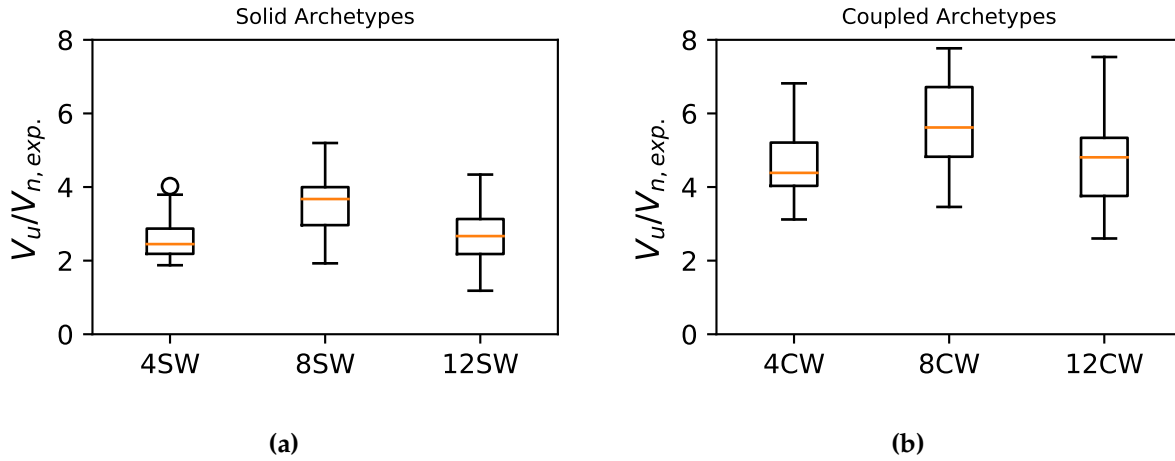


Figure 7.30: Box-and-whisker diagram showing the max. shear (due to dynamic amplification) at MCE normalized by the expected shear strength of the (a) solid wall archetypes and (b) coupled wall archetypes.

nonlinear dynamic analysis at MCE to the amplified shear demand values calculated using Article 9.01.010 of SEAOC (2009), which is based on Paulay and Priestley (1992). The amplified shear demands are estimated using the following SEAOC (2009) equation:

$$V_{u,SEAOC} = \frac{V_{u,ELF}M_{pr}}{M_{u,ELF}}\Omega_d \quad (7.2)$$

where $V_{u,ELF}$ and $M_{u,ELF}$ are the base shear and moment demand from static lateral force analysis (i.e., ELF), respectively, M_{pr} is the probable moment capacity at the base of the wall accounting for material over-strength, and Ω_d is defined as:

$$\Omega_d = \begin{cases} 0.9 + \frac{N}{10} & \text{if } N \leq 6; \\ 1.3 + \frac{N}{30} & \text{if } N > 6. \end{cases} \quad (7.3)$$

where N is the number of stories. Here, M_{pr} is estimated as the maximum moment (including coupling action) from a pushover of the non-linear *OpenSees* models previously used in this chapter.

Figure 7.31 shows the variability of the maximum shear from the nonlinear dynamic analyses normalized by the shear predicted from Eq. 7.2. The normalized shears for both solid and coupled

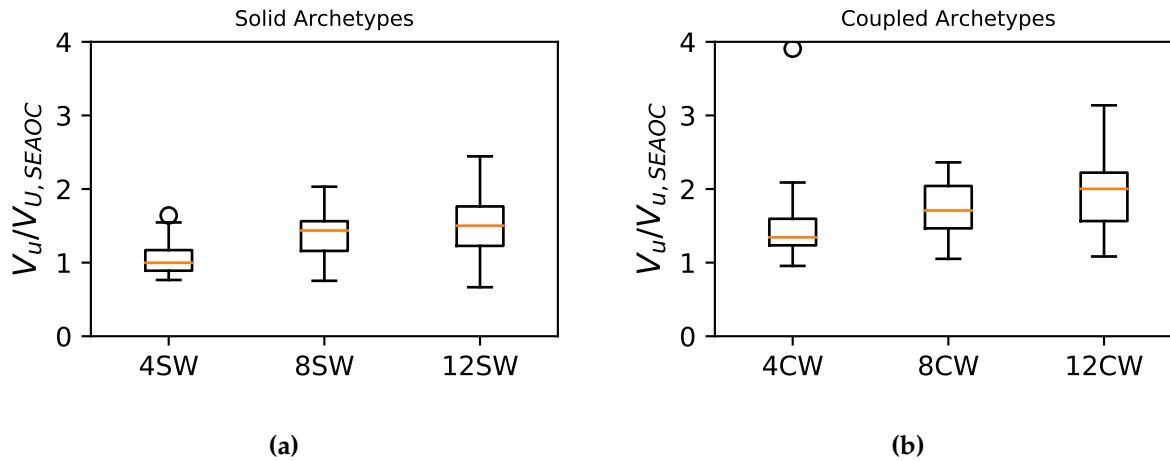


Figure 7.31: Box-and-whisker diagram showing the max. shear (due to dynamic amplification) at MCE normalized by SEAOC (2009) (shown here in Eq. 7.3) for the (a) solid wall archetypes and (b) coupled wall archetypes.

walls are shown to (1) on average exceed 1.0 and (2) increase with the number of stories. Thus, the data show that Eq. 7.2 underestimates shear demand.

7.7 Building Performance: Probability of Exceeding *res* (Concrete Crushing)

In performance-based seismic design, the size, strength, stiffness and detailing of a wall is determined to achieve a specific structural damage state. Birely (2012) surveyed damaged wall buildings after several major earthquakes around the world and concluded that only 9% of the surveyed buildings collapsed. However, even though many buildings did not collapse, the economic losses due to damage downtime were expected to be high because buildings were deemed irreparable or unsafe for immediate occupancy. This section investigates the impact of the parameters previously considered on a damage state corresponding to the onset of concrete crushing.

The onset of concrete crushing (i.e., crushing of the BE concrete) is determined from the strain demands computed during the IDAs for each of the concrete fibers, where the damage state is

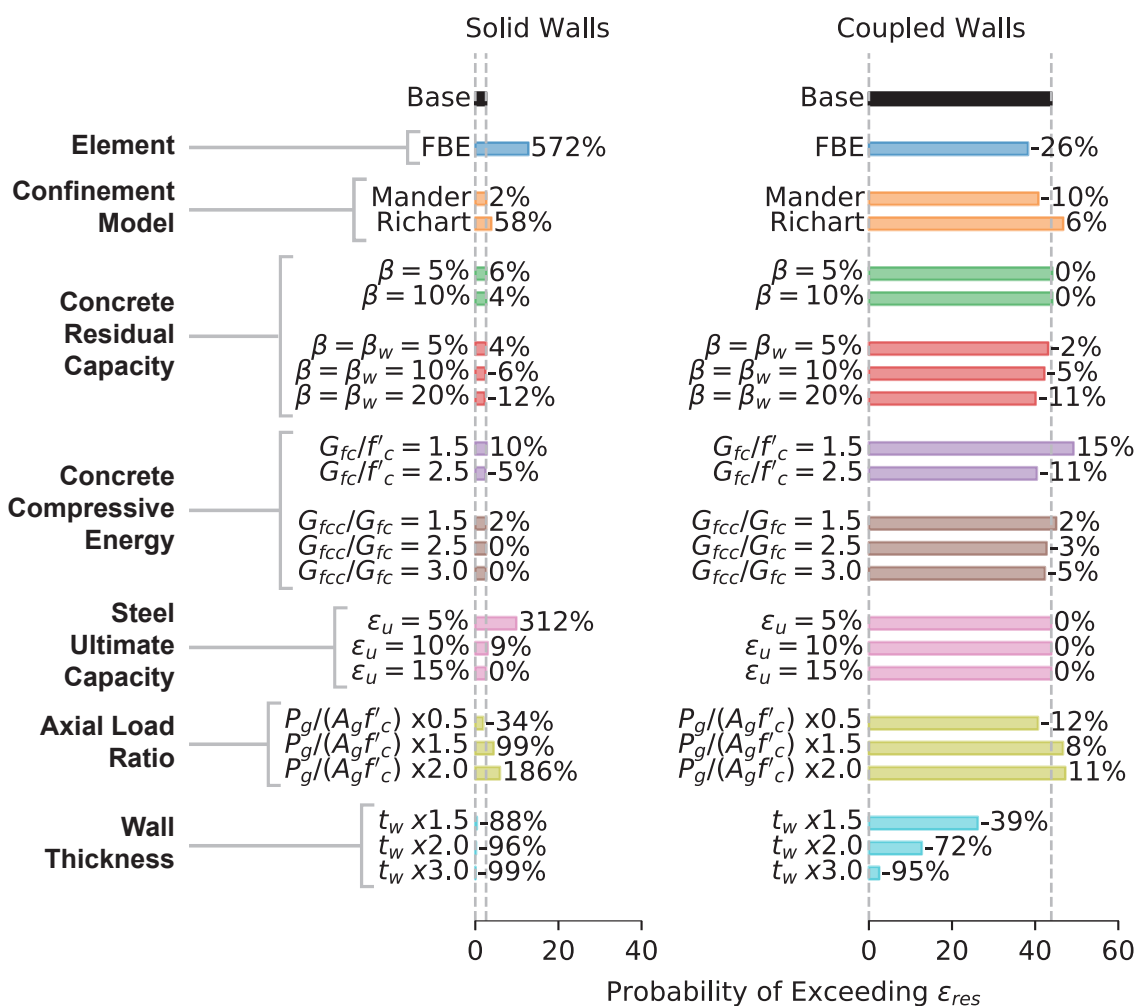


Figure 7.32: The average change in the probability of exceeding ϵ_{res} at MCE for (a) solid wall archetypes and (b) coupled wall archetypes. Note that the top bar (solid black) corresponds to the base model and the length of each of the bars corresponds to the probability of exceeding ϵ_{res} .

considered to be reached once the maximum compressive strain in any concrete fiber exceeds ϵ_{res} . Analysis results for the "onset of concrete crushing" are summarized in Figure 7.32. The data in Figure 7.32 show that the onset of concrete crushing is more likely for coupled walls than for solid walls, suggesting coupling action leads to damage in coupled planar walls.

For the solid walls, the parameters that resulted in more than a 50% change in the probably of onset of crushing were found to be: (1) element formulation (FBE vs. DBE), (2) the confined concrete material model by Richart, (3) reduction in the reinforcing bar ultimate strain capacity, (4) increase of wall axial load by >150%, and an (5) increase in wall thickness. For the coupled walls, only increasing wall thickness by 100% resulted in 50% reduction in the probability of crushing.

7.8 Chapter Conclusions

Current building codes are intended to achieve a probability of collapse at MCE of less than 10% (FEMA, 2009). This chapter investigated the collapse probability of solid and coupled wall archetypes designed using current code requirements and standards of practice. This study also quantified the change in collapse probability resulting from variations in element formulation, and concrete and steel material modeling assumptions. As well as variation in axial and shear demand and deformation capacity of the gravity-load resisting system.

For both the solid and coupled walls the collapse probability was found to be highly sensitive to the non-linear element formulation where non-converged analyses observed in force-based elements resulted in a significant over prediction in collapse probability at MCE. While the use of displacement-based elements significantly reduced the number of non-converged analyses, there were still a few instances (up to ≤ 6 out of 44) of non-converged analyses (especially for coupled walls) that were deemed to have collapsed. These assumed collapse states affected the collapse probabilities at MCE, therefore, future work should develop modelling methodologies that eliminate non-converged solutions.

All archetypes were found to be insensitive to the concrete confinement model (-5% to 21% average change in collapse probability at MCE) and crushing energy parameters (G_{fc}/f'_c , and G_{fcc}/G_{fc} , change between -10% to 4%). The residual strength of the concrete was found to have a significant impact on the collapse probability of coupled walls (-28% to 105% change) but much less impact of the collapse probability of solid walls (-3% to 13% change). The tensile strain capacity of reinforcing steel affected collapse probability if the strain capacity equaled 5%, which resulted in a tension-controlled failure mechanism (i.e., bar fracture) that on average increased the collapse probably by 112% for solid walls and by 44% for the coupled walls.

Currently, US design codes do not limit wall axial load, however, results from this study show wall axial load has a significant impact on collapse performance. Doubling the wall axial load approximately doubles the collapse probability for the solid and coupled walls. However, this effect is more prominent in taller structures where the axial load ratio is already high from gravity loads alone.

The probability of collapse in the MCE was found to be 4 times larger for coupled vs. solid walls. The coupled and solid walls had a similar overall wall geometry (fitted within the same standard framing configuration) and designed to resist the same ELF forces leading to a similar overall system strength. The shear stress demand (Table 7.1) and axial load ratio under gravity (Table 7.1) increased marginally between the two wall types. While these solid and coupled walls were deemed equivalent, they resulted in different collapse performance. This increase in collapse probability is attributed to the larger compressive strains that develop in coupled wall piers due to coupling action, which trigger a compression-controlled failure, and typically at lower drift than in the solid walls. The impact of this on collapse risk could be reduced by either reducing the axial load due to gravity or by increasing the wall thickness (cross-sectional area). Doubling the thickness of coupled walls resulted in a collapse probability that was similar to that of the solid wall archetypes. In designing coupled walls, engineers are recommended to consider the effects of (1) increased axial compressive forces due to over-strength of coupling action and coupling beams, and the (2) redistribution of moments and shears due to the stiffening (and strengthening under P-M interaction) of the pier in compression (Aktan and Bertero, 1987). Recommendations that consider these effects are described in more detail in (1) SEAOC 2009, (2) Lehman et al. (2013), or (3) NZS 3101.1&2:2006 (2015).

The assumed drift capacity of the gravity system has a large effect on collapse probability for both coupled and solid walls if it is much lower than the drift capacity of the wall. If the gravity system drift capacity is increased, collapse probability increases marginally because the drift capacity of the wall controlled collapse. Further work is needed to (1) reduce the uncertainty in the gravity system drift capacity, and (2) develop gravity connections that can achieve large drift capacities.

Under MCE-level shaking, the shear forces in the walls were found to be much larger than expected shear capacity; shear demand was approximately 2.5 times expected shear capacity for the solid archetypes and up to four times expected shear capacity for coupled wall archetypes. SEAOC (2009) provides recommendations for estimating shear amplification based on work by Paulay and Priestley (1992); however, the SEAOC recommendations were found to still underestimate shear demands, especially for taller coupled walls.

The modelling approach used here captures only flexural failure modes. Future studies should extend this study using a modelling approach that captures shear-flexure interaction (Kolozvari et al., 2015a) and consider additional design parameters such as the (1) cross-sectional aspect ratio (l_w/b), (2) wall aspect ratio (h_w/l_w), and (3) shear-span-to-depth ratio. It is important to note that the probability of collapse computed here only includes uncertainty from record-to-record variability, however, the FEMA P695 methodology includes additional uncertainty due to design and modelling. Further work is needed to accurately quantify the modelling/design parameter uncertainties for solid and coupled walls for inclusion into the FEMA P695 methodology. For ease of comparison with other studies and for convenience, the chapter predicted collapse at MCE level using the 22 ground-motion pairs part of the FEMA P695 document. It is noted that the collapse probability at the tail ends of a log-normal distribution is likely affected by the outcomes of a few ground-motions part of the set. Therefore, increasing the number of motions used would result in a more robust prediction of collapse probability. Future studies should investigate the use of more motions in the collapse prediction at the MCE.

Chapter 8

PERFORMANCE OF RC CORE-WALLS DURING SIMULATED M9 CASCADIA SUBDUCTION ZONE EARTHQUAKE SCENARIOS

8.1 Chapter Overview

Chapter 6 showed that the simulated motions in Seattle from a magnitude-9 earthquake are expected to be more damaging than motions currently considered in the design. Current design of tall buildings typically consider basin effects and subduction earthquake motions using nonlinear performance-based analysis. This chapter assembles over 32 reinforced-concrete wall archetypes for Seattle using the modelling methodology developed in Chapter 7 to study the impact of an M9 CSZ. The archetypes are subjected to the suite of thirty M9 CSZ motions for Seattle and motions that are representative of the MCE_R . The performance of these archetypes are compared in terms of collapse probability during an M9 scenario and during the MCE_R .

8.2 Introduction

Geologic evidence indicates that the Cascadia Subduction Zone (CSZ) is capable of producing large-magnitude, megathrust earthquakes at the interface between the Juan de Fuca and North American plates (Atwater et al., 1995; Goldfinger et al., 2012). These events are expected to have an average return period of about 500 years (Petersen et al., 2002), which is considerably less than the 2475-year return period for the Maximum Considered Earthquake MCE, or the approximately 2000-year return period for risk-adjusted MCE (MCE_R). The most recent large-magnitude, interface earthquake on the CSZ occurred in 1700 (Atwater et al., 1995), and according to Petersen et al. (2002), there is a 10-14% chance that a magnitude-9 (M9) earthquake will occur along the Cascadia Subduction Zone within the next 50 years.

There has been much uncertainty about the characteristics of the ground motions that would result from a large-magnitude, interface CSZ earthquake, because no seismic recordings are

available from such an event. To compensate for the paucity of recorded interface events, Frankel et al. (2018b) simulated the generation and propagation of M9 CSZ earthquakes for thirty rupture scenarios, and Wirth et al. (2018) evaluated the sensitivity of the generated motions to the rupture model parameters. These realizations represent a variety of M9 full-length ruptures of the CSZ, including variations in hypocenter location, inland extent of the rupture plane, and the location of high stress-drop subevents along the fault plane. The extent of the down-dip rupture was varied to be consistent with the logic tree branches for a full-length rupture of the CSZ used in the U.S. National Seismic Hazard Maps (Petersen et al., 2014). For frequencies up to 1 Hz, the motions were generated using a finite-difference code (Liu and Archuleta, 2002) that uses a 3D seismic velocity model (Stephenson et al., 2017), which reflects the geological structure of the CSZ and the Puget Sound region. This region is founded on glacial deposits that overlay sedimentary rocks that fill the troughs between the Olympic and the Cascade mountain ranges. The model includes several deep sedimentary basins within the Puget Lowland region, including the Seattle basin, which is the deepest.

A one-dimensional measure of the basin depth is the depth to very stiff material with a shear-wave velocity (V_S) of 2.5 km/s, denoted as $Z_{2.5}$. Campbell and Bozorgnia (2014) used this measure of basin depth in their ground-motion model (GMM) for crustal earthquakes. Figure 8.1 shows the variation of $Z_{2.5}$ within the Puget Lowland region, in which $Z_{2.5}$ is 4 to 5 km over a wide area. Seattle and its nearby suburbs are located above the Seattle basin, a region where $Z_{2.5}$ reaches values of up to 7 km. The map also shows that there are shallower basins near Everett (north of Seattle) and Tacoma (southwest of Seattle). In contrast, $Z_{2.5}$ is approximately 0.5 km for the reference location of La Grande, WA.

For frequencies above 1 Hz, the motions were generated with a stochastic procedure (Frankel, 2009) assuming a generic rock site profile (Boore and Joyner, 1997) without considering basin effects. To create a broadband motion, the low-frequency and high-frequency components of the simulated motions were combined using third-order, low-pass and high-pass Butterworth filters, respectively, at 1 Hz.

Figure 8.2 illustrates the results of one rupture scenario. The figure illustrates the geospatial velocity wave propagation across the Pacific Northwest, and the velocity time history for two

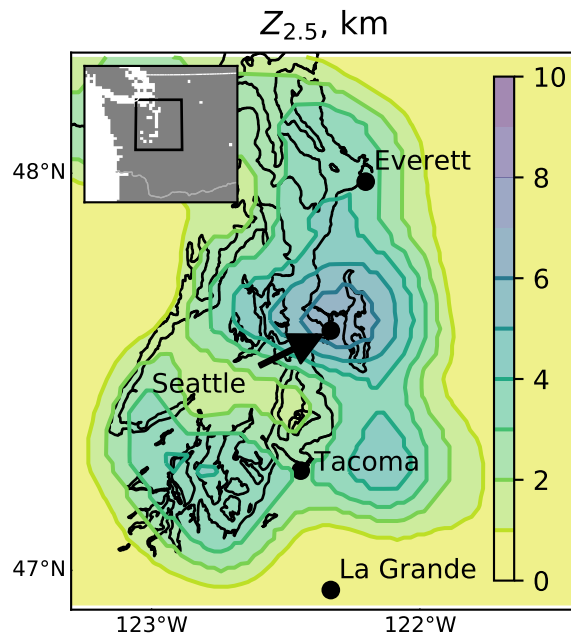


Figure 8.1: Map of $Z_{2.5}$ for the Puget Lowland Region.

locations in Washington State (Seattle and La Grande) at 47 s and 205 s after the initial earthquake rupture. Each scenario generated 500,000 motions on a 1-by-1 km grid spacing for a region ranging from Northern California to Vancouver Island, and from off the West Coast to as far inland as central Washington and Oregon. High-resolution (1-by-1 km) and low-resolution (20-by-20 km) datasets are publically available (<https://doi.org/10.17603/DS2WM3W>) from DesignSafe, a data archive supported by the National Science Foundation (Frankel et al., 2018a).

This chapter evaluates the impact of the simulated motions on the response of a series of reinforced concrete core wall archetypes designed for Seattle using ASCE 7-10 (2013) and ASCE 7-16 (2017), with prescriptive and performance-based design approaches. For each code version, an archetype performance group was developed that reflects typical practice which includes specific performance-based design considerations for buildings over 73 m (240 ft). A second archetype performance group was developed that represents designs that barely meet the minimum code requirements. The response of these archetypes to the simulated motions are compared with the response to ground motions selected and scaled to match the conditional

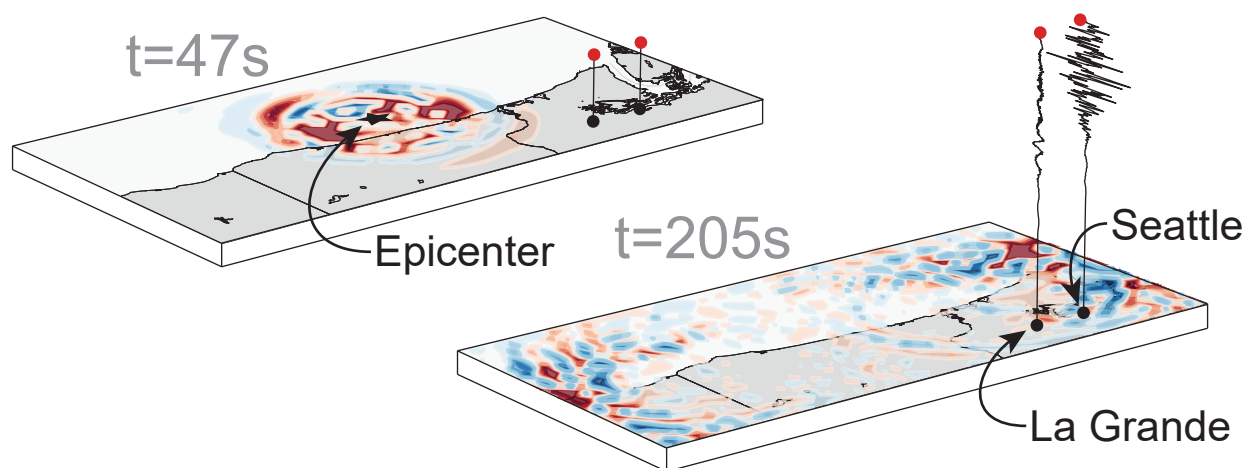


Figure 8.2: Realization of an M9 CSZ earthquake showing velocity time history for Seattle and La Grande, Washington.

mean spectrum (CMS) for crustal, intraslab, and interface earthquake sources that dominate the seismic hazard in Seattle. Uncertainty in the drift capacity of the gravity slab-column connections are taken into account to estimate the archetype's collapse vulnerability. Finally, collapse probabilities under the M9 CSZ scenarios are compared with the motions representing the MCE_R earthquakes.

8.3 Spectral Acceleration

In the United States, equivalent-linear seismic design loads (e.g., ASCE 7-10, ASCE 7-16, AASHTO 2017) are derived from the spectral acceleration (for a damping ratio of 5%) at the fundamental period of a structure. Figure 8.3a shows the spectral acceleration (S_a) in the orientation (direction) corresponding to the maximum spectral response ($S_{a,ROTD100}$) versus period for the 30 realizations for a site in downtown Seattle. At each period, the geometric mean of $S_{a,ROTD100}$ is denoted with a solid black line, and the dashed black lines denote one lognormal standard deviation above and below the mean. For comparison, the design spectrum corresponding to the ASCE 7-16 risk-adjusted maximum considered earthquake (MCE_R) (assuming Site Class C) is shown with a solid red line. Structural design per ASCE 7-16 seeks to

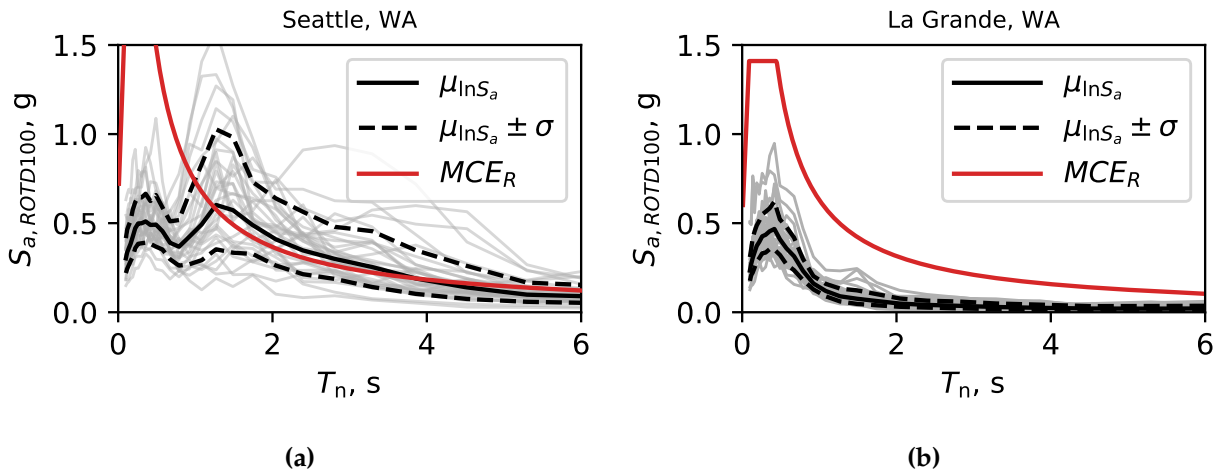


Figure 8.3: Maximum direction spectral acceleration for all 30 M9 simulations for (a) Seattle and (b) La Grande. Response spectra corresponding to the risk-targeted maximum considered earthquake for Seattle and La Grande (using the 2014 USGS NSHM) are shown in red.

ensure a less than 1% probability of collapse in 50 years; this probability roughly translates to less than 10% probability of collapse for MCE_R level shaking (ASCE 7-16).

For Seattle, the spectral accelerations of the M9 simulations are much smaller than the MCE_R values for periods below 1 s. However, for periods ranging from 1 to 4 s, the geometric mean of the M9 spectral accelerations are just slightly above the MCE_R values, and the spectral accelerations for many of the simulated motions greatly exceed the MCE_R values. For example, 67% (20 of 30) of the motions exceed the MCE_R values at a period of 2.0s. This exceedance is important, because the return period for the M9 Cascadia event (~500 years) is much less than that of the MCE_R (~2000-year return for Seattle). In addition, M9 interface earthquakes represent only part of the seismic hazard in Seattle, which has a large contribution from the Seattle Fault and deeper intraslab events. For example, at a period of 2.0 s, the CSZ full-rupture earthquake (M8.8 to 9.3) contributes only 43% of the total seismic hazard.

Figure 8.3b shows the same information as Figure 8.3a but for a reference site 73 km south of Seattle (near La Grande, Washington). This site was selected, because La Grande and Seattle have

similar values of closest distance to the fault-rupture plane and similar V_{S30} values (shear wave velocity in the upper 30 m of the site). As a result, ground-motion models with no basin terms (e.g., Abrahamson et al., 2016) predict similar spectral accelerations for both locations. For periods greater than 0.5 s, the values of S_a for the simulated motions are much lower for La Grande than for Seattle, and than the MCE_R values. The differences between the spectral accelerations of the simulated motions for Seattle and La Grande (Figure 8.3) can be attributed mainly to the effects of the deep sedimentary basin that underlies Seattle (see Chapter 6).

8.4 Spectral Shape

Spectral acceleration does not by itself adequately characterize the effects of ground motions on damage. Numerous researchers have found that the shape of the spectrum at periods near the fundamental period of the structure affects the response of nonlinear systems, because the fundamental period of a structure elongates as damage progresses. For example, Haselton et al. (2011a), Eads et al. (2015), and Chapter 3 have shown that spectral shape influences collapse probabilities for structures. Similarly, Deng et al. (2018) developed an intensity measure that accounts for the effects of spectral shape on the ductility demand of a bilinear SDOF system.

Chapter 3 developed a measure of spectral shape, SS_a , that accounts for the differences in period elongation between brittle and ductile structures, and between the effect of period elongation for low and high deformation demands. This measure correlated well with collapse performance for recorded crustal and subduction earthquake ground motions. SS_a is defined using the integral of the ground-motion response spectrum (damping ratio of 5%) between the fundamental period of the building (T_n) and the nominal elongated period (αT_n). To make SS_a independent of the spectral amplitude at the fundamental period, the integral is normalized by the area of a rectangle with a height of $S_a(T_n)$ and width of $(\alpha-1)T_n$.

$$SS_a(T_n, \alpha) = \frac{\int_{T_n}^{\alpha T_n} S_a(T) dT}{S_a(T_n)(\alpha - 1)T_n} \quad (8.1)$$

where αT_n accounts for the period elongation of the structure. For evaluating the likelihood of exceeding a target displacement ductility, μ_{target} , the upper limit of the period range is taken as equal to the period derived from the secant stiffness; therefore α is taken as target. For evaluating

the likelihood of collapse, α is taken as $\sqrt{\mu_{50}}$, where μ_{50} is the displacement ductility at a strength loss of 50%. A ground motion with a larger SS_{α} will likely be more damaging than a motion with a smaller SS_{α} , because the spectral accelerations are larger at periods beyond the elastic period of the structure.

To compare the spectral shape of the M9 motions with those of motions used in current practice for tall buildings (PEER, 2017), conditional mean spectra Baker (2011) were developed for the MCE_R , denoted as MCE_R CMS. The MCE_R CMS is meant to represent the expected ground motion response spectra conditioned on the occurrence of a target S_{α} (taken as the risk-adjusted uniform hazard spectra that targets a 1% chance of collapse in 50-years, Luco et al., 2007). To be consistent with current practice in Seattle for tall buildings, these conditional spectra were scaled to include basin amplifications as predicted using the Campbell and Bozorgnia (2014) basin term (Chang et al., 2014) assuming a value of $Z_{2.5} = 7$ km for Seattle. The resulting basin amplification factors applied to the CMS ranged from 1.23 at short periods to 1.74 at longer periods.

As an example, Figure 8.4 shows the response spectra for 100 motions selected and scaled to the MCE_R risk-adjusted CMS, adjusting from geometric mean to maximum direction ground motions (Shahi and Baker, 2011) and accounting for basin effects as described previously. Crustal, intraslab and interface motions were included in each ground motion set in proportion to their contribution to the overall seismic hazard at that period. At a period of 2.0 seconds, 47, 6, and 47 motions were used to represent the contribution of the crustal, intraslab and interface events, respectively. The process used to select and scale motions is described in Appendix C.

Figure 8.5 compares the geometric mean of SS_{α} for a downtown Seattle site for the simulated M9 ground motions and with MCE_R CMS. The spectral shapes for the Seattle M9 motions are more damaging (larger SS_{α}) up to a period of about 4 s. The differences are particularly large in the range of 0.5 s to 3.0 s. These differences are consistent with the response spectra shown in Figure 8.3. For example, the spectral acceleration in Seattle reaches a maximum at a period of about 1.5s, so SS_{α} is above 1.0 near a period of 1.0s.. Periods above 1.5 s have decreasing spectral accelerations, which leads to values of SS_{α} below 1.0.

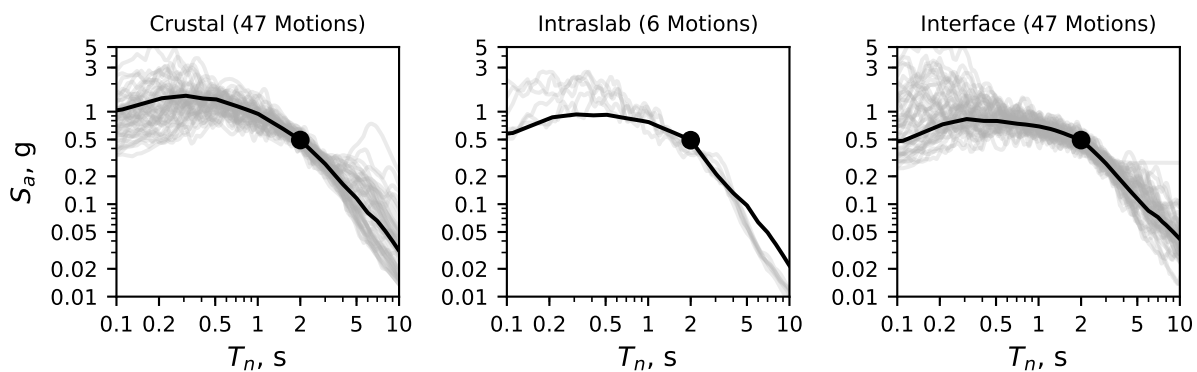


Figure 8.4: Ground motions selected and scaled to the target 2475-year return conditional mean spectrum at 2.0 s for crustal, intraslab, and interface earthquakes.

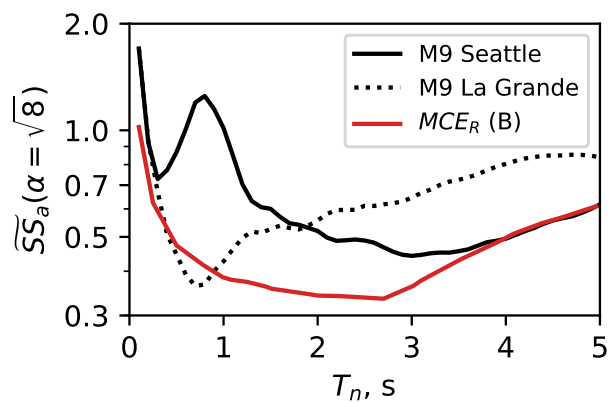


Figure 8.5: SS_a with respect to period for M9 Seattle and motions selected to match the MCE_R CMS considering basins. SS_a computed for α equal to 8 which is typical for ductile systems.

8.5 Ground-Motion Duration

Researchers have shown that the duration of the ground motion can affect structural response (e.g., Marsh and Gianotti, 1995; Bommer et al., 2004; Raghunandan et al., 2015; Chandramohan et al., 2016b). For example, Bommer et al. (2004) found that the effects of duration are pronounced in structures that undergo strength and stiffness degradation with cyclic loading. Hancock and Bommer (2007), and Chandramohan et al. (2016b) found that significant duration, D_s , correlated well with structural collapse, and this measure has the advantage of being scale independent.

Figure 8.6 shows the empirical probability density for $D_{s,5-95\%}$ for the M9 Seattle simulated motions, the Tohoku earthquake measured motions, and the FEMA P695 (2009) motions (typical of design motions for crustal earthquakes). The geometric mean values of $D_{s,5-95\%}$ for simulated M9 CSZ ground-motions for Seattle was 115s. This duration is similar to the geometric mean of $D_{s,5-95\%}$ for records measured during the M9 Tohoku earthquake (89 s), considering stations between 100 and 200 km from the earthquake source. These durations are much longer than the FEMA P695 (2009) ground-motions, which have a geometric mean of 13s.

The log-normal standard deviation of $D_{s,5-95\%}$ was 0.21 for the M9 Seattle motions, 0.15 for the Tohoku earthquake, and 0.51 for the FEMA motions. The standard deviation is smaller for the Tohoku earthquake than the simulations, because the Tohoku motions were recorded for a single event, whereas the simulated motions were derived from 30 realizations. The standard deviation is largest for the FEMA motions, because the FEMA set is comprised of motions from distinct events with a wide range of magnitudes and source-to-site distances.

8.6 Archetype Development

The effects of the M9 simulated motions were evaluated for a series of modern, mid- and high-rise reinforced concrete core-wall archetypal structures, ranging from 4 to 40 stories. To reflect current practice in Seattle, all of the archetypes were designed and detailed as special reinforced concrete shear walls (Chapter 18 of ACI 318-14, 2014), with a seismic force reduction factor (R) of 6. The archetypes were developed with the assistance of members of the Earthquake Engineering Committee of the Structural Engineering Association of Washington. These

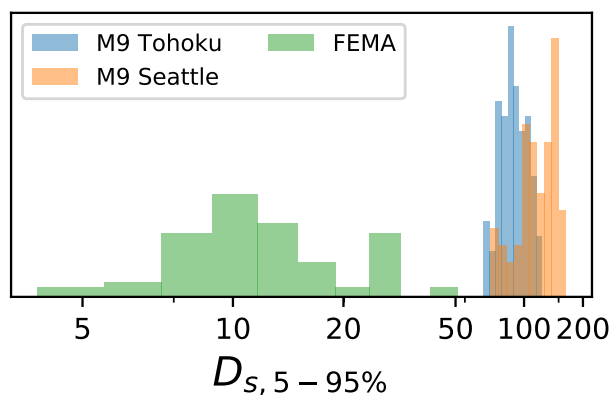


Figure 8.6: Empirical probability density function of $D_{s,5-95\%}$ for FEMA P695 motions, M9 Tohoku motions recorded at stations with a source-to-site distance between 100 and 200 km, and M9 CSZ Simulated motions in Seattle.

engineers have extensive experience in the design of mid- and high-rise concrete core wall buildings, using both prescriptive and performance-based design approaches.

8.6.1 Archetype Layout

Figure 8.7a shows typical floor plans for the archetypes. The floor plate was 30.5 m (100 ft.) long by 30.5 m (100 ft.) wide with three 9.15 m (30 ft.) bays of slab-column gravity framing in each orthogonal direction. The 4-story archetype had two planar walls in each orthogonal direction. Archetypes with 8-stories or more used a central core-wall archetype that was symmetrical in both directions, in which one direction used two uncoupled C-shaped walls, whereas the other direction used coupled C-shaped walls. As is typical for residential buildings, the 4- and 8-story archetypes included 2 and 3 basement levels, respectively, and all of the taller archetypes had 4 basement levels. The basements were assumed to have plan dimensions of 48.8 m x 48.8 m (160 ft x 160 ft) (Figure 8.7b).

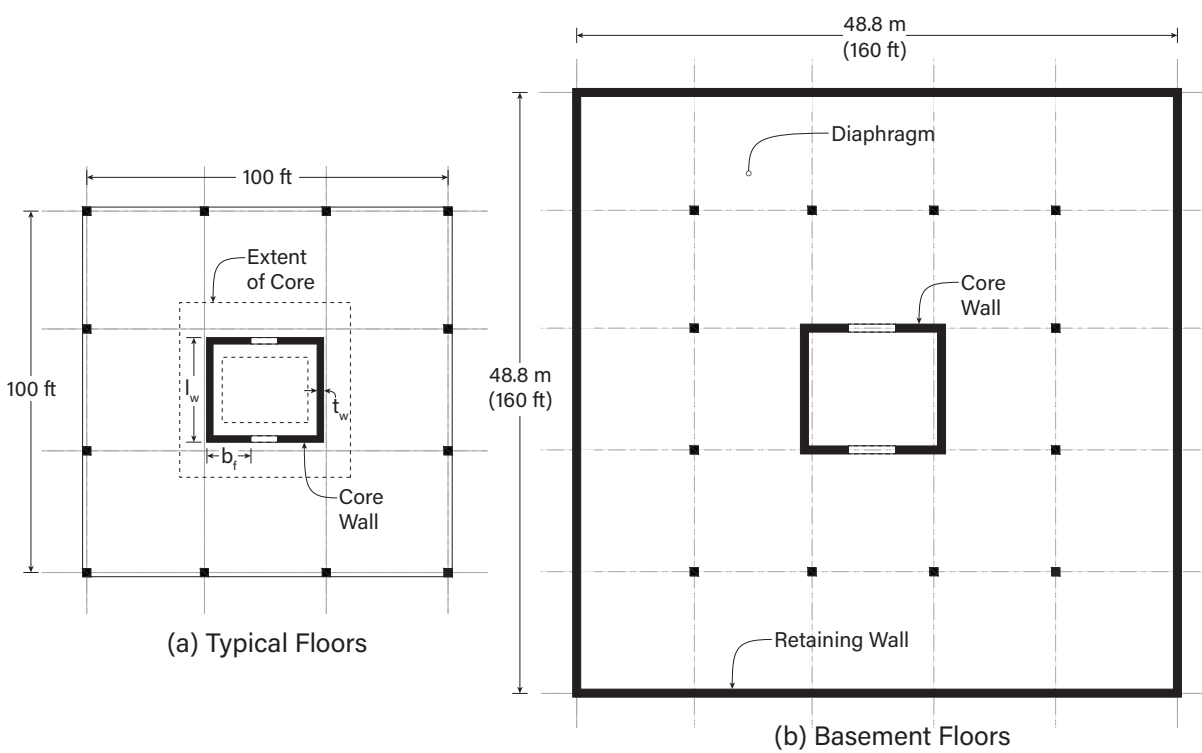


Figure 8.7: Archetype typical floor plans for the (a) typical floors and (b) basements.

8.6.2 Performance Groups

Four strategies were implemented (resulting in four performance groups) to design a total of 32 archetypical buildings. Six buildings, ranging from 4 to 24 stories, were designed to barely meet the prescriptive, equivalent lateral-force (ELF) requirements of ASCE 7-10 (2013), following the modal response spectrum analysis (MRSa) procedure. Another six buildings were designed similarly, but following the minimum requirements of ASCE 7-16. For both of these code minimum performance groups, the maximum allowable drift was 2% under elastic conditions, and the flexural demand-to-capacity ratio was set to be near 1.0 at the ground floor. These sets of archetypes are referred to as “code-minimum” performance groups.

The City of Seattle (Director’s Rule 5, 2015) requires that buildings with a height above 73 m (240 ft), which corresponds to about 24 stories in a residential building, be evaluated with performance-based design (PBD) procedures. To reflect current practice, 10 buildings, with 4 to 40 stories, were designed to satisfy: (a) a stricter drift target of 1.25%, and (b) a higher flexural demand-to-capacity ratio of 1.25. For buildings 24-stories and taller, nonlinear analysis was performed to check the strain, force, and drift limits of the Tall Building Initiative (2017) guidelines. In many cases, the nonlinear checks were satisfied without further modifying the archetypes, but in a few cases, the flexural reinforcement ratio was increased (especially in the upper stories) to satisfy the TBI strain limits. Another 10 buildings were designed similarly, using the ASCE 7-16 provisions. These two sets of archetypes are referred as “code-enhanced” performance groups.

8.6.3 Design Loads

The seismic weight was assumed to consist of the weight of the core wall, the weight of the gravity system, and the superimposed dead loads (e.g., mechanical equipment, ceilings and partitions). The gravity system and superimposed loads were modeled as a uniform load of 6.2 kPa (130 psf), 11.0 kPa (230 psf), 7.4 kPa (155 psf) for typical, ground, and basements levels, respectively. Uniformly distributed live loads of 2.4 kPa (50 psf), 4.8 kPa (100 psf), 1.9 kPa (40 psf) for typical, ground, and basements levels, respectively, were assumed in the LRFD ASCE load combinations.

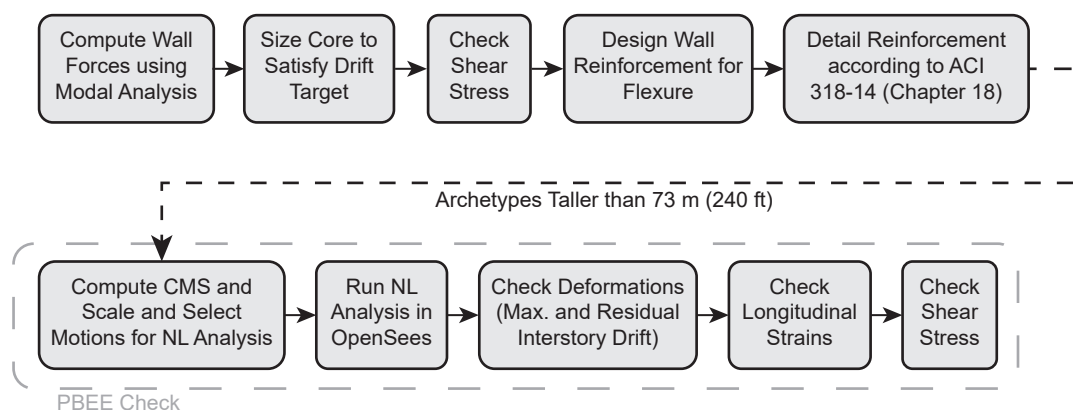


Figure 8.8: Archetype design flow chart.

All of the archetypes were assumed to be founded on glacially-compacted sediments that are common in the Puget Sound region. In Seattle, this material typically has a shear-wave velocity in the upper 30 m (V_{S30}) near 500 m/s, which corresponds to NEHRP Site Class C. For the ASCE 7-10 archetypes, the design short-period spectral acceleration, S_{DS} , was 0.94g, and the 1-s spectral acceleration, SD_1 , was 0.42 g. The design accelerations for the ASCE 7-16 archetypes were 19% and 12% higher, respectively ($S_{DS} = 1.12$ g; $SD_1 = 0.49$ g). This increase was attributable to the change in seismic hazards (NSHMP) and site-amplification factors. All archetypes were assumed to fall into occupancy Risk Category II, which corresponded to Seismic Design Category D for both the ASCE 7-10 and ASCE 7-16 provisions.

8.6.4 ASCE-7 and ACI 318 Design Process

The design process for all of the archetypes is summarized in Figure 8.8. The seismic forces induced in the core-wall were computed using MRSA, in which the total seismic base shear was determined using ASCE 7 §12.8. Note that the MRSA procedure differed between the two standards; ASCE 7-10 permits a 15% reduction in the lateral-design loads under MRSA whereas ASCE 7-16 does not.

All core-wall archetypes were designed and detailed according to Chapter 18 in ACI 318-14. The core wall concrete was assumed to have a specified compressive strength (f'_c) of 34.5 MPa

(5,000 psi) and reinforced with ASTM A706 steel, which has a nominal yield stress (f_y) of 414 MPa (60 ksi). The sizes and thicknesses of the wall, and reinforcement layout was determined by meeting the following criteria:

- Satisfy drift limit (using MRSA, according to ASCE 7-10 §12.12) assuming an effective stiffness of $0.5E_cI_g$, as permitted in ACI 318-14. This drift limit was 2.0% for the code-minimum performance group, whereas it was 1.25% for the code-enhanced performance group, as recommended by the archetype committee.
- Check that the base shear stress demand resulting from the MRSA demands are less than $0.33f'_c$ MPa ($4f'_c$ psi) for the code-minimum design, and are less than $0.17f'_c$ MPa ($2f'_c$ psi) in the code-enhanced designs, and
- Provide adequate flexural strength, such that $\phi M_n > M_u$ where $\phi = 0.9$; M_n corresponds to the nominal flexural strength as per ACI, M_u is based on moment demand as per ASCE 7. The demand-to-capacity ($M_u/\phi M_n$) ratio was approximately 1.0 for the code-minimum performance groups and 0.8 for the code-enhanced groups.

The wall length, measured as the distance between the inner flange faces ($l_w - 2t_w$) and flange width (b_f), was kept constant through the height of the archetypes. The wall thickness varied approximately every 12 stories (as recommended by the archetype committee). Consequently, the overall wall length (l_w in Figure 8.7) also varied slightly along the height.

8.6.5 PBEE Check

For archetypes taller than 73.2 m (240 ft), corresponding to 24 stories or more, nonlinear time history analyses were performed, and the demands were checked with the limits specified in the 2017 Tall Building Initiative Guidelines. (denoted as TBI check in Figure 8.8). These archetypes were subjected to ground-motions selected and scaled to the 2475-year return period, risk-adjusted, maximum direction conditional mean spectrum (see Appendix C) as per Chapter 16 in ASCE 7-16. To be consistent with current practice for tall buildings (Chang et al., 2014), these conditional mean spectra were scaled to include basin amplifications as predicted using the Campbell and Bozorgnia (2014) basin term. Appendix E summarizes the results of the TBI

performance checks (i.e., peak inter-story drifts, residual drifts, wall axial strains, shear forces) for the archetypes with 24 stories or more.

8.6.6 Archetype Properties

Table 8.1 lists key properties for the archetype buildings. The resulting seismic weights per unit floor area (excluding the basement levels) ranged from 8.16 kPa (171 psf) for the eight-story, ASCE 7-10, code-minimum archetype (S8-10-M) to 9.81 kPa (205 psf) for the forty-story, ASCE 7-16, code-enhanced archetype (S40-16-E). Table 8.1 also lists the upper-bound limit on design period ($C_u T_d$) used to compute C_s , and the computed elastic period with cracked concrete properties used in the modal analysis. The total base shear as a percentage of the total building weight (variable C_s listed in Table 8.1) ranged from 0.04 to 0.18 depending on the code year and archetype height. The minimum base shear controlled for 24-stories and taller for the ASCE 7-10 archetypes, and for 20-stories and taller for the ASCE 7-16 archetypes.

The resulting ratio of horizontal shear force (due to seismic loads) to the concrete shear capacity, V_u/V_c , ranged from 0.53 to 1.56, which is far below the allowable values (i.e., $V_u/V_c \leq 5$). Table 8.1 lists the resulting axial load ratio, $P_g/(A_g f'_c)$, where P_g is computed using the 1.0D + 0.5L load combination, A_g is the gross cross-sectional area of the wall. The load P_g was computed as the sum of the self-weight of the concrete core and the gravity load corresponding to the tributary area resisted by the core that is equal to 50% of the total floor area, equaling 464 m² (5000 ft²). The resulting axial load ratio ranged from 8% to 17%.

8.7 Archetype Nonlinear Modelling

For all walled buildings, the collapse risk was assessed using 2D models in *OpenSees* (McKenna, 2016) with earthquake demands applied only in one direction. The effects of torsional response and in-place asymmetry were not considered. The nonlinear behavior of the wall was modelled using a methodology that was calibrated with approximately 15 experimental tests, originally developed by Pugh et al. (2015). Chapter 7 extended the methodology to use displacement-based beam-column elements (DBE). This methodology used the DBE formulated with lumped plasticity fiber sections with a series of material models to capture the axial and flexural

Table 8.1: Key archetype properties.

| Performance Group | Arch. ID | # of Stories (Basements) | $C_u T_d$ (s) | Computed Period ¹ (s) | C_s | W^2 (MN) | $\frac{\phi M_n}{M_u}$ ³ | $\frac{V_u}{V_c}$ ³ | Drift Ratio (%) | Axial Load Ratio ($P_g/f'_c A_g$) |
|------------------------------|----------|--------------------------------|------------------|--|-------|---------------|-------------------------------------|--------------------------------|-----------------------|--|
| Code Minimum (ASCE 7-10) | S4-10-M | 4(2) | 0.45 | 1.45 | 0.152 | 30.6 | 1.02 | 1.7 | 1.91 | 0.17 |
| | S8-10-M | 8(3) | 0.75 | 2.25 | 0.102 | 60.8 | 1.05 | 1.53 | 1.74 | 0.12 |
| | S12-10-M | 12(4) | 1.02 | 3.10 | 0.075 | 90.9 | 1.06 | 1.33 | 1.77 | 0.13 |
| | S16-10-M | 16(4) | 1.26 | 4.06 | 0.061 | 122.1 | 1.05 | 1.11 | 1.88 | 0.13 |
| | S20-10-M | 20(4) | 1.49 | 4.96 | 0.051 | 154.6 | 1.05 | 0.95 | 1.93 | 0.14 |
| | S24-10-M | 24(4) | 1.71 | 5.33 | 0.045 | 188.8 | 1.06 | 0.73 | 1.80 | 0.12 |
| Code Minimum (ASCE 7-16) | S4-16-M | 4(2) | 0.45 | 1.08 | 0.183 | 30.9 | 1.05 | 1.74 | 1.82 | 0.11 |
| | S8-16-M | 8(3) | 0.75 | 1.93 | 0.109 | 61.8 | 1.06 | 1.49 | 1.80 | 0.10 |
| | S12-16-M | 12(4) | 1.02 | 2.70 | 0.08 | 92.3 | 1.01 | 1.32 | 1.89 | 0.11 |
| | S16-16-M | 16(4) | 1.26 | 3.53 | 0.065 | 125.1 | 1.03 | 1.05 | 1.96 | 0.11 |
| | S20-16-M | 20(4) | 1.49 | 4.36 | 0.055 | 158.5 | 1.05 | 0.92 | 2.03 | 0.11 |
| | S24-16-M | 24(4) | 1.71 | 5.11 | 0.049 | 195.0 | 1.04 | 0.85 | 2.00 | 0.11 |
| Code Enhanced (ASCE 7-10) | S4-10-E | 4(2) | 0.45 | 0.99 | 0.152 | 30.8 | 1.32 | 1.36 | 1.35 | 0.12 |
| | S8-10-E | 8(3) | 0.75 | 1.51 | 0.102 | 61.2 | 1.17 | 1.56 | 1.16 | 0.11 |
| | S12-10-E | 12(4) | 1.02 | 2.15 | 0.075 | 92.1 | 1.18 | 1.32 | 1.09 | 0.13 |
| | S16-10-E | 16(4) | 1.26 | 3.02 | 0.061 | 122.9 | 1.18 | 1.28 | 1.22 | 0.15 |
| | S20-10-E | 20(4) | 1.49 | 3.91 | 0.051 | 154.3 | 1.19 | 1.22 | 1.32 | 0.16 |
| | S24-10-E | 24(4) | 1.71 | 4.37 | 0.045 | 189.4 | 1.50 | 0.92 | 1.29 | 0.14 |
| | S28-10-E | 28(4) | 1.92 | 5.17 | 0.040 | 223.4 | 1.44 | 0.89 | 1.34 | 0.16 |
| | S32-10-E | 32(4) | 2.12 | 5.74 | 0.040 | 260.9 | 1.32 | 0.86 | 1.33 | 0.15 |
| | S36-10-E | 36(4) | 2.31 | 6.23 | 0.040 | 295.2 | 1.20 | 0.82 | 1.30 | 0.15 |
| | S40-16-E | 40(4) | 2.50 | 6.70 | 0.040 | 334.6 | 1.18 | 0.80 | 1.17 | 0.15 |
| Code Enhanced (ASCE 7-16) | S4-16-E | 4(2) | 0.45 | 0.78 | 0.183 | 31.2 | 1.18 | 1.36 | 1.3 | 0.08 |
| | S8-16-E | 8(3) | 0.75 | 1.25 | 0.109 | 62.2 | 1.19 | 1.49 | 1.12 | 0.09 |
| | S12-16-E | 12(4) | 1.02 | 2.00 | 0.08 | 93.9 | 1.19 | 1.25 | 1.19 | 0.10 |
| | S16-16-E | 16(4) | 1.26 | 2.36 | 0.065 | 129.9 | 1.19 | 0.99 | 1.15 | 0.10 |
| | S20-16-E | 20(4) | 1.49 | 2.95 | 0.055 | 164.8 | 1.19 | 0.88 | 1.19 | 0.10 |
| | S24-16-E | 24(4) | 1.71 | 3.53 | 0.049 | 201.6 | 1.48 | 0.82 | 1.24 | 0.11 |
| | S28-16-E | 28(4) | 1.92 | 4.09 | 0.049 | 240.3 | 1.27 | 0.83 | 1.27 | 0.11 |
| | S32-16-E | 32(4) | 2.12 | 4.62 | 0.049 | 281.3 | 1.19 | 0.84 | 1.28 | 0.11 |
| | S36-16-E | 36(4) | 2.31 | 5.13 | 0.049 | 324.8 | 1.19 | 0.84 | 1.27 | 0.12 |
| | S40-16-E | 40(4) | 2.50 | 5.55 | 0.049 | 364.9 | 1.17 | 0.84 | 1.30 | 0.12 |

Notes: ¹Period computed using cracked concrete properties, ²Building seismic weight only includes stories above ground floor,

³computed at ground level, ⁴Minimum base shear controls

non-linear responses of the RC walls. The modelling was further improved by modifying the stress-strain behavior of the steel fibers to include the cyclic strength degradation (Kunnath et al., 2009) expected during strong long-duration shaking. In addition, the pre-peak stress-strain relationship of the concrete material model (*OpenSees* Concrete02) was modified to use Popovics stress-strain relationship (1973). Appendix D provides further details on the modelling methodology.

8.8 Maximum Interstory Drift

The seismic performance of the four performance groups was evaluated for: (1) the simulated M9 Motions, both for the Seattle and the La Grande sites, (2) Conditional Mean Spectra (CMS) motions selected and scaled to match Maximum Considered Earthquake, both with and without considering the basin amplification, and (3) MCE-compatible motions selected and scaled to match the conditional mean and variance spectra (CMS+V).

8.8.1 Performance for Simulated M9 Motions

The archetypes were subjected to the M9 CSZ motions for Seattle and La Grande in the *RotD100* orientation that corresponds to the direction with the maximum spectral acceleration ($S_{a,ROT100}$) at each structure's fundamental period. This approach is consistent with the ASCE 7-16 (Chapter 16) nonlinear evaluation provisions. The relative rotations and strains at the ground level were usually the largest, so that is where one would expect the largest amount of damage to the wall. However, the performance of the gravity slab-column connections, and slab-wall connections, facade system, and other non-structural components, depend more on the story drift than wall relative rotation.

Figure 8.9 shows the maximum story drift for every story for a representative eight-story archetype (S8-10-E) and a 32-story archetype (S32-10-E), subjected to M9 Seattle motions. As expected, the story drifts in the basement are near zero because the basement walls are very stiff. In contrast, the maximum story drifts occur near the top levels of the archetypes, because the cantilever walls accumulate rigid-body rotations over their height.

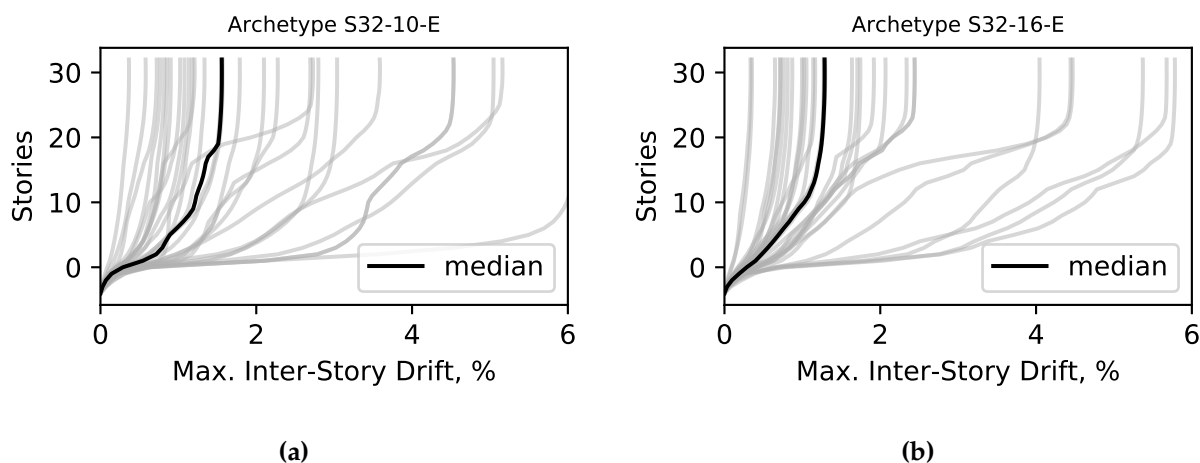


Figure 8.9: Distribution of inter-story drift with height for (a) 8-story and (b) 32-story ASCE 7-10 code enhanced archetypes, subjected to Simulated M9 Motions in Seattle.

For all four performance groups, Figure 8.10 plots the median (computed for each set of 30 motions) of the maximum interstory drift (computed over the height of each archetype) for the M9 CSZ motions in Seattle and La Grande. For Seattle, the maximum drift ratios for the code-minimum designs averaged 3.4% and 2.7% for the ASCE 7-10 and ASCE 7-16 buildings, respectively. In comparison, the TBI guidelines specify a mean maximum interstory drift limit of 3.0%. The computed drift ratios were larger than this limit for 5 out of 6 ASCE 7-10 archetypes and 2 out of 6 ASCE 7-16 archetypes. The drift ratios for the code-enhanced buildings were considerably lower, averaging 1.7% for these two performance groups. None (out of 20) of the code-enhanced designs had drift ratios that exceeded 3.0%.

The story drifts for the M9 La Grande motions were much lower (by a factor of 7 on average). They ranged between 0.2 to 0.5% for all performance groups. Since the Seattle and La Grande sites have similar source-to-site distances, these large differences in performance are attributable to the influence of the Seattle Basin.

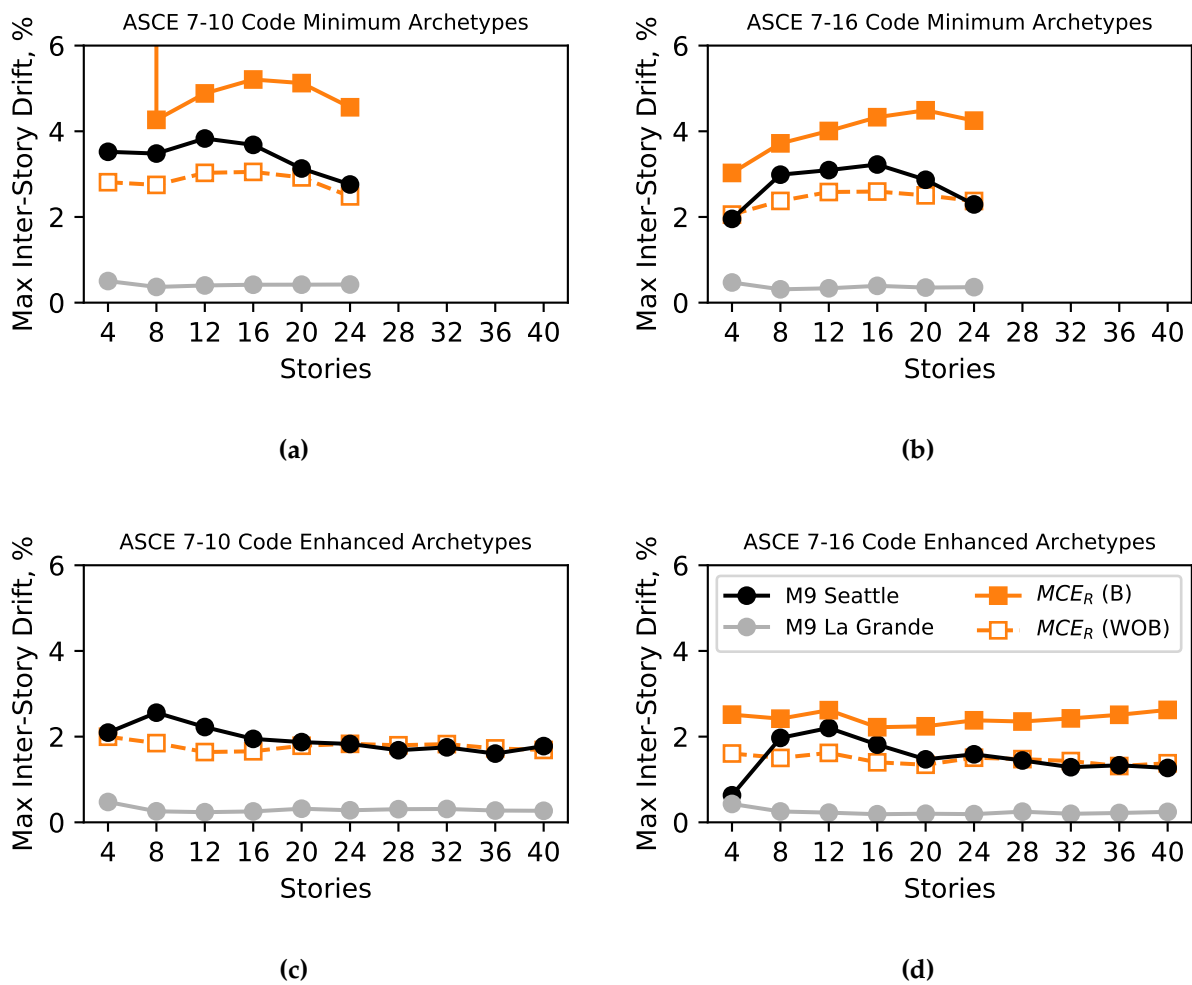


Figure 8.10: Median of the maximum inter-story drift with respect to archetype story for (a) code-minimum ASCE 7-10 archetypes, (b) code-minimum ASCE 7-16 archetypes, (c) code-enhanced ASCE 7-10 archetypes, and (d) code-enhanced ASCE 7-16 archetypes

8.8.2 Comparison with Performance for MCE_R CMS Motions

The results of the M9 simulations can be placed in the context of current design practice. In Figure 8.10, the calculated drift demands for the simulated M9 CSZ scenarios are compared with the drift demands for earthquake motions matching the Conditional Mean Spectra (CMS) for two versions of the risk-adjusted maximum considered earthquake (MCE_R). The effects of the basin is neglected in current practice for most buildings, so a suite of 100 MCE_R motions were developed without considering the basin (MCE_R WOB), based on the national seismic hazard model used in ASCE 7-16. However, basins are taken into consideration for the nonlinear evaluation of tall buildings (> 240 ft) (Chang et al., 2014), so a second suite of 100 motions was developed that accounted for the basin using the Campbell and Bozorgnia (2014) basin amplification term.

All archetypes were subjected to the two MCE_R ground-motion sets, one without basin amplification MCE_R (WOB) and with basin amplification, MCE_R (B). For almost all the archetypes in the four performance groups, the median story drifts for M9 Seattle motions were larger than those computed for the MCE_R (WOB) motions that are consistent with the national seismic hazard maps. These maps do not consider the effects of sedimentary basins. In contrast, the computed drift ratios for the M9 motions in Seattle were all lower than the drift ratios for the MCE_R (B) "with basin" motions currently used to evaluate the performance tall structures in Seattle.

8.8.3 Comparison with MCE_R CMS + Variance Motions

Figure 8.10, discussed earlier, compares the median maximum interstory drift demands for several ground-motions sets. These comparisons are consistent with the PBEE design practice (e.g., for tall buildings), in which the performance of a structure is evaluated for its median response for a limited set of ground motions (minimum of 7). However, the variability in the thirty M9 simulations is larger than that of the MCE CMS motions, because the simulations account for interevent variability, but the MCE CMS motions do not. Unlike the simulations, the CMS process selects and scales motions to fit a target spectrum (Figure 8.4), representing a "median" event, without considering the variability in the spectra for these motions.

To be consistent with the M9 simulations, MCE motions were developed to account for uncertainty of the MCE motions (Moehle and Deierlein, 2004). To capture the inter-event uncertainty in the conditional spectra, the MCE motions were selected and scaled to match the target mean and variance conditional spectra (CMS+V Jayaram et al., 2011a) in the maximum direction (Shahi and Baker, 2011). As an example, Figure 8.11 shows the response spectra for 100 motions selected to represent the three earthquake source mechanisms for a MCE_R response spectra conditioned at a 2.0 s period. To capture the uncertainty in the response spectra, motions were selected to have spectral shapes that are within two standard deviations of the target conditional spectra whilst achieving the target mean S_a and variance at each period. Note that the median of the motions in Figure 8.11 is similar to that for Figure 8.4, but the spectral ordinates for the motions in Figure 8.11 vary more. The ground-motions used in the selection process are discussed in Appendix C. Figure 8.12, shows the probability of exceeding a maximum interstory drift for the 8-story and 32-story ASCE 7-10 code-enhanced archetypes for three ground-motions sets: M9 Seattle, conditional mean spectra (CMS), and the conditional mean and variance spectra (CMS+V), both including basin effects. As expected, the maximum interstory drift corresponding to a 50% probability of exceedance was similar (within $\sim 0.2\%$ drift) between the conditional mean spectra (hollow dots in Figure 8.12) and conditional mean and variance spectra (solid dots in Figure 8.12). However, the maximum interstory drift (MISD) corresponding to the tails of the fragility function (high and low likelihood of exceedance) occur at more extreme drift levels for the CMS+V motions than the CMS motions.

The M9 simulations have even more variability than the CMS+V motions. For example, consider archetype S32-10-E. The drift ratio for a probability of exceedance of 16% (i.e., one σ below μ) is 2.63 times the median value for the M9 Seattle simulations. That ratio reduced to 1.36 for the CMS+V motions and to 1.15 for the CMS motions. As a result, even for ground-motion sets with similar median performance, the higher variability in the M9 simulated motions would likely translate to a higher risk of collapse.

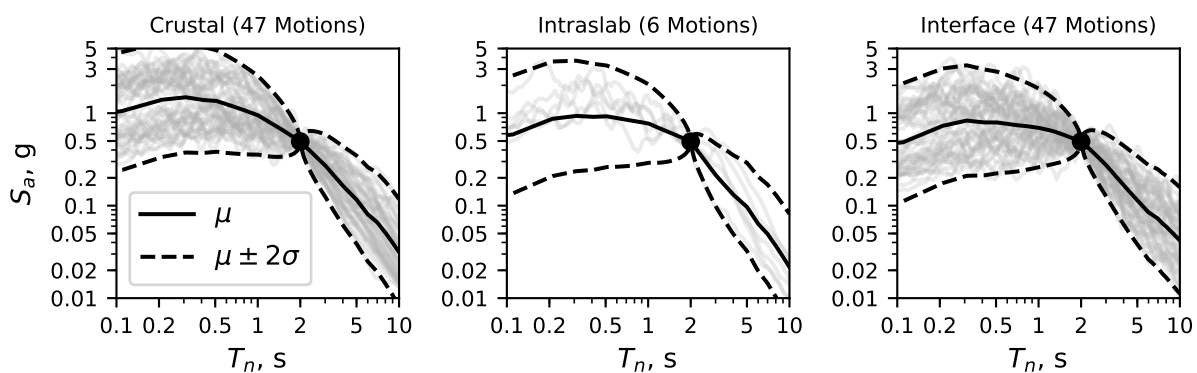


Figure 8.11: Ground motion targeting mean and variation of the conditional spectrum at 2.0s (corresponding to the period of archetype S12-16-E) for crustal, intraslab, and interface earthquakes.

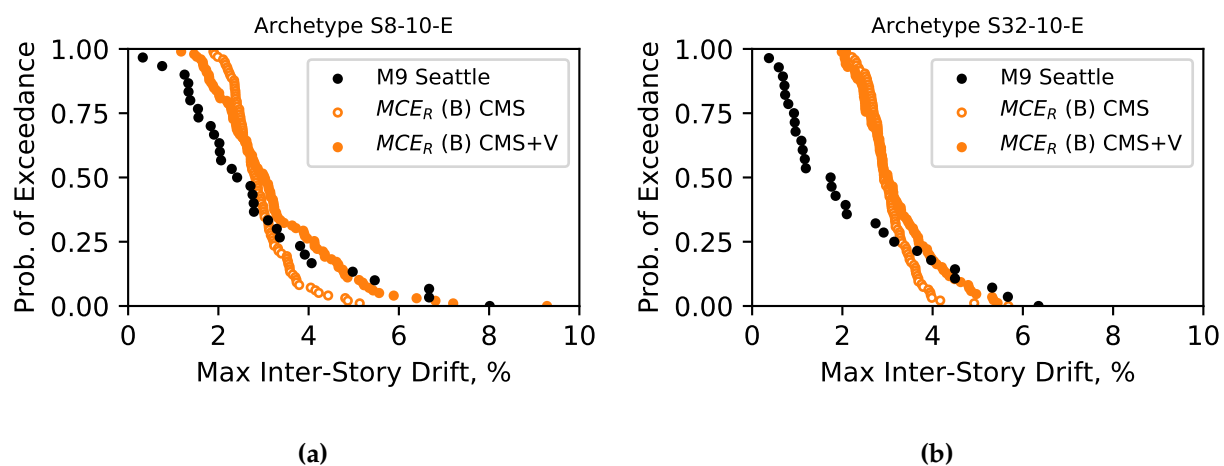


Figure 8.12: Probability of exceedance with respect to maximum inter-story drift for ASCE 7-10 code-minimum (a) 8-Story and (b) 32-Story archetypes.

8.9 Probability of Collapse

Building seismic provisions in the United States target a 1% likelihood of collapse during a period of 50 years. Using a generic collapse fragility, the values of S_a for the MCE_R are selected such that a collapse likelihood of 10% during the MCE_R event will meet the 1% in 50 year target reliability. These targets assume that the motion are oriented to produce the maximum spectral ordinate at the fundamental period of the structure. Building collapse may occur due to a side-sway mechanism that results in dynamic instability, in which the lateral drift of the building increases essentially without bound (Haselton et al., 2011) under earthquake shaking. A building may also partially or totally collapse due to the failure of components of the gravity system.

8.9.1 Drift Capacity of Gravity System

The response of the gravity system was not modeled explicitly, because the stiffness and strength contribution of the gravity system is assumed to be low compared to that of the lateral system. Instead, experimental data were used to evaluate the likelihood of collapse of a gravity system for a particular drift demand. The flat plate and flat slab systems are the most common gravity system in modern RC core-wall structures. In this chapter, the failure of the gravity system is assumed to be triggered by the failure of the slab-column or slab-wall connection.

Hueste et al. (2007 and 2007) found that the drift capacity of slab-column connections depended on (a) the ratio of shear stress due to gravity loads to the nominal shear-stress capacity provided by the concrete slab (gravity shear ratio), and (b) the presence of shear reinforcement. To be consistent with design practice, this chapter assumes that the archetype's slab-column connections are reinforced with shear studs and have a gravity shear ratio between 0.4 to 0.6. For all tests that satisfy these two criteria, Figure 8.13 summarizes the data collected by Hueste et al. (2009) on the connection rotations at the failure of slab-column connections (experiments by Dilger and Cao, 1991; Dilger and Brown, 1995; Megally and Ghali, 2000). The data shown in the figure do not include more recent test results reported by Matzke et al. (2015), who found much lower drift capacities than those determined from previous, similar tests. Figure 8.13 also shows the cumulative distribution (black dots) of the slab-column drift capacity, as well as the

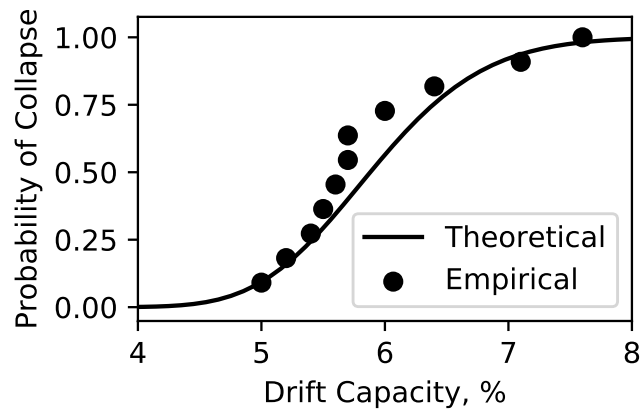


Figure 8.13: Probability of collapse due to slab-column connection failure with respect to the max. inter-story drift (filtered for experiments with shear-reinforcements and a gravity shear ratio between 0.4 to 0.6).

corresponding fitted lognormal cumulative distribution (black line). The geometric mean of the drift capacity is 5.9%, and the lognormal standard deviation is 0.12.

Other failure modes in the gravity system are not considered here., because of limited experimental testing. Klemencic et al. (2006) showed that the drift capacity of two slab-wall connections exceed 5% story drift, but the connections were not tested to failure. This chapter assumes that the the failure would initiate in the slab-column connections.

8.9.2 Racking Deformations

The drift demands on the slab-column connections result from the in-plane rotational deformations of the gravity system bay. These rotations are affected by: (1) the rigid-body rotation of the core wall at the elevation of the floor slab, and (2) the added deformations due to racking effects that result from difference in vertical deformations between the edge of the core-wall and the adjacent gravity-system column, usually located on the perimeter of the building (Figure 8.7).

The total relative rotation between the slab-column and edge of wall (due to both of these effects) can be computed as the interstory drift ratio, amplified by a racking factor, γ_{rack} . Assuming rigid-body rotation of the wall and floor system, and assuming no axial shortening in the gravity system columns, the racking factor can be approximated (Charney, 1990) as:

$$\gamma_{\text{rack}} = 1 + l_c / (2l_{\text{bay}}) \quad (8.2)$$

where l_w is length of the central core, and l_{bay} is the span length of the slab between the core and the gravity columns. The length of the core relative to the length of the gravity system bay (for a constant 30.5 m, 100 ft, floor width) varied among the archetypes. Consequently, γ_{rack} varied among the archetypes from 1.11 (Archetype S4-10-M) to 1.56 (Archetype S40-16-E).

8.9.3 Collapse Probability

For each archetype and ground-motion set, the collapse probabilities were computed considering the uncertainties in interstory drift (Figure 8.12) and drift capacity (Figure 8.13), as follows:

$$P[\text{collapse}] = \frac{1}{N} \sum_{i=1}^N P[\text{collapse} | \gamma_{\text{rack}} \text{MISD}_i] \quad (8.3)$$

where N corresponds to the number of motions in a set (e.g., M9 Seattle, MCE_R with and without basin effects using CMS+V), $P[\text{collapse} | \gamma_{\text{rack}} \text{MISD}_i]$ is probability of collapse for a given a value of slab rotation (Figure 8.13), γ_{rack} is the racking factor for that archetype, and MISD_i is the maximum interstory drift for ground-motion i . Figure 8.12 shows the probability of collapse for each archetype, performance group, and ground-motion set. For comparison, the figure also shows the target value of 10% for the conditional probability of collapse in the MCE_R (ASCE 7-16). For the MCE_R motions developed without considering the effect of the basin, denoted as MCE_R (WOB), nearly all (30 /32) of archetypes (for all performance groups, even the minimum design ones) satisfied the 10% limit on collapse probability. Table 8.2 summarizes the mean and range collapse probability for all ground-motion sets and archetype performance groups. This result shows that the archetypes performed acceptably for motions that are consistent with those anticipated in the ASCE 7 design spectra, which were developed without considering the effects of basins.

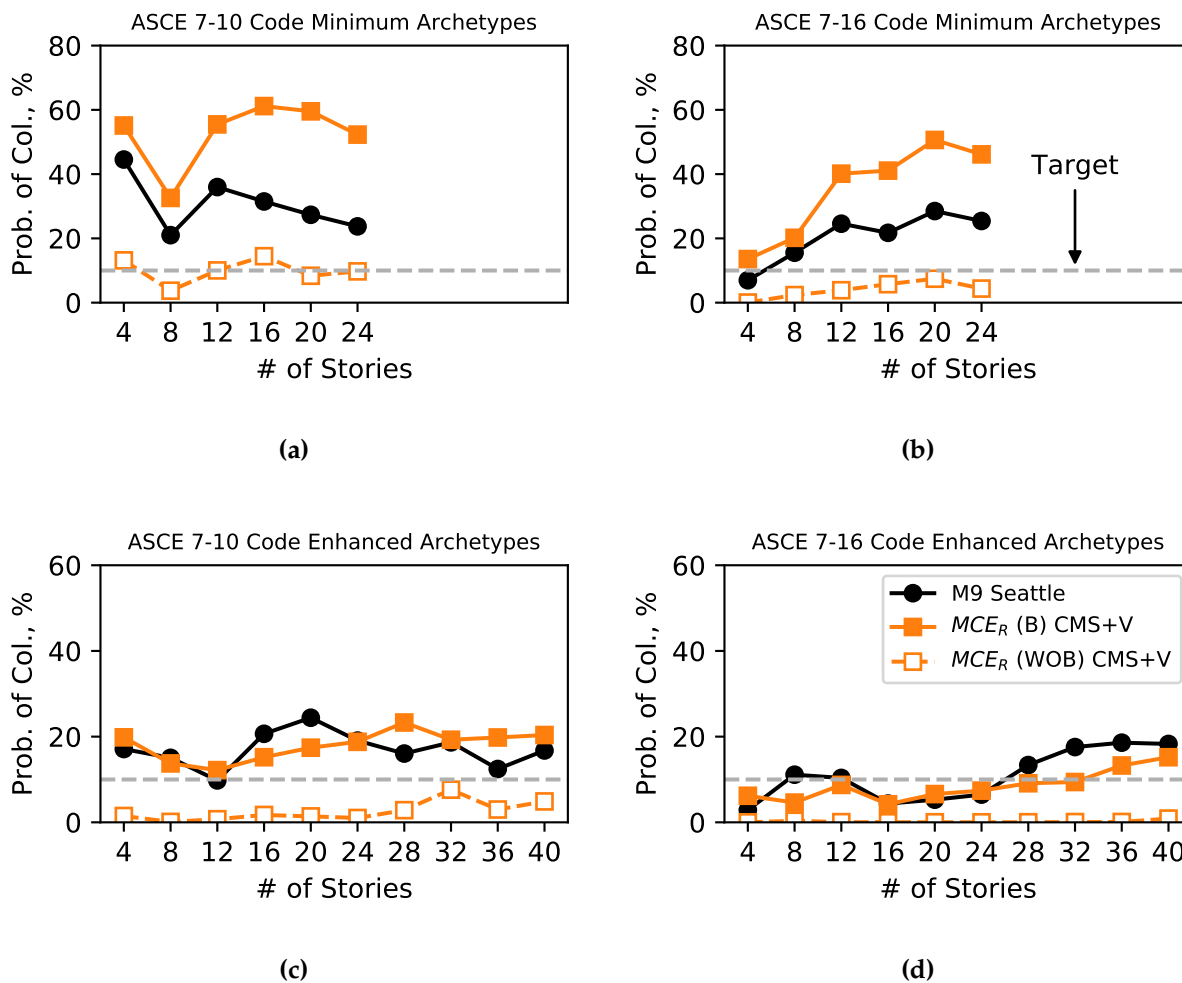


Figure 8.14: Probability of Collapse with respect to archetype story for (a) code-minimum ASCE 7-10 (10-E) archetypes, (b) code-minimum ASCE 7-16 (16-M) archetypes, (c) code-enhanced ASCE 7-10 (10-E) archetypes, and (d) code-enhanced ASCE 7-16 (16-E) archetypes.

The collapse probabilities were much larger for the MCE_R motions that reflected the effects of the basin, denoted as MCE_R (B). For the ASCE 7-16 code-enhanced archetypes, the collapse probabilities for MCE_R (B) motions were near the target values. This result is expected, because the lower target drift ratio (1.25% vs 2.0%) and lower demand-to-capacity ratio are usually used by engineers to satisfy the PBEE evaluation with motions that include a basin factor. The ASCE 7-10 code-enhanced archetypes had higher collapse probabilities, as expected, because the design forces were lower. The collapse probabilities exceeded the target values, ranging from 12% to 26% (Table 8.2). In contrast, the code-minimum designs had collapse probabilities that far exceeded the 10% limit, reaching 61% and 51% for the ASCE 7-10 and 7-16 minimum designs.

The collapse probabilities for the M9 Seattle motions differed greatly, depending on whether the archetypes were designed to code-minimum levels or code-enhanced levels. For the code-enhanced performance groups, the collapse probabilities for the M9 Seattle motions were similar to those of the MCE_R (B) motions. For the code-minimum groups, the collapse probabilities for the M9 motions fell between the values for the MCE_R (WOB) and MCE_R (B) motions.

The code minimum archetype results are consistent with current building codes that do not explicitly consider basin amplification on design spectral acceleration. Unlike for the tall buildings, the City of Seattle does not have PBEE requirements for buildings shorter than 73 m (240 ft). It should also be noted that these collapse predictions would even larger if additional uncertainty (similar to FEMA P695) is included in the collapse prediction due to the "quality of the design criteria", "modeling fidelity", and "laboratory test data" (ASCE 7-16).

The trends in collapse probability with number of stories are affected by differences in the racking factors. The racking factors tend to increase with structure height, as the wall size increases whereas the location of the gravity columns remain the same. For example, S4-16-E four-story archetype had γ_{rack} equal to 1.19, which increased the calculated collapse probability from 2.3% (no racking) to 6.2% (with racking). In comparison, the S40-16-E forty-story archetype had γ_{rack} equal to 1.56, which increased the calculated collapse probability from 0.8% (no racking) to 15.2% (with racking). The average and range in collapse probability without considering racking deformations are summarized in Table 8.2

Table 8.2: Summary of Mean Collapse Probabilities for simulated M9 motions in Seattle.

| Ground Motion Set | Model Assumption | Code Minimum Archetypes ASCE 7-10 | | Code Minimum Archetypes ASCE 7-16 | | Code Enhanced Archetypes ASCE 7-10 | | Code Enhanced Archetypes ASCE 7-16 | |
|------------------------------|------------------|-----------------------------------|-----------|-----------------------------------|-----------|------------------------------------|-----------|------------------------------------|-----------|
| | | Mean | Range | Mean | Range | Mean | Range | Mean | Range |
| M9 Seattle | Racking | 30.7 | 21.0-44.5 | 20.5 | 7.0-28.5 | 17.3 | 9.8-24.4 | 10.8 | 2.9-18.6 |
| | No Racking | 24.0 | 15.0-43.7 | 15.8 | 6.7-25.8 | 9.7 | 2.2-16.7 | 3.2 | 0.5-6.4 |
| | 84th Per. | 62.4 | 45.8-93.0 | 49.4 | 31.6-68.7 | 52.6 | 37.0-64.8 | 37.1 | 15.0-56.0 |
| MCE _R (B) CMS+V | Racking | 52.7 | 32.6-61.2 | 35.3 | 13.6-50.6 | 17.8 | 12.2-25.7 | 8.3 | 4.2-15.2 |
| | No Racking | 35.2 | 19.8-52.9 | 20.5 | 10.0-30.4 | 6.7 | 1.7-18.3 | 1.3 | 0.2-2.7 |
| MCE _R (WOB) CMS+V | Racking | 12.9 | 4.3-19.5 | 2.6 | 0.0-4.7 | 2.0 | 0.3-5.6 | 0.1 | 0.0-0.4 |
| | No Racking | 8.4 | 2.3-19.0 | 0.5log | 0.0-0.9 | 1.2 | 0.0-4.4 | 0.0 | 0.0-0.03 |

8.10 Relating Collapse Probabilities to Ground-Motion Characteristics

The large collapse probabilities estimated for an M9 earthquake in Seattle (Figure 8.14) results mainly from those scenarios that caused large maximum interstory drifts (Figure 8.12). These collapse probabilities are high due to the combined effects of spectral acceleration, spectral shape, and ground-motion duration. A scalar intensity measure, developed in Chapter 3, makes it possible to identify and account for the impact of each of these ground-motion characteristics on structural performance. This intensity measure, referred to as the effective spectral acceleration, $S_{a,eff}$, can be computed as:

$$S_{a,eff}(T_n) = S_a(T_n)\gamma_{dur}\gamma_{shape} \quad (8.4)$$

where γ_{dur} and γ_{shape} are non-dimensional factors that account the effects of duration and spectral shape on ground-motion intensity. The duration factor, $\gamma_{dur} = (D_s/(12T_n))^{C_{dur}}$ and the quantity D_s/T_n is related to the number of force-deformation cycles. The normalization constant of 12 corresponds to a nominal significant duration of 12s (the geometric mean for a commonly used crustal ground motion set, FEMA P695), divided by a nominal period of 1s. The exponent C_{dur} accounts for the structure's sensitivity to duration. In general, this exponent varies with properties of the structural system, i.e., ductility capacity and properties that affect the cyclic

degradation of the system, and the optimal values of C_{dur} can be determined using regression analyses (see Chapter 3). For convenience, this exponent can be taken as 0.10 for evaluating the likelihood structural collapse.

The spectral shape factor, $\gamma_{shape} = (SS_a(T_n, \alpha)/SS_{a,0})^{C_{shape}}$ where the value of SS_a is normalized by $SS_{a,0}$ which is taken as $\ln\alpha/(\alpha - 1)$. This relationship can be derived from Eq. 8.1 with the assumption that $S_a(T_n)$ varies as $1/T_n$, as is the case for the constant velocity part of the design spectrum, where the linear and nonlinear deformation demands are nearly equal (Newmark and Hall, 1982). The C_{shape} exponent accounts for the structure's sensitivity to spectral shape and for convenience can be taken as 1.0 for collapse prediction of ductile systems that are expected to undergo large period elongation (see Chapter 6).

As previously discussed, the value of α accounts for period elongation expected in ductile systems, therefore, α is taken as expected where $\mu_{expected}$ is the expected ductility demand and can be approximated as the spectral acceleration of the motion normalized by the strength of the structure, S_a/η (i.e., Newmark and Hall's (1982) constant displacement rule), but less than the maximum ductility capacity. $\mu_{expected}$ was taken as 10 for specially reinforced concrete core walls (approximated as 1.7R, see Chapter 3). The value of η was approximated as the maximum base shear the structure can resist under a pushover (with forces distributed along each floor using modal analysis), normalized by the seismic weight of the structure.

Collapse fragility functions were derived for all 20 code-minimum archetypes for two motions sets: the M9 Seattle set (30 motions), as well as the MCE_R motions, with and without basin effects (200 motions for each archetype). To be able to compare the effective spectral accelerations among the archetypes, the fragility curves were defined using the normalized intensity measures S_a/η and $S_{a,eff}/\eta$. For each normalized intensity measure, the fragility curves were computed by (i) binning the data with respect to the intensity measure in log-scale (11 bins), (ii) calculating the total collapse probability for each bin:

$$P[\text{collapse}|\text{bin}] = \frac{1}{m} \sum_{i=1}^m P[\text{collapse}|\gamma_{rack}x_i] \quad (8.5)$$

where m is the total number of instances per bin, and (iii) calculating the median normalized intensity measure for that bin intensity. Figure 8.15 shows the likelihood of collapse for each bin (hollow dots) and a fitted collapse fragility for the M9 Seattle and MCE_R motions.

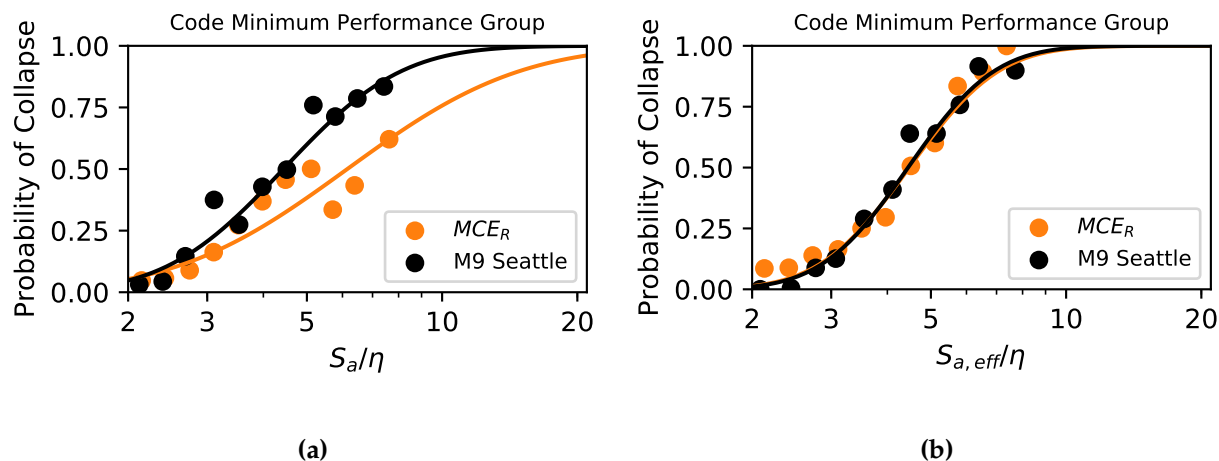


Figure 8.15: Collapse fragility for all code minimum archetypes subjected to M9 Seattle motions and MCE_R (with and without basins) with respect to (a) normalized spectral acceleration and (b) normalized effective spectral acceleration.

The use of $S_{a,eff}$ (as opposed to S_a) improved the estimates of collapse in two ways. As shown in Figure 8.15a, the likelihood of collapse estimated from S_a differed greatly between the two sets of motions. For example, the value of S_a/η at a collapse probability of 50% (collapse capacity) was 6.2 for the MCE_R motions and 4.4 for the M9 Seattle motions, a difference of 29%. This lower collapse capacity for the M9 motions is a result of the sets' damaging spectral shapes (Figure 8.15) and durations (Figure 8.6) that are not captured by S_a/η alone. The collapse fragilities defined using $S_{a,eff}/\eta$ resulted in much closer collapse capacities between the two ground-motion sets (4.5 for MCE_R and 4.1 for M9, a difference of only 8%).

In addition, the fragilities for each individual set had a larger uncertainty for S_a/η than $S_{a,eff}/\eta$. This uncertainty is typically quantified using the standard deviation of a log-normal distribution (σ_{\ln}). For the M9 motions, σ_{\ln} reduced from 0.48 for S_a/η to 0.27 for $S_{a,eff}/\eta$ (a 43% reduction). The standard deviation of the fragility curves derived for the MCE_R motions decreased similarly (0.70 to 0.35, corresponding to a 50% reduction).

8.11 Implementation Considerations

The collapse probabilities (Figure 8.14) for the simulated M9 motions greatly exceed the allowable values for many archetypes, particularly the code-minimum ones, reaching a peak collapse probability of 61% for M9 simulations. It would be possible to incorporate the M9 simulation into the PSHA used in the national seismic hazard maps, which would likely result in drastic increases in seismic design values for the Seattle region. One could also modify the allowable drift levels, or accept higher collapse risks, such as been done in some regions of the U.S. Any of these approaches would have large implications for in the Pacific Northwest. For this reason, it is important to consider the reliability of the computed results (ground motions and archetype response), as well as the appropriate performance expectations for an M9 earthquake.

8.11.1 Reliability of Results

No measured ground motions are available for the Pacific Northwest, and it is impossible to be sure that any of the 30 simulations represent the next M9 earthquake on the CSZ. To provide some assurance that the ground motions are reasonable, the implemented ground-motion simulation methodology (Frankel et al., 2018b) was calibrated to reproduce key characteristics (e.g., wave forms, spectral accelerations, durations) of the observed ground motions during the Tohoku earthquake (Frankel, 2013) and Maule earthquake (Frankel, 2017). Wirth et al. (2018) showed the effects of variations of key rupture properties on ground-motion characteristics were consistent with expectations.

Outside of the sedimentary basins, the simulated M9 motions were consistent with subduction earthquake ground-motions models (Abrahamson et al., 2016; Morikawa and Fujiwara, 2013). The effects of the basin on the simulated motions were similar to those observed for the Niigata, Yufutsu, and Kosen sedimentary basins in Japan during many subduction interface earthquakes (Chapter 4). Frankel et al. (2009) found that the effects of the Seattle basin on ground motions measured during the Nisqually earthquake were also similar to that observed for the simulations.

The reliability of the structural analyses needs also to be evaluated. The wall modeling methodology was developed to reproduce the results of over 30 cyclic tests of reinforced concrete walls (Chapter 7 and the ATC-123 project report, 2018). However, none of these tests considered

the number of cycles induced by the long-duration shaking (Bazaez and Dusicka, 2016), or of the interaction between period elongation and basin amplification. A limited parametric study found that the collapse probability varied little for small variations of the steel model parameters that govern low-cycle fatigue (Appendix F). In addition, the lateral-force resistance of the gravity system was neglected, and three-dimensional response was not considered.

Despite these model uncertainties, the results are generally consistent with other results. The collapse results were consistent with the performance of deteriorating, single-degree-of-freedom oscillators, with properties that were representative of buildings (Chapter 6). The collapse results were also consistent with code expectations. For example, the average calculated collapse probability (8.3%) was near the 10% target for the ASCE 7-16, code-minimum archetypes when they were subjected to motions that were consistent with the design assumptions (MCE_R WOB CMS+V). Therefore the differences in collapse probabilities are attributable to differences in the motion characteristics, rather than to the details of the building model.

8.11.2 Performance Expectations for Archetypes During M9 Earthquake

In Figure 8.14, the performance of the archetypes for the M9 motions was compared with the 10% collapse target for the MCE_R motions. The direct comparison of the M9 motions with MCE_R motions and MCE_R collapse targets can be misleading for two reasons.

The large-magnitude CSZ interface events are only part (47% at 2.0 s) of the seismic hazard in Seattle. A full risk assessment, with a target collapse risk of 1% in 50 years, would need to include the contributions from or all the other sources that contribute to the hazard, such as the Seattle fault and deep intraslab events. This would be difficult, because it would necessary to account for the effects of the deep Seattle basin on intraslab earthquake motions and near-fault, crustal earthquake motions.

A second consideration that complicates the comparison is the differences in return period between the design event and M9 CSZ event. M9 motions, with a return period of 500 years, are likely to happen several times during the approximate 2000-year, risk-adjusted return period for the MCE_R . Assuming a Poisson distribution, there is a 57% chance that the M9 event will occur at least four times. If one assumes that the 30 earthquake realizations correspond to 30

independent events, then the maximum of four events would, on average, correspond to the 84 percentile motion (25/30) for a single event (i.e., $0.50 = 0.844$). For the 84th percentile M9 motions, the average collapse probabilities for code-enhanced archetypes increased to 53% for ASCE 7-10 archetypes and increased to 37% for ASCE 7-16 archetypes. This corresponded to an increase in collapse probability of a factor of 3.1 and 3.9 for the ASCE 7-10 and 7-16 archetypes, respectively. For the code-minimum archetypes, the average the collapse probabilities for the 84% M9 motions were 62% and 49% for the ASCE 7-10 and 7-16 archetypes, respectively. The collapse probability reached a maximum of 94% for the 4-story archetype (S4-10-M).

8.12 Chapter Conclusions

Thirty physics-based ground-motion simulations (Frankel et al., 2018b) provided the opportunity to evaluate the impacts of an M9 CSZ earthquake and the Seattle basin on the reinforced concrete core wall structures in Seattle. The motions were particularly damaging because: (a) their spectral accelerations exceeded the MCE_R spectra for periods between 1.0 to 4.0 s (Figure 8.3), (b) the spectral shapes were more damaging (up to a period of 4.0 s) than those typically considered in design (MCE_R CMS, Figure 8.15), and (c) the motions were much longer (in terms of $D_{s,5-95\%}$) than crustal motions typically considered to evaluate structural systems (FEMA P695) and even longer than motions recorded during the magnitude-9 Tohoku earthquake (Figure 8.6).

The impact of these motions were evaluated for thirty two archetypes, ranging from 4 to 40 stories, representing modern residential concrete wall buildings in Seattle. Archetypes were developed to reflect the ASCE 7-10 and ASCE 7-16 code provisions, for both code-minimum and code-enhanced practice. The code-enhanced performance group was designed to meet a stringent drift criteria of 1.25% and a demand-to-capacity ratio of 0.8, whereas the code-minimum archetypes were designed to the maximum 2.00% limit and a demand-to-capacity ratio of 1.00. Maximum interstory drifts and collapse probabilities were computed with nonlinear analysis and a gravity system fragility relationship derived from experiments.

The median (for 30 motions) of the maximum inter-story drift ratio (for each archetype) for the M9 simulations generally exceeded the drift ratios for the motions that are consistent with the ASCE 7-16 MCE_R (without basin), which govern the design of most buildings in Seattle (Figure

8.10). The median of the maximum drift for the M9 motions were generally lower than for the MCE_R that included a basin term, which is representative of the PBEE design of tall buildings. However, the drift ratios for the M9 motions varied more than the MCE_R motions, even accounting for variance in the conditional spectrum (MCE_R (B) CMS+V, Figure 8.12).

The code-minimum archetypes met the 10% collapse probability target for motions that are consistent with the MCE_R earthquake considered in the ASCE 7 design spectra, which were developed without considering the effects of basins. This result suggests that the archetype design and modeling approaches are consistent with code expectations (10% in MCE_R) when the motions are consistent with the seismic hazard reflected in the code.

As expected, the collapse probabilities for the ASCE 7-10 archetypes exceeded that of the ASCE 7-16 archetypes, and the collapse probabilities for the code-minimum archetypes exceeded that for the code-enhanced archetypes (Figure 8.14 and Table 8.2). The collapse probabilities were much larger for the M9 (and MCE_R with basin) motions, which that reflected the effect of the basins. For the code-minimum, ASCE 7-10 structures, the average collapse probability for the archetypes was 31%. In contrast, for the code-enhanced, ASCE 7-16 archetypes, the average collapse probability was 11%.

The variations in collapse probability among the various archetypes and motions were not captured by S_a alone. The effective spectral acceleration, $S_{a,eff}$, which accounts for ground-motion spectral acceleration, spectral shape and duration, was able to reduce the uncertainty in collapse prediction.

In interpreting these results, it is important to consider that: (a) the return period for the M9 scenarios is around 500 years, which is far shorter than the return period corresponding to the risk-adjusted maximum considered earthquake, and (b) other sources of earthquakes contribute to the hazard in Seattle. It is also important also to note that the implications of the M9 simulations may be far greater for other structural systems, which might be much weaker, or might be even more sensitive to the effects of spectral shape and duration.

Chapter 9

CONCLUSIONS

The Cascadia Subduction Zone (CSZ) is capable of producing large-magnitude earthquakes (up to magnitude 9), whose motions are expected to be long and to be affected by the deep sedimentary basins that underlie much of the Puget Sound region. Current codes do not account for the effects of long durations and basins; these effects need to be understood to evaluate the risk faced by buildings and infrastructure in the Pacific Northwest (PNW).

9.1 A New Ground-Motion Intensity Measure

The design of most structures is governed by the specified spectral acceleration at the fundamental period of the structure. However, the calculated nonlinear structural responses of a building can vary greatly, even if recorded ground motions have similar spectral accelerations. To reduce the variation in structural response at a particular ground-motion intensity a combined scalar intensity measure was formulated that accounts for the effects of spectral acceleration, ground-motion duration, and response spectrum shape (Chapter 3). This new IM includes a measure of spectral shape that integrates the spectrum over a period range that depends on the structure's ductility. The new IM is efficient, sufficient, scalable, transparent, and versatile. These features made it suitable for evaluating the intensities of measured and simulated ground motions. In Chapter 6, the new intensity measure, $S_{a,eff}$, is normalized to make it easier to compare with spectral acceleration, S_a .

9.2 Basin Effects in Japan

The effects of deep sedimentary basins are not unique to the Pacific Northwest. Chapter 4 quantified the effects of deep basins in Japan during subduction zone earthquakes. These basins were found to amplify spectral acceleration at long periods, which resulted in damaging spectral

shapes, especially for structures that were expected to soften and undergo long period elongation. The ground-motions were long, because the magnitudes were large, but basins were found to only weakly increase ground-motion duration, as measured with significant duration.

The combination of the larger spectral acceleration, damaging spectral shapes, and longer durations, resulted in increased damage in reinforced concrete special moment frame buildings, compared to the damage expected for crustal earthquake motions (FEMA P695) typically used to evaluate structural systems.

9.3 Evaluation of Simulated Ground Motions

To compensate for the paucity of recorded subduction events in the PNW, thirty M9 CSZ scenarios were generated by Frankel et al. (2018b). These motions were generated using physics-based simulations that use large 3D seismic velocity model which includes the geological structure of the CSZ and several deep sedimentary basins. Ground-motion components for low frequencies (below 1 Hz) were generated deterministically using 3D simulations that accounted for the basin geometry. Components for high frequencies (above 1 Hz) did not include basin effects and were generated stochastically.

Chapter 5 showed that the characteristics of the simulated motions were within the range expected based on recorded earthquakes. Specifically sites located outside the basin resulted in motions that were within 0.5 natural log of S_a of the BC-Hydro (2016) GMM prediction (GMM residuals). In contrast, inside basins the GMM residuals were much larger for sites located inside basins. This large variability in GMM residuals inside and near basins could be explained using basin proxies (e.g., $Z_{2.5}$) with simple linear regression analyses (Chapter 5).

9.4 Regional Impacts on Idealized Systems

The consequences of the thirty M9 earthquake scenarios on structural response was studied using deteriorating single-degree-of-freedom oscillators (Chapter 6). These oscillators had properties that resembled several various building types (low strength vs. high strength, and brittle vs. ductile). The effects of the 30 simulations were quantified regionally across the Puget Sound regions in terms of the likelihood of structural collapse and damage states prior to collapse. The

regional variation of damage was estimated by combining probabilistic characterizations of the seismic resistance of structures and of the effective spectral acceleration, $S_{a,eff}$, which accounts for the effects of spectral accelerations, spectral shape, and ground-motion duration. For many locations above basins (e.g., $Z_{2.5} > 6$ km), the likelihood of collapse of low-strength-ductile and high-strength-brittle systems exceeded 14% at a period of 1s. As expected, increasing strength and/or ductility resulted in lower deformation demands and collapse likelihood.

For simulated M9 motions in Seattle, the geometric mean of the two horizontal components of S_a exceeded the risk-adjusted, maximum considered earthquake, MCE_R , for 13 out of the 30 scenarios at a period of 2 s. In addition, the simulated motions in Seattle had more damaging spectral shapes (particularly at a period of 1s) than the spectral shapes typically used to compute the conditional mean spectra. The large magnitude of all 30 simulations also resulted in longer-duration motions (significant durations near 110 s) than those measured in typical crustal earthquakes.

9.5 Modeling of RC Core Wall Buildings

The response of building archetypes during an M9 CSZ earthquake was evaluated using a modelling methodology developed for reinforced concrete core wall buildings. This methodology extended the work by Pugh et al. (2015) to use *OpenSees* displacement-based beam-column elements with fiber sections at each integration point. The modelling approach was calibrated to over fifteen experimental walls tests to predict the onset of strength loss.

Using this methodology, the sensitivity of collapse predictions was tested using a series of planar, solid and coupled wall, archetypes with varying modelling parameters (e.g., element formulation, constitutive parameters affecting the concrete and steel material) as well as design parameters that affected the axial and shear demands and deformation capacities of the gravity-load resisting system. The study found that the collapse prediction was highly sensitive to whether displacement-based or force-based formulations were used for the beam-column element formulation. The displacement-based element was able to reach converged solutions at high intensity shaking, and as a result, it was able to give robust predictions of collapse without altering the *OpenSees* convergence tolerances. In addition, the methodology concluded that both

the collapse probability of planar solid and coupled walls were sensitive to the axial load, the concrete residual strength, and the drift capacity of the gravity system.

9.6 Suite of RC Core Wall Archetypes and Models

Numerical models were developed for thirty two archetypes, ranging from 4 to 40 stories, representing modern residential concrete wall buildings in Seattle. The archetypes were developed to reflect the ASCE 7-10 and ASCE 7-16 code provisions. For each code version, code-minimum archetypes were developed that barely met the code requirements, and code-enhanced archetypes were developed to reflect typical practice for performance-based tall building design in Seattle. These archetypes were developed with the assistance of the Earthquake Engineering Committee of the Structural Engineering Association of Washington.

9.7 Impact of M9 Motions on RC Core Wall Buildings

The design and modelling approaches for the archetypes appear to be consistent with the underlying performance expectations during the MCE_R . For example, the ASCE 7-16 code-minimum archetypes had an average collapse probability of 2.6% for motions that were consistent with the MCE_R earthquake, which does not consider the effects of basins. This percentage is below the 10% collapse probability target.

The collapse percentages were much higher for motions that reflected the influence of the sedimentary basins. As a result of the damaging ground-motion characteristics identified previously, the collapse likelihood under the M9 CSZ scenarios far exceeded the 10% target for the maximum considered earthquake. The variations in collapse probability among the various archetypes and motions were explained using a ground-motion intensity measure ($S_{a,eff}$) that accounted for the ground-motion spectral acceleration, spectral shape, and duration.

The designs of the code-enhanced archetypes met the requirements of the Tall Building Initiative guidelines (2017). As a result of the more stringent drift (1.25%) and strength ($DCR=0.8$) requirements, these archetypes also met the 10% collapse probability target for MCE_R motions that included basin effects. The collapse probability of the code-enhanced archetype under an M9 scenarios was similar to the MCE_R motions (10%).

The collapse probabilities for the M9 scenarios cannot be directly compared with the MCE_R expectations, because an M9 CSZ earthquake has a return period of only ~500 years whereas the MCE_R typically corresponds to a ~2000 year event for Seattle. In addition, multiple sources typically contribute to the seismic hazard. Therefore, if one were to consider the maximum M9 CSZ earthquake possible in a ~2000 year return period and other sources, the collapse probability would increase even further. Alternatively, if the M9 simulations were considered in the full probabilistic seismic collapse risk assessment then these archetypes would likely exceed the 1% collapse risk in 50 years (set by the ASCE 7-16 provisions) if their collapse probability was already near 10%.

9.8 Broader Impacts

The findings of this dissertation will help the community anticipate areas with great vulnerability to catastrophic natural disasters. The research outcomes here will provide structural engineers insight on how to account for the effects of large-magnitude earthquakes and deep sedimentary basins on building design and evaluation. Additionally, to facilitate the transition of research outcomes into practice, the ground-motions (DOI: [10.17603/DS2WM3W](https://doi.org/10.17603/DS2WM3W)) and structural models were made public through online data repositories (see <https://github.com/nassermarafi/>), journal publications, and workshops with practicing engineers.

Although not considered here, it is likely that other structural systems may even be more vulnerable to these motions. The research findings here are not unique to the Pacific Northwest as many cities are founded on deep sedimentary basins, and some are near subduction zones. In addition, the process used for evaluating synthetic motions can be used with physics-based ground-motion simulations of other earthquake faults (e.g., San Andreas, Seattle Fault).

Appendix A

CONDITIONAL MEAN SPECTRUM SUMMARY

In design procedures that use nonlinear time-history analysis, ASCE 7-16 permits the use of ground motions scaled and selected to match a conditional mean spectrum (CMS) to evaluate building response. The CMS is an alternative to the uniform hazard spectrum (UHS) typically obtained from a probabilistic seismic hazard analysis (PSHA) (Baker, 2011), and is defined as the expected response spectrum, conditioned on a target spectral acceleration at a given period of interest. The CMS ideally represents a more realistic ground motion spectrum than the UHS, which tends to be overly conservative as a target for ground motion selection in regions dominated by multiple sources of seismicity. For a given site and return period, a CMS was generated for a seismic source mechanism (i.e. crustal, intraslab, and interface). In order to compare the M9 simulated motions to what would be expected using ASCE 7-16, motions were selected and scaled to the mean conditional mean spectra for the crustal, intraslab, and interface earthquake sources that contribute to the seismic hazard in Seattle. The CMS was computed using EZ-Frisk (Fugro, 2018), a software package that performs site-specific PSHA and hazard source deaggregation. For each of the considered structural periods (T_n), the CMS were conditioned such that $S_a(T_n)$ was equal to the $S_a(T_n)$ of the Seattle MCE_R as determined from the PSHA. For a given ground motion suite, the proportion of crustal, intraslab, and interface motions was selected in accordance to the contribution of each source mechanism to the overall hazard, based on the deaggregated hazard data. The candidate motions from each source mechanism were selected and amplitude-scaled to match the corresponding source-specific target CMS.

For crustal earthquakes, motions with a peak ground acceleration (PGA) greater than 0.05 g were selected from the NGA-West-2 database (PEER, 2014). In downtown Seattle, the crustal earthquake hazard is typically controlled by the Seattle Fault (e.g., 68% at 0.5 s). Therefore, a percentage of the crustal earthquake motions were selected with pulse-like characteristics as per the recommendation by Appendix C in ATC-82 (NIST, 2011). The motions with pulse-like

characteristics were oriented so that they are 30-degrees off fault-normal, which is the typical orientation of most building in downtown Seattle relative to the Seattle Fault (due to the street grid layout). For intraslab earthquakes, 100 ground-motion pairs were retrieved from the NGA-Subduction database (PEER 2018) with the following search criteria: (1) recordings from intraslab earthquakes, (2) stations located in the forearc (similar to Seattle), (4) $M_w > 6$, (5) R_{CD} between 42-65 km, (5) V_{S30} between 190 and 760 m/s, and (6) PGA larger than 0.1g. For interface earthquakes, ground-motions were selected from three large-magnitude interface earthquakes (M_w 7.9 Tohoku aftershock, M_w 8.3 Tokachi-Oki, and M_w 9.0 Tohoku) in Japan from the K-Net and KiK-NET database (NIED 2018). For each of the structural periods considered, 100 ground-motions were selected and distributed to match the total contribution from the three source mechanisms. Note that selected ground motion records were occasionally repeated between period sets (although typically with different scaling factors), but never within a particular set. For all selected ground-motions, scaling factors were selected to minimize a weighted mean-squared error (MSE) between the candidate ground motion record and the target spectrum (in log-scale), and were limited to be no greater than five. As an example, Figure A.1 shows the 2.0 s conditional mean spectra (solid black line) for the three source mechanisms and the selected ground motions to match the mean CMS on average within the period range of interest. For a 2.0 s period, the number of motions considered per source-mechanism was 47, 6, and 47 for crustal, intraslab, and interface earthquakes, respectively.

Ground-motion duration was not explicitly considered in the ground-motion selection process but instead considered implicitly by selecting motions from similar source-mechanisms, source-site distances, and earthquake magnitudes that control the MCE_R hazard. The resulting median $D_{s,5-95\%}$ of the motions was found to be around 17 s, 19 s, and 97 s long for crustal, intraslab, and interface earthquakes, respectively.

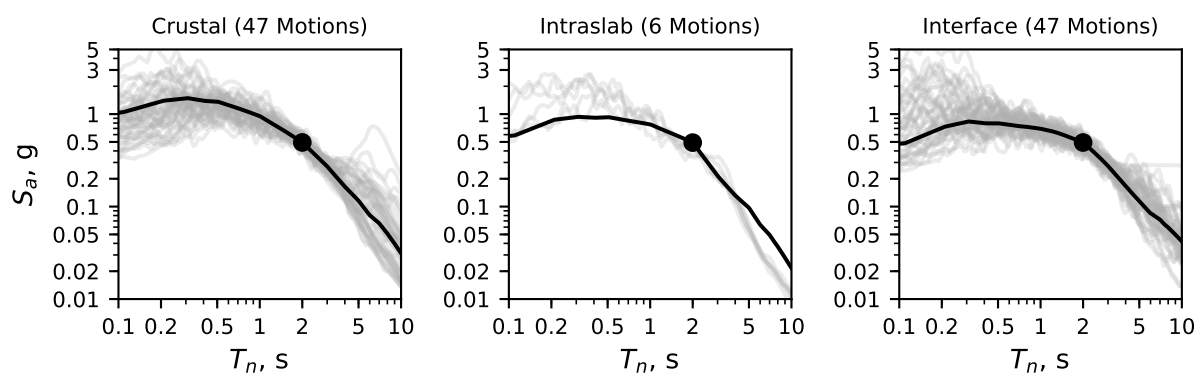


Figure A.1: Ground motions selected to match the mean CMS for Seattle at 2.0 s period for (a) crustal, (b) intraslab, and (c) interface earthquakes.

Appendix B

ARCHETYPE CHARACTERISTICS

A total of thirty two core-wall archetypes were designed ranging from 4- to 40-stories tall using ASCE 7-10 and ASCE 7-16 based on the methodology described above. Appendix Table B.1-B.6 summarizes the core length (l_w), and core width (b_w) for all archetypes. For each archetypes 8-stories and taller, the wall thickness (t_w), and longitudinal reinforcement ratio (ρ_l) at various story ranges above the archetypes are summarized in Appendix Table B.1-B.6. Note that the four-story archetype was designed as a planar wall with boundary elements (i.e., $b_w = t_w$). The boundary element length sizes (l_{be}) and longitudinal reinforcement ratios ($\rho_{l,be}$) are summarized in Appendix Table B.7 for all 4-story archetypes. Minimum longitudinal reinforcement was used in the web region as permitted by ACI 318, where the reinforcement area equaled 0.25% of the wall cross-section area.

The wall's longitudinal reinforcement was tied in the transverse direction and detailed according to the requirements in ACI 318-14 §18.10. The transverse reinforcement ratio is summarized in column ρ_v in Table B.1-B.6. The variation in wall reinforcement layout along the wall height was optimized to balance efficiency (the required versus the provided reinforcement) and constructability (the number of variations in the section reinforcement layout).

Table B.1: Archetype dimensions and reinforcement layout for ASCE 7-10 code minimum archetypes.

| Arch. ID | Stories | l_w (in) | b_w (in) | t_w (in) | ρ_l | ρ_v |
|----------|----------|------------|------------|------------|----------|----------|
| S4-10-M | -1 to 4 | 120 | 0 | 14 | 0.00 | 0.00 |
| S8-10-M | -2 to 3 | 132 | 66 | 20 | 2.00 | 3.33 |
| S8-10-M | 4 to 6 | 132 | 66 | 20 | 1.10 | 0.92 |
| S8-10-M | 7 to 8 | 132 | 66 | 20 | 0.25 | 0.25 |
| S12-10-M | -3 to 3 | 168 | 84 | 20 | 1.60 | 2.67 |
| S12-10-M | 4 to 6 | 168 | 84 | 20 | 1.00 | 0.83 |
| S12-10-M | 7 to 9 | 160 | 84 | 16 | 0.45 | 0.25 |
| S12-10-M | 10 to 12 | 160 | 84 | 16 | 0.25 | 0.25 |
| S16-10-M | -3 to 4 | 192 | 96 | 22 | 1.40 | 2.57 |
| S16-10-M | 5 to 8 | 192 | 96 | 22 | 1.00 | 0.92 |
| S16-10-M | 9 to 12 | 180 | 96 | 16 | 0.35 | 0.25 |
| S16-10-M | 13 to 16 | 180 | 96 | 16 | 0.25 | 0.25 |
| S20-10-M | -3 to 4 | 216 | 108 | 24 | 1.20 | 2.40 |
| S20-10-M | 5 to 8 | 216 | 108 | 24 | 0.90 | 0.90 |
| S20-10-M | 9 to 12 | 204 | 108 | 18 | 0.50 | 1.50 |
| S20-10-M | 13 to 20 | 204 | 108 | 18 | 0.25 | 0.25 |
| S24-10-M | -3 to 4 | 252 | 126 | 28 | 0.70 | 4.18 |
| S24-10-M | 5 to 8 | 252 | 126 | 28 | 0.50 | 1.49 |
| S24-10-M | 9 to 12 | 232 | 126 | 18 | 0.50 | 1.50 |
| S24-10-M | 13 to 24 | 232 | 126 | 18 | 0.25 | 0.25 |

Table B.2: Archetype dimensions and reinforcement layout for ASCE 7-16 code minimum archetypes.

| Arch. ID | Stories | l_w (in) | b_w (in) | t_w (in) | ρ_l | ρ_v |
|----------|----------|------------|------------|------------|----------|----------|
| S4-16-M | -1 to 4 | 144 | 0 | 18 | 0.00 | 0.00 |
| S8-16-M | -2 to 3 | 144 | 72 | 24 | 2.00 | 4.00 |
| S8-16-M | 4 to 6 | 144 | 72 | 24 | 1.00 | 1.00 |
| S8-16-M | 7 to 8 | 144 | 72 | 24 | 0.25 | 0.25 |
| S12-16-M | -3 to 3 | 180 | 90 | 24 | 1.60 | 3.20 |
| S12-16-M | 4 to 6 | 180 | 90 | 24 | 1.20 | 1.20 |
| S12-16-M | 7 to 9 | 168 | 90 | 18 | 0.70 | 2.10 |
| S12-16-M | 10 to 12 | 168 | 90 | 18 | 0.25 | 0.25 |
| S16-16-M | -3 to 4 | 204 | 102 | 28 | 1.50 | 3.50 |
| S16-16-M | 5 to 8 | 204 | 102 | 28 | 1.00 | 1.17 |
| S16-16-M | 9 to 12 | 188 | 102 | 20 | 0.60 | 1.28 |
| S16-16-M | 13 to 16 | 188 | 102 | 20 | 0.25 | 0.25 |
| S20-16-M | -3 to 4 | 228 | 114 | 30 | 1.40 | 2.77 |
| S20-16-M | 5 to 8 | 228 | 114 | 30 | 0.95 | 1.19 |
| S20-16-M | 9 to 12 | 212 | 114 | 22 | 0.70 | 1.14 |
| S20-16-M | 13 to 20 | 212 | 114 | 22 | 0.25 | 0.25 |
| S24-16-M | -3 to 4 | 252 | 126 | 32 | 1.30 | 2.74 |
| S24-16-M | 5 to 8 | 252 | 126 | 32 | 1.10 | 1.47 |
| S24-16-M | 9 to 12 | 240 | 126 | 26 | 0.80 | 1.13 |
| S24-16-M | 13 to 16 | 240 | 126 | 26 | 0.35 | 0.25 |
| S24-16-M | 17 to 24 | 240 | 126 | 26 | 0.25 | 0.25 |

Table B.3: Archetype dimensions and reinforcement layout for ASCE 7-10 code enhanced archetypes.

| Arch. ID | Stories | l_w (in) | b_w (in) | t_w (in) | ρ_l | ρ_v |
|----------|----------|------------|------------|------------|----------|----------|
| S4-10-E | -1 to 4 | 168 | 0 | 14 | 0.00 | 0.00 |
| S8-10-E | -2 to 3 | 192 | 96 | 14 | 0.90 | 1.37 |
| S8-10-E | 4 to 6 | 192 | 96 | 14 | 0.55 | 0.82 |
| S8-10-E | 7 to 8 | 192 | 96 | 14 | 0.25 | 0.25 |
| S12-10-E | -3 to 3 | 240 | 120 | 14 | 0.50 | 1.49 |
| S12-10-E | 4 to 6 | 240 | 120 | 14 | 0.50 | 0.75 |
| S12-10-E | 7 to 9 | 240 | 120 | 14 | 0.35 | 0.25 |
| S12-10-E | 10 to 12 | 240 | 120 | 14 | 0.25 | 0.25 |
| S16-10-E | -3 to 4 | 264 | 132 | 14 | 0.50 | 1.04 |
| S16-10-E | 5 to 8 | 264 | 132 | 14 | 0.50 | 0.75 |
| S16-10-E | 9 to 16 | 264 | 132 | 14 | 0.25 | 0.25 |
| S20-10-E | -3 to 4 | 288 | 144 | 14 | 0.50 | 1.04 |
| S20-10-E | 5 to 8 | 288 | 144 | 14 | 0.50 | 0.75 |
| S20-10-E | 9 to 12 | 288 | 144 | 14 | 0.35 | 0.25 |
| S20-10-E | 13 to 20 | 288 | 144 | 14 | 0.25 | 0.25 |

Table B.4: Archetype dimensions and reinforcement layout for ASCE 7-10 code enhanced archetypes (continued).

| Arch. ID | Stories | l_w (in) | b_w (in) | t_w (in) | ρ_l | ρ_v |
|----------|----------|------------|------------|------------|----------|----------|
| S24-10-E | -3 to 4 | 312 | 156 | 18 | 1.00 | 1.96 |
| S24-10-E | 5 to 8 | 312 | 156 | 18 | 0.75 | 1.00 |
| S24-10-E | 9 to 12 | 312 | 156 | 18 | 0.60 | 0.80 |
| S24-10-E | 13 to 16 | 312 | 156 | 18 | 0.50 | 0.96 |
| S24-10-E | 17 to 20 | 304 | 156 | 14 | 0.50 | 0.75 |
| S24-10-E | 21 to 24 | 304 | 156 | 14 | 0.50 | 0.25 |
| S28-10-E | -3 to 4 | 336 | 168 | 18 | 0.85 | 1.67 |
| S28-10-E | 5 to 8 | 336 | 168 | 18 | 0.60 | 0.80 |
| S28-10-E | 9 to 16 | 336 | 168 | 18 | 0.50 | 0.67 |
| S28-10-E | 17 to 28 | 332 | 168 | 16 | 0.50 | 0.59 |
| S32-10-E | -3 to 4 | 360 | 180 | 20 | 0.75 | 2.22 |
| S32-10-E | 5 to 16 | 360 | 180 | 20 | 0.50 | 0.74 |
| S32-10-E | 17 to 32 | 356 | 180 | 18 | 0.50 | 0.67 |
| S36-10-E | -3 to 4 | 384 | 192 | 22 | 0.60 | 1.96 |
| S36-10-E | 5 to 16 | 384 | 192 | 22 | 0.50 | 0.81 |
| S36-10-E | 17 to 36 | 372 | 192 | 16 | 0.50 | 0.59 |
| S40-10-E | -3 to 4 | 408 | 204 | 24 | 0.60 | 2.13 |
| S40-10-E | 5 to 8 | 408 | 204 | 24 | 0.60 | 1.07 |
| S40-10-E | 9 to 16 | 408 | 204 | 24 | 0.50 | 0.89 |
| S40-10-E | 17 to 32 | 396 | 204 | 18 | 0.50 | 0.67 |
| S40-10-E | 33 to 40 | 392 | 204 | 16 | 0.50 | 0.59 |

Table B.5: Archetype dimensions and reinforcement layout for ASCE 7-16 code enhanced archetypes.

| Arch. ID | Stories | l_w (in) | b_w (in) | t_w (in) | ρ_t | ρ_v |
|----------|----------|------------|------------|------------|----------|----------|
| S4-16-E | -1 to 4 | 192 | 0 | 18 | 0.00 | 0.00 |
| S8-16-E | -2 to 3 | 216 | 108 | 16 | 0.95 | 1.65 |
| S8-16-E | 4 to 6 | 216 | 108 | 16 | 0.70 | 1.19 |
| S8-16-E | 7 to 8 | 216 | 108 | 16 | 0.25 | 0.25 |
| S12-16-E | -3 to 3 | 240 | 120 | 18 | 0.85 | 2.27 |
| S12-16-E | 4 to 6 | 240 | 120 | 18 | 0.60 | 0.80 |
| S12-16-E | 7 to 9 | 240 | 120 | 18 | 0.40 | 0.25 |
| S12-16-E | 10 to 12 | 240 | 120 | 18 | 0.25 | 0.25 |
| S16-16-E | -3 to 4 | 288 | 144 | 22 | 0.60 | 1.44 |
| S16-16-E | 5 to 8 | 288 | 144 | 22 | 0.50 | 0.81 |
| S16-16-E | 9 to 12 | 288 | 144 | 22 | 0.40 | 0.25 |
| S16-16-E | 13 to 16 | 288 | 144 | 22 | 0.25 | 0.25 |
| S20-16-E | -3 to 4 | 312 | 156 | 24 | 0.55 | 1.44 |
| S20-16-E | 5 to 8 | 312 | 156 | 24 | 0.50 | 1.28 |
| S20-16-E | 9 to 12 | 312 | 156 | 24 | 0.45 | 0.25 |
| S20-16-E | 13 to 16 | 312 | 156 | 24 | 0.25 | 0.25 |
| S20-16-E | 17 to 20 | 304 | 156 | 20 | 0.25 | 0.25 |

Table B.6: Archetype dimensions and reinforcement layout for ASCE 7-16 code enhanced archetypes (continued).

| Arch. ID | Stories | l_w (in) | b_w (in) | t_w (in) | ρ_l | ρ_v |
|----------|----------|------------|------------|------------|----------|----------|
| S24-16-E | -3 to 4 | 336 | 168 | 26 | 1.10 | 2.38 |
| S24-16-E | 5 to 8 | 336 | 168 | 26 | 0.75 | 1.06 |
| S24-16-E | 9 to 12 | 336 | 168 | 26 | 0.60 | 1.16 |
| S24-16-E | 13 to 16 | 336 | 168 | 26 | 0.50 | 0.96 |
| S24-16-E | 17 to 24 | 328 | 168 | 22 | 0.50 | 0.81 |
| S28-16-E | -3 to 4 | 360 | 180 | 28 | 0.95 | 2.90 |
| S28-16-E | 5 to 8 | 360 | 180 | 28 | 0.70 | 1.07 |
| S28-16-E | 9 to 12 | 360 | 180 | 28 | 0.60 | 1.24 |
| S28-16-E | 13 to 16 | 360 | 180 | 28 | 0.50 | 1.04 |
| S28-16-E | 17 to 28 | 352 | 180 | 24 | 0.50 | 0.89 |
| S32-16-E | -3 to 4 | 384 | 192 | 30 | 0.95 | 3.10 |
| S32-16-E | 5 to 8 | 384 | 192 | 30 | 0.80 | 1.31 |
| S32-16-E | 9 to 12 | 384 | 192 | 30 | 0.70 | 1.14 |
| S32-16-E | 13 to 16 | 384 | 192 | 30 | 0.50 | 1.60 |
| S32-16-E | 17 to 32 | 376 | 192 | 26 | 0.50 | 0.96 |
| S36-16-E | -3 to 4 | 408 | 204 | 32 | 1.10 | 2.93 |
| S36-16-E | 5 to 8 | 408 | 204 | 32 | 0.80 | 1.07 |
| S36-16-E | 9 to 12 | 408 | 204 | 32 | 0.70 | 1.22 |
| S36-16-E | 13 to 16 | 408 | 204 | 32 | 0.60 | 1.04 |
| S36-16-E | 17 to 36 | 400 | 204 | 28 | 0.50 | 1.04 |
| S40-16-E | -3 to 4 | 432 | 216 | 34 | 1.20 | 3.40 |
| S40-16-E | 5 to 8 | 432 | 216 | 34 | 1.00 | 1.42 |
| S40-16-E | 9 to 12 | 432 | 216 | 34 | 0.80 | 1.48 |
| S40-16-E | 13 to 16 | 432 | 216 | 34 | 0.80 | 2.01 |
| S40-16-E | 17 to 20 | 420 | 216 | 28 | 0.70 | 2.09 |
| S40-16-E | 21 to 32 | 420 | 216 | 28 | 0.50 | 1.04 |
| S40-16-E | 33 to 40 | 412 | 216 | 24 | 0.50 | 0.89 |

Table B.7: Boundary element information for the 4-story archetypes.

| Archetype ID | Stories | l_{be} | $\rho_{l,be}$ |
|--------------|---------|----------|---------------|
| S4-10-E | -1 to 2 | 42 in | 0.030 |
| S4-10-E | 2 to 4 | 26 in | 0.030 |
| S4-16-E | -1 to 2 | 54 in | 0.023 |
| S4-16-E | 2 to 4 | 34 in | 0.023 |
| S4-10-M | -1 to 2 | 58 in | 0.029 |
| S4-10-M | 2 to 4 | 26 in | 0.030 |
| S4-16-M | -1 to 2 | 50 in | 0.037 |
| S4-16-M | 2 to 4 | 42 in | 0.037 |

Appendix C

CONDITIONAL MEAN AND VARIANCE SPECTRA SUMMARY

In design procedures that use nonlinear time-history analysis, ASCE 7-16 permits the use of ground motions scaled and selected to match a conditional mean spectrum (CMS) to evaluate building response. The CMS is an alternative to the uniform hazard spectrum (UHS) typically obtained from a probabilistic seismic hazard analysis (PSHA) (Baker, 2011), and is defined as the expected response spectrum, conditioned on a target spectral acceleration at a given period of interest. The CMS ideally represents a more realistic ground motion spectrum than the UHS, which tends to be overly conservative as a target for ground motion selection in regions dominated by multiple sources of seismicity.

For a given site and return period, a CMS was generated for each seismic source mechanism (i.e. crustal, intraslab, and interface) that contributes to the overall seismic hazard in Seattle. In order to compare the M9 simulated motions to what would be expected using ASCE 7-16, motions were selected and scaled to the mean conditional mean spectra for the crustal, intraslab, and interface earthquake sources. The CMS was computed using EZ-Frisk (Fugro, 2018), a software package that performs site-specific PSHA and hazard source deaggregation. The spectral acceleration correlation functions used to calculate the CMS were assumed to be similar for both crustal and subduction earthquakes (Jayaram et al., 2011b). For each of the considered structural periods (T_n), the CMS were conditioned such that $S_a(T_n)$ was equal to the $S_a(T_n)$ of the Seattle MCE_R . The MCE_R was determined from 2,475-year PSHA using the USGS National Seismic Hazard Mapping Project Code (USGS 2018). The resulting uniform hazard ground motions were then adjusted to target 1% probability of collapse in 50 years, from geometric mean to maximum direction, and to account for basin effects in the Seattle area.

For each ground motion suite (one suite per each structural period), the proportion of crustal, intraslab, and interface motions was selected in accordance to the contribution of each source mechanism to the overall hazard, based on the deaggregated hazard data in EZ-Frisk. The

candidate motions from each source mechanism were selected and amplitude-scaled to match the corresponding source-specific target CMS.

For crustal earthquakes, motions with a peak ground acceleration (PGA) greater than 0.05 g were selected from the NGA-West-2 database (PEER, 2014). In downtown Seattle, the crustal earthquake hazard is typically controlled by the Seattle Fault (e.g., 68% at 0.5 s), the northern trace of which lies less than 4 km from the city center. Therefore, a percentage of the crustal earthquake motions were selected with pulse-like characteristics as per the recommendation in Appendix C in ATC-82 (NIST, 2011). The motions with pulse-like characteristics were oriented so that they are 30-degrees northwest of fault-normal, which is the typical orientation of most buildings in downtown Seattle relative to the Seattle Fault (due to the street grid layout). For intraslab earthquakes, 100 ground-motion pairs were retrieved from the NGA-Subduction database (PEER, 2018) with the following search criteria: (1) recordings from intraslab earthquakes, (2) stations located in the forearc (similar to Seattle), (4) $M_w > 6$, (5) R_{CD} between 42-65 km, (5) V_{S30} between 190 and 760 m/s, and (6) PGA larger than 0.1g. For interface earthquakes, ground-motions were selected from three large-magnitude interface earthquakes (M_w 7.9 Tohoku aftershock, M_w 8.3 Tokachi-Oki, and M_w 9.0 Tohoku) in Japan from the K-Net and KiK-NET database (NIED, 2018).

For each of the structural periods considered, 100 ground-motions were selected and distributed to match the total contribution from the three source mechanisms. For a 2.0 s period, the number of motions considered per source-mechanism was 47, 6, and 47 for crustal, intraslab, and interface earthquakes, respectively. Note that selected ground motion records were occasionally repeated between period sets (although typically with different scaling factors), but never within a particular set. For all selected ground-motions, scaling factors were selected to minimize a weighted mean-squared error (MSE) between the candidate ground motion record and the target spectrum (in log-scale), and were limited to be no greater than five. In addition to motions matching a conditional mean spectra (used for the non-linear checks as per TBI 2017), additional motions sets were compiled to match mean and variance conditional spectra as per a methodology discussed in Jayaram et al. (2011a).

As an example, Figure 8.11 shows the 2.0 s conditional mean (solid black) and variance (dashed line) spectra for the three source mechanisms and the selected ground motions to match

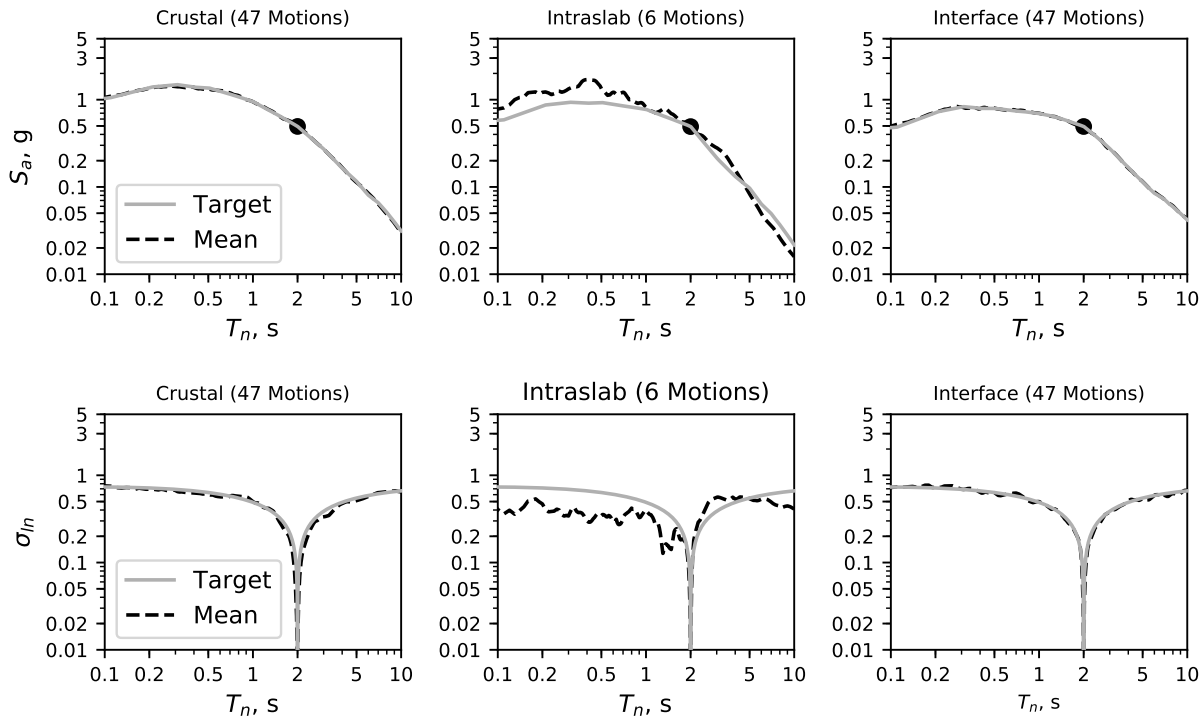


Figure C.1: Mean and standard deviation of the motions selected to match the conditional mean spectrum at 2.0s.

the mean and variance conditional spectra within the period range of interest. The variance at periods between 0.1 and 10 s was compared to the target as shown in Figure C.1. The target variance was taken as 0.74 for crustal, intraslab, and interface earthquakes.

Ground-motion duration was not explicitly considered in the ground-motion selection process but instead considered implicitly by selecting motions from similar source-mechanisms, source-site distances, and earthquake magnitudes that control the MCE_R hazard. The resulting median significant duration ($D_{s,5-95\%}$) of the motions was found to be around 17 s, 19 s, and 97 s for crustal, intraslab, and interface earthquakes, respectively.

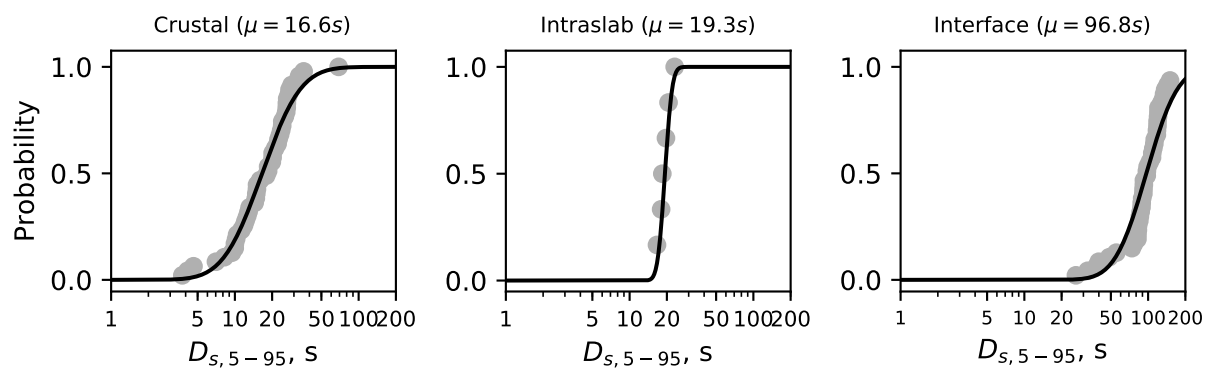


Figure C.2: Cumulative distribution function for significant duration ($D_{S5-95\%}$) for the three ground motions sets used for (a) crustal, (b) intraslab, and (c) interface earthquakes for a conditional mean and variance spectra at 2-second period.

Appendix D

ARCHETYPE MODELLING

For all walled buildings, collapse risk was assessed using 2D models in *OpenSees* (McKenna, 2016) with earthquake demands applied only in one direction. Figure D.3 shows a schematic of the *OpenSees* models where the walls were modeled using six displacement-based beam-column elements (DBE) per story, with five integration points per element and applying the Gauss-Lobatto numerical integration scheme. The axial and flexural response of each RC cross-section is modeled using a fiber-based approach at each integration point. To account for shear deformations along the wall height, each DBE included a shear spring. Figure D.3 illustrate the fiber cross-section for the walls.

D.0.1 Constitutive Modeling

Constitutive models are shown in Figure D.1. Expected concrete and steel material strengths are defined as $f'_{ce} = 1.3f'_c$ and $f_{ye} = 1.17f_y$, respectively, per PEER TBI (2017). A modified version of the *OpenSees* Steel02 material model was used to simulate the cyclic response of reinforcing steel that accounts for cyclic strength-deterioration (Kunnath et al., 2009). This material model called Steel02Fatigue herein, uses the stress-strain backbone curve and unload/reload paths are defined using the model by Menegotto and Pinto (1973). The cumulative strength degradation of the material is based on the model by the Coffin (1954, 1971) and Manson (1965) fatigue life expression and Miner's (1945) linear damage rule. A detailed discussion of this implementation can be found in Kunnath et al. (2009). The reinforcing bar assumed a modulus of elasticity, $E_s = 200$ GPa (29,000 ksi), a constant post-yield strain-hardening ratio of 0.6% (shown as parameter b in Figure D.1). For the Steel02Fatigue material, the deterioration parameters C_d , C_f , α , and β were taken as 0.2, 0.12, 0.44, and 0.45, respectively, as recommended by Kunnath et al. (2009).

Figure D.2b compares the stress-strain response of Steel02 and Steel02Fatigue illustrating the cyclic degradation of strength.

The longitudinal reinforcing bars inside RC members exhibit excessive buckling once the surrounding concrete crushes. Pugh developed a simple model to simulate full bar buckling, using the *OpenSees* MinMax wrapper to force the reinforcing steel to lose compression and tension strength once the surrounding concrete reaches residual strain (ϵ_{res} in Figure D.1a). To simulate tensile fracture of the reinforcing bars, the MinMax wrapper forces the material to lose strength once the strains exceed the ultimate tensile strain, ϵ_u , taken as 20%.

For concrete materials, a modified version of the *OpenSees* Concrete02 material model Yassin (1994) was used to simulate the cyclic response of the concrete. This material model is called Concrete02IS herein, was modified to use Popovics (1973) pre-peak stress-strain relationship that enabled the user to specify a initial elastic stiffness (E_c) of the concrete irrespective of the peak-stress and strain. For post-peak stress-strain response, the stresses were assumed to be linear from peak-stress (f_p) to the residual concrete capacity (f_{res}) as shown in Figure D.1b. The strain at maximum stress is denoted as ϵ_p . For unconfined concrete, ϵ_p is set as $2f_p/E_c$ where E_c is defined as $4,750f_p$ MPa ($57,000f_p$ psi, as recommended by ACI 318-14). For the base model, the confined concrete variables $f_p = f'_{c,c}$ and ϵ_p were defined using recommendations by Saatcioglu and Razvi (1992). The residual concrete capacity, f_{res} , is takes as βf_p where β is defined as 0.01 for unconfined concrete and 0.2 for confined concrete. The tensile strength is equal to $0.33f'_{c,e}$ MPa ($4f'_{c,e}$ psi, as per Wong et al. (2013) and a tensile softening stiffness (E_t) equal to $0.05 E_c$ (Yassin, 1994). The parameter Λ in Concrete02 is 0.1, which is the ratio of unloading slope at ϵ_p to E_c .

Birely (2012) showed that the majority of walls sustain a compression-type failure characterized by simultaneous concrete crushing and buckling of the longitudinal reinforcement. Coleman and Spacone (2001) and Pugh et al. (2015) show that when wall failure occurs and accompanying strength loss is simulated, deformations localize in the failing element or section, which results in mesh-dependent results if steps are not taken to mitigate this. To minimize mesh dependences, work by Coleman and Spacone (2001) and Pugh et al. (2015) regularize concrete compression softening with post-peak concrete compression stress-strain response using the concrete compressive energy (G_f) and a measure of the element mesh size. Specifically,

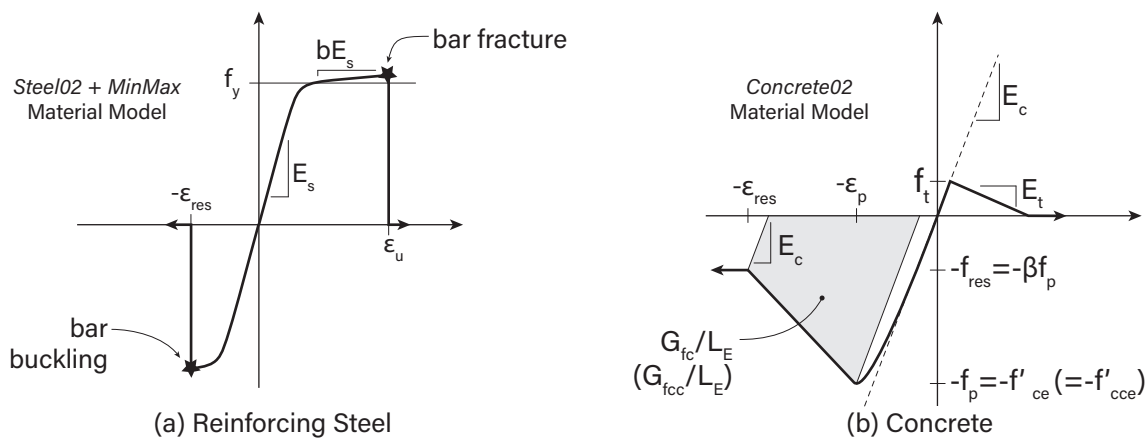


Figure D.1: Stress-strain relationship for the fiber-section (a) reinforcing steel and (b) concrete. Confined concrete properties are shown in parenthesis.

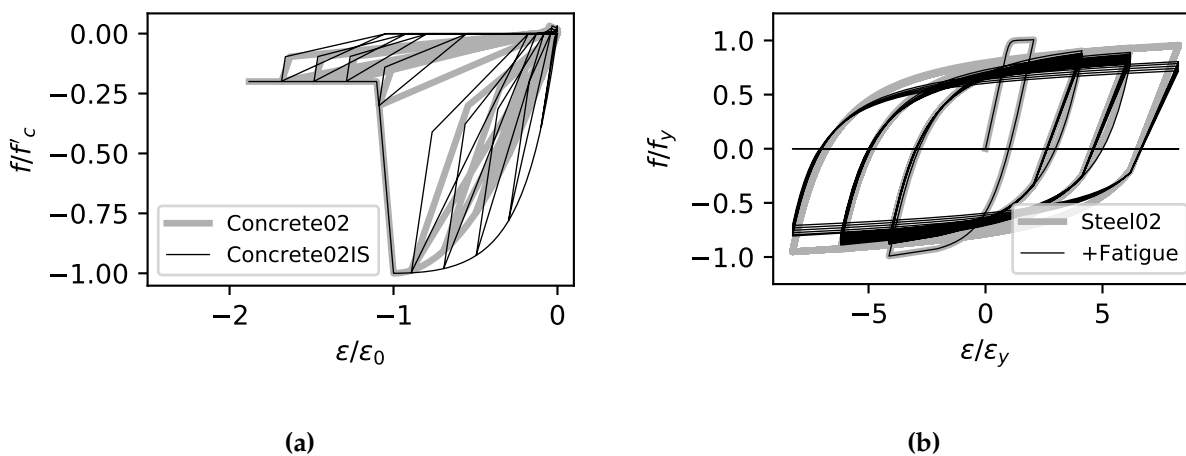


Figure D.2: Stress-strain response of a modified *OpenSees* (a) Concrete02 model with revised pre-peak properties and (b) Steel02 model that accounts for cyclic strength degradation based on Kunnath et al. (2009).

regularized strain at onset of residual compressive strength, ϵ_{res} , shown in Figure D.2 is computed as,

$$\epsilon_{res} = \frac{2G_f}{(\beta + 1)f_p L_E} + \epsilon_p \frac{\beta + 1}{2} \quad (D.1)$$

where G_f is defined as the concrete crushing energy in N/mm (kips per in), β is the percentage of f_p corresponding to the residual compressive strength, and L_E is the length over which softening occurs in the model. For DBE, L_E is length of the entire element because the DBE formulations forces localization within a single element (Coleman and Spacone, 2001). The optimal value of G_f was determined in Marafi et al. 2018 and taken as $2.0f'_{ce}$ N/mm ($0.0134f'_{ce}$ kips/in) and $3.5f'_{ce}$ N/mm ($0.0268f'_{ce}$ kips/in) for unconfined and confined concrete.

Shear deformations were modeled using a linear spring, as shown in Figure D.3. The elastic shear stiffness of a cantilevered column can be estimated as GA_v/L_E where G is the shear modulus, A_v is the effective shear area, and L_E is the length of the wall element. This chapter approximates G as $0.4E_c$, as per ACI 318-14, and A_v is taken as .

D.0.2 Other Modelling Assumptions

A P-delta column was used to model the effects of the gravity system, as shown in Figure D.3, connected to the RC wall using rigid-truss elements at every story. The P-delta column is a rigid axial element with a pinned support. The vertical load resisted by the P-Delta column at each level is a percentage of the floor area resisted by the gravity system multiplied by the total seismic weight resisted by the wall (i.e., the remainder of the archetype's total vertical load due to gravity not resisted by the wall). The *OpenSees* models used modal damping and supplemented with stiffness-only Rayleigh damping to dampen the dynamic amplifications associated with higher mode effects Clough and Penzien (2010). The number of modes that were dampened was equal to the total number of stories, N , where the total damping (modal plus stiffness-only Rayleigh) in each mode equalled to 2.5%, as recommended by the TBI 2017.

The retaining walls and basement-level diaphragms were modelled using elastic spring element shown in Figure D.3. The diaphragm stiffnesses (axial spring shown in Figure D.3) and basement wall stiffnesses (shear spring shown in Figure D.3) were estimated using a 3-dimensional elastic finite-element model. The basement walls were 305 mm (12 in) thick by

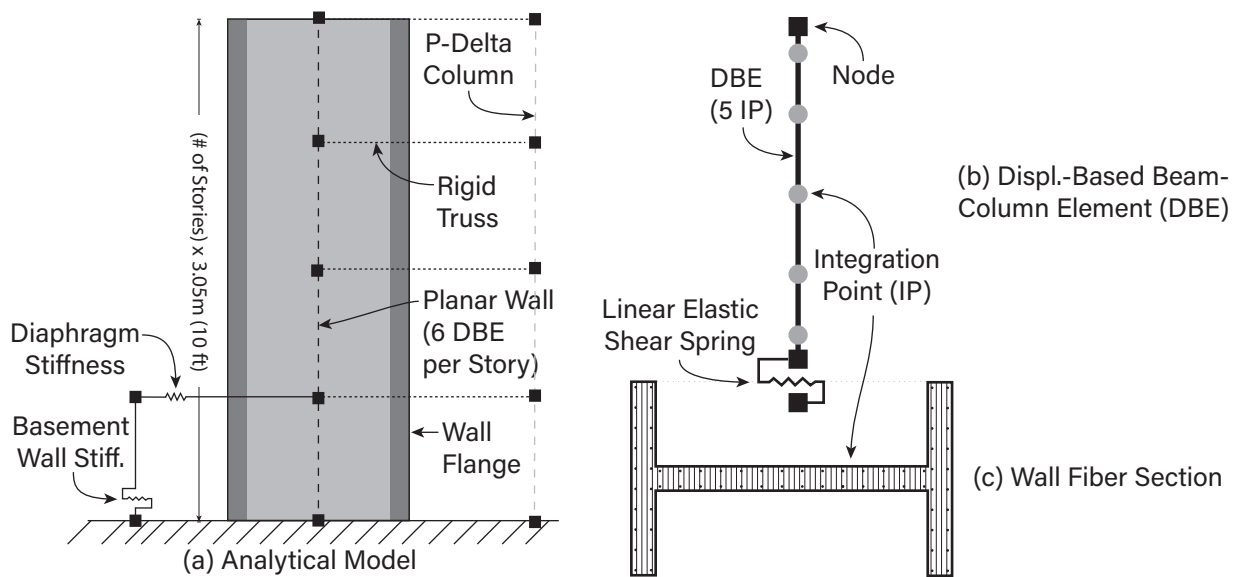


Figure D.3: Diagram of the (a) *OpenSees* analytical model, (b) wall element modeled using displacement-based elements, and (c) wall fiber section.

48.8 m (160 ft) long retaining walls around the basement wall perimeter (shown in Figure 8.7) connected to a 356 mm (14 in) thick basement slab at the ground level and 254 mm (10 in) thick at levels below ground. The elastic properties of the retaining wall and diaphragms was estimated as per the recommendation in the TBI 2017 where the basement wall used flexural and shear stiffness equal to $0.8E_c I_g$ and $0.2E_c A_g$, respectively, and the diaphragm axial and shear stiffness is equal to $0.25E_c A_g$ and $0.25E_c I_g$, respectively.

Appendix E

TALL BUILDING INITIATIVE CHECKS

This appendix sections summarizes the engineering demand parameters that are checked by the Tall Building Initiative (TBI, 2017) guidelines. These checks were performed for all ASCE 7-10 and ASCE 7-16 Archetypes Code Enhanced archetypes that were 24-stories are taller. Figures E.1 to Figures E.8 summarizes the peak inter-story drifts, residual inter-story drifts, maximum tensile and compressive strains, and story shears with respect to each story. Each figure also shows the limits prescribed in the TBI (2017) guidelines.

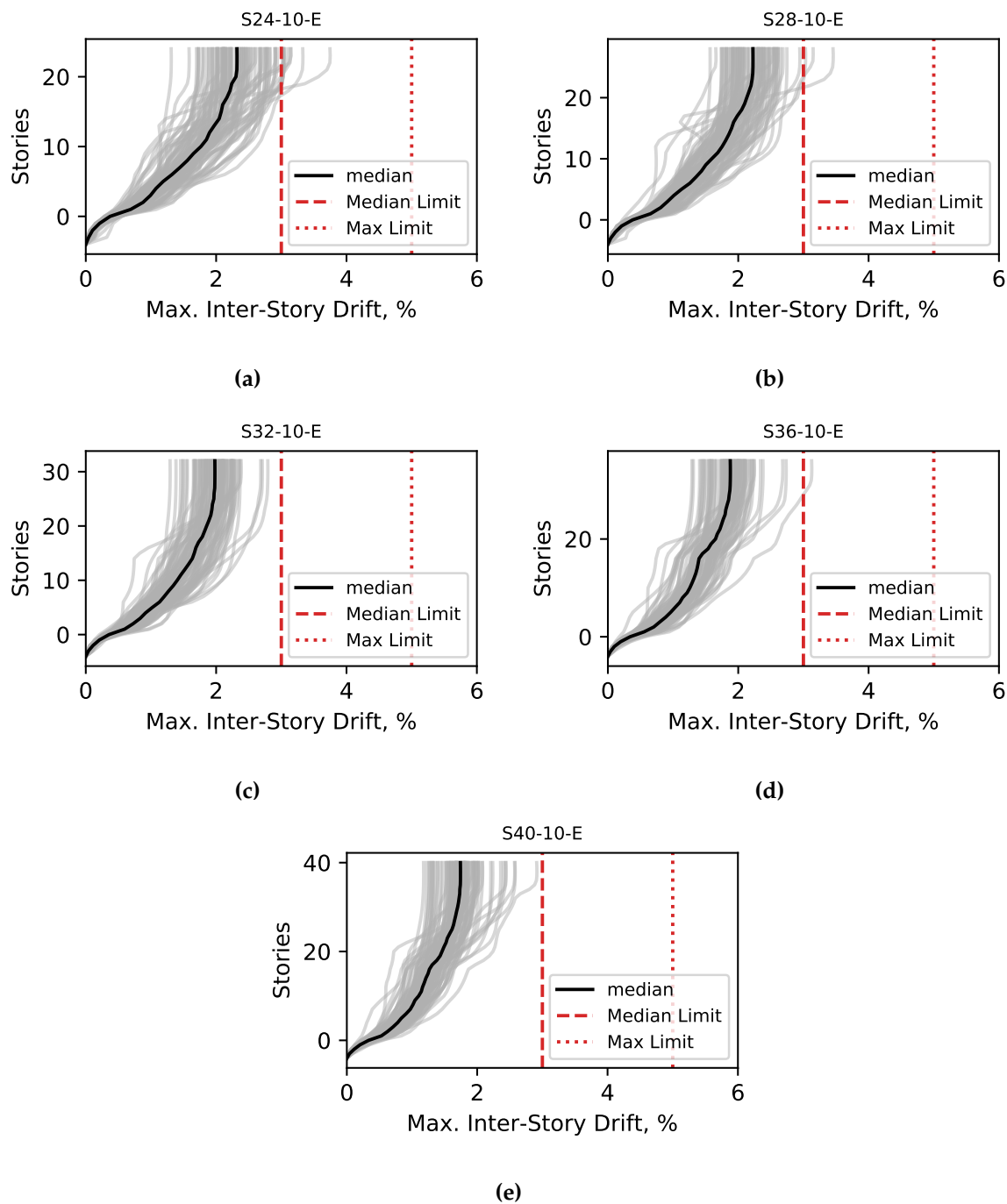


Figure E.1: Peak interstory drifts with respect to story for all ASCE 7-10 Code Enhanced Designs 24-stories and taller.

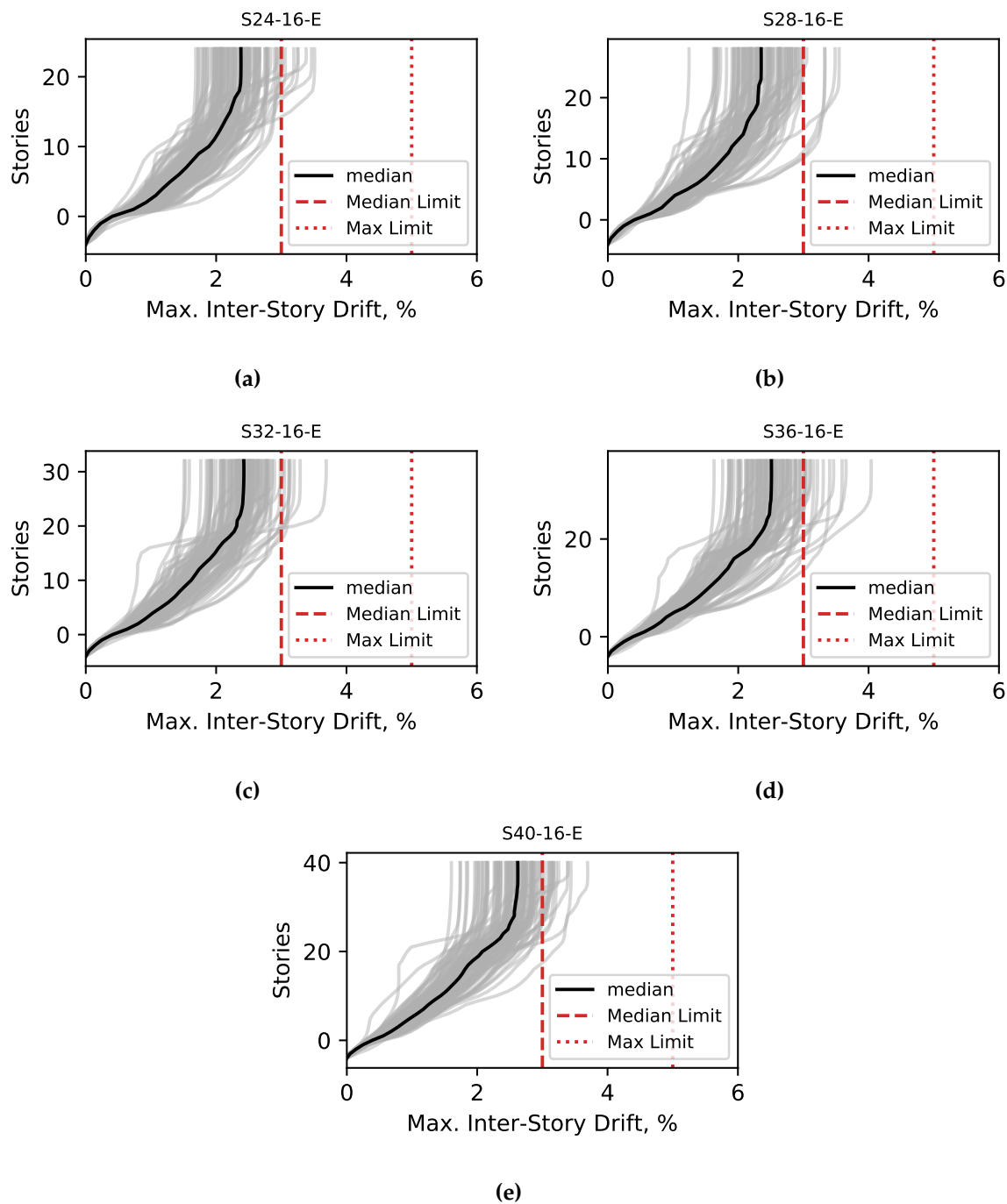


Figure E.2: Peak interstory drifts with respect to story for all ASCE 7-16 Code Enhanced Designs 24-stories and taller.

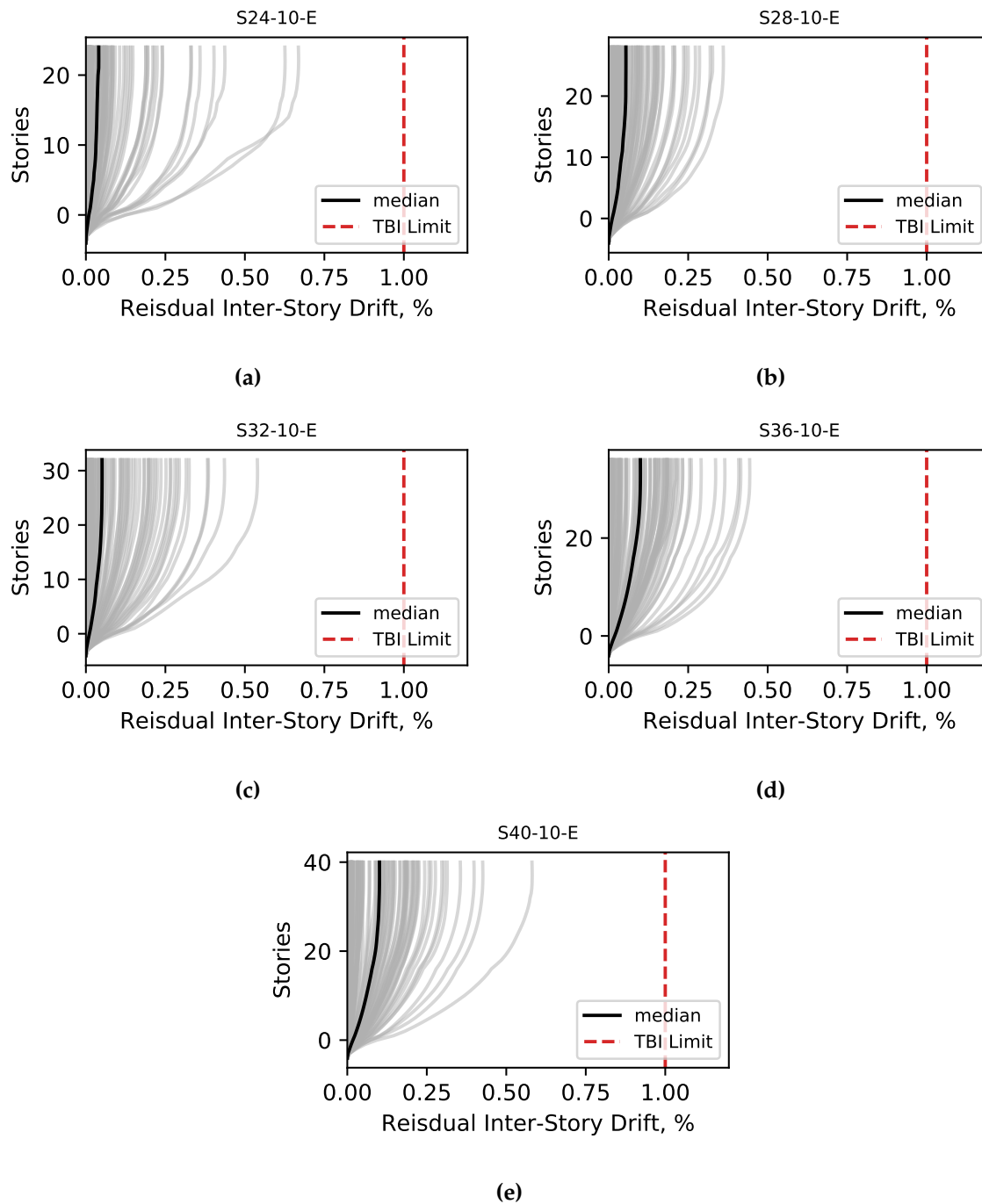


Figure E.3: Residual interstory drifts with respect to story for all ASCE 7-10 Code Enhanced Designs 24-stories and taller.

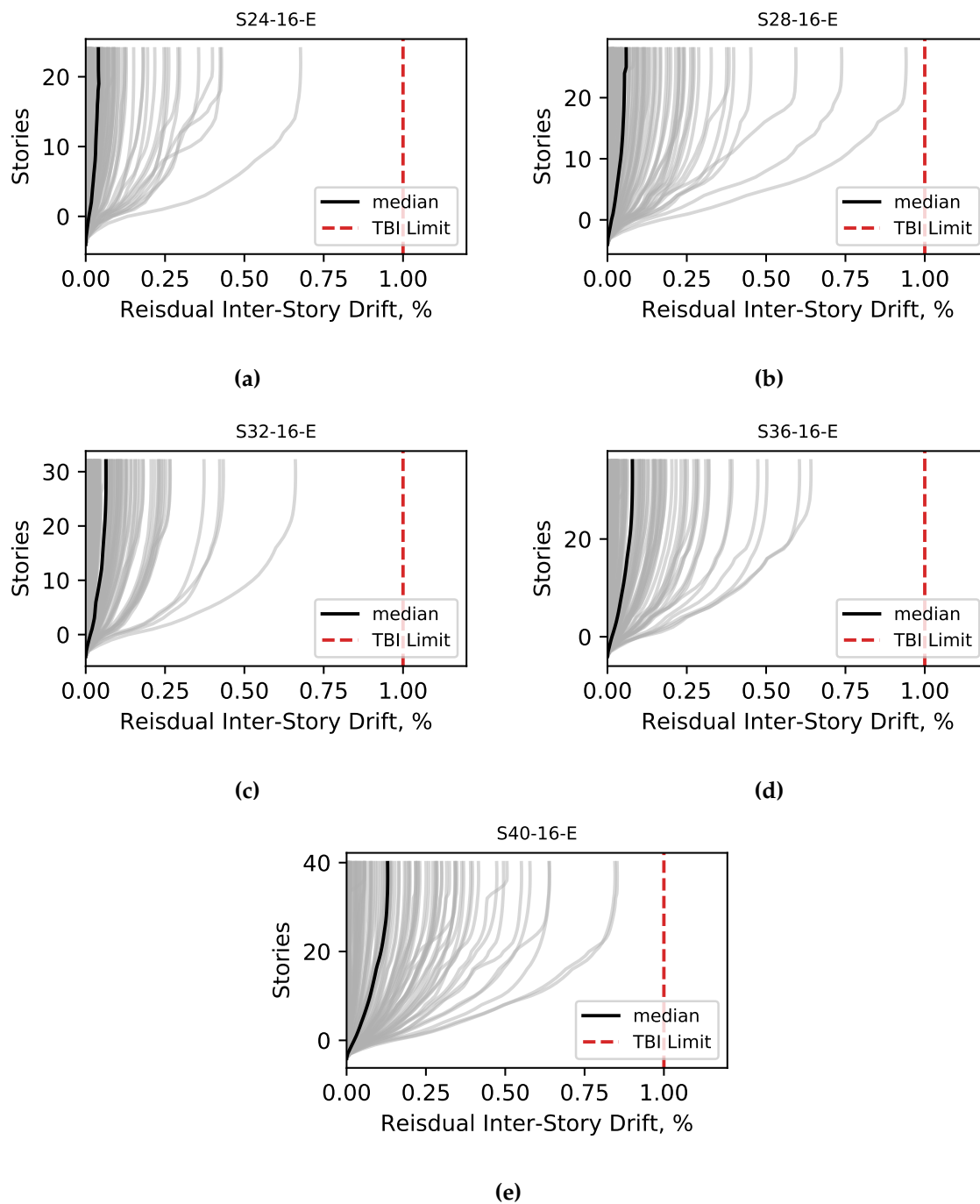


Figure E.4: Residual interstory drifts with respect to story for all ASCE 7-16 Code Enhanced Designs 24-stories and taller.

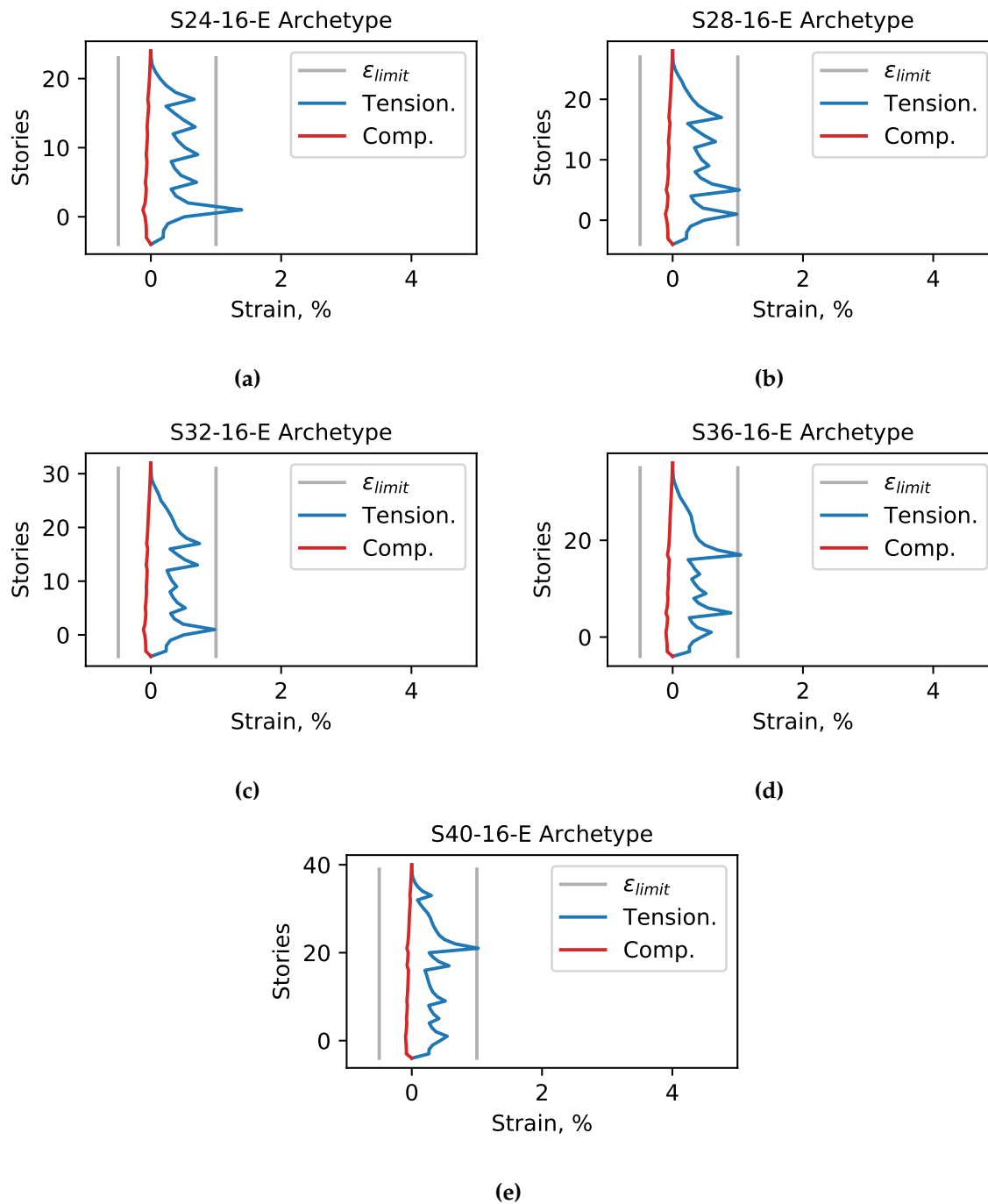


Figure E.5: Min. and Max. Strains with respect to story for all ASCE 7-10 Code Enhanced Designs 24-stories and taller.

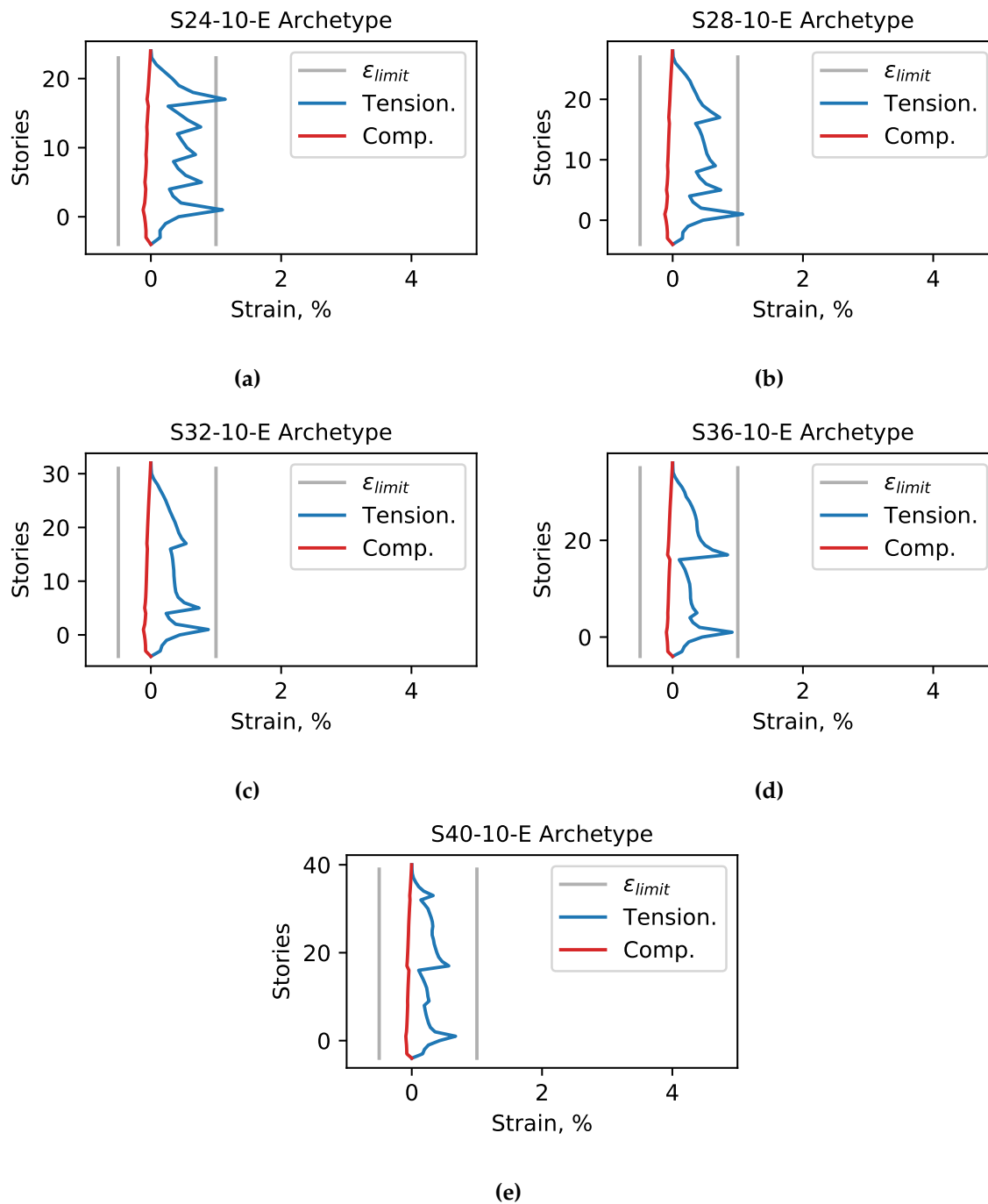


Figure E.6: Min. and Max. Strains with respect to story for all ASCE 7-16 Code Enhanced Designs 24-stories and taller.

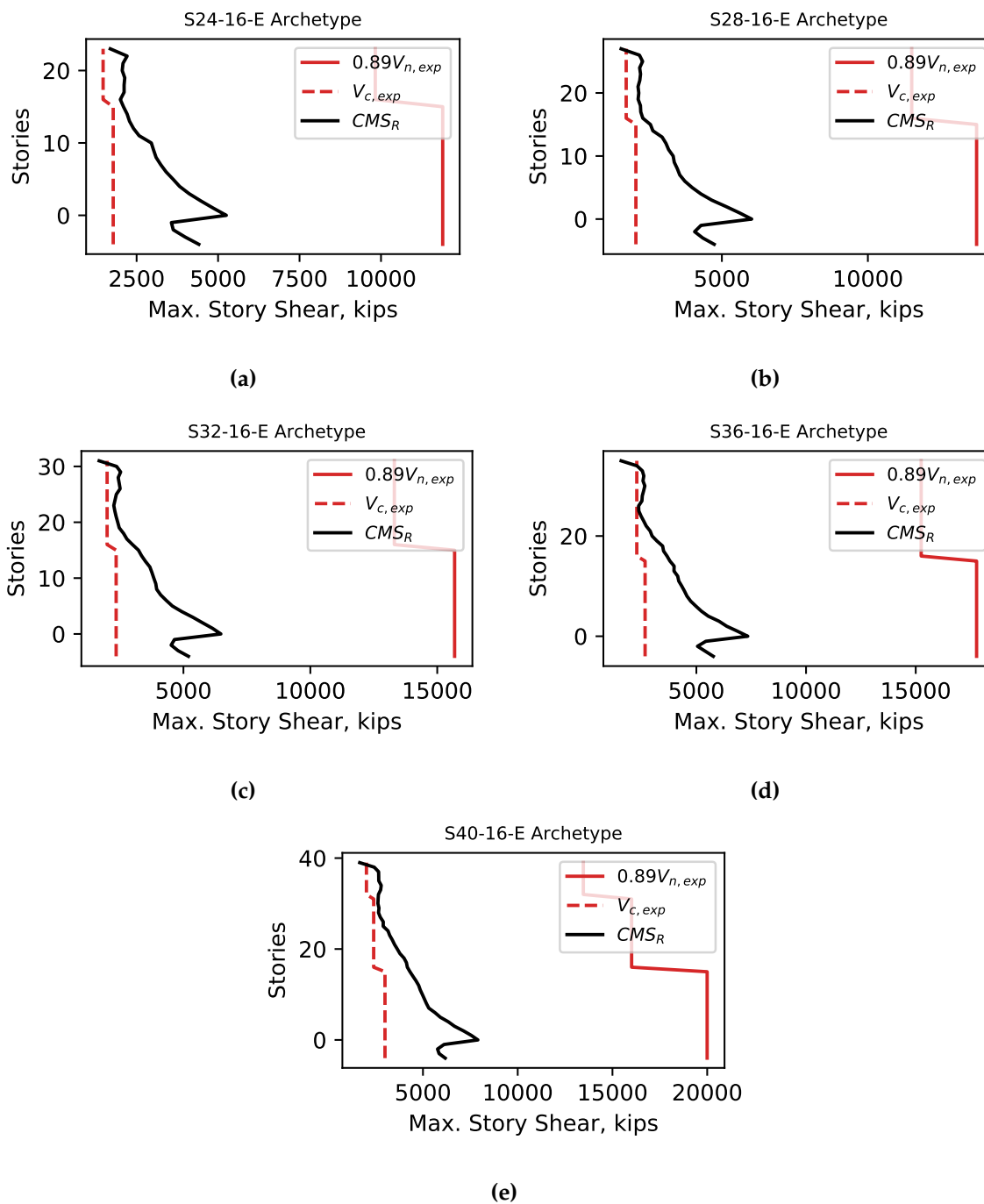


Figure E.7: Story Shear with respect to story for all ASCE 7-10 Code Enhanced Designs 24-stories and taller.

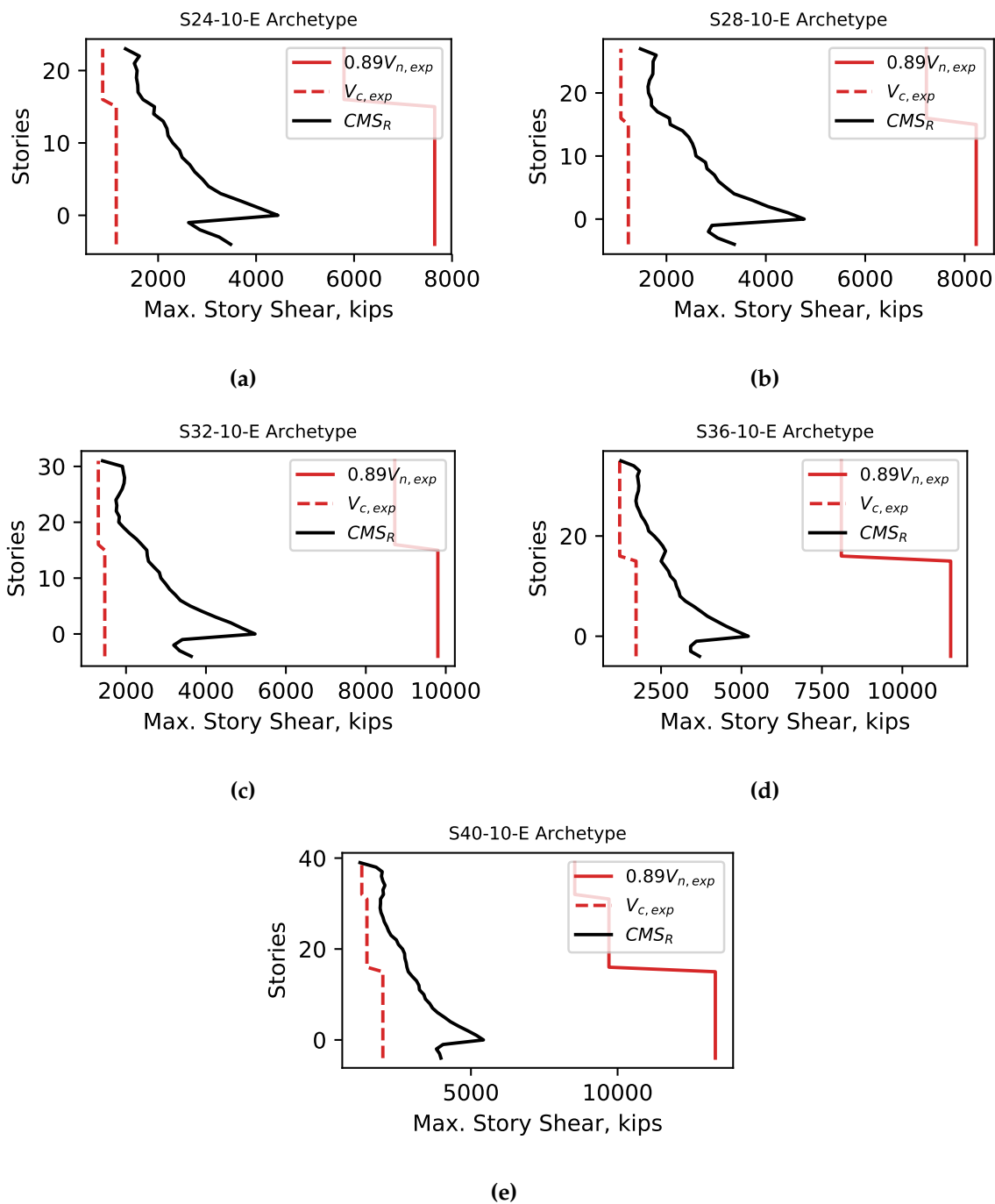


Figure E.8: Story Shear with respect to story for all ASCE 7-16 Code Enhanced Designs 24-stories and taller.

Appendix F

RC WALL ARCHETYPE RESPONSE SENSITIVITY

Previous studies Pugh et al. (2015) and the analysis in Chapter 7 have used *OpenSees* Concrete02 to define the concrete material model. Concrete02 uses Hognestad (1951) stress-strain relationship to define the pre-peak backbone. This definition of the backbone defines the initial stiffness as per the ACI 318 equation for unconfined concrete, however, in confined concrete the initial stiffness is severely underestimated (as much as 50%). This under estimation of initial stiffness can affect the drift response especially in areas of the wall that are in the elastic range. To estimate the sensitivity of the analysis results shown above, for a subset of the archetypes the analyses were repeated using the Concrete02 material model instead of the modified version, Concrete02IS (Concrete02 with a modified initial stiffness). Figure F.1a shows how the probability of exceeding maximum inter-story drift increases (for e.g., ~2% increase in probability at 6% MISD) with respect to the reference (base) model. This indicates that the under estimating the initial stiffness of the concrete results in an overestimation in drift under severe earthquake loading. For all ASCE 7-10 code minimum archetypes, the probability of collapse under an M9 CSZ scenario was found to increase on average by 18% from the reference model (shown in Figure F.1b).

The modelling methodology used here, has been calibrated to experimental tests with loading protocols that may not be representative of building response due to long duration ground shaking. This is illustrated in Figure F.2 where the number of cycles at each target drift (computed at l_w from the support) is compared to over 40 wall experiments and the response of Archetype S24-16-E subjected to an M9 CSZ scenario for Seattle. The number of cycles the wall is subjected to is much larger under an M9 earthquake than what is typically tested. As a result, the effect of fatigue is yet to be investigated for concrete walls. Kunnath et al. (2009) have calibrated models that capture the effects of low-cycle fatigue using cyclic tests of bare reinforcing bars. However, it is uncertain how these bare bar model calibrations predict the effects of fatigue on

full-scale RC specimen tests (with reinforcing bars that are hooked with cross ties and encased in concrete) subjected to many cycles (> 57 cycles at > 0.5% drift). Recent tests by Lopez et al. (2018) are quantifying the performance of bridge RC column specimens subjected subduction earthquake shaking that are expected to undergo many cycles. Future work should recalibrate the fatigue parameters by (Kunnath et al., 2009) using short- and long-duration wall tests to accurately account for the effects of strength degradation due to low-cycle fatigue.

Nevertheless, this sections attempts to quantify the effect of this uncertainty on collapse probability by varying the reinforcing steel model to (1) ignore the effects of low-cycle fatigue (using the Steel02 material), (2) accelerate the effects of fatigue over the base model (by using $C_d = 0.05$ instead of $C_d = 0.2$ as recommended in Kunnath et al., 2009). For archetype S20-10-M, Figure F.1a shows the fragility curves are similar (within 1% probability at 6% MISD) for the reference model (solid line) and without fatigue model (dotted red line). Accelerating the effects of fatigue (dashed dot line) resulted in up to a 1.44 times the probability of exceeding 6% MISD than the base model. For 12-story to 24-story ASCE 7-10 code-minimum archetypes, the collapse probability in the M9 CSZ for Seattle decreased by 3% on average when excluding low-cycle fatigue and increased on average by 12% when accelerating fatigue from the base model (shown in Figure F.1b). While the effects of low-cycle fatigue (resulting in strength degradation) is generally important (Bommer et al., 2004), however, the results here seem to indicate that the mechanism that is controlling collapse risk here is not currently influenced by strength degradation.

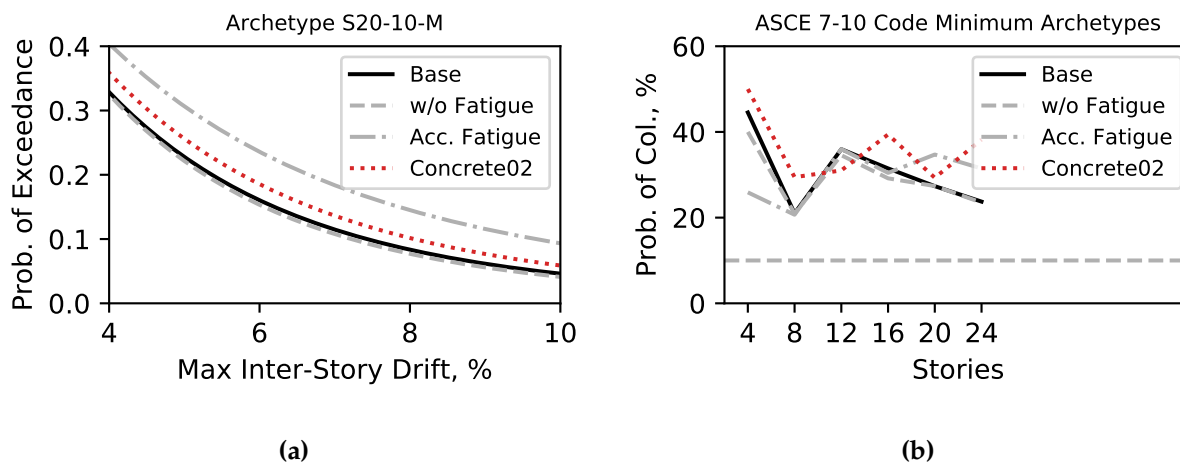


Figure F.1: (a) Probability of Exceedance with respect to maximum inter-story drift during the M9 CSZ motions in Seattle with varying material modelling assumptions for a 24-story ASCE 7-10 Code-Minimum archetypes (b) Probability of collapse with respect to story for ASCE 7-10 Code-Minimum Archetypes during the M9 CSZ with varying material modelling assumptions.

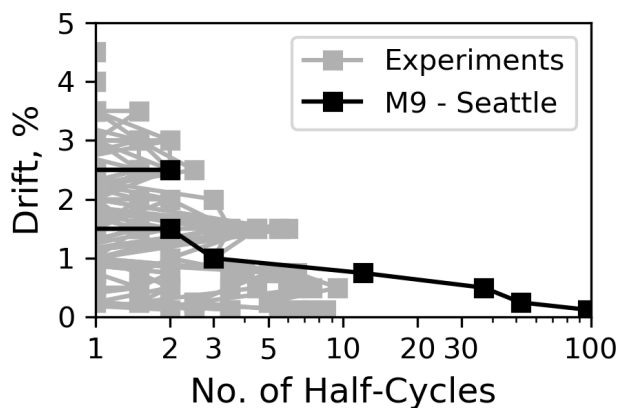


Figure F.2: Drift target with respect to rainflow cycle count for a series of experiments and Archetype S20-16-E subjected to an M9 CSZ Scenario for Seattle.

BIBLIOGRAPHY

- Abrahamson, N A and W J Silva (1996). *Empirical ground motion models*. Tech. rep. Upton, NY.
- Abrahamson, Norman, Nicholas Gregor, and Kofi Addo (2016). "BC Hydro Ground Motion Prediction Equations for Subduction Earthquakes". In: *Earthquake Spectra* 32.1, pp. 23–44. ISSN: 8755-2930. DOI: [10.1193/051712EQS188MR](https://doi.org/10.1193/051712EQS188MR).
- Abrahamson, Norman A., Walter J. Silva, and Ronnie Kamai (2014). "Summary of the ASK14 Ground Motion Relation for Active Crustal Regions". In: *Earthquake Spectra* 30.3, pp. 1025–1055. ISSN: 8755-2930. DOI: [10.1193/070913EQS198M](https://doi.org/10.1193/070913EQS198M).
- ACI (2014). *Building Code Requirements for Structural Concrete and Commentary*, p. 520.
- Adams, J. and S. Halchuk (2002). *Knowledge of in-slab earthquakes needed to improve seismic hazard estimates for southwestern British Columbia, The Cascadia Subduction Zone and Related Subduction Systems* Seismic Structure, Intraslab Earthquakes and Processes, and Earthquake Hazards: U.S. Tech. rep., p. 182.
- Addo, K., N. Abrahamson, and R. Youngs (2012). *Probabilistic Seismic Hazard Analysis (PSHA) Model Ground Motion Characterization (GMC) Model*, tech. rep. Technical Report E658, BC Hydro.
- Afshari, Kioumars and Jonathan P Stewart (2016). "Physically Parameterized Prediction Equations for Significant Duration in Active Crustal Regions". In: *Earthquake Spectra* 32.4, pp. 2057–2081. ISSN: 8755-2930. DOI: [10.1193/063015EQS106M](https://doi.org/10.1193/063015EQS106M).
- Aktan, A. E. and V. V. Bertero (1987). "Evaluation of Seismic Response of RC Buildings Loaded to Failure". In: *Journal of Structural Engineering* 113.5, pp. 1092–1108. ISSN: 0733-9445. DOI: [10.1061/\(ASCE\)0733-9445\(1987\)113:5\(1092\)](https://doi.org/10.1061/(ASCE)0733-9445(1987)113:5(1092)).

- Aktan, Ahmet E. and Vitelmo V. Bertero (1984). "Seismic Response of R/C FrameWall Structures". In: *Journal of Structural Engineering* 110.8, pp. 1803–1821. ISSN: 0733-9445. DOI: [10.1061/\(ASCE\)0733-9445\(1984\)110:8\(1803\)](https://doi.org/10.1061/(ASCE)0733-9445(1984)110:8(1803)).
- Aragon, Theresa C., Yahya C. Kurama, and Donald F. Meinheit (2017). "Effects of Grout and Energy-Dissipating Bar Properties on a Type III Grouted Seismic Connection for Precast Structures". In: *In-review*.
- ASCE (2013). *Minimum design loads for buildings and other structures*. Ed. by American Society of Civil Engineers. ASCE standard. Reston, Virginia: Published by American Society of Civil Engineers. ISBN: 978-0-7844-1291-6.
- (2014). *Seismic Evaluation and Retrofit of Existing Buildings (ASCE/SEI Standard 41-13)*. Reston, VA. DOI: [10.1061/9780784412855](https://doi.org/10.1061/9780784412855).
- (2017). *Minimum Design Loads and Associated Criteria for Buildings and Other Structures, ASCE/SEI 7-16*. Reston, VA: American Society of Civil Engineers, p. 800. ISBN: 9780784414248.
- ASHTO (2017). *LRFD Bridge Design Specifications*. American Association of State Highway and Transportation Officials.
- ATC (2018). *Improving Seismic Design of Buildings with Configuration Irregularities (ATC-123)*. Tech. rep. Applied Technology Council.
- Atik, Linda Al, Norman Abrahamson, Julian J. Bommer, Frank Scherbaum, Fabrice Cotton, and Nicolas Kuehn (2010). "The Variability of Ground-Motion Prediction Models and Its Components". In: *Seismological Research Letters* 81.5.
- Atkinson, G M (2003). "Empirical Ground-Motion Relations for Subduction-Zone Earthquakes and Their Application to Cascadia and Other Regions". In: *Bulletin of the Seismological Society of America* 93.4, pp. 1703–1729. ISSN: 0037-1106. DOI: [10.1785/0120020156](https://doi.org/10.1785/0120020156).
- Atkinson, G M and D M Boore (2006). "Earthquake Ground-Motion Prediction Equations for Eastern North America". In: *Bulletin of the Seismological Society of America* 96.6, pp. 2181–2205. ISSN: 0037-1106. DOI: [10.1785/0120050245](https://doi.org/10.1785/0120050245).

- Atkinson, G M and M Macias (2009). "Predicted Ground Motions for Great Interface Earthquakes in the Cascadia Subduction Zone". In: *Bulletin of the Seismological Society of America* 99.3, pp. 1552–1578. ISSN: 0037-1106. DOI: [10.1785/0120080147](https://doi.org/10.1785/0120080147).
- Atwater, Brian F, Alan R Nelson, John J Clague, Gary A Carver, David K Yamaguchi, Peter T Bobrowsky, Joanne Bourgeois, Mark E Darienzo, Wendy C Grant, Eileen HemphillHaley, Harvey M Kelsey, Gordon C Jacoby, Stuart P Nishenko, Stephen P Palmer, Curt D Peterson, and Mary Ann Reinhart (1995). "Summary of Coastal Geologic Evidence for Past Great Earthquakes at the Cascadia Subduction Zone". In: *Earthquake Spectra* 11.1, pp. 1–18. ISSN: 8755-2930. DOI: [10.1193/1.1585800](https://doi.org/10.1193/1.1585800).
- Baker, Jack W. (2011). "Conditional Mean Spectrum: Tool for Ground-Motion Selection". In: *Journal of Structural Engineering* 137.3, pp. 322–331. ISSN: 0733-9445. DOI: [10.1061/\(ASCE\)ST.1943-541X.0000215](https://doi.org/10.1061/(ASCE)ST.1943-541X.0000215).
- Baker, Jack W and C. Allin Cornell (2006). "Spectral shape, epsilon and record selection". In: *Earthquake Engineering & Structural Dynamics* 35.9, pp. 1077–1095. ISSN: 0098-8847. DOI: [10.1002/eqe.571](https://doi.org/10.1002/eqe.571).
- Baker, Jack W. and C. A. Cornell (2006). "Spectral shape, epsilon and record selection". In: *Earthquake Engineering & Structural Dynamics* 35.9, pp. 1077–1095. ISSN: 0098-8847. DOI: [10.1002/eqe.571](https://doi.org/10.1002/eqe.571).
- Baker, Jack W. and Nirmal Jayaram (2008). "Correlation of Spectral Acceleration Values from NGA Ground Motion Models". In: *Earthquake Spectra* 24.1, pp. 299–317. ISSN: 8755-2930. DOI: [10.1193/1.2857544](https://doi.org/10.1193/1.2857544).
- Bard, Pierre-Yves and Michel Bouchon (1985). "The two-dimensional resonance of sediment-filled valleys". In: *Bulletin of the Seismological Society of America* 75.2, pp. 519–541. ISSN: 0037-1106.
- Bazaez, Ramiro and Peter Dusicka (2016). "Cyclic Loading for RC Bridge Columns Considering Subduction Megathrust Earthquakes". In: *Journal of Bridge Engineering*

- 21.5, p. 04016009. ISSN: 1084-0702. DOI: 10.1061/(ASCE)BE.1943-5592.0000891.
- Bijelić, Nenad, Ting Lin, and Greg G. Deierlein (2018). "Validation of the SCEC Broadband Platform simulations for tall building risk assessments considering spectral shape and duration of the ground motion". In: *Earthquake Engineering & Structural Dynamics*. ISSN: 00988847. DOI: 10.1002/eqe.3066.
- Birely, Anna C (2012). "Seismic Performance of Slender Reinforced Concrete Structural Walls". PhD thesis. University of Washington, p. 983.
- Blakely, Richard J, Ray E Wells, Craig S Weaver, and Samuel Y Johnson (2002). "Location, structure, and seismicity of the Seattle fault zone, Washington: Evidence from aeromagnetic anomalies, geologic mapping, and seismic-reflection data". In: *Geological Society of America Bulletin* 114.2, pp. 169–177. ISSN: 00167606. DOI: 10.1130/0016-7606(2002)114<0169:LSASOT>2.0.CO;2.
- Blakely, R.J., T.M. Brocher, and R.E. Wells (2000). *How the Jell-O shakes depends on the shape of the bowl: a three-dimensional view of the Seattle basin*.
- Boivin, Yannick and Patrick Paultre (2012). "Seismic force demand on ductile reinforced concrete shear walls subjected to western North American ground motions: Part 2 new capacity design methods". In: *Canadian Journal of Civil Engineering* 39.7, pp. 738–750. ISSN: 0315-1468. DOI: 10.1139/12012-044.
- Bojórquez, Edn and Iunio Iervolino (2011). "Spectral shape proxies and nonlinear structural response". In: *Soil Dynamics and Earthquake Engineering* 31.7, pp. 996–1008. ISSN: 02677261. DOI: 10.1016/j.soildyn.2011.03.006.
- Bommer, J J, P J Stafford, and J E Alarcon (2009). "Empirical Equations for the Prediction of the Significant, Bracketed, and Uniform Duration of Earthquake Ground Motion". In: *Bulletin of the Seismological Society of America* 99.6, pp. 3217–3233. ISSN: 0037-1106. DOI: 10.1785/0120080298.
- Bommer, Julian J, Guido Magenes, Jonathan Hancock, and Paola Penazzo (2004). "The Influence of Strong-Motion Duration on the Seismic Response of Masonry Structures".

- In: *Bulletin of Earthquake Engineering* 2.1, pp. 1–26. ISSN: 1570-761X. DOI: [10.1023/B:BEEE.0000038948.95616.bf](https://doi.org/10.1023/B:BEEE.0000038948.95616.bf).
- Boore, D M (1983). “Stochastic simulation of high-frequency ground motions based on seismological models of the radiated spectra,” in: *Bull. Seismol. Soc. Am.* 73, pp. 1865–1894.
- (1996). *SMSIM-Fortran programs for simulating ground motions from earthquakes: version 1.0*. Tech. rep. 96-80-A. U.S. Geol. Surv., p. 73.
- Boore, D M and W b. Joyner (1997). “Site Amplifications for Generic Rock Sites”. In: *Bulletin of the Seismological Society of America* 87.2, pp. 327–341.
- Boore, D. M., E. M. Thompson, and H. Cadet (2011). “Regional Correlations of VS30 and Velocities Averaged Over Depths Less Than and Greater Than 30 Meters”. In: *Bulletin of the Seismological Society of America* 101.6, pp. 3046–3059. ISSN: 0037-1106. DOI: [10.1785/0120110071](https://doi.org/10.1785/0120110071).
- Boore, David M, Jonathan P Stewart, Emel Seyhan, and Gail M Atkinson (2014). “NGA-West2 Equations for Predicting PGA, PGV, and 5% Damped PSA for Shallow Crustal Earthquakes”. In: *Earthquake Spectra* 30.3, pp. 1057–1085. ISSN: 8755-2930. DOI: [10.1193/070113EQS184M](https://doi.org/10.1193/070113EQS184M).
- Booth, D B (2004). “Chimney Damage in the Greater Seattle Area from the Nisqually Earthquake of 28 February 2001”. In: *Bulletin of the Seismological Society of America* 94.3, pp. 1143–1158. ISSN: 0037-1106. DOI: [10.1785/0120030102](https://doi.org/10.1785/0120030102).
- Bournonville, M., J. Dahnke, and D. Darwin (2004). *Statistical analysis of the mechanical properties and weight of reinforcing bars*. Tech. rep. Lawrence, KS: Structural Engineering and Materials Laboratory, The University of Kansas, p. 198.
- Bradley, Brendon A. (2010). “A generalized conditional intensity measure approach and holistic ground-motion selection”. In: *Earthquake Engineering & Structural Dynamics*, n/a–n/a. ISSN: 00988847. DOI: [10.1002/eqe.995](https://doi.org/10.1002/eqe.995).
- Bradley, Brendon A, Lynne S Burks, and Jack W Baker (2015). “Ground motion selection for simulation-based seismic hazard and structural reliability assessment”. In:

- Earthquake Engineering & Structural Dynamics* 44.13, pp. 2321–2340. ISSN: 00988847. DOI: [10.1002/eqe.2588](https://doi.org/10.1002/eqe.2588).
- Brocher, Thomas M., Tom Parsons, Richard J. Blakely, Nikolas I. Christensen, Michael A. Fisher, and Ray E. Wells (2001). “Upper crustal structure in Puget Lowland, Washington: Results from the 1998 Seismic Hazards Investigation in Puget Sound”. In: *Journal of Geophysical Research: Solid Earth* 106.B7, pp. 13541–13564. ISSN: 01480227. DOI: [10.1029/2001JB000154](https://doi.org/10.1029/2001JB000154).
- Building Seismic Safety Council (BSSC) (2009). *NEHRP Recommended Seismic Provisions for New Buildings and Other Structures (FEMA P-750)*. Tech. rep. Report prepared for the Federal Emergency Management Agency (FEMA), National Institute of Building Sciences, Washington, D.C.
- Campbell, Kenneth W and Yousef Bozorgnia (2014). “NGA-West2 Ground Motion Model for the Average Horizontal Components of PGA, PGV, and 5% Damped Linear Acceleration Response Spectra”. In: *Earthquake Spectra* 30.3, pp. 1087–1115. ISSN: 8755-2930. DOI: [10.1193/062913EQS175M](https://doi.org/10.1193/062913EQS175M).
- Çelebi, Mehmet, Toshihide Kashima, S. Farid Ghahari, Fariba Abazarsa, and Ertugrul Taciroglu (2016a). “Responses of a Tall Building with U.S. Code-Type Instrumentation in Tokyo, Japan, to Events Before, During, and After the Tohoku Earthquake of 11 March 2011”. In: *Earthquake Spectra* 32.1, pp. 497–522. ISSN: 8755-2930. DOI: [10.1193/052114EQS071M](https://doi.org/10.1193/052114EQS071M).
- Çelebi, Mehmet, Yoshiaki Hisada, Roshanak Omrani, S. Farid Ghahari, and Ertugrul Taciroglu (2016b). “Responses of Two Tall Buildings in Tokyo, Japan, Before, During, and After the M9.0 Tohoku Earthquake of 11 March 2011”. In: *Earthquake Spectra* 32.1, pp. 463–495. ISSN: 8755-2930. DOI: [10.1193/092713EQS260M](https://doi.org/10.1193/092713EQS260M).
- Chandramohan, R., J. W. Baker, and G. G. Deierlein (2017). “Robust and efficient nonlinear structural analysis using the central difference time integration scheme”. In: *Proc. of the 1st European Conference on OpenSees*.

- Chandramohan, Reagan (2016). "Duration of earthquake ground motion: Influence on structural collapse risk and integration in design and assessment practice." PhD thesis. Stanford University.
- Chandramohan, Reagan, Jack W Baker, and Gregory G Deierlein (2016a). "Impact of hazard-consistent ground motion duration in structural collapse risk assessment". In: *Earthquake Engineering & Structural Dynamics* 45.8, pp. 1357–1379. ISSN: 00988847. DOI: [10.1002/eqe.2711](https://doi.org/10.1002/eqe.2711).
- (2016b). "Quantifying the Influence of Ground Motion Duration on Structural Collapse Capacity Using Spectrally Equivalent Records". In: *Earthquake Spectra* 32.2, pp. 927–950. ISSN: 8755-2930. DOI: [10.1193/122813EQS298MR2](https://doi.org/10.1193/122813EQS298MR2).
- Chang, S W, A D Frankel, and C S Weaver (2014). *Report on Workshop to Incorporate Basin Response in the Design of Tall Buildings in the Puget Sound region, Washington*. Tech. rep. 20141196. U.S. Geological Survey, p. 28. DOI: [10.3133/ofr20141196](https://doi.org/10.3133/ofr20141196)..
- Charney, Finley A. (1990). "Wind drift serviceability limit state design of multistory buildings". In: *Journal of Wind Engineering and Industrial Aerodynamics* 36, pp. 203–212. ISSN: 01676105. DOI: [10.1016/0167-6105\(90\)90305-v](https://doi.org/10.1016/0167-6105(90)90305-v).
- Chiou, Brian S.-J. and Robert R Youngs (2014). "Update of the Chiou and Youngs NGA Model for the Average Horizontal Component of Peak Ground Motion and Response Spectra". In: *Earthquake Spectra* 30.3, pp. 1117–1153. ISSN: 8755-2930. DOI: [10.1193/072813EQS219M](https://doi.org/10.1193/072813EQS219M).
- Choi, Y., Jonathan P. Stewart, and Robert W Graves (2005). "Empirical Model for Basin Effects Accounts for Basin Depth and Source Location". In: *Bulletin of the Seismological Society of America* 95.4, pp. 1412–1427. ISSN: 0037-1106. DOI: [10.1785/0120040208](https://doi.org/10.1785/0120040208).
- City of Seattle Department of Planning and Developments (2015). *Alternate Design Requirements for Use of Special Reinforced Concrete Shear Walls in Over Height Buildings*.
- Clough, R. W. and J. Penzien (2010). *Dynamics of Structures*. Computers and Structures inc; 2nd Revised edition (2010), p. 738.

- Coffin L. F., Jr. (1954). "A study of the effect of cyclic thermal stresses on a ductile metal." In: *Trans. ASME* 76, pp. 931–950.
- (1971). "A note on low cycle fatigue laws." In: *J. Mater.* 6, pp. 388–402.
- Coleman, J and Enrico Spacone (2001). "Localization Issues in Force-Based Frame Elements". In: *Journal of Structural Engineering* 127.11, pp. 1257–1265. ISSN: 0733-9445. DOI: [10.1061/\(ASCE\)0733-9445\(2001\)127:11\(1257\)](https://doi.org/10.1061/(ASCE)0733-9445(2001)127:11(1257)).
- Cordova, Paul P, Gregory G Deierlein, Sameh S F Mehanny, and C Allin Cornell (2000). "Development of a two-parameter seismic intensity measure and probabilistic assessment procedure". In: *The Second US-Japan Workshop on Performance-Based Earthquake Engineering Methodology for Reinforced Concrete Building Structures*, pp. 187–206.
- Cox, Brady R, Ross W Boulanger, Kohji Tokimatsu, Clinton M Wood, Akio Abe, Scott Ashford, Jennifer Donahue, Kenji Ishihara, Robert Kayen, Kota Katsumata, Tadahiro Kishida, Takaji Kokusho, H Benjamin Mason, Robb Moss, Jonathan P Stewart, Kazushi Tohyama, and Dimitrios Zekkos (2013). "Liquefaction at Strong Motion Stations and in Urayasu City during the 2011 Tohoku-Oki Earthquake". In: *Earthquake Spectra* 29.S1, S55–S80. ISSN: 8755-2930. DOI: [10.1193/1.4000110](https://doi.org/10.1193/1.4000110).
- CSI (2018). *Perform 3D*.
- Day, Steven M., Robert Graves, Jacobo Bielak, Douglas Dreger, Shawn Larsen, Kim B. Olsen, Arben Pitarka, and Leonardo Ramirez-Guzman (2008). "Model for Basin Effects on Long-Period Response Spectra in Southern California". In: *Earthquake Spectra* 24.1, pp. 257–277. ISSN: 8755-2930. DOI: [10.1193/1.2857545](https://doi.org/10.1193/1.2857545).
- Dazio, Alessandro, Katrin Beyer, and Hugo Bachmann (2009). "Quasi-static cyclic tests and plastic hinge analysis of RC structural walls". In: *Engineering Structures* 31.7, pp. 1556–1571. ISSN: 01410296. DOI: [10.1016/j.engstruct.2009.02.018](https://doi.org/10.1016/j.engstruct.2009.02.018).
- De Biasio, Marco, Stephane Grange, Frederic Dufour, Frederic Allain, and Ilie Petre-Lazar (2014). "A Simple and Efficient Intensity Measure to Account for Nonlinear Structural

- Behavior". In: *Earthquake Spectra* 30.4, pp. 1403–1426. ISSN: 8755-2930. DOI: [10.1193/010614EQS006M](https://doi.org/10.1193/010614EQS006M).
- Deger, Zeynep Tuna and John W. Wallace (2015). "Collapse Assessment of the Alto Rio Building in the 2010 Chile Earthquake". In: *Earthquake Spectra* 31.3, pp. 1397–1425. ISSN: 8755-2930. DOI: [10.1193/060812EQS209M](https://doi.org/10.1193/060812EQS209M).
- Deng, Peng, Shiling Pei, Stephen Hartzell, Nicolas Luco, and Sanaz Rezaeian (2018). "A response spectrum-based indicator for structural damage prediction". In: *Engineering Structures* 166, pp. 546–555. ISSN: 01410296. DOI: [10.1016/j.engstruct.2018.03.046](https://doi.org/10.1016/j.engstruct.2018.03.046).
- Denolle, Marine A, Hiroe Miyake, Shigeki Nakagawa, Naoshi Hirata, and Gregory C Beroza (2014). "Long-period seismic amplification in the Kanto Basin from the ambient seismic field". In: *Geophysical Research Letters* 41.7, pp. 2319–2325. ISSN: 00948276. DOI: [10.1002/2014GL059425](https://doi.org/10.1002/2014GL059425).
- Detweiler, S.T. and A.M. Wein (2018). *The HayWired earthquake scenario Engineering implications: U.S. Geological Survey Scientific Investigations Report*. Tech. rep., p. 429. DOI: [10.3133/sir20175013v2](https://doi.org/10.3133/sir20175013v2).
- Dilger, W. and H. Cao (1991). "Behaviour of Slab-Column Connections under Reversed Cyclic Loading". In: *Proceedings of the Second International Conference of High-Rise Buildings*. China, p. 10.
- Dilger, W. G. and S. J. Brown (1995). *Earthquake Resistance of Slab-Column Connection*. Tech. rep. Zurich, Switzerland: ETH Zurich, pp. 22–27.
- Dobry, Ricardo and Susumu Iai (2000). "Recent Developments in the Understanding of Earthquake Site Response and Associated Seismic Code Implementation". In: *Conference proceedings - GeoEng 2000, an International Conference on Geotechnical & Geological Engineering : 19 - 24 November 2000, Melbourne, Australia*.
- Eads, Laura, Eduardo Miranda, and Dimitrios G Lignos (2015). "Average spectral acceleration as an intensity measure for collapse risk assessment". In: *Earthquake*

- Engineering & Structural Dynamics* 44.12, pp. 2057–2073. ISSN: 00988847. DOI: [10.1002/eqe.2575](https://doi.org/10.1002/eqe.2575).
- EduPro Civil Systems Inc. (2018). *ProShake 2.0*.
- Eibl, J and E Keinzel (1988). “Seismic shear forces in RC cantilever shear walls”. In: *9th World Conference on Earthquake Engineering*. Tokyo-Kyoto.
- FEMA (Federal Emergency Management Agency) (2009). *Quantification of Building Seismic Performance Factors*. Tech. rep. FEMA P695. Redwood, CA: Federal Emergency Management Agency.
- (2018). *Hazus*.
- Frankel, A (2009). “A Constant Stress-Drop Model for Producing Broadband Synthetic Seismograms: Comparison with the Next Generation Attenuation Relations”. In: *Bulletin of the Seismological Society of America* 99.2A, pp. 664–680. ISSN: 0037-1106. DOI: [10.1785/0120080079](https://doi.org/10.1785/0120080079).
- Frankel, A. (2013). “Rupture History of the 2011 M 9 Tohoku Japan Earthquake Determined from Strong-Motion and High-Rate GPS Recordings: Subevents Radiating Energy in Different Frequency Bands”. In: *Bulletin of the Seismological Society of America* 103.2B, pp. 1290–1306. ISSN: 0037-1106. DOI: [10.1785/0120120148](https://doi.org/10.1785/0120120148).
- Frankel, A., W. Stephenson, and D. Carver (2009). “Sedimentary Basin Effects in Seattle, Washington: Ground-Motion Observations and 3D Simulations”. In: *Bulletin of the Seismological Society of America* 99.3, pp. 1579–1611. ISSN: 0037-1106. DOI: [10.1785/0120080203](https://doi.org/10.1785/0120080203).
- Frankel, A., E. Wirth, and N. Marafi (2018a). *The M9 Project Ground Motions*. DOI: [10.17603/DS2WM3W](https://doi.org/10.17603/DS2WM3W).
- Frankel, Arthur (2017). “Modeling StrongMotion Recordings of the 2010 M w 8.8 Maule, Chile, Earthquake with High StressDrop Subevents and Background Slip”. In: *Bulletin of the Seismological Society of America* 107.1, pp. 372–386. ISSN: 0037-1106. DOI: [10.1785/0120160127](https://doi.org/10.1785/0120160127).

- Frankel, Arthur, Erin Wirth, Nasser Marafi, John Vidale, and William Stephenson (2018b). "Broadband Synthetic Seismograms for Magnitude 9 Earthquakes on the Cascadia Megathrust Based on 3D Simulations and Stochastic Synthetics, Part 1: Methodology and Overall Results". In: *Bulletin of the Seismological Society of America*. ISSN: 0037-1106. DOI: [10.1785/0120180034](https://doi.org/10.1785/0120180034).
- Frankel, Arthur D., Mark D. Petersen, Charles S. Mueller, Kathleen M. Haller, Russell L. Wheeler, E.V. Leyendecker, Robert L. Wesson, Stephen C. Harmsen, Chris H. Cramer, David M. Perkins, and Kenneth S. Rukstales (2002). *Documentation for the 2002 Update of the National Seismic Hazard Maps*. Tech. rep. U.S. Geological Survey Open-File Report 02-420, p. 33. DOI: <http://pubs.usgs.gov/of/2002/ofr-02-420/>.
- Frankel, Arthur D., William J. Stephenson, David L. Carver, Robert A. Williams, Jack K. Odum, and Susan Rhea (2007). *Seismic Hazard Maps for Seattle, Washington, Incorporating 3D Sedimentary Basin Effects, Nonlinear Site Response, and Rupture Directivity*. Tech. rep. USGS Open-File Report, p. 82.
- Frohlich, Cliff (2001). "Display and quantitative assessment of distributions of earthquake focal mechanisms". In: *Geophysical Journal International* 144.2, pp. 300–308. ISSN: 0956540X. DOI: [10.1046/j.1365-246x.2001.00341.x](https://doi.org/10.1046/j.1365-246x.2001.00341.x).
- Fugro (2018). *EZ-FRISK*. Walnut Creek, CA.
- Goda, Katsuichiro, Takashi Kiyota, Rama Mohan Pokhrel, Gabriele Chiaro, Toshihiko Katagiri, Keshab Sharma, and Sean Wilkinson (2015). "The 2015 Gorkha Nepal Earthquake: Insights from Earthquake Damage Survey". In: *Frontiers in Built Environment* 1. ISSN: 2297-3362. DOI: [10.3389/fbuil.2015.00008](https://doi.org/10.3389/fbuil.2015.00008).
- Gogus, Aysegul and John W. Wallace (2015). "Seismic Safety Evaluation of Reinforced Concrete Walls through FEMA P695 Methodology". In: *Journal of Structural Engineering* 141.10, p. 04015002. ISSN: 0733-9445. DOI: [10.1061/\(ASCE\)ST.1943-541X.0001221](https://doi.org/10.1061/(ASCE)ST.1943-541X.0001221).
- Goldfinger, C, C H Nelson, A E Morey, J E Johnson, J R Patton, E Karabanov, J Gutiérrez-Pastor, A T Eriksson, E Gràcia, G Dunhill, R J Enkin, A Dallimore, and T Vallier (2012).

- Turbidite Event History Methods and Implications for Holocene Paleoseismicity of the Cascadia Subduction Zone*. Tech. rep. U.S. Geological Survey, 170 p.
- Grammatikou, Sofia, Dionysis Biskinis, and Michael N. Fardis (2015). "Strength, deformation capacity and failure modes of RC walls under cyclic loading". In: *Bulletin of Earthquake Engineering* 13.11, pp. 3277–3300. ISSN: 1570-761X. DOI: [10.1007/s10518-015-9762-x](https://doi.org/10.1007/s10518-015-9762-x).
- Graves, Robert, Thomas H Jordan, Scott Callaghan, Ewa Deelman, Edward Field, Gideon Juve, Carl Kesselman, Philip Maechling, Gaurang Mehta, Kevin Milner, David Okaya, Patrick Small, and Karan Vahi (2011). "CyberShake: A Physics-Based Seismic Hazard Model for Southern California". In: *Pure and Applied Geophysics* 168.3-4, pp. 367–381. ISSN: 0033-4553. DOI: [10.1007/s00024-010-0161-6](https://doi.org/10.1007/s00024-010-0161-6).
- Graves, Robert W, Arben Pitarka, and Paul G Somerville (1998). "Ground-motion amplification in the Santa Monica area: Effects of shallow basin-edge structure". In: *Bulletin of the Seismological Society of America* 88.5, pp. 1224–1242.
- Gregor, Nick, Norman A Abrahamson, Gail M Atkinson, David M Boore, Yousef Bozorgnia, Kenneth W Campbell, Brian S.-J. Chiou, I M Idriss, Ronnie Kamai, Emel Seyhan, Walter Silva, Jonathan P Stewart, and Robert Youngs (2014). "Comparison of NGA-West2 GMPEs". In: *Earthquake Spectra* 30.3, pp. 1179–1197. ISSN: 8755-2930. DOI: [10.1193/070113EQS186M](https://doi.org/10.1193/070113EQS186M).
- Hall, John F and James L Beck (1986). "Structural damage in Mexico City". In: *Geophysical Research Letters* 13.6, pp. 589–592. ISSN: 00948276. DOI: [10.1029/GL013i006p00589](https://doi.org/10.1029/GL013i006p00589).
- Hancock, Jonathan and Julian J Bommer (2007). "Using spectral matched records to explore the influence of strong-motion duration on inelastic structural response". In: *Soil Dynamics and Earthquake Engineering* 27.4, pp. 291–299. ISSN: 02677261. DOI: [10.1016/j.soildyn.2006.09.004](https://doi.org/10.1016/j.soildyn.2006.09.004).
- Haselton, C B, A B Liel, S T Lange, and G G Deierlein (2008). *Beam-Column Element Model Calibrated for Predicting Flexural Response Loading to Global Collapse of RC Frame Buildings*. Tech. rep. PEER 2007/03. Pacific Earthquake Engineering Research Center.

- Haselton, Curt B, Jack W Baker, Abbie B Liel, and Gregory G Deierlein (2011a). "Accounting for Ground-Motion Spectral Shape Characteristics in Structural Collapse Assessment through an Adjustment for Epsilon". In: *Journal of Structural Engineering* 137.3, pp. 332–344. ISSN: 0733-9445. DOI: 10.1061/(ASCE)ST.1943-541X.0000103.
- Haselton, Curt B., Abbie B. Liel, Gregory G. Deierlein, Brian S. Dean, and Jason H. Chou (2011b). "Seismic Collapse Safety of Reinforced Concrete Buildings. I: Assessment of Ductile Moment Frames". In: *Journal of Structural Engineering* 137.4, pp. 481–491. ISSN: 0733-9445. DOI: 10.1061/(ASCE)ST.1943-541X.0000318.
- Hatayama, K, T Kanno, and K Kudo (2007). "Control Factors of Spatial Variation of Long-Period Strong Ground Motions in the Yufutsu Sedimentary Basin, Hokkaido, during the Mw 8.0 2003 Tokachi-oki, Japan, Earthquake". In: *Bulletin of the Seismological Society of America* 97.4, pp. 1308–1323. ISSN: 0037-1106. DOI: 10.1785/0120060200.
- Heaton, T. H. and S. H. Hartzell (1987). "Earthquake Hazards on the Cascadia Subduction Zone". In: *Science* 236.4798, pp. 162–168. ISSN: 0036-8075. DOI: 10.1126/science.236.4798.162.
- Heaton, T J, J Yang, and J Hall (2006). "Simulated performance of steel moment-resisting frame buildings in the 2003 Tokachi-Oki earthquake". In: *Bull. Earthq. Res. Inst., Univ. Tokyo* 81, pp. 325–329.
- Hognestad, Eivind (1951). *A Study of Combined Bending and Axial Load in Reinforced Concrete Members*. Tech. rep. University of Illinois at Urbana-Champaign, p. 128.
- Hsiao, Po-Chien, Dawn E Lehman, and Charles W Roeder (2013). "Evaluation of the response modification coefficient and collapse potential of special concentrically braced frames". In: *Earthquake Engineering & Structural Dynamics* 42.10, pp. 1547–1564. ISSN: 00988847. DOI: 10.1002/eqe.2286.
- Hueste, Mary Beth D., JoAnn Browning, Andres Lepage, and John W. Wallace (2007). "Seismic Design Criteria for Slab-Column Connections". In: *ACI Structural Journal* 104.4, pp. 448–458.

- Hueste, Mary Beth D., Thomas H.-K. Kang, and Ian N. Robertson (2009). "Lateral Drift Limits for Structural Concrete Slab-Column Connections Including Shear Reinforcement Effects". In: *Structures Congress 2009*. Reston, VA: American Society of Civil Engineers, pp. 1–10. ISBN: 9780784410318. DOI: [10.1061/41031\(341\)165](https://doi.org/10.1061/41031(341)165).
- Ibarra, Luis and Helmut Krawinkler (2011). "Variance of collapse capacity of SDOF systems under earthquake excitations". In: *Earthquake Engineering & Structural Dynamics* 40.12, pp. 1299–1314. ISSN: 00988847. DOI: [10.1002/eqe.1089](https://doi.org/10.1002/eqe.1089).
- Ibarra, Luis F, Ricardo A Medina, and Helmut Krawinkler (2005). "Hysteretic models that incorporate strength and stiffness deterioration". In: *Earthquake Engineering & Structural Dynamics* 34.12, pp. 1489–1511. ISSN: 0098-8847. DOI: [10.1002/eqe.495](https://doi.org/10.1002/eqe.495).
- IRIS (2013). *Wilber* 3.
- Jalayer, F. and C. A. Cornell (2009). "Alternative non-linear demand estimation methods for probability-based seismic assessments". In: *Earthquake Engineering & Structural Dynamics* 38.8, pp. 951–972. ISSN: 00988847. DOI: [10.1002/eqe.876](https://doi.org/10.1002/eqe.876).
- Jayaram, Nirmal, Ting Lin, and Jack W. Baker (2011a). "A Computationally Efficient Ground-Motion Selection Algorithm for Matching a Target Response Spectrum Mean and Variance". In: *Earthquake Spectra* 27.3, pp. 797–815. ISSN: 8755-2930. DOI: [10.1193/1.3608002](https://doi.org/10.1193/1.3608002).
- Jayaram, Nirmal, Jack W. Baker, Hajime Okano, Hiroshi Ishida, Martin W. Jr. McCann, and Yoshinori Mihara (2011b). "Correlation of response spectral values in Japanese ground motions". In: *Earthquakes and Structures* 2.4, pp. 357–376. ISSN: 2092-7614. DOI: [10.12989/eas.2011.2.4.357](https://doi.org/10.12989/eas.2011.2.4.357).
- Kawase, H (1996). "The Cause of the Damage Belt in Kobe: "The Basin-Edge Effect," Constructive Interference of the Direct S-Wave with the Basin-Induced Diffracted/Rayleigh Waves". In: *Seismological Research Letters* 67.5, pp. 25–34. ISSN: 0895-0695. DOI: [10.1785/gssr1.67.5.25](https://doi.org/10.1785/gssr1.67.5.25).

- Kempton, Justin J and Jonathan P Stewart (2006). "Prediction Equations for Significant Duration of Earthquake Ground Motions Considering Site and Near-Source Effects". In: *Earthquake Spectra* 22.4, pp. 985–1013. ISSN: 8755-2930. DOI: [10.1193/1.2358175](https://doi.org/10.1193/1.2358175).
- Kim, Sunai (2016). "Reliability of Structural Wall Shear Design for Tall Reinforced Concrete Core Wall Buildings". PhD thesis. University of California Los Angeles, p. 279.
- King County (2016). *King County Department of Assessments*.
- Klemencic, Ron, J. Andrew Fry, Gabriel Hurtado, and Jack P. Moehle (2006). "Performance of Post-Tensioned Slab-Core Wall Connections". In: *PTI Journal* 4.2.
- Koketsu, Kazuki, Hiroe Miyake, Afnimar, and Yasuhisa Tanaka (2009). "A proposal for a standard procedure of modeling 3-D velocity structures and its application to the Tokyo metropolitan area, Japan". In: *Tectonophysics* 472.1-4, pp. 290–300. ISSN: 00401951. DOI: [10.1016/j.tecto.2008.05.037](https://doi.org/10.1016/j.tecto.2008.05.037).
- Kolozvari, Kristijan, Kutay Orakcal, and John W. Wallace (2015a). "Modeling of Cyclic Shear-Flexure Interaction in Reinforced Concrete Structural Walls. I: Theory". In: *Journal of Structural Engineering* 141.5, p. 04014135. ISSN: 0733-9445. DOI: [10.1061/\(ASCE\)ST.1943-541X.0001059](https://doi.org/10.1061/(ASCE)ST.1943-541X.0001059).
- Kolozvari, Kristijan, Thien A. Tran, Kutay Orakcal, and John W. Wallace (2015b). "Modeling of Cyclic Shear-Flexure Interaction in Reinforced Concrete Structural Walls. II: Experimental Validation". In: *Journal of Structural Engineering* 141.5, p. 04014136. ISSN: 0733-9445. DOI: [10.1061/\(ASCE\)ST.1943-541X.0001083](https://doi.org/10.1061/(ASCE)ST.1943-541X.0001083).
- Kramer, Steven L (2014). "Performance-based design methodologies for geotechnical earthquake engineering". In: *Bulletin of Earthquake Engineering* 12.3, pp. 1049–1070. ISSN: 1570-761X, 1573-1456. DOI: [10.1007/s10518-013-9484-x](https://doi.org/10.1007/s10518-013-9484-x).
- Kramer, Steven Lawrence (1996). *Geotechnical earthquake engineering*. Prentice-Hall international series in civil engineering and engineering mechanics. Upper Saddle River, N.J: Prentice Hall. ISBN: 0-13-374943-6.

- Kulkarni, R, I Wong, J Zachariasen, C Goldfinger, and M Lawrence (2013). "Statistical Analyses of Great Earthquake Recurrence along the Cascadia Subduction Zone". In: *Bulletin of the Seismological Society of America* 103.6, pp. 3205–3221. ISSN: 0037-1106. DOI: [10.1785/0120120105](https://doi.org/10.1785/0120120105).
- Kunnath, Sashi K., YeongAe Heo, and Jon F. Mohle (2009). "Nonlinear Uniaxial Material Model for Reinforcing Steel Bars". In: *Journal of Structural Engineering* 135.4, pp. 335–343. ISSN: 0733-9445. DOI: [10.1061/\(ASCE\)0733-9445\(2009\)135:4\(335\)](https://doi.org/10.1061/(ASCE)0733-9445(2009)135:4(335)).
- Kwong, N Simon, Anil K Chopra, and Robin K McGuire (2015). "A ground motion selection procedure for enforcing hazard consistency and estimating seismic demand hazard curves". In: *Earthquake Engineering & Structural Dynamics* 44.14, pp. 2467–2487. ISSN: 00988847. DOI: [10.1002/eqe.2593](https://doi.org/10.1002/eqe.2593).
- Lehman, Dawn E, Jacob A Turgeon, Anna C Birely, Christopher R Hart, Kenneth P Marley, Daniel A Kuchma, and Laura N Lowes (2013). "Seismic Behavior of a Modern Concrete Coupled Wall". In: *Journal of Structural Engineering* 139.8, pp. 1371–1381. ISSN: 0733-9445. DOI: [10.1061/\(ASCE\)ST.1943-541X.0000853](https://doi.org/10.1061/(ASCE)ST.1943-541X.0000853).
- Liel, Abbie B, Nicolas Luco, Meera Raghunandan, and Casey P Champion (2015). "Modifications to risk-targeted seismic design maps for subduction and near-fault hazards". In: Vancouver, Canada. DOI: [10.14288/1.0076228](https://doi.org/10.14288/1.0076228).
- Liu, Hui (2004). "Effect of Concrete Strength on the Response of Ductile Shear Walls". PhD thesis. McGill University. ISBN: 9780494556603. DOI: [10.1177/001088048102200214](https://doi.org/10.1177/001088048102200214).
- Liu, P C and R J Archuleta (2002). "The effect of a low-velocity surface layer on simulated ground motion". In: *Seismological Research Letters* 73.2, pp. 195–272. ISSN: 0895-0695. DOI: [10.1785/gssrl.73.2.195](https://doi.org/10.1785/gssrl.73.2.195).
- Lopez, Alvaro, Peter Dusicka, and Ramiro Bazaiez (2018). "Performance of Seismically Sub-standard Bridge Reinforced Concrete Columns Subjected to Subduction Earthquakes". In: *Submitted to ASCE Journal of Bridge Engineering*.

- Luco, N., B.R. Ellingwood, R.O. Hamburger, J.D. Hooper, J.K. Kimball, and C.A. Kircher (2007). "Risk-Targeted versus Current Seismic Design Maps for the Conterminous United States." In: *Proceedings of the Structural Engineers Association of California 76th Annual Convention*.
- Maechling, P. J., F. Silva, S. Callaghan, and T. H. Jordan (2015). "SCEC Broadband Platform: System Architecture and Software Implementation". In: *Seismological Research Letters* 86.1, pp. 27–38. ISSN: 0895-0695. DOI: [10.1785/0220140125](https://doi.org/10.1785/0220140125).
- Mahin, Stephen A. and Vitelmo V. Bertero (1976). "Nonlinear Seismic Response of a Coupled Wall System". In: *Journal of the Structural Division* 102.9, pp. 1759–1780.
- Mander, J B, M J N Priestley, and R Park (1988). "Observed Stress-Strain Behavior of Confined Concrete". In: *Journal of Structural Engineering* 114.8, pp. 1827–1849.
- Manson, S. S. (1965). "Fatigue: A complex subject-Some simple approximations." In: *Exp. Mech.* 5.7, pp. 193–226.
- Marafi, N. A., M. O. Eberhard, J. W. Berman, E. A. Wirth, and Frankel A. D. (2018a). "Impacts of Simulated M9 Cascadia Subduction Zone Motions on Idealized Systems". In: *Earthquake Spectra*, In-review.
- Marafi, Nasser A., Jeffrey W. Berman, and Marc O. Eberhard (2016). "Ductility-dependent intensity measure that accounts for ground-motion spectral shape and duration". en. In: *Earthquake Engineering & Structural Dynamics* 45.4, pp. 653–672. ISSN: 00988847. DOI: [10.1002/eqe.2678](https://doi.org/10.1002/eqe.2678).
- Marafi, Nasser A., Marc O. Eberhard, Jeffrey W. Berman, Erin A. Wirth, and Arthur D. Frankel (2017). "Effects of Deep Basins on Structural Collapse during Large Subduction Earthquakes". In: *Earthquake Spectra* 33.3, pp. 963–997. ISSN: 8755-2930. DOI: [10.1193/071916EQS114M](https://doi.org/10.1193/071916EQS114M).
- Marafi, Nasser A., Andrew J. Makdisi, Marc O. Eberhard, and Jeffrey W. Berman (2018b). "Performance of RC Core-Walls during Simulated M9 Cascadia Subduction Zone Earthquake Scenarios". In: *Journal of Structural Engineering*.

- Marafi, Nasser A., Kamal A. Ahmed, Dawn E. Lehman, and Laura N. Lowes (2018c). "Variability in Seismic Collapse Probabilities of Solid and Coupled-Wall Buildings". In: *Journal of Structural Engineering*, In-review.
- Marsh, M. Lee and Christopher M. Gianotti (1995). "Inelastic Structural Response to Cascadia Subduction Zone Earthquakes". In: *Earthquake Spectra* 11.1, pp. 63–89. ISSN: 8755-2930. DOI: [10.1193/1.1585803](https://doi.org/10.1193/1.1585803).
- Matzke, Eric M., Rmy D. Lequesne, Gustavo J. Parra-Montesinos, and Carol K. Shield (2015). "Behavior of Biaxially Loaded Slab-Column Connections with Shear Studs". In: *ACI Structural Journal* 113.3, pp. 335–346.
- McKenna, F (2016). *OpenSees*.
- McPhee, D.K., V.E. Langenheim, R.E. Wells, and R.J. Blakely (2014). "Tectonic evolution of the Tualatin basin, northwest Oregon, as revealed by inversion of gravity data". In: *Geosphere* 10.2, pp. 264–275. ISSN: 1553-040X. DOI: [10.1130/GES00929.1](https://doi.org/10.1130/GES00929.1).
- Megally, S. and A. Ghali (2000). "Punching Shear Design of Earthquake-Resistant Slab-Column Connections". In: *ACI Structural Journal* 97.5, pp. 720–730.
- Menegotto, M. and P. Pinto (1973). *Method of analysis for cyclically loaded reinforced concrete plane frames including changes in geometry and non-elastic behavior of elements under combined normal force and bending*. Tech. rep. IABSE symposium on resistance and ultimate deformability of structures acted on by well-defined repeated loads.
- MezaFajardo, Kristel C, JeanFranois Semblat, Stphanie Chaillat, and Luca Lenti (2016). "SeismicWave Amplification in 3D Alluvial Basins: 3D/1D Amplification Ratios from Fast Multipole BEM Simulations". In: *Bulletin of the Seismological Society of America* 106.3, pp. 1267–1281. ISSN: 0037-1106. DOI: [10.1785/0120150159](https://doi.org/10.1785/0120150159).
- Miller, Rupert G. (1981). *Simultaneous Statistical Inference*. Springer Series in Statistics. New York, NY: Springer New York. ISBN: 978-1-4613-8124-2. DOI: [10.1007/978-1-4613-8122-8](https://doi.org/10.1007/978-1-4613-8122-8).
- Miner, M. A. (1945). "Cumulative damage in fatigue." In: *J. Appl. Mech.* 12, A159A164.

- Moehle, Jack P and Gregory G. Deierlein (2004). "A Framework methodology for Performance-Based Earthquake Engineering". In: *13th World Conference on Earthquake Engineering*.
- Morikawa, N and H Fujiwara (2013). "A New Ground Motion Prediction Equation for Japan Applicable up to M9 Mega-Earthquake". In: *Journal of Disaster Research* 8.5, pp. 878–888. ISSN: 1883-8030. DOI: [10.20965/jdr.2013.p0878](https://doi.org/10.20965/jdr.2013.p0878).
- Newmark, N M and W J Hall (1982). *Earthquake Spectra and Design*. Berkeley, CA: Earthquake Engineering Research Institute.
- NIED (National Research Institute for Earth Science and Disaster Resilience) (2018). *Strong-motion Seismograph Networks (K-NET, KiK-net)*.
- NIST (2011). *Selecting and Scaling Earthquake Ground Motions for Performing Response-History Analyses*. Tech. rep. Gaithersburg, MD: National Institute of Standards and Technology, p. 256.
- NZS (2015). *Draft Number: DZ 3101:2006 Amendment 3 Part 1 Public Comment Draft*. Wellington, New Zealand.
- Oh, Young-hun, Sang Whan Han, and Li-hyung Lee (2002). "Effect of boundary element details on the seismic deformation capacity of structural walls". In: *Earthquake Engineering & Structural Dynamics* 31.January, pp. 1583–1602. DOI: [10.1002/eqe.177](https://doi.org/10.1002/eqe.177).
- Okazaki, Taichiro, Dimitrios G. Lignos, Mitsumasa Midorikawa, James M. Ricles, and Jay Love (2013). "Damage to Steel Buildings Observed after the 2011 Tohoku-Oki Earthquake". In: *Earthquake Spectra* 29.S1, S219–S243. ISSN: 8755-2930. DOI: [10.1193/1.4000124](https://doi.org/10.1193/1.4000124).
- Olsen, Kim B., William J. Stephenson, and Andreas Geisselmeyer (2008). "3D crustal structure and long-period ground motions from a M9.0 megathrust earthquake in the Pacific Northwest region". In: *Journal of Seismology* 12.2, pp. 145–159. ISSN: 1383-4649. DOI: [10.1007/s10950-007-9082-y](https://doi.org/10.1007/s10950-007-9082-y).

- Park, R., M. J. Priestley, and W. D. Gill (1982). "Ductility of Square-Confined Concrete Columns". In: *Journal of the Structural Division* 108.4, pp. 929–950.
- Paulay, Thomas and M J Nigel Priestley (1992). *Seismic Design of Reinforced Concrete and Masonry Buildings*. New York: Wiley.
- PEER (2010). *Guidelines for Performance Based Seismic Design of Tall Buildings*. Tech. rep. 2010/05. Pacific Earthquake Engineering Research Center.
- (2014). *NGA West 2*. Berkeley, CA.
- (2017). *Tall Building Initiative: Guidelines for Performance-Based Seismic Design of Tall Buildings*. Tech. rep. Berkeley, CA: Pacific Earthquake Engineering Research Center.
- (2018). *NGA Subduction*. Berkeley, CA.
- Petersen, M D, C H Cramer, and A D Frankel (2002). "Simulations of Seismic Hazard for the Pacific Northwest of the United States from Earthquakes Associated with the Cascadia Subduction Zone". In: *Pure and Applied Geophysics* 159.9, pp. 2147–2168. ISSN: 0033-4553. DOI: [10.1007/s00024-002-8728-5](https://doi.org/10.1007/s00024-002-8728-5).
- Petersen, M D, C S Mueller, M P Moschetti, S M Hoover, J L Rubinstein, and et al. (2015). *Incorporating Induced Seismicity in the 2014 United States National Seismic Hazard Model Results of 2014 Workshop and Sensitivity Studies*. Tech. rep. 20151070. United States Geological Survey, p. 69.
- Petersen, M.D., M.P. Moschetti, P.M. Powers, C.S. Mueller, K.M. Haller, A.D. Frankel, Yuehua Zeng, Sanaz Rezaeian, S.C. Harmsen, O.S. Boyd, Ned Field, Rui Chen, K.S. Rukstales, Nico Luco, R.L. Wheeler, R.A. Williams, and A.H. Olsen (2014). *Documentation for the 2014 Update of the United States National Seismic Hazard Maps*. Tech. rep. U.S. Geological Survey Open-File Report 20141091, p. 243. DOI: [10.3133/ofr20141091](https://doi.org/10.3133/ofr20141091).
- Popovics, Sandor (1973). "A numerical approach to the complete stress-strain curve of concrete". In: *Cement and Concrete Research* 3.5, pp. 583–599. ISSN: 00088846. DOI: [10.1016/0008-8846\(73\)90096-3](https://doi.org/10.1016/0008-8846(73)90096-3).

- Priestley, M., G. Calvi, and M. Kowalsky (2007). *Displacement-based seismic design of structures*. IUSS Press, Italy.
- Pugh, Joshua S. (2012). "Numerical Simulation of Walls and Seismic Design Recommendations for Walled Buildings". PhD thesis. University of Washington, p. 448.
- Pugh, Joshua S., Laura N. Lowes, and Dawn E. Lehman (2015). "Nonlinear line-element modeling of flexural reinforced concrete walls". In: *Engineering Structures* 104, pp. 174–192. ISSN: 01410296. DOI: [10.1016/j.engstruct.2015.08.037](https://doi.org/10.1016/j.engstruct.2015.08.037).
- (2017). "Accurate Methods for Elastic Seismic Demand Analysis of Reinforced Concrete Walled Buildings". In: *Journal of Structural Engineering* 143.8, p. 04017062. ISSN: 0733-9445. DOI: [10.1061/\(ASCE\)ST.1943-541X.0001669](https://doi.org/10.1061/(ASCE)ST.1943-541X.0001669).
- Raghunandan, Meera and Abbie B. Liel (2013). "Effect of ground motion duration on earthquake-induced structural collapse". In: *Structural Safety* 41, pp. 119–133. ISSN: 01674730. DOI: [10.1016/j.strusafe.2012.12.002](https://doi.org/10.1016/j.strusafe.2012.12.002).
- Raghunandan, Meera, Abbie B Liel, and Nicolas Luco (2015). "Collapse Risk of Buildings in the Pacific Northwest Region due to Subduction Earthquakes". In: *Earthquake Spectra* 31.4, pp. 2087–2115. ISSN: 8755-2930. DOI: [10.1193/012114EQS011M](https://doi.org/10.1193/012114EQS011M).
- Rathje, Ellen M., Clint Dawson, Jamie E. Padgett, Jean-Paul Pinelli, Dan Stanzione, Ashley Adair, Pedro Arduino, Scott J. Brandenberg, Tim Cockerill, Charlie Dey, Maria Esteva, Fred L. Haan, Matthew Hanlon, Ahsan Kareem, Laura Lowes, Stephen Mock, and Gilberto Mosqueda (2017). "DesignSafe: New Cyberinfrastructure for Natural Hazards Engineering". In: *Natural Hazards Review* 18.3, p. 06017001. ISSN: 1527-6988. DOI: [10.1061/\(ASCE\)NH.1527-6996.0000246](https://doi.org/10.1061/(ASCE)NH.1527-6996.0000246).
- Richart, Frank Erwin, Anton Brandtzaeg, and Rex Lenoir Brown (1928). "A Study of The Failure of Concrete Under Combined Compressive Stresses". In: *University of Illinois Bulletin* XXVI.12, p. 110.
- Saatcioglu, Murat and Salim R Razvi (1992). "Strength and ductility of confined concrete". In: *Journal of Structural Engineering* 118.6, pp. 1590–1607.

- SEAOC (Structural Engineers Association of California) (2009). *The SEAOC Blue Book Compilation 2009*. 2009th ed. Sacramento, CA.
- Sengara, I. Wayan, Nanang Puspito, Engkon Kertapati, and Hendarto (2006). "Survey of Geotechnical Engineering Aspects of the December 2004 Great Sumatra Earthquake and Indian Ocean Tsunami and the March 2005 NiasSimeulue Earthquake". In: *Earthquake Spectra* 22.S3, pp. 495–509. ISSN: 8755-2930. DOI: [10.1193/1.2205199](https://doi.org/10.1193/1.2205199).
- Shahi, S. K. and J. W. Baker (2011). "An Empirically Calibrated Framework for Including the Effects of Near-Fault Directivity in Probabilistic Seismic Hazard Analysis". In: *Bulletin of the Seismological Society of America* 101.2, pp. 742–755. ISSN: 0037-1106. DOI: [10.1785/0120100090](https://doi.org/10.1785/0120100090).
- Shegay, A. V., C. J. Motter, D. E. Lehman, L. N. Lowes, K. J. Elwood, and R. S. Henry (2017). "Impact of Axial Load on the Seismic Response of Rectangular Walls". In: *Journal of Structural Engineering, Submitted*.
- Skarlatoudis, A, M Hosseini, and P Somerville (2015). *Basin Amplification Factors for Cascadia from the 2011 Tohoku Earthquake*. Tech. rep. United States Geological Survey.
- Song, Cheng, Santiago Pujol, and Andrs Lepage (2012). "The Collapse of the Alto Río Building during the 27 February 2010 Maule, Chile, Earthquake". In: *Earthquake Spectra* 28.S1, S301–S334. ISSN: 8755-2930. DOI: [10.1193/1.4000036](https://doi.org/10.1193/1.4000036).
- Stephenson, William J, Nadine G Reitman, and Stephen J Angster (2017). *P- and S-wave velocity models incorporating the Cascadia subduction zone for 3D earthquake ground motion simulations* Update for Open-File Report 20071348. English. Tech. rep. Reston, VA, p. 28. DOI: [10.3133/ofr20171152](https://doi.org/10.3133/ofr20171152).
- Stewart, Jonathan P, Saburoh Midorikawa, Robert W Graves, Khatareh Khodaverdi, Tadahiro Kishida, Hiroyuki Miura, Yousef Bozorgnia, and Kenneth W Campbell (2013). "Implications of the M w 9.0 Tohoku-Oki Earthquake for Ground Motion Scaling with Source, Path, and Site Parameters". In: *Earthquake Spectra* 29.S1, S1–S21. ISSN: 8755-2930. DOI: [10.1193/1.4000115](https://doi.org/10.1193/1.4000115).

- Thomsen, John H and John W Wallace (2004). "Displacement-Based Design of Slender Reinforced Concrete Structural Walls Experimental Verification". In: *Journal of Structural Engineering* 130.4, pp. 618–630. ISSN: 0733-9445. DOI: [10.1061/\(ASCE\)0733-9445\(2004\)130:4\(618\)](https://doi.org/10.1061/(ASCE)0733-9445(2004)130:4(618)).
- Tothong, Polsak and Nicolas Luco (2007). "Probabilistic seismic demand analysis using advanced ground motion intensity measures". In: *Earthquake Engineering & Structural Dynamics* 36.13, pp. 1837–1860. ISSN: 00988847. DOI: [10.1002/eqe.696](https://doi.org/10.1002/eqe.696).
- Tran, Thien A and John W Wallace (2015). "Cyclic Testing of Moderate-Aspect-Ratio Reinforced Concrete Structural Walls". In: *ACI Structural Journal* 112.06. DOI: [110.14359/51687907](https://doi.org/10.14359/51687907).
- Trifunac, M D and A G Brady (1975). "A study on the duration of strong earthquake ground motion". In: *Bulletin of the Seismological Society of America* 65.3, pp. 581–626. ISSN: 0037-1106.
- USGS (United States Geological Survey) (2001). *Configuration of the Seattle Urban Seismic Array for the February 28, 2001, M6.8, Nisqually Earthquake and Its Aftershocks*.
- (2008). *2008 NSHMP PSHA Interactive Deaggregation*.
- (2011). *Report on the 2010 Chilean Earthquake and Tsunami Response*. Tech. rep., p. 68.
- (2018a). *National Seismic Hazard Mapping Project (NSHMP) Code*.
- (2018b). *ShakeMaps*.
- (2018c). *US Seismic Design Maps*.
- Vallenas, Jose Miguel, Vitelmo V Bertero, and Egor P Popov (1979). *Hysteretic Behavior of Reinforced Concrete Structural Walls*. Tech. rep. UCB/EERC 79-20. Berkeley, California: University of California, Berkeley.
- Vamvatsikos, Dimitrios and C Allin Cornell (2002). "Incremental dynamic analysis". In: *Earthquake Engineering & Structural Dynamics* 31.3, pp. 491–514. ISSN: 0098-8847. DOI: [10.1002/eqe.141](https://doi.org/10.1002/eqe.141).
- Wallace, John W., Leonardo M. Massone, Patricio Bonelli, Jeff Dragovich, Ren Lagos, Carl Lüders, and Jack Moehle (2012). "Damage and Implications for Seismic Design of RC

- Structural Wall Buildings". In: *Earthquake Spectra* 28.S1, S281–S299. ISSN: 8755-2930. DOI: [10.1193/1.4000047](https://doi.org/10.1193/1.4000047).
- Wirth, Erin A., Arthur D. Frankel, Nasser Marafi, John E. Vidale, and W. J. Stephenson (2018). "Broadband Synthetic Seismograms for Magnitude 9 Earthquakes on the Cascadia Megathrust Based on 3D Simulations and Stochastic Synthetics, Part 2: Rupture Parameters and Variability". In: *Bulletin of the Seismological Society of America*. ISSN: 0037-1106. DOI: [10.1785/0120180029](https://doi.org/10.1785/0120180029).
- Wong, P. S., F. J. Vecchio, and H. Trommels (2013). *VECTOR2 & FORMWORKS USERS MANUAL*. Tech. rep.
- Yang, Jing (2009). "Nonlinear Responses of High-Rise Buildings in Giant Subduction Earthquakes". PhD thesis. California Institute of Technology, p. 185.
- Yassin, Mohd Hisham Mohd (1994). "Nonlinear Analysis of Prestressed Concrete Structures under Monotonic and Cyclic Loads". PhD thesis. University of California, Berkeley.
- Yong, A, E. M. Thompson, D. J. Wald, K. L. Knudsen, Jack K. Odum, W. J. Stephenson, and S. Haefner (2015). "Compilation of Vs30 Data for the United States". In: *U.S. Geological Survey Data Series 978*, p. 8.
- Zhao, J X (2006). "Attenuation Relations of Strong Ground Motion in Japan Using Site Classification Based on Predominant Period". In: *Bulletin of the Seismological Society of America* 96.3, pp. 898–913. ISSN: 0037-1106. DOI: [10.1785/0120050122](https://doi.org/10.1785/0120050122).